

TECHNISCHE UNIVERSITÄT MÜNCHEN

MAX-PLANCK-INSTITUT FÜR EXTRATERRESTRISCHE PHYSIK

**On the population of supernova remnants in the
Large Magellanic Cloud observed with XMM-Newton**

Pierre Maggi

Vollständiger Abdruck der von der Fakultät für Physik der Technischen Universität München zur Erlangung des akademischen Grades eines

Doktors der Naturwissenschaften

genehmigten Dissertation.

Vorsitzender: Univ.-Prof. Dr. B. Garbrecht

Prüfer der Dissertation:

1. Priv.-Doz. Dr. J. Greiner
2. Univ.-Prof. Dr. L. Oberauer

Die Dissertation wurde am 17.12.2014 bei der Technischen Universität München eingereicht und durch die Fakultät für Physik am 23.03.2015 angenommen.

“**M**^{AN} has a hunger to know. And to many a man, being endowed with the capacity to know, he has a duty to know. All knowledge, however small, however irrelevant to progress and well-being, is a part of the whole. It is of this that the scientist partakes. That is the challenge and joy of science.”

Vincent Dethier (1962), *To Know a Fly*

Zusammenfassung

SUPERNOVAÜBERRESTE (SNRs) prägen das interstellare Medium (ISM) durch Sterne, welche ihr Leben in einer Supernovaexplosion beenden. SNRs setzen große Mengen an Energie in ihre Umgebung frei und transportieren die Produkte der Nukleosynthese in das ISM, wobei sie dieses mit neu erzeugten schweren Elementen anreichern und mischen. Daher ist eine Untersuchung von SNRs grundlegend für ein besseres Verständnis der dynamischen und chemischen Entwicklung von Galaxien.

In dieser Dissertation untersuche ich die umfangreiche Population der SNRs in der Großen Magellanschen Wolke (LMC) mittels Daten des XMM-Newton Observatoriums. Die LMC ist eine sternbildende Galaxie, welche wir in der Draufsicht beobachten, sich nahe unserer Milchstraße befindet und nur durch geringe Vordergrundabsorption beeinflusst wird. Als solche eignet sie sich ideal als Laboratorium für Populationsstudien, insbesondere in Kombination mit der hohen Sammelfläche von XMM-Newton.

Hierfür berücksichtigte ich alle verfügbaren XMM-Newton Beobachtungen der LMC, welche Archivbeobachtungen, eigene Pointierungen auf SNRs, sowie Daten der großflächigen Durchmusterung der LMC umfassen. Die Daten wurden mittels einer für die Analyse von SNRs optimierten Programmsequenz reduziert.

Im ersten Teil der Arbeit konzentriere ich mich auf *einzelne* SNRs. Zunächst werden Daten einer XMM-Newton Beobachtungskampagne des SNRs der historischen SN 1987A analysiert, welcher als jüngster SNR der LMC eine Schlüsselrolle im Verständnis der frühen SNR-Entwicklung zukommt. Anschließend präsentiere ich die Entdeckung und wellenlängenübergreifende Analyse sechs *neuer* SNRs, die in der XMM-Newton LMC Durchmusterung gefunden wurden. Von diesen stellten sich drei als weit entwickelte Typ Ia SNRs heraus und helfen nun diese bislang unerkannte späte Entwicklungsphase zu definieren.

Im zweiten Teil untersuche ich die *Population* der LMC SNRs. Hierfür erarbeitete ich eine aktuelle Zusammenstellung von SNRs in der LMC, einschließlich der neu entdeckten Objekte, und analysierte alle verfügbaren XMM-Newton Spektren systematisch. Da SNRs zur Sondierung der sie beinhaltenen Galaxie verwendet werden können, konnte ich Elementhäufigkeiten der heißen Phase des ISM in der LMC bestimmen. Die unterschiedlichen Verhältnisse von Eisen zu leichten Elementen verglichen mit der Milchstraße reflektieren unterschiedliche Sternbildungen und chemische Entwicklungen beider Galaxien. Eine neue Methode, basierend auf der lokalen stellaren Umgebung und spektraler Information, wurde entwickelt um eine erste Klassifizierung von SNRs zu ermöglichen. Mit dieser kann das Verhältnis der Kernkollaps SN zu Typ Ia SN Rate zu $N_{CC}/N_{Ia} = 1.35^{(+0.11)}_{-0.24}$ bestimmt werden, was niedrig ist, verglichen mit den Ergebnissen von Durchmusterungen lokaler SNe und Galaxienhaufen. Die Implikationen dieser Messung werden weiter diskutiert. Schließlich wird die Population der LMC SNRs mit denen anderer Galaxien der Lokalen Gruppe mit unterschiedlichen Metallizität und Sternbildungshistorie verglichen.

Abstract

SUPERNOVA REMNANTS (SNRs) are the imprints of stars that died in supernova (SN) explosions on the interstellar medium (ISM). SNRs release enormous amounts of energy in their surrounding and return nucleosynthesis products to the ISM, enriching and mixing it with freshly-produced heavy elements. The study of SNRs is therefore crucial to our understanding of the dynamical and chemical evolution of galaxies.

In this dissertation, I study the rich population of SNRs in the Large Magellanic Cloud (LMC), using data from the *XMM-Newton* observatory. The LMC is a star-forming galaxy viewed almost face-on, in close proximity to our own Milky Way, and with little foreground absorption. As such, it is an ideal laboratory for population studies, in particular when combined with the high collecting power of *XMM-Newton*.

For this work, I use all available *XMM-Newton* observations towards the LMC, combining archival observations, dedicated pointings of SNR candidates, and data from a large area survey of the LMC. Data are reduced using a pipeline tailored to the analysis of SNRs.

In a first part, I focus on *individual* SNRs. First, I analyse data from a monitoring campaign with *XMM-Newton* of the remnant of the historical SN 1987A. As the youngest remnant in the LMC, it is a key system to understand the very early evolution of SNRs. Then, I present the discovery and multi-wavelength analysis of six *new* SNRs discovered serendipitously in the LMC survey with *XMM-Newton*. Three of those are amongst the most evolved type Ia SNRs, and help to define a late-time evolutionary phase previously unrecognised.

In a second part, I study LMC SNRs as a *population*. I compile an up-to-date sample of SNRs in the LMC, augmented of the newly-found objects. I perform a systematic analysis of all *XMM-Newton* spectra available. SNRs are used as probes of their host galaxy, thanks to which I can derive chemical abundances in the hot phase of the LMC ISM. The difference that is found in the abundance ratio of iron to lighter elements, compared to that of the Milky Way, reflects the different star formation and chemical enrichment histories (SFHs) of the two galaxies. Then, a new method is devised to tentatively type all SNRs, based on their local stellar environments, combined with spectral information. This constrains the current ratio of core-collapse to type Ia SN rates to $N_{CC}/N_{Ia} = 1.35^{+0.11}_{-0.24}$, which is lower in the LMC than in local SNe surveys and galaxy clusters. I discuss the implications of this measurement. Finally, the population of SNRs in the LMC is compared to other Local Group galaxies with different metallicities and star formation histories.

Contents

	Page
Zusammenfassung	v
Abstract	vii
I. Introduction	1
1. Overview	3
2. Observations of X-rays	5
2.1. Historical perspective and rationale for space observations	5
2.2. X-ray optics	6
2.2.1. Aperture modulation	6
2.2.2. Grazing-incidence optics	6
2.3. X-ray detectors	6
3. The physics of X-ray astronomy	9
3.1. X-ray emission processes	9
3.1.1. Non-thermal processes	9
3.1.2. Thermal processes	9
3.2. Absorption of X-rays	10
3.3. X-ray emission of hot plasmas	10
3.3.1. Continuum emission	10
3.3.2. Line emission	11
3.3.3. Non-equilibrium ionisation and plasma diagnostic	11
3.4. Shock waves in the interstellar medium	12
3.5. Accretion power	13
4. The Large Magellanic Cloud from an observational point of view	15
4.1. The LMC as a galaxy	15
4.1.1. Historical perspective	15
4.1.2. Properties and structure of the LMC	15
4.1.3. Star formation history	16
4.2. Multi-wavelength observations of the LMC	17
4.3. The LMC in X-rays	19
4.3.1. Previous X-ray observations	19
4.3.2. X-ray sources from the LMC region	19
4.3.2. A. Interlopers	19
4.3.2. B. Sources in the LMC	21

5. Supernova remnants and associated problematics	25
5.1. Supernovae: The swan song of dying stars	25
5.2. Life after death: Evolution of SNRs	26
5.3. Impact on the ISM	28
5.4. Observations of SNRs	28
5.5. Typing SNRs	30
II. Material and Methods	33
6. Technical description of XMM-Newton	35
6.1. Spacecraft and operations	35
6.2. Telescopes	36
6.3. EPIC instruments	36
6.3.1. The EPIC-pn camera	36
6.3.2. The EPIC-MOS cameras	36
6.4. Instrumental background	37
7. XMM-Newton observations and data reduction	39
7.1. Covering the LMC	39
7.2. Data reduction	39
8. Method of X-ray analysis for extended sources	43
8.1. Spectral extraction	43
8.2. Modelling the instrumental background	43
8.3. Modelling the astrophysical background	44
8.4. Simultaneous fitting	44
III. Results and discussion	47
9. The X-ray evolution of SNR 1987A	49
9.1. Introduction	49
9.2. Observations and data reduction	50
9.3. The spectra of SNR 1987A	51
9.3.1. Spectral model	51
9.3.2. Spectral evolution	51
9.4. X-ray light curve	54
9.5. Fe K lines	55
9.6. Discussion	56
10. Study of individual supernova remnants	59
10.1. Confirmation of the supernova remnant status of DEM L205	59
10.1.1. Observations and data reduction	59
10.1.1. A. X-rays	59
10.1.1. B. Other wavelengths	60
10.1.2. Data analysis and results	61
10.1.2. A. X-ray images	61
10.1.2. B. X-ray spectra	61
10.1.2. C. Radio morphology	64

10.1.2. D. Radio spectral energy distribution	65
10.1.2. E. Infrared flux measurement	66
10.1.3. Discussion	67
10.1.3. A. Origin of the IR emission	67
10.1.3. B. Properties of DEM L205 derived from the X-ray observations	67
10.1.3. C. Multi-wavelength morphology	68
10.1.3. D. Past and present star formation activity around the SNR	70
10.1.4. Summary	71
10.2. New iron-rich SNRs : The most evolved remnants of type Ia supernovae	72
10.2.1. Source identification and observations	72
10.2.2. Data analysis	73
10.2.3. Results	74
10.2.3. A. Multi-wavelength morphology	74
10.2.3. B. X-ray spectroscopy	78
10.2.3. C. Multi-component plasma fits	81
10.2.4. Discussion	82
10.3. MCSNR J0514–6840 and J0517–6759: the role of the environment in shaping SNRs	85
10.3.1. Source identification and observations	85
10.3.2. Data analysis	85
10.3.3. Results	85
10.3.3. A. Multi-wavelength morphology	85
10.3.3. B. X-ray spectroscopy	88
10.3.4. Discussion	90
11. On the X-ray properties of the rich population of LMC supernova remnants	95
11.1. Compiling a complete sample of LMC SNRs	95
11.1.1. Literature survey	96
11.1.2. Cleaning the sample: Objects not included	96
11.1.3. The final sample	99
11.2. The X-ray spectra of LMC SNRs	100
11.2.1. Extraction of the spectra	100
11.2.2. Spectral analysis and models	101
11.2.3. Results	103
11.2.3. A. General properties	103
11.2.3. B. The analysis of the brightest SNRs	104
11.2.3. C. Fe K emission from LMC SNRs	106
11.2.3. D. Detection of SN ejecta	108
11.2.3. E. Metal abundances of the LMC ISM	108
11.3. Phenomenology as function of SNR type	114
11.3.1. Selection of SNRs with secured classifications	114
11.3.1. A. Type Ia SNRs	114
11.3.1. B. Core-collapse SNRs	115
11.3.2. Snapshots of type Ia SNRs life: A new evolutionary phase	116
11.3.3. The wide variety of core-collapse SNRs	120
11.4. Measuring the ratio of CC to type Ia SNe using “SFH-typing”	122
11.4.1. Evaluating the local stellar environment	122
11.4.2. “SFH-typing” all LMC SNRs	124
11.4.3. Ratio of CC to type Ia SNe and implications	127

11.5. X-ray luminosity function of SNRs in the Local Group	129
11.6. 3D spatial distribution	134
IV. Conclusion and Outlook	139
Acknowledgments	145
Bibliography	147
A. SNR sample and X-ray spectral results	159
B. X-ray images, spectral extraction regions, and SFH for all LMC SNRs	171
Publication list	183

List of Figures

2.1. ROSAT PSPC and X-ray colour image from the ROSAT all-sky survey	7
4.1. Star formation history of the LMC	17
4.2. X-ray colour images combining all ROSAT PSPC pointings towards the LMC	20
6.1. Sketch of XMM-Newton spacecraft and close-up view of the mirrors	35
6.2. EPIC effective area curves	37
9.1. Evolution of the best-fit spectral parameters of SNR 1987A between and 2012	52
9.2. Light curve of SNR 1987A in the soft and hard X-ray ranges	54
9.3. Fe K lines of SNR 1987A between 2009 and 2013	55
9.4. Details of the Fe K lines region of the spectrum from December 2011	57
10.1. Optical view of the giant H II complex LHA 120-N 51	60
10.2. A multicolour view of DEM L205	62
10.3. EPIC-pn spectrum of DEM L205	63
10.4. Radio contours of DEM L205 overlaid on the X-ray image	65
10.5. Radio spectral index map of DEM L205 between wavelength of 36 cm, 20 cm, and 6 cm	65
10.6. <i>Spitzer</i> images of DEM L205 at 8, 24, and 70 μm	66
10.7. Stellar content around and high-resolution H α image of DEM L205	69
10.8. A multicolour view of MCSNR J0508–6830	74
10.9. A multicolour view of MCSNR J0511–6759	76
10.10. X-ray, optical, and radio images of MCSNR J0508–6902	77
10.11. H α quotient image of MCSNR J0508–6902	78
10.12. X-ray spectra of the MCSNR J0508–6830 and MCSNR J0511–6759	79
10.13. X-ray spectrum of MCSNR J0508–6902	80
10.14. A multicolour view of MCSNR J0514–6840	86
10.15. A multicolour view of MCSNR J0517–6759	87
10.16. X-ray spectra of the MCSNR J0514–6840 and MCSNR J0517–6759	89
10.17. X-ray image of MCSNR J0514–6840 overlaid with H I column density contours	90
10.18. Annotated view of MCSNR J0517–6759, as seen at 24 μm , H α , and [S II]	91
10.19. X-ray image of MCSNR J0517–6759 overlaid with H I column density and CO contours	91
11.1. The rejected SNR candidate in DEM L203 in optical lines with soft X-ray contours	98
11.2. Extraction regions used to extract spectra of MCSNR J0519–6902 and J0547–6943	102
11.3. Example of a strong SPC affecting the spectral analysis of MCSNR J0529–6653	103
11.4. Abundance ratio diagrams of LMC SNRs with fitted abundances	109
11.5. LMC ISM abundances (relative to solar values) measured in a sample of 16 X-ray SNRs	110
11.6. [O/Fe] and [Mg/Fe] vs. [Fe/H] diagrams for various LMC populations	111
11.7. Evolutionary sequence of type Ia SNRs in the LMC (X-ray)	118
11.8. Evolutionary sequence of type Ia SNRs in the LMC (optical)	119
11.9. X-ray images of core-collapse SNRs in the LMC	121

11.10. CMD of the MCPS stars around MCSNR J0534–6955	122
11.11. Star formation history around MCSNR J0528–6727 and J0534–6955	123
11.12. Count distribution of LMC SNRs as function of N_{OB} and r	124
11.13. r – N_{OB} diagram of LMC SNRs	125
11.14. Count distribution of the LMC SNRs as function of “Hint-SF”	126
11.15. Count distribution of the LMC SNRs as function of “Hint-final”	127
11.16. Cumulative X-ray luminosity function of SNRs in Local Group galaxies	130
11.17. Distribution of LMC SNRs on an HI column density map	134
11.18. Location of LMC SNRs relative to H α and red continuum emission.	135
11.19. N_H fraction = $N_H^X/N_H^{21\text{cm}}$ as function of broad-band X-ray luminosity	136
11.20. “Pseudo-3D” distribution of LMC SNRs, using N_H fractions as indicators of location along the line of sight	137

List of Tables

7.1. Energy bands used for X-ray images	41
9.1. Details of the XMM-Newton EPIC-pn observations of SNR 1987A	50
9.2. Spectral results, abundances, fluxes, and Fe K line properties of SNR 1987A	53
10.1. XMM-Newton observations of DEM L205	60
10.2. X-ray spectral results for DEM L205	64
10.3. Physical properties of DEM L205.	68
10.4. Physical properties of MCSNR J0508–6902 derived from the Sedov model.	80
10.5. Results of the multi-component plasma fits for the iron-rich SNRs.	82
10.6. X-ray spectral results for new LMC SNRs discovered in the XMM-Newton survey.	83
10.7. XMM-Newton log for observations of new SNRs discovered in the LMC survey.	84
10.8. Physical properties of MCSNR J0514–6840 derived from the Sedov model.	89
11.1. LMC objects erroneously classified as SNRs or candidates, not included in the final sample.	99
11.2. Fe K line properties of LMC SNRs	107
11.3. Constraints used for the identification of ejecta in SNR spectra.	108
11.4. SNRs with detected ejecta	112
11.5. LMC abundances	113
11.6. LMC remnants with a secured SN classification	116
11.7. Criteria and “Hints” attributed to SNRs as function of N_{OB} and r	125
11.8. “Hint-spec” attributed to SNRs as function of spectral results.	126
A.1. SNRs in the LMC	160
A.2. X-ray spectral results of LMC SNRs.	163
A.3. X-ray spectral results for bright LMC SNRs.	170

Part I.

Introduction

1. Overview

SUPERNOVA REMNANTS (SNRs) are the imprints of stars that died in supernova (SN) explosions on the interstellar medium (ISM). SNRs return nucleosynthesis products to the ISM, enriching and mixing it with freshly-produced heavy elements. A core-collapse (CC) SN is the explosion of a massive star and produces large quantities of α -group elements (e.g. O, Ne, Mg, Si, S). Thermonuclear (or type Ia) SNe mark the disruption of a carbon-oxygen white dwarf (WD) that reached the Chandrasekhar limit. Despite the essential role of type Ia SNe in cosmology as standard candles, leading to the discovery that the expansion of the Universe is accelerating, the exact nature of the progenitor system, being either a white dwarf accreting from a companion, or a merger of two white dwarves is still hotly debated. The thermonuclear burning front in a type Ia SN incinerates most of the progenitor to Fe-group elements.

SNe of either types release a tremendous amount of energy ($\sim 10^{51}$ erg), and have consequently a profound and long-lasting impact on their surrounding environment. SN ejecta are launched to velocities in excess of 10000 km s^{-1} , producing shock waves which heat the ISM and ejecta up to X-ray emitting temperatures ($> 10^6$ K). SNe are the main source of energy for the ISM, both in the form of kinetic energy or in the form of cosmic-rays that are accelerated at SNR shock fronts. As such, the study of SNRs is crucial to our understanding of the dynamical and chemical evolution of galaxies.

At the typical electron temperatures of SNR shocks ($kT \sim 0.2 - 5$ keV), all astrophysically abundant elements have emission lines in the range accessible to X-ray space observatories, making X-ray observations a powerful tool to study SNRs. Furthermore, SNRs are visible for a few tens of thousands of years. Thus, even though SNe are rare events in a galaxy (typically one per century or less), there will be tens or hundreds of SNRs for us to access. In our own Galaxy, the Milky Way (MW), about 300 SNRs are known. However, studies of Galactic SNRs are plagued by the large distance uncertainties towards sources in the Galactic plane. In addition, many important X-ray lines of O, Ne, Mg, and Fe are emitted at energies $kT < 2$ keV and are readily absorbed by the high column densities in front of Galactic sources.

On the other hand, the Large Magellanic Cloud (LMC), our closest neighbour galaxy, offers an ideal laboratory for such studies: First, the distance towards the LMC is relatively small (50 kpc) and very well studied. Second, the moderate inclination angle and small line-of-sight depth of the LMC mean that we can assume all LMC sources to be at a very similar distance. Third, the interstellar absorption by gas in the foreground is much smaller towards the LMC ($N_H < 10^{21} \text{ cm}^{-2}$) than towards the Galactic plane ($N_H > 10^{22} \text{ cm}^{-2}$), allowing observations even in the soft X-ray regime, below 1 keV. Finally, a wealth of data is available for the LMC, allowing for easier detection and multi-wavelength analysis of SNRs. For all these reasons, we can attempt to discover and study the *complete* sample of SNRs in the LMC.

The X-ray observatory *XMM-Newton*, flagship of the European Space Agency (ESA), was launched in December 1999. Thanks to its capability, including an unprecedented (and yet unmatched) sensitivity, it is an ideal instrument to study the population of SNRs in the LMC. Prior to this work, *XMM-Newton* had already performed many observations towards the LMC, often targeted at previously-known LMC SNRs. To this, one must add the ambitious project of the LMC survey, proposed as an *XMM-Newton* Very Large Programme (VLP, PI: Frank Haberl). This comprises 70 observations for a total exposure time of ~ 2 Ms, providing a contiguous coverage of the central region of the LMC.

Aims of this work

My PhD thesis is aimed at gaining new insights on SNRs, their evolution, and the interplay with their host galaxy (in that case, the LMC). My dissertation is the result of two distinct yet complementary approaches:

In the first one, the emphasis is put on *individual* objects. In particular, new SNRs discovered serendipitously in the large XMM-Newton survey of the central regions of the LMC, performed during my PhD, are examined in detail. Together with collaborators, I led multi-wavelength studies of six *new* SNRs. Thanks chiefly to XMM-Newton data, I measure physical conditions of the hot plasmas, search for SN ejecta emission, and constrain the SNR properties. Complementary data at optical, infrared, and radio wavelengths are used to investigate the role played by the local environment in the current appearance of the remnants. In addition, I analysed recent data from a monitoring campaign with XMM-Newton of SNR 1987A. It is the youngest remnant in the LMC (less than 30 years old), and therefore a key system to understand the very early evolution of a remnant.

In the second approach, the sample of LMC SNRs, augmented of the newly-found objects, is analysed as a *population*. I perform a systematic and homogeneous analysis of the X-ray spectra of all SNRs, which allows meaningful comparisons of objects at various evolutionary stages. Thanks to SNRs I can derive chemical abundances in the hot phase of the LMC ISM, and compare them to abundances measured in older populations (globular clusters and red giant stars). I investigate the connection between LMC SNRs and their local environment, characterised by different star formation histories (SFHs). Doing so, I devise a new method to tentatively type all LMC SNRs, which can then be used to retrieve the ratio of core-collapse to type Ia SN rates in the LMC. Then, via their X-ray luminosity function, I compare SNR populations in galaxies of the Local Group (M31, M33, LMC, SMC), which have different metallicities and SFHs. Finally, I study the spatial distribution of SNRs in the LMC with respect to cool gas, star-forming regions, and stars.

Outlines

This dissertation is organised as follows. In a first Part, I introduce the historical and physical bases of X-ray astronomy (Chapters 2 and 3), before presenting in detail the LMC (Chapter 4). In Chapter 5, I expand the description of SNRs and their astrophysical relevance. Part II presents the material and methods, starting with a technical description of XMM-Newton and its X-ray instruments (Chapter 6). All the XMM-Newton observations used in this thesis and the reduction of data are explicated in Chapter 7. The analysis method tailored to the X-ray emission of SNRs I developed and used is explained in Chapter 8.

My results are given and discussed in Part III. The X-ray evolution of SNR 1987A is the topic of Chapter 9. Multi-wavelength studies of new SNRs are the basis of Chapter 10. Then, various aspects of the population study of LMC SNRs are making up the sections of the long Chapter 11. Finally, I summarise the conclusions of the present thesis and present future prospects in Part IV. In Appendix A, I list the sample of LMC SNRs I compiled for this work, and give the results of the X-ray spectral analysis of the whole sample. In Appendix B, I present for each SNR an X-ray image, the regions used for spectral analysis, and the SFH local to the remnant.

2. Observations of X-rays

2.1. Historical perspective and rationale for space observations

WHILE studying electrical discharge in gas in 1895 at Würzburg University, Wilhelm Conrad Röntgen discovered a new form of radiation that he called “X-rays”¹. It is one of the most famous examples of a serendipitous discovery, that is, a discovery “by chance”². No X-ray interference could be observed, though they were believed to be a wave phenomenon. Max von Laue, in 1914 at the Ludwig-Maximilians-Universität (LMU) of Munich, thought in 1912 that the reason why no interference was seen was that slits in the gratings used were too large compared to the wavelengths of X-rays. He suggested that atoms in crystals could be used as gratings with much smaller spacings. The experiment by his assistants Walter Friedrich and Paul Knipping verified his predictions. Not only had they proved atoms were real, they also demonstrated that X-rays were indeed a form of electro-magnetic radiation with very short wavelengths (between $\sim 10^{-8}$ m and $\sim 10^{-11}$ m).

This would turn out to be both the blessing and the curse of X-ray astronomy. Because of their short wavelength, X-ray photons carry large amount of energies (of the order of keV). They are then naturally produced by hot, energetic, and violent phenomena in the Universe. Observations of cosmic X-rays can, and did, reveal a large number of such phenomena. On the other hand, X-rays interact easily with atoms: The many atoms in the atmosphere absorb efficiently X-ray photons. About half of the 1 keV incident radiation is stopped before reaching an altitude of 100 km. To observe high-energy light, it is therefore necessary to place telescopes and detectors high above the ground, using balloons, sounding rockets, or satellites. Consequently, it is not surprising that X-ray astronomy started only with the dawning of the space age.

X-ray astronomy began in 1949 with the detection of X-rays from the hot corona of the Sun by the group of Herbert Friedman (Naval Research Laboratory), using detectors aboard V-2 rockets evacuated from Germany at the end of World War II. The same group searched for non-solar X-ray sources in the 1950s, though without success. The breakthrough came in June 1962, when a rocket carried improved detectors above the atmosphere with the goal of detecting lunar X-rays. The experiment was led by Riccardo Giacconi of the American Science and Engineering (AS&E) company. Instead of detecting the Moon, a strong peak was recorded some 30° away. Upon studying several other explanations, they concluded that they had discovered the first cosmic X-ray source³ (Giacconi et al. 1962). After verification in subsequent rocket flights (Gursky et al. 1963) and the identification of a second source associated to the Crab Nebula (Bowyer et al. 1964), the field underwent a very rapid growth (Hirsh 1983). Progress culminated in 1970 with the launch of “Uhuru”, the first orbiting X-ray observatory, conducting in its $2\frac{1}{4}$ year lifespan the first all-sky X-ray survey.

Besides the development of space technology, the success of X-ray astronomy has been possible thanks to the joint progress of X-ray optics and detectors. I introduce those topics in the following sections.

¹In his honour, X-rays are still called “Röntgenstrahlung” (Röntgen radiation) in German.

²But to that I quote Louis Pasteur’s words “Chance favours only the prepared minds” (French: “*Le hasard ne favorise que les esprits préparés*”, speech in Douai, 1854).

³It turned out that the detection threshold of Friedman’s detectors, in the previous decade, was just above what would have been needed to make that discovery.

2.2. X-ray optics

Contrary to visible light, X-rays are not reflected but absorbed by mirror surfaces. The design of telescopes used in “standard” astronomy cannot be employed. Two methods were derived to measure the position of X-ray sources and/or focus X-ray light : Aperture modulation and grazing-incidence telescopes.

2.2.1. Aperture modulation

It is possible to spatially locate X-rays with a *temporal* modulation of the “aperture” of the instrument (i. e. the portion of the sky exposed to the detector). One possibility is via Moon (or Earth) occultation, where an X-ray source is occulted as the Moon passes in front of it. One then knows the position of the source (and angular extent for extended sources). Another common way is (or was) to use collimators, such as two or more grids of absorbing material. As the instrument scans the sky, or as the collimator rotates, the signal of a source produces a unique modulated signal that is used to reconstruct its position.

Alternatively, a *spatial* modulation of the aperture is achieved by a pattern of holes (a “code”) in an X-ray-absorbing mask, placed in front of a position-sensitive detector. Thus, the observed distribution of intensity is the result of the folding of the sky distribution by the modulation function of the coded-mask. Though far from being straightforward, the sky distribution can be reconstructed by inverting the problem.

2.2.2. Grazing-incidence optics

X-rays can be reflected off a surface in the case of *total reflection*, when the incident angle is below a critical angle i_g , which is typically less than 1° – 2° . Using this grazing-incidence total reflections, Hans Wolter (1952) noted that a segment of paraboloid of revolution could be used to focus X-rays, though no image can be formed because of severe aberrations. He further demonstrated that using a system with an even number of mirrors (limited in practice to two), images could be formed. He proposed three configurations using combinations of paraboloid, hyperboloid, and ellipsoid mirrors.

In the pioneering years of X-ray astronomy, Giacconi & Rossi (1960) realised that Wolter’s idea, originally developed for the purpose of X-ray microscopy, was exactly what was needed to build X-ray telescopes. Very importantly, they suggested to “nest” several mirrors of decreasing diameter to increase the collecting area. The design usually adopted is the so-called Wolter-I configuration⁴. X-rays are first reflected off a paraboloid, before undergoing a second reflection off a hyperboloid. Such telescopes were first tested for solar observations in 1963 and 1965, aboard rocket flights. Further developments culminated with the launch of *Einstein* in 1978, the first satellite carrying an X-ray telescope (effective area of 100 cm^2 at 1 keV) for extrasolar observations. This opened a new page of (X-ray) astronomy.

Since then, most orbiting X-ray observatories use Wolter telescopes, which have been vastly improved in terms of collecting area (peaking at 4260 cm^2 for *XMM-Newton*) and angular resolution (less than $1''$ for *Chandra*). Coded-mask telescopes are still used for major hard X-ray observatories (such as *Integral* and *Swift*) because at higher energies the required grazing angles are vanishingly small, demanding too long focal lengths.

2.3. X-ray detectors

Because the X-ray (photon) flux of sources is much less than at lower energies, one is able to record individual photons hitting the detector. An observation then consists of a list of *events*. Each event carries several pieces of information : usually time of detection, energy of the incoming photons, and eventually

⁴It is the only one allowing nesting.

the position on the detector. Measuring the polarisation of the X-ray photon as well would be very valuable, (e. g. Weisskopf et al. 2008; Marin et al. 2014).

Gaseous detectors were the first type of instrument used. X-ray photons enter a gas-filled chamber through an entrance window. Ionisation of gas atoms by the X-ray photon produces electron-ion pairs. In the tube, an anode wire placed at high voltage accelerates and collects the electrons. Usually, the voltage is set such that electrons gain enough energy to ionise more atoms, leading to charge multiplication (avalanche). The strength of the signal (called *pulse-height amplitude*, PHA) is proportional to the initial number of electrons released by the X-ray photon, and is as such related to the energy of the photon. These detectors are therefore called **proportional counters**. Late-type proportional counters gained imaging capabilities by using multi-wire grids. The charge avalanche is distributed on a limited number of wires. Reading the signal distribution on each wire allows to reconstruct the two-dimensional position of the event. The best example is the Position Sensitive Proportional Counters (PSPCs), two identical detectors used by the German mission ROSAT, which performed the first *imaging* all-sky X-ray survey (Fig. 2.1).

Proportional counters have been the workhorse of X-ray astronomy in the first 40 years. They were overthrown by the advent of *solid state detectors*. The incoming X-ray is absorbed in a thin layer of semi-conducting silicon. The first electron-hole pair can be greatly amplified, and many free electrons are collected. The strength of the signal then yields a measurement of the incident photon energy with good resolution. Solid state detectors operate at low temperature to avoid thermal noise. *Einstein's* instrument Solid State Spectrometer (SSS) was the first of its kind to be placed in orbit.

Rapid progress made possible to stack small SSS in arrays of $\sim 10^6$ pixels that are read sequentially, providing high-resolution imaging performances. These detectors are called **charge-coupled devices** (CCDs) and possess an extremely high quantum efficiency. The Japanese mission ASCA was the first to utilise imaging CCD arrays. All large mission since then (*Chandra*, *XMM-Newton*, *Suzaku*) carry CCD cameras as prime instruments. Upcoming missions, such as *Astro-H* or *Athena*, will use (micro-) **calorimeters**, which are active pixels cooled down below 1 K, measuring the heat pulse of an absorbed X-ray photons. This will allow high-resolution imaging (i. e. non-dispersive) spectroscopy.

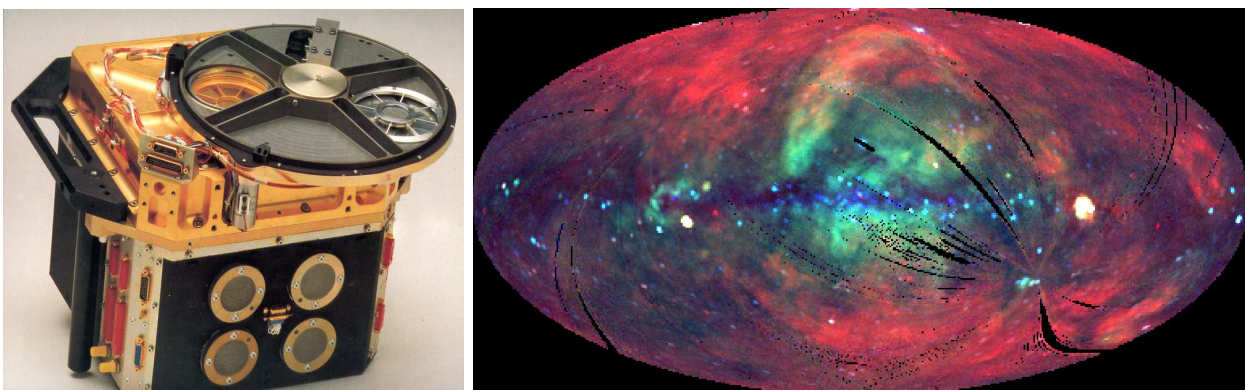


FIGURE 2.1 – *Left*: One of ROSAT PSPC with filter wheel and front end electronics. *Right*: X-ray colour image from the ROSAT all-sky survey in Galactic coordinates. Credit: Max-Planck-Institut für extraterrestrische Physik (<http://www.mpe.mpg.de/>) and S. L. Snowden.

3. The physics of X-ray astronomy

3.1. X-ray emission processes

HERE, I summarise briefly the physical processes leading to X-ray emission that are the most relevant to high-energy astronomy. There are either thermal or non-thermal processes, meaning that the emission properties are controlled (or not) by the temperature T of the source.

3.1.1. Non-thermal processes

3.1.1. A. Synchrotron radiation from relativistic electrons

Charged particles travelling in a magnetic field \mathbf{B} are accelerated by the Lorentz force and therefore radiate. As electrons have a much lower mass than ions, they are more easily accelerated and dominate the emission. The distribution of energetic electrons usually follows a power law, and the resulting synchrotron spectrum produced by these particles is also a power law. The average photon energy is proportional to BE^2 , where E is the energy of the electron. To produce appreciable X-ray synchrotron radiation, as in the Crab Nebula, electrons with energies of about 10 TeV must be present.

3.1.1. B. Inverse Compton scattering

Ultra-relativistic electrons can up-scatter photons to higher energies in the so-called inverse Compton scattering process. A photon with energy $h\nu$ can be up-scattered by an electron with a Lorentz factor γ ($= 1/\sqrt{1 - (v/c)^2}$) to an energy of $\gamma^2 h\nu$. Important sources are e. g. photons from the cosmic microwave background, which pervades all space, or quasar jets, since the photon energy density is high and relativistic particles abound.

3.1.2. Thermal processes

3.1.2. A. Black-body radiation

When matter and radiation are in thermodynamical equilibrium, the radiated spectrum has a well-known continuum, following the Planck spectrum :

$$I(E, T) = \frac{2E^3}{h^2 c^2} \frac{1}{e^{E/kT} - 1} \quad (3.1)$$

where h is the Planck constant and c the speed of light. The energy of the peak emission is only dependent on T (Wien's displacement law). For $T \gtrsim 10^5$ K, the black-body spectrum will enter the X-ray regime. The hot surface of white dwarfs or young (isolated) neutron stars are well described by hot black-body emission.

3.1.2. B. Bremsstrahlung

In a plasma, electrons radiate as they are accelerated in the Coulomb fields of ions. This emission is called Bremsstrahlung (German for "braking radiation"). At thermal equilibrium, electrons have a Maxwellian velocity distribution and radiate in a continuum with a well-defined spectrum, determined only by the

temperature and proportional to $Z_i^2 n_e n_i g(T) (kT)^{1/2} e^{-E/kT}$, with g the Gaunt factor, n_i and Z_i the density and charge number of the ion i . Bremsstrahlung is an important component of the thermal emission of hot gas which is reviewed in Sect. 3.3.

3.2. Absorption of X-rays

It was already said that X-rays interact easily with atoms. Let us now explore the consequence of absorption for observations of distant sources. Consider a beam of X-ray photons travelling through a slab of width dx filled with matter (e.g. gas). Atoms in the slab have a cross-section σ for interaction with the photons. Let I_0 be the intensity $I(x)$ of the beam at the position x where the photons enter the slab. The emerging radiation has intensity $I(x + dx) = I(x) - \delta I$, where δI is the loss of intensity, i. e. the total number of photons which interacted with atoms in the slab. Therefore $\delta I = \sigma n dx I(x)$, n being the number density of atoms. One can then write $I(x + dx) - I(x) = -\sigma n dx I(x)$ or ;

$$\frac{dI(x)}{I(x)} = -\sigma n dx \quad (3.2)$$

which gives $I(x) = I_0 e^{-\sigma n x}$. X-rays are exponentially absorbed when travelling through matter.

In astronomy, light is absorbed by all the matter integrated along the line of sight towards the source, such that one replaces $n x$ by N_H , the number density in a 1-cm² column between the observer and the source. In addition, the cross-section is a strong function of the atom charge number Z and energy E of the photon. σ varies as $Z^3 E^{-3}$, which means that : *i*) heavier elements have much greater cross-sections than H, but with low abundances, so hydrogen is still the most absorbing species in astrophysical settings; *ii*) for a given element, σ decreases with increasing photon energy. However, as the energy becomes sufficient to knock-out one of the more tightly bound electron, there is an abrupt rise of the cross-section, causing *absorption edges*.

3.3. X-ray emission of hot plasmas

In many astrophysical situations where hot ($T > 10^5$ K) plasmas are found, the *coronal approximation* can be used: the plasma is ionised, has a low density ($n_e \ll 10^8$ cm⁻³), and is therefore optically thin to its own radiation. The emission spectrum of the plasma, thermal in nature, can be easily calculated since no radiation transfer models are needed. Such plasmas are ubiquitous in the Universe, from the coronae of cool stars (like our Sun) to galaxy clusters. More importantly for this work, the vast majority of SNR emission is that of a hot, optically thin plasma.

3.3.1. Continuum emission

The source of continuum predominantly seen in hot plasmas is Bremsstrahlung (free-free emission). Its nature has been introduced in Sect. 3.1. Here, however, one has to account for the many ion species present. Assuming again a Maxwellian distribution for the electrons, the emissivity of the plasma is (e. g. [Vink 2012](#)) :

$$\epsilon(E, T_e) = \frac{2^5 \pi e^6}{3 m_e c^3} \left(\frac{2\pi}{3 k m_e} \right)^{1/2} g(T_e) T_e^{-1/2} e^{-E/kT_e} \times n_e \sum_i n_i Z_i^2 \quad (3.3)$$

where the sum \sum_i is done over all ions present, which is function of the temperature, ionisation state, and composition of the plasma. *Metal-rich* plasmas have higher emissivity, due to the Z_i^2 factor, and because ionised metals contribute more free electrons than H and He.

Free-bound emission is also present. It arises when an electron collides with an ion and recombines on one of the atomic shells. This produces a so-called *radiative recombination continuum* (RRC). The energy of the emitted photon is the sum of the electron kinetic energy and the ionisation potential of the level it recombines on. Since the kinetic energy is not quantised this radiation is a continuum, which however shows a sharp edge near the series limit and then declines (exponentially) with increasing energy above the edge (e. g. Liedahl 1999).

Another source of continuum emission is the two-photon process. Electrons in H- and He-like ions are excited to the metastable $2s$ level. Because of selection rules, the $2s$ electrons cannot decay by a single-photon transition. Instead, it can decay by the simultaneous emission of two photons that share the total energy of the transition (hence the spectrum is a continuum). Collisional de-excitation is possible (and dominant) only in high density cases, unsuited to astrophysical plasmas.

3.3.2. Line emission

The line emission of hot plasmas originates in collisional excitation of ions by free electrons. The ion is left in an excited state and quickly relaxes to its ground state by emitting photon(s) carrying the energy of the transition(s). In the coronal approximation: *i*) ions are assumed to be in the ground state, *ii*) ions do not de-excite collisionally (the density is too low), and *iii*) the emitted photons leave the optically thin system unaffected. The volume emissivity of a particular line transition (level $a \mapsto$ level b) in an ion Z^{+i} is written :

$$P_{Z^{+i}}^{ab} = n_e n_H a_Z F_Z^i S_{Z^{+i}}^{ga} B_{ab} \quad (3.4)$$

with a_Z the abundance relative to H of element Z and F_Z^i the ionic fraction of the ion Z^{+i} . B_{ab} is the radiative branching ratio of transition $a \mapsto b$, and $S_{Z^{+i}}^{ga}$ is the electron excitation rate of ion Z^{+i} from ground state to level a , that is integrated over the electron Maxwellian velocity distribution. To obtain the actual spectrum, one needs to calculate the line flux of all possible transitions⁵ of each ion of each element present in the plasma, for a given set of parameters, essentially temperature and abundances. These parameters are set externally and are not part of the model. The calculations are performed by plasma emission codes. Popular codes are for instance Mekal (which stands for MEwe-KAastra-Liedahl Mewe & Gronenschild 1981; Mewe et al. 1985; Kaastra & Mewe 1993; Liedahl et al. 1995) or the Astrophysical Plasma Emission Code (APEC Smith et al. 2001; Foster et al. 2012).

Another process causing line emission is *fluorescence*. This designates the radiative adjustment of an ion from which an electron is removed from the *inner shell* (e. g. from the K-shell, whilst L- and M-shells are still filled). The probability of having radiative transition in the case of inner-shell ionisation⁶ is called the fluorescence yield. It increases with higher nuclear charge Z , being particularly large ($\sim 34\%$) for iron (Bambynek et al. 1972). The energy of the transition is also a function of the ionisation state, as the more numerous outer-shell electrons of near-neutral ions reduce the effective charge of the nucleus. For instance in the case of Fe, the $K\alpha$ line energy is ~ 6.4 keV for Fe II – Fe XVII and then slowly rises to 6.7 keV for Fe XVII – Fe XXV.

The composite (continuum + line) spectrum of a hot plasma allows us to measure the physical conditions of the plasma. The temperature can be obtained from the shape of the continuum and the particular lines present, whilst the strength of the lines of an element relative to the continuum or to lines of other elements reveals the composition of the plasma.

3.3.3. Non-equilibrium ionisation and plasma diagnostic

So far it was assumed that the ionisation state of the plasma (i. e. the ionic fraction F_Z^i for each ion i of all element Z) is known, allowing the continuum+line spectrum to be calculated. At the so-called collisional

⁵more than tens of thousands in modern emission codes.

⁶Non-radiative de-excitations are called Auger transitions.

ionisation equilibrium (CIE), the ionic fraction can be completely determined as function of the temperature T_e and atomic physics (i. e. with the rates of ionisation and recombination by electron collision, [Arnaud & Rothenflug 1985](#)). For instance, Fe XVII (Ne-like) is the dominating ion for temperatures between 2.5 MK and 8 MK (0.2 keV – 0.7 keV), whilst at higher temperature (16 MK – 80 MK, or 1.4 keV – 7 keV), iron is mostly in the He-like form Fe XXV ([Arnaud & Raymond 1992](#)).

Ionisations occur through collisions with electrons. The ionisation balance depends critically on the electron density n_e . In extremely low-density plasma, collisions are rare. There are long delays between a thermodynamic event and the establishment of ionisation equilibrium : elements are less ionised than at CIE for a given temperature. This is particularly true for the X-ray emitting plasma created by supernova shocks (see Sect. 3.4), which are often out of CIE.

The ionisation balance time evolution for a given element of charge number Z is (e. g. [Liedahl 1999](#)) :

$$\frac{dF_i}{dt} = n_e [\alpha_{i-1}(T_e) F_{i-1} - (\alpha_i(T_e) + R_{i-1}(T_e)) F_i + R_i(T_e) F_{i+1}] \quad (3.5)$$

where F_i is the ionic fraction of the i th ion ($i = 1$, neutral; $i = 2$, singly ionised;...; $i = Z + 1$, fully ionised), $\alpha_i(T_e)$ is the collisional ionisation rate *from* state i to $i + 1$, and R_i is the recombination rate *from* $i + 1$ to i . Equation (3.5) is valid only if multiple ionisations can be neglected. For each element there is a set of $Z + 1$ coupled equations. Instead of direct numerical integration, most spectral codes use the fast approach of [Masai \(1984\)](#) and [Hughes & Helfand \(1985\)](#). The $(Z + 1)$ version of eq. (3.5) are rewritten in matrix form :

$$\frac{d\mathbf{F}}{dt} = n_e \mathbf{A}(\mathbf{T}_e) \mathbf{F} \quad (3.6)$$

where \mathbf{F} is the $(Z + 1)$ vector containing the ionic fractions and $\mathbf{A}(\mathbf{T}_e)$ is the tridiagonal matrix formed with the rates α_i and R_i . After the eigen-values and vectors are known, one can solve the uncoupled equations :

$$\frac{d\mathbf{F}'}{dt} = n_e \lambda \mathbf{F}' \quad (3.7)$$

where λ is the diagonal matrix containing the eigenvalues and $\mathbf{F}' = \mathbf{V}^{-1} \mathbf{F}$, with \mathbf{V}^{-1} the inverse matrix formed from the eigenvectors.

3.4. Shock waves in the interstellar medium

I have presented some of the emission processes occurring in hot (multi-million degrees) plasmas, without discussing what heating sources could produce such plasmas. One possible route is via **shock-heating**, where (part of) the kinetic energy of shock waves is transformed in thermal energy. It is the predominant energy input process in supernova remnants and therefore most relevant to this work.

The ISM obeys the magneto-hydrodynamic (MHD) equations that govern the evolution of mass, energy, pressure, etc... Stellar winds or supernova ejecta reach velocities (greatly) in excess of 1000 km s^{-1} , which is much larger than the ISM sound speed (about 10 km s^{-1} for the diffuse phase). Upon impacting the ambient ISM they will drive a shock into it that will propagate ahead. The interstellar gas is highly perturbed at the shock front, and physical values (density, velocity, pressure) have physical *discontinuities* at the interface between the shocked and unshocked gas. The properties of the gas just behind the shock can be obtained by the fluid equations applied in the shock frame (travelling at velocity v_s in the ISM frame). We note the density, velocity, and pressure ahead of the shock (“upstream”) as ρ_1, v_1, p_1 , respectively, and those behind the shock (“downstream”) as ρ_2, v_2, p_2 . We further assume that the pressure is only the *thermal* pressure of the gas (i. e. we neglect the magnetic field and cosmic-ray contributions). We can then write the jump conditions :

$$\rho_1 v_1 - \rho_2 v_2 = 0 \quad (3.8)$$

$$(\rho_1 v_1^2 + P_1) - (\rho_2 v_2^2 + P_2) = 0 \quad (3.9)$$

$$\left[v_1 \left(\frac{1}{2} \rho_1 v_1^2 + \frac{\gamma}{\gamma-1} P_1 \right) \right] - \left[v_2 \left(\frac{1}{2} \rho_2 v_2^2 + \frac{\gamma}{\gamma-1} P_2 \right) \right] = 0 \quad (3.10)$$

where γ is the ratio of specific heats ($\gamma = 5/3$ in an ideal monoatomic gas or non-relativistic fully ionised plasma). When the Mach number is sufficiently high ($v_s \gg c_{\text{sound}}$) one can use the *strong shock approximation*. The pre-shock pressure is neglected ($P_1 = 0$). The upstream velocity is simply $\mathbf{v}_1 = -\mathbf{v}_s$ and one replaces ρ_1 with the ambient mass density ρ_0 . Equations (3.8), (3.9), and (3.10) are recasted to form the *Rankine-Hugoniot relations*:

$$v_2 = -\frac{\gamma-1}{\gamma+1} v_s \stackrel{\gamma=5/3}{=} -0.25 v_s \quad (3.11)$$

$$\rho_2 = \frac{\gamma+1}{\gamma-1} \rho_0 \stackrel{\gamma=5/3}{=} 4 \rho_0 \quad (3.12)$$

$$P_2 = -\frac{2}{\gamma+1} \rho_0 v_s^2 \stackrel{\gamma=5/3}{=} 0.75 \rho_0 v_s^2 \quad (3.13)$$

The temperature in the shocked region is obtained from the ideal gas law $P = (\rho/\mu)kT$ with μ the mean particle mass. E. g. in a fully ionised plasma with He/H = 0.1 (by number) there will be one proton (mass m_p), 0.1 helium nucleus (mass $4 \times m_p$) and $1 + 0.1 \times 2$ electrons (negligible mass). Therefore μ is $(1.4/2.3)m_p \approx 0.61 m_p$. Using eqs. (3.12) and (3.13) gives the temperature:

$$kT_s = \frac{2(\gamma-1)}{(\gamma+1)^2} \mu v_s^2 \stackrel{\gamma=5/3}{=} \frac{3}{16} \mu v_s^2 \quad (3.14)$$

$$T_s = 1.39 \times 10^7 \left(\frac{v_s}{1000 \text{ km s}^{-1}} \right)^2 \text{ K} = 1.19 \left(\frac{v_s}{1000 \text{ km s}^{-1}} \right)^2 \text{ keV} \quad (3.15)$$

3.5. Accretion power

An efficient way of producing energy to power X-ray sources is the **accretion** of matter onto compact objects. A unit mass of gas falling from infinity onto a (compact) object with mass M_X and radius R_X will gain a kinetic energy $(GM_X)/R_X$. If most of this energy is converted to heat and radiated away, then the accretion luminosity is:

$$L_{\text{acc}} = \frac{G\dot{M}M_X}{R_X} \quad (3.16)$$

with $\dot{M} = dM/dt$ the mass accretion rate. Neutron stars and black holes are simultaneously massive *and* small. Consequently, accretion luminosity is large as can be easily shown by expressing L_{acc} in terms of the fraction of mass rest energy converted in radiation:

$$L_{\text{acc}} = \eta \dot{M} c^2 \quad ; \quad \eta = \frac{GM_X}{R_X c^2} \quad (3.17)$$

The efficiency η is between 0.1 and 0.5 for typical neutron stars and black holes. This can be compared to nuclear fusion, where only 0.7% of the rest energy is released. Accretion is undeniably an efficient process. It was first suggested as a power source for quasars or newly-discovered ‘‘X-ray stars’’ in the 1960s by [Zel’dovich \(1964\)](#) and [Salpeter \(1964\)](#). The accreted matter can be provided by a mass-losing companion in a binary system. Only a small accretion rate of $10^{-8} M_{\odot} \text{ yr}^{-1}$ is required to power luminosities of about $10^{38} \text{ erg s}^{-1}$, close to the maximum luminosity of Galactic X-ray sources.

4. The Large Magellanic Cloud from an observational point of view

4.1. The LMC as a galaxy

4.1.1. Historical perspective

EASILY VISIBLE with the unaided eye, the Magellanic Clouds were known (under other names) in the southern hemisphere for thousands of years. Their first written mention can be found in the masterpiece “Book of fixed stars” by the Persian astronomer Al Sufi (903-986 AD). He reports an object he called “Al Bakr”, the White Ox, of the southern Arabs (it is only visible from the southernmost latitudes of Arabia), now identified as the LMC. The two Clouds were known to and used by navigators to locate the South pole. In particular, they are depicted by the Venetian scholar Antonio Pigafetta, in his account ([Lord Stanley of Alderley 1874](#), p. 66) of the first circumnavigation of the globe (1519-1522) by the Portuguese Fernão de Magalhães (Ferdinand Magellan). The term “Magellanic” was attributed to the Clouds in his honour, albeit much later.

The first observations with modern telescopes were performed at the end of the XIXth century with the establishment of the Lick and Harvard Observatory southern stations. One of the most important results was the discovery by Henrietta Leavitt ([1908](#)) of many variable stars in the MCs, which allowed her and Pickering ([1912](#)) to establish the period-luminosity (PL) relation for Cepheids, the first mean of measuring extragalactic distances. Fast-forwarding in time, the MCs have always been an important target across all the electromagnetic spectrum. For instance, the first extragalactic HI emission was found in the MCs ([Pawsey 1959](#)). Huge progress ensued the installation of ever larger telescopes for the southern sky since the 1950s-1960s, now able to resolve all the stellar content of the Clouds. Last but not least, the LMC offered in 1987 the nearest supernova since Kepler’s (in 1604), providing astronomers with a bonanza of results.

4.1.2. Properties and structure of the LMC

The LMC is the nearest irregular dwarf galaxy to our Milky Way. The exact meaning of “nearest” is intensively discussed, because the distance to the LMC (in terms of distance modulus $\mu = (m - M)_0$) is critical for the establishment of an accurate extragalactic distance ladder. Indeed, more distant galaxies are measured relative to the LMC. Historically, a large scatter was found for μ , reported between 18.1 mag and 18.8 mag (for a comprehensive review of pre-1995 results see [Westerlund 1997](#), Chap. 1). The *Hubble Space Telescope* (HST) Key Project to measure the Hubble constant ([Freedman et al. 2001](#)) adopted a “canonical” value of $\mu = 18.50$ mag, close to the unweighted mean of previously-published values. The most accurate measurement of the distance to the LMC (at the time of the writing of this thesis) is based on late-type eclipsing-binary systems: [Pietrzyński et al. \(2013\)](#) report $\mu = 18.493 \pm 0.008_{(\text{stat})} \pm 0.047_{(\text{syst})}$ (or $D = 49.97 (\pm 0.19_{(\text{stat})} \pm 1.11_{(\text{syst})})$ kpc, an impressive 2.2 % accuracy). Distance measurements published after the results of [Freedman et al. \(2001\)](#) cluster tightly around the “canonical” value, which prompted some concern of “publication bias” ([Schaefer 2008, 2013](#)). [de Grijs et al. \(2014\)](#) criticised this claim and attribute it to other reasons (e. g. correlated methods and non-independent tracer samples). At any rate, for the sake of simplicity and in agreement with [Pietrzyński et al. \(2013\)](#), **the distance to the LMC of $D = 50$ kpc is assumed throughout all the Thesis.**

The main structure of the LMC is a disc of stars and gas with an extent of up to 14° . As the distance, measurements of the orientation of the disc, i. e. inclination i (with 0° defined as face-on) and position angle of line of nodes Θ (the intersection of the disc and sky planes, measured eastwards of north), are widely scattered but are in the range $25^\circ < i < 40^\circ$ and $120^\circ < \Theta < 155^\circ$ (Westerlund 1997; Subramanian & Subramanian 2013; van der Marel & Kallivayalil 2014). The north-eastern side of the LMC is closer than the south-western side, leading to magnitude variations as function of position angle (with peak-to-peak amplitude of ~ 0.25 mag, van der Marel & Cioni 2001). The thickness of the LMC disc is similar to that of the *thick* disc of the Milky Way (van der Marel et al. 2002), with a depth of 2.4 – 4.0 kpc, possibly decreasing from north to south (Subramanian & Subramanian 2009). The three-dimensional rotation field of the LMC around its systemic line-of-sight velocity of $261.1 \pm 2.2 \text{ km s}^{-1}$ is presented in van der Marel & Kallivayalil (2014). They derived a mass within a 8.7 kpc radius ($\approx 10^\circ$) of $(1.7 \pm 0.7) \times 10^{10} M_\odot$.

An important sub-structure of the LMC is the Bar, covering about $3^\circ \times 1^\circ$ at a position angle $\sim 120^\circ$ (eastwards of north). The Bar is not a structure seen in HI, nor in $H\alpha$, nor in mid-infrared emission; it is traced by the stars, both in young and intermediate-age populations (de Vaucouleurs & Freeman 1972; van der Marel 2001, respectively). Furthermore, the photometric centre of the Bar is offset by more than 1 kpc away from the dynamical centre of the HI disc, a feature that can be induced by tidal interactions with the SMC (Bekki 2009; Besla et al. 2012). The Bar might also be on the near side of the LMC, “floating” ~ 0.5 kpc to 5 kpc above the plane of the disc, as evidenced from NIR star count maps and distances to Cepheids, red clump, and RR Lyrae stars (Zhao & Evans 2000; Nikolaev et al. 2004; Koerwer 2009; Haschke et al. 2012)). This interpretation is challenged by red clump stars distance measurements of Subramanian & Subramanian (2009) and Subramanian & Subramanian (2013). Zaritsky (2004) proposed an alternative model, where the Bar is a stellar bulge (with a z scale height of 2.5–3 kpc) whose south-eastern part is obscured by the disc. Consequently, the photometric centre is offset (in the plane of the sky), and distance measurement are biased to stars in the near side of the bulge. I briefly touch upon these issues in Sect. 11.6.

4.1.3. Star formation history

The first studies of the LMC’s stellar content in the 1960s suggested a different star formation history (SFH) than for the Milky Way (Hodge 1960, 1961). Most of the early studies used age-dating of LMC clusters. The most striking feature they revealed was the “Age Gap”, i. e. the lack of clusters between ages of ~ 5 Gyr and ~ 12 Gyr (e. g. Da Costa 1991). Studies of *field star* populations (e. g. with *HST*, Holtzman et al. 1999; Smecker-Hane et al. 2002) reveal essentially the same results, i. e. a dearth of star formation between an initial burst ($\gtrsim 12$ Gyr) and a second episode 4–5 Gyr ago.

The first truly global analysis of the LMC’s SFH was conducted by Harris & Zaritsky (2009). They used the results from their *UBVI* photometric survey (MCPS, Zaritsky et al. 2004, see Sect. 4.2) to perform colour-magnitude diagram fitting. They obtained a reconstruction of the star formation rate (SFR, in $M_\odot \text{ yr}^{-1}$) in 13 time bins and four metallicity bins, for 1380 cells, most of them having a size of $12' \times 12'$. Although poorly sensitive to old ages because the survey does not reach the main-sequence turn-off (MSTO) in the crowded fields⁷, the SFH obtained is extremely useful to study the recent and intermediate-age star formation episodes, and to compare the integrated SFH of small- and medium-scale regions.

The SFH integrated over the whole LMC is shown in Fig. 4.1. The main features are: *i*) the aforementioned “Age Gap” between ~ 5 Gyr and ~ 12 Gyr; *ii*) the resumption of star formation 5 Gyr ago, plausibly associated to a merger or interaction with the SMC, as the latter exhibits a “simultaneous” resumption of star formation (Harris & Zaritsky 2004, 2009); and *iii*) episodes of enhanced star formation at 12 Myr, 100 Myr, 500 Myr, and 2 Gyr ago. The SFH is highly non-uniform. Harris & Zaritsky (2009) examine the SFH of several large substructures of the galaxy. Most notably, very prominent peaks of recent

⁷in the Bar the old ($\gtrsim 4$ Gyr) SFH is constrained to match that obtained with *HST*.

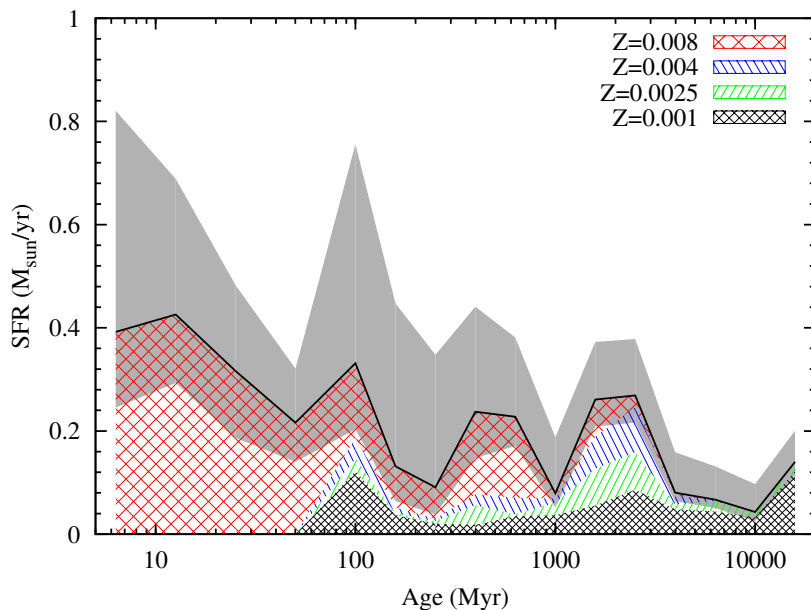


FIGURE 4.1 – Star formation history of the LMC. Data are taken from [Harris & Zaritsky \(2009\)](#). The star formation rate in four metallicity bins are plotted against lookback time. The errors (combining all metallicities) are shown by the gray shading.

(< 30 Myr) star formation are seen in the giant H II region 30 Doradus and in Constellation III, an enigmatic region with an arc of thousands of young bright stars and star clusters embedded in the supergiant shell LMC 4 (see also analysis in [Harris & Zaritsky 2008](#)). The stellar Bar shows activity peaks at 100 Myr, 500 Myr, and 5 Gyr ago. Although it is difficult to strictly define the Bar population, it appears that the Bar has been an integral part of the LMC for a large fraction of its history.

Other attempts at a reconstruction of the spatially-resolved SFH of the LMC include that undertaken with the VMC survey, a deep near-infrared (YJK_S) survey of the Magellanic system with the VISTA telescope ([Cioni et al. 2011](#)). The survey’s depth reaches the oldest MSTO, allowing a reliable determination of the old history. At the time of the writing, only the very first regions of the survey have been analysed ([Rubele et al. 2012](#)). Results regarding the strongest peaks at ~ 5 Gyr and ~ 12 Gyr ago are consistent with the MCPS-based SFH and interpreted as record of past (Milky Way-)LMC-SMC interactions. An archival study of all deep *HST* pointings to both Magellanic Clouds to compare their joint SFH is presented in [Weisz et al. \(2013\)](#).

4.2. Multi-wavelength observations of the LMC

The LMC is probably one of the best-studied galaxies over all the electromagnetic spectrum. I list here the recent surveys from radio to γ -rays, focusing on those I used in this thesis for the multi-wavelength study of sources. The X-ray observations are detailed in Sect. 4.3.

Radio: The neutral hydrogen (H I) content and structure of the LMC has been studied (at 21 cm) by [Staveley-Smith et al. \(2003\)](#) and [Kim et al. \(2003\)](#). The former used data from the 64-m single-dish Parkes radio-telescope, sensitive to large-scale structures (200 pc to 10 kpc). They show the distribution of H I in a well-defined disc and three “arms” interpreted as tidal features. Several H I holes (the largest ones) are associated to supergiant shells (SGS). The total H I mass derived is $4.8 (\pm 0.2) \times 10^8 M_\odot$. In [Kim et al. \(2003\)](#), the Parkes data are merged with data from the Australia Telescope Compact Array (ATCA) interferometer, which provides a view of the smaller structures (15 pc to 500 pc). The resulting maps (in terms of peak surface brightness or column density) reveal the clumpiness of the H I distribution, or in their words, “the filamentary, bubbly, and flocculent structures of the ISM in the LMC”.

Surveys at radio-continuum frequencies reveal radio-emitters within the Clouds *and* background sources (much like in X-rays). Combined with the spectral information obtained from multi-frequency observations, one can classify radio-continuum sources in the direction of the LMC (Filipovic et al. 1996) as either *i*) thermal sources, e. g. H II regions in the Clouds; *ii*) non-thermal sources, like the synchrotron radiation from supernova remnants; and *iii*) background quasars and galaxies. A catalogue of almost 500 radio-continuum sources in the LMC, at five frequencies from 1.40 GHz to 8.55 GHz (using the Parks telescope) is presented in Filipovic et al. (1995, 1998). Finally, the molecular content of the LMC is assessed by the ~ 30 deg² survey with the NANTEN telescope in the ¹²CO ($J = 1 - 0$) line (Fukui et al. 2008).

Mid- and far-infrared: During the SAGE survey (Meixner et al. 2006), the *Spitzer Space Telescope* observed a $7^\circ \times 7^\circ$ area in the LMC with the Infrared Array Camera (IRAC; Fazio et al. 2004) in its 3.6, 4.5, 5.8, and 8 μm bands, and with the Multiband Imaging Photometer (MIPS; Rieke et al. 2004) in its 24, 70, and 160 μm bands. The observations revealed the distribution and properties of the dust, the population of young stellar objects, and evolved stars.

Ground-based near-infrared and optical surveys: The LMC field is obviously included in the Two Micron All Sky Survey (2MASS Skrutskie et al. 2006, extended by the 6X2MASS) which provide JHK_s photometry. The VMC survey (Cioni et al. 2011) will provide the largest, deepest LMC survey in NIR. The Magellanic Clouds Photometric Survey (Zaritsky et al. 2004, MCPS,) features $UBVI$ photometry for 24 million stars in the central ~ 64 deg² of the LMC, down to $V \sim 20 - 21$ mag (depending on crowding). The Optical Gravitational Lensing Experiment (OGLE) is a long-term monitoring survey of LMC stars using a telescope based at Las Campanas, Chile (see Udalski et al. 2008). More than 20 million stars have I -band light curves spanning up to 20 years, with an almost daily sampling and occasional V -band data.

Emission line surveys: Most of the nomenclature of optical nebulosities (in particular H II regions and optically-bright SNRs) is due to the early photographic $H\alpha$ surveys by Henize (1956) and Davies, Elliott, & Meaburn (1976). More recently, the Magellanic Clouds Emission Line Survey (MCELS, e.g. Smith et al. 2000) was carried out at the Cerro Tololo Inter-American Observatory (CTIO). It is a spatially complete, flux-limited survey with the 0.6/0.9 m Curtis Schmidt telescope from the University of Michigan. A $8^\circ \times 8^\circ$ region centred on the LMC was imaged with three narrow-band filters [S II] $\lambda\lambda 6716, 6731$ Å, $H\alpha$ ⁸, and [O III] $\lambda 5007$ Å. Observations with green and red broad-band filters centred at 5130 Å and 6850 Å were obtained to subtract stellar continua. The pixel size of the mosaiced data is $2'' \times 2''$.

Ultraviolet: Only a few UV observations of the LMC are available, with the notable exception of the survey performed with the *Swift's* Ultraviolet/Optical Telescope (UVOT)⁹. 2200 pointings in three UV filters, from 1600 Å to 3300 Å, were assembled in an image showing the region around the Bar and 30 Doradus, with an angular resolution of $2.5''$. The UV mosaic reveals the distribution of the young hot stars.

Gamma rays: Very high energy emission from the LMC was first detected with the Energetic Gamma Ray Experiment Telescope (EGRET) aboard the *Compton Gamma Ray Observatory* (Sreekumar et al. 1992). It remains the only normal galaxy detected in high-energy γ -rays. Observations with the *Fermi* Large Area Telescope (LAT) enable to characterise the LMC spectrum in the 0.1 GeV – 20 GeV range (Abdo et al. 2010). Despite the very limited spatial resolution of *Fermi*/LAT, it appears that the γ -ray emission does not follow the LMC gas distribution but is better correlated with massive star forming regions (e. g.

⁸All the $H\alpha$ filters used in the mentioned surveys include the [N II] $\lambda\lambda 6548, 6584$ Å doublet in their bandpass.

⁹PI: S. Immler, see http://www.nasa.gov/mission_pages/swift/bursts/magellanic-uv.html

30 Doradus). This is taken as evidence for the γ -ray emission originating in cosmic-ray interactions with the ISM and radiation field. Finally, [Komin et al. \(2012\)](#) report early results from the High Energy Stereoscopic System (H.E.S.S.) collaboration, including the detection (above the 10σ level) of TeV emission attributed to PSR J0537-6910 inside the pulsar-wind nebula N157B, the non-detection of SNR 1987A, and the absence of TeV emission from 30 Doradus.

4.3. The LMC in X-rays

4.3.1. Previous X-ray observations

X-ray emission from the LMC was first detected in 1968 in the heyday of rocket astronomy ([Mark et al. 1969](#)), at a total luminosity of 4×10^{38} erg s⁻¹. [Price et al. \(1971\)](#) confirmed this result, identifying two source regions, one of them close to 30 Doradus. With the scans of Uhuru, [Leong et al. \(1971\)](#) revealed three permanent X-ray sources (LMC X-1, LMC X-2, and LMC X-3) and one possible variable source, later confirmed as LMC X-4 ([Giacconi et al. 1972](#)). Many missions followed (*Copernicus*, SAS 3, Ariel V, HEAO-1) to re-observe these sources and reveal two more, LMC X-5 and LMC X-6. [McKee et al. \(1980\)](#) reported soft X-ray sources in the Bar region and associated the brightest with the SNR N132D¹⁰.

The first dedicated survey with an imaging instrument was conducted by [Long et al. \(1981\)](#). A hundred pointings with *Einstein*'s Imaging Proportional Counter (IPC) revealed 97 sources, including at least 25 SNRs. A re-analysis of the same data ([Wang et al. 1991](#)) increased the number of sources to 105 and revealed large scale diffuse emission, attributed to hot ISM (10^6 K - 10^7 K). In the 1990s, ROSAT was the instrument of choice to survey the Clouds. The analysis of ROSAT All Sky Survey (RASS) data and early pointed observations in the LMC fields were presented in [Pietsch & Kahabka \(1993\)](#). After the end of the mission, [Haberl & Pietsch \(1999a, hereafter HP99\)](#) analysed more than 200 ROSAT PSPC pointings towards the LMC (Fig. 4.2) to derive the largest catalogue (758 objects) of LMC X-ray sources to date. The hot ISM was studied with this dataset in [Sasaki et al. \(2002\)](#). The analysis of time variability for objects covered by multiple PSPC observations is presented in [Haberl & Pietsch \(1999b\)](#). Finally, a similar work (catalogue and variability study), but using the High Resolution Imager (HRI) of ROSAT was conducted by [Sasaki, Haberl, & Pietsch \(2000\)](#).

4.3.2. X-ray sources from the LMC region

Observing the LMC, one can detect X-rays in many ‘‘flavours’’. Various types of objects, not only within the LMC, but also in the fore- and background, contribute to the total emission. In the Section below, I present the possible sources most relevant to this work. The particular case of supernova remnants is presented in more details in Sect. 5.

4.3.2. A. Interlopers

Foreground non-degenerate stars: Stars of virtually all spectral types and luminosity classes have been found to be X-ray emitters ([Vaiana et al. 1981](#); [Huensch et al. 1998a,b](#)). In hot, early-type stars, the X-ray production mechanism is thought to be shocks formed in the instabilities of the strong stellar winds. The X-ray luminosity is about 10^{-7} times the bolometric luminosity L_{bol} , i. e. $L_X \lesssim 10^{33}$ erg s⁻¹, and is approximately constant.

In late-type stars, magnetic reconnection and instabilities in the outer convective zone (which is at 3×10^3 K - 10^4 K) heat the corona to very high temperatures (10^6 K - 10^7 K), producing thermal X-ray emission. The X-ray luminosity scales with rotation velocity ([Pallavicini et al. 1981](#)), most likely because rotation

¹⁰their source A can obviously be identified as SNR B0519-69.0, a bright SNR confirmed with *Einstein* ([Long et al. 1981](#)) and detected in radio only later ([Mathewson et al. 1983](#)).

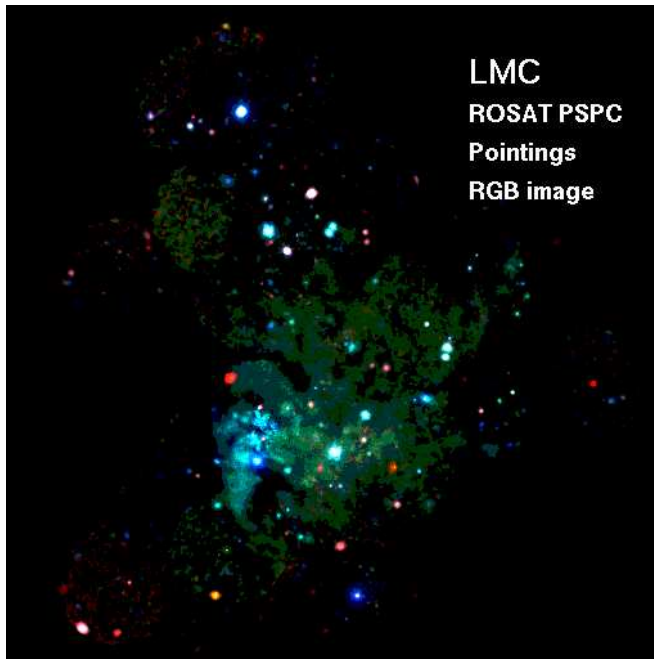


FIGURE 4.2 – X-ray colour images combining all ROSAT PSPC pointings towards the LMC. (Unpublished image prepared by Drs. Frank Haberl and Wolfgang Pietsch, using data described in [HP99](#).)

drives the dynamo producing the magnetic field. For rotation period less than five days, stars are in the “saturation limit” ([Pizzolato et al. 2003](#)) with $L_X/L_{\text{bol}} \sim 10^{-3}$. F- to M-type stars are thus relatively stronger X-ray emitters than early-type stars.

At the high Galactic latitudes of the LMC (b from -35° to -30°), foreground stars detected in the field are likely to be late-type stars. Those are detected as point sources with a hot plasma spectrum, low absorption, and often variability on timescales of hours. Since these objects are nearby, the optical counterparts are usually bright and easily identified. The large proper motions of nearby objects is another tell-tale sign of their foreground nature.

Background active galactic nuclei: Active Galactic Nuclei (AGN) are bright X-ray sources at cosmological distances. Their emission is powered by accretion onto supermassive black holes (SMBHs, $M \sim 10^6 - 10^{10} M_\odot$) that lie at the centre of all massive galaxies. AGN form a very broad class of objects, whose properties are very diverse at all wavelengths: radio-loud or quiet, broad or narrow optical emission lines, late- and early-type host galaxies, etc...

The so-called “Unified model” postulates that the various types of AGN are similar objects simply viewed at different orientation angles to our line of sight (see e. g. [Urry & Padovani 1995](#), for a review). In this model, all AGN have a luminous accretion disc surrounding the central black hole, orbited by clouds producing emission lines. A dusty “torus” in the equatorial plane can obscure broad-line emission and light from the accretion disc in the transverse line of sight. A jet is launched at the base of the disc and can be observed from radio to X-rays.

In X-rays, AGN appear as hard sources with a power-law spectrum. The observed spectral index is typically $\Gamma \sim 1.7$ ([Turner & Pounds 1989](#)). With higher spectral resolution, one can explain the AGN spectra as a softer intrinsic power law ($\Gamma \sim 1.9 - 2.0$) reflected off the disc, producing a prominent Fe K fluorescence line ([Nandra & Pounds 1994](#)). The intrinsic power-law spectrum originates in thermal Comptonisation of UV radiation from the accretion disc by hot electrons in a “corona” above the disc ([Sunyaev & Titarchuk 1980](#); [Zdziarski et al. 2000](#)).

The vast majority of X-ray point sources out of the Galactic plane are AGN. The contamination by background objects in the observed point source population of nearby galaxies is significant to high (e. g.

in M31 and the SMC [Stiele et al. 2011](#); [Sturm et al. 2013](#), respectively). Owing to its very high extent on the sky, the AGN contamination is even worse in the LMC. Judging by the source density of the *Chandra* Deep Field South (CDF-S [Bauer et al. 2004](#)) at a flux limit of $\sim 7 \times 10^{-15}$ erg cm $^{-2}$ s $^{-1}$ (or luminosity of 2×10^{33} erg s $^{-1}$ in the LMC), which is about 200 deg $^{-2}$, one expects 3000 to 4000 AGN in the fields covered with *XMM-Newton*. To identify intrinsic LMC sources is akin to “separate the wheat from the chaff”. AGN behind the LMC are however a valuable sample: Because they are distant, they have fixed positions on the sky. They are thus excellent reference objects for studies of proper motions of the LMC ([Piatek et al. 2008](#); [Cioni et al. 2013, 2014](#)), or to correct the boresight of *XMM-Newton* observations, reducing positional uncertainties (e. g. [Watson et al. 2009](#); [Sturm 2012](#)). Bright AGN also allow to probe the ISM in the LMC, since their light is absorbed by the foreground galaxy ([Kahabka et al. 2001](#); [Haberl et al. 2001](#)). At other wavelengths, AGN behind the LMC can be separated from stars via their distinctive colours and/or association to radio sources. [Kozłowski & Kochanek \(2009\)](#) selected a sample of 4700 AGN candidates from mid-IR photometry, optical variability, and X-ray emission (from ROSAT). They later performed spectroscopy of 2248 of the candidates in a ~ 30 deg 2 field and confirmed 565 as AGN ([Kozłowski et al. 2012, 2013](#)).

Clusters of Galaxies: Clusters of galaxies are the largest virialised structures in the Universe. They consist of hundreds to thousands of galaxies, which, although dominating the optical brightness of clusters, constitute only 2 % of the mass. The bulk mass of clusters (~ 87 %) is made of dark matter which builds the large gravity potential in which galaxies and the remaining part, the intra-cluster medium (ICM), fall. During gravitational collapse, compression and shocks heat the ICM to very high temperature. Clusters of galaxies appear as extended X-ray sources, the hot ICM filling the space between the galaxies and radiating as an optically thin thermal plasma (for a general discussion see e. g. [Rosati et al. 2002](#); [Böhringer & Werner 2010](#)).

The temperatures of the plasma range from 2 keV to 10 keV. The relatively hard X-ray emission of clusters makes them insensitive to the moderate absorption column densities in most LMC fields. Consequently, clusters of galaxies behind the LMC can easily be detected with *XMM-Newton*, much like they are found behind the SMC ([Haberl et al. 2012b](#)). They are identified by *i*) their extent, *ii*) their temperature markedly hotter than other extended sources (SNRs, superbubbles, hot ISM), and *iii*) the lack of associated extended emission in optical (e. g. H α).

4.3.2. B. Sources in the LMC

X-ray binaries: The nature of the first X-ray sources discovered was mysterious until it became clear, from the study of their optical companions, that most of the objects were binary systems. Furthermore, identification of rapid pulsations and mass measurements of the X-ray source established that the compact object in these systems was a neutron star (NS) or a black hole (BH), accreting matter from a stellar companion. This is the very general definition of an X-ray binary (XRB). I briefly discuss these objects, as they are such an important class: They dominate (by number and luminosity) the X-ray output of normal galaxies ([Fabbiano 2006](#)); they are tracers of star formation ([Grimm et al. 2003](#)); and they are ideal probes for many astrophysical problems (accretion, supra-nuclear densities in NS, general relativity around BH).

X-ray binaries are broadly classified according to the mass/type of their companions. In low-mass X-ray binaries (LMXBs), the compact object orbits a late-type (A to M), low-mass ($\lesssim 2 M_{\odot}$) donor star which fills its Roche lobe. Matter is transferred to the compact object through the inner Lagrangian point, accreting in an X-ray bright disc. Because of the nature of the companion, LMXBs are long-lived systems, found in old stellar populations. The number of LMXB in a galaxy scales with its stellar mass. In the SMC, no LMXBs are known so far ([Coe et al. 2010](#)), whilst only LMC X-2 is established as a LMXB in the Large Cloud ([Pakull 1978](#); [Bonnet-Bidaud et al. 1989](#)).

In contrast, high-mass X-ray binaries (HMXBs) have early-type (O or B) donor stars and are therefore short-lived systems, associated to star forming regions. They are further separated in two major sub-classes. Systems with early-type *supergiant* (luminosity class I-II) companions are (appropriately) called supergiant X-ray binaries (SgXRBs). There, the NS or BH ploughs through the strong stellar wind of the supergiant, which is dense enough to power X-ray emission once the material accretes onto the compact object. In rare cases, mass transfer occurs via Roche-lobe overflow. Such sources, like SMC X-1 or LMC X-1, are bright ($\sim 10^{37}$ erg s $^{-1}$ – 10^{38} erg s $^{-1}$) and *permanent* X-ray sources.

Be/X-ray binaries (hereafter BeXRBs) are the second major sub-class of X-ray binaries. In these systems, a compact object accretes material from a normal companion star. The optical counterparts are non-supergiant, emission-line stars, which have spectral classes later than O5 and earlier than B9, with the bulk of the population concentrated around B0–B1 (Coe et al. 2005). Classical OBe stars are rapid rotators surrounded by an equatorial disc of circumstellar material. The disc emits lines, chiefly the Balmer and Paschen series of hydrogen, but also a few He and Fe lines. An infrared excess is also produced by the equatorial disc (for a recent review, see e.g. Reig 2011).

In the vast majority of BeXRBs, the compact object is a NS. There is only one confirmed black hole/Be X-ray binary so far (Casares et al. 2014; Munar-Adrover et al. 2014), which is explained either because BH/Be systems are hard to find (long quiescent states, Zhang et al. 2004), or are rarely formed (Belczynski & Ziolkowski 2009). Binary evolution models also predict a higher number of white dwarf (WD)/Be systems than NS/Be (Raguzova 2001), but very few are known. They can either emit hard X-ray emission as in NS/Be, but at a much lower luminosity (γ Cas-like objects, Haberl 1995; Lopes de Oliveira et al. 2006), or very soft emission if stable nuclear burning occurs on the WD (see next paragraph). The first such supersoft WD/Be X-ray binary was found in the LMC (Kahabka et al. 2006). A similar system was discovered in the SMC (Sturm et al. 2012a). The remainder of the discussion present the phenomenology of NS/BeXRBs, which are the most common.

The NS in a BeXRB is usually in a wide orbit with a significant eccentricity (orbital periods of tens to a few hundred of days, and $0.3 \lesssim e \lesssim 0.9$, Townsend et al. 2011) around its companion, leading to a transient nature of the system in X-rays. Copious amounts of X-rays can be produced when the neutron star captures material from the equatorial disc of the Be star. This occurs when the separation between the two components is the smallest, i.e. at or near periastron passage, and leads to the so-called Type I X-ray outbursts, which last for a small fraction of the orbital period and have X-ray luminosities $L_X \sim 10^{36-37}$ erg s $^{-1}$. A population of low-eccentricity systems with persistent X-ray emission (at lower luminosity $L_X \sim 10^{35}$ erg s $^{-1}$) also exists, possibly formed through a different channel (Pfahl et al. 2002). Less frequently, giant (Type II) outbursts can occur, reaching luminosities in excess of 10^{37} erg s $^{-1}$ and lasting for several orbital periods. Although many questions remain open, it has been suggested that giant outbursts are associated to warping episodes of a Be disc misaligned with respect to the orbital plane (see Okazaki et al. 2013, and references therein).

In recent years a large population of BeXRBs has been identified in the SMC, with a total of ~ 60 confirmed systems (Haberl & Pietsch 2004; Coe et al. 2005, 2010). About 45 candidates have also been identified during the XMM-Newton survey of the SMC (Sturm et al. 2013). Whilst the LMC is about ten times as massive as the SMC, it contains (as of 2014) less than 20 confirmed BeXRBs (Vasilopoulos et al. 2014, and references therein). This discrepancy is possibly explained by different star formation histories (SFHs). Antoniou et al. (2010) find that the locations of SMC BeXRBs correlate with stellar populations of ages ~ 25 – 60 Myr. Despite large spatial variations, the most recent episodes of enhanced star formation activity in the LMC occurred 12 Myr and 100 Myr ago (Harris & Zaritsky 2009). This is different from the time at which most Be stars develop their equatorial discs, which was found to peak at ~ 40 Myr (McSwain & Gies 2005). However, the X-ray coverage of the LMC is still not as complete as for the SMC, precluding early interpretations on the role of different SFHs.

Super-soft X-ray sources: In surveys performed with *Einstein* and ROSAT, objects with very soft X-ray spectra were discovered (Long et al. 1981; Trümper et al. 1991). They have almost no emission above 0.5 keV. Their spectra are well described as a black body with temperatures in the range 20 eV to 100 eV. At the same time they have high luminosities ($L_X \sim 10^{36-38} \text{ erg s}^{-1}$). CAL 83 and CAL 87, in the LMC, were the prototypes of this class, called super-soft source (SSS). Their discovery in an external galaxy is unsurprising, as their very soft emission is readily absorbed by the neutral hydrogen at low Galactic latitudes. The canonical model of van den Heuvel et al. (1992) to explain the bright SSS assumes they are WDs in close binary systems, accreting material at a rate sufficient to maintain the *steady* nuclear burning of hydrogen at the surface of the WD. Such rate is in a narrow range ($\sim 10^{-8} - 10^{-7} M_\odot \text{ yr}^{-1}$).

At lower rate, a hydrogen layer builds up on the WD until conditions for a thermonuclear runaway are reached, producing a classical nova explosion. Note that the high temperature of the thermonuclear explosion and subsequent nuclear burning still produce X-rays. The ejected material obscures the X-ray emission, but it keeps expanding until it ultimately becomes optically thin to soft X-rays. Therefore the WD can be observed as SSS a few weeks to years after a nova explosion (see Henze 2011, and references therein). Several novae have been observed in the LMC to follow their light curve from the explosion to the SSS phase: e. g. NOVA LMC 1995 (Orio & Greiner 1999), NOVA LMC 2000 (Greiner et al. 2003), NOVA LMC 2005 (Ness et al. 2007), and NOVA LMC 2009a (Schwarz et al. 2011). Other sources of fainter super-soft X-ray emission also involve WDs, but this time isolated: Hot cooling WDs, or planetary nebulae. It is not clear whether such sources can be reached in the LMC by (shallow) XMM-Newton observations.

Superbubbles: Massive stars inject energy in their surrounding via ionising radiation, stellar winds, and ultimately SN explosions. As massive stars often cluster (in OB association), these combined processes create large structures ($\sim 100 \text{ pc}$) in the ISM called superbubbles (SBs, for a review see Chu 2008). The gas inside the SB is shock-heated to UV and X-ray-emitting temperatures ($\gtrsim 10^6 \text{ K}$). Models for the structure and evolution were developed in Castor et al. (1975); Weaver et al. (1977).

Early imaging X-ray observations of the Large Magellanic Cloud with *Einstein* confirmed that SBs were X-ray sources (Chu & Mac Low 1990; Wang & Helfand 1991). These studies found that the SBs X-ray luminosities were an order of magnitude *higher* than predicted by the Weaver et al. model. ROSAT observations confirmed that most LMC SBs were X-ray bright (Dunne et al. 2001), although some other SBs were consistent with the Weaver et al. model (“X-ray dim SBs”, Chu et al. 1995a). The explanation proposed by Chu & Mac Low (1990); Wang & Helfand (1991), which remained the favoured one, is that off-centre SNe (i. e. near the SB shells) hitting the shell *temporarily* increase the X-ray luminosity.

5. Supernova remnants and associated problematics

THIS WORK is concerned mostly with supernova remnants. Thus, I describe here this type of objects, their origin in supernova explosions, their subsequent evolution, and their astrophysical relevance. The classification the SN explosion (the “typing” of SNRs) is addressed in Sect. 5.5.

5.1. Supernovae: The swan song of dying stars

Supernovae are undoubtedly impressive celestial events. Once every few centuries a “new star” (nova) appears, possibly becoming the brightest object in the sky¹¹. The observations of such events in 1572 and 1604 AD (Tycho’s and Kepler’s SNe, respectively) came in handy to refute the 18 centuries old Aristotelian idea of an eternal and incorruptible sky. With the advent of telescopic observations, more of these exceptional “new stars” were found in a variety of “stellar systems” (i. e. galaxies) and became known as supernovae, in the term first coined by Fritz Zwicky and Walter Baade¹². They recognised (Baade & Zwicky 1934), from energetics considerations, that “*the phenomenon of a super-nova represents the transition of an ordinary star into a body of considerably smaller mass*”, i. e. the death of a star.

An early classification scheme by Minkowski (1941) distinguished the class of SNe *with* hydrogen absorption in their spectra (type I) from those *without* (type II). Type I are further divided in Ia, Ib, and Ic, depending on the presence or absence of Si and He lines (e. g. Elias et al. 1985; Heger et al. 2003). For type II, the sub-division is based on the light-curve shape. Type IIP have a plateau (hence “P”) in their light curve, a feature due to the presence of a large hydrogen envelope, as opposed to type IIL SNe, where the progenitors have lost most of the outer H layers. The light curve then decreases linearly (hence “L”; for a review see e. g. Filippenko 1997).

A more coherent classification scheme appeared once the progenitors of various class of SNe were identified. The similarity of type Ia light curves suggests very common progenitors; these should not be very massive, as type Ia SNe are found in all types of environment, including the old stellar populations of elliptical galaxies. Therefore, it is generally thought that type Ia SNe are the thermonuclear disruptions of C/O white dwarfs close to the Chandrasekhar mass (Whelan & Iben 1973; Nomoto 1982). On the other hand, SNe of type Ib/c and II are much less uniform and are associated to the collapse of the iron cores of massive stars into neutron stars or black holes. Stars with main sequence mass $\gtrsim 8 M_{\odot}$ end up as core-collapse SNe, and the ranges of masses and evolution states of the progenitors at the time of the explosion (red/blue supergiant, Wolf-Rayet) produce the collection of SN sub-types. I will hereafter only use the latter classification: Type Ia SNe are *thermonuclear SNe*, and all other types are *core-collapse (CC) SNe*.

All chemical elements are not born equal: The lighter elements (H, He, and traces of Li, Be, and B) formed in the very young Universe (*primordial* nucleosynthesis, Alpher, Bethe, & Gamow 1948; Alpher & Herman 1950). The rest of the periodic table is forged in stars (Burbidge, Burbidge, Fowler, & Hoyle 1957, and Nomoto et al. 2013 for a modern review). *Stellar* nucleosynthesis can occur “quietly”, in stellar cores or

¹¹Excluding of course the Sun and full Moon; for instance the peak brightness of SN 1006, perhaps the most spectacular stellar outburst ever recorded, was estimated to be of apparent magnitude -9.5 , i. e. that of the half Moon (Clark & Stephenson 1977).

¹²Others, like Knut Lundmark, Heber D. Curtis, or Edwin Hubble used other terms for this special class of novae (see Osterbrock 2001), but physicists always had a special ear for everything “super-”.

in thin shells around the core during most of the life time of stars. By successively using hydrogen, helium, carbon, neon, oxygen, and silicon as nuclear fuel, most of the stable elements up to ^{56}Ni are produced in (intermediate mass/massive) stars¹³. All the other elements are created via *explosive* nucleosynthesis. This occurs during core-collapse SNe, when the shock wave propagates outwards from the star's iron core, compressing and heating the outer layers to conditions sufficient for nuclear reactions to take place. In addition to the incineration of the metal-rich shell of the dying star, heavy isotopes are created by neutrino irradiation (ν -process) and *rapid* neutron capture (r -process, where the neutron capture rate exceeds that of β^- decay). Explosive nucleosynthesis occurs in thermonuclear SNe as well. When (some part of) the white dwarf reaches a critical mass and ignites, the burning front propagates through the WD, incinerating the matter into heavier elements¹⁴. Depending on the explosion mechanism (detonation or deflagration, i. e. supersonic and subsonic propagation, respectively), distinct nucleosynthesis products are formed. A detonation will transform almost all of the WD into iron-group elements, while a pure deflagration produces a large amount of intermediate mass elements (IME, such as Mg, Si, S, and Ca).

In addition to their roles as nuclear furnaces, SNe are extremely bright and can be seen at cosmological distances (redshift $z > 1$). Furthermore, the empirical relation between the peak brightness of type Ia SNe and the decline rate of their light curves (Branch & Tammann 1992; Phillips 1993) allows to calibrate their *absolute* brightness. Type Ia SNe are *standardisable candles* and therefore good distance indicators for cosmological studies. This led to the discovery that the expansion of the Universe is accelerating (Riess et al. 1998; Perlmutter et al. 1999), with far-reaching consequences for the energy content of the Universe (Nobel prize in Physics 2011 for Saul Perlmutter, Brian P. Schmidt, and Adam G. Riess). Embarrassingly enough, however, the identity of the progenitor channel leading to type Ia SNe remains elusive. Two competing scenarios are hotly debated: the single degenerate scenario (SD), where a WD accretes material from a red giant or main-sequence companion and reaches the Chandrasekhar mass (Whelan & Iben 1973); and the double degenerate (DD) scenario, where two WDs in a binary spiral-in and merge, resulting in the thermonuclear disruption of the binary (Webbink 1984; Iben & Tutukov 1984). Direct searches for the surviving companion in the SD scenario have yielded ambiguous results (Ruiz-Lapuente et al. 2004; Maoz & Mannucci 2008; Li et al. 2011a; Schaefer & Pagnotta 2012). Indirect searches have been unable to find the numerous accreting WDs predicted in the SD case (Gilfanov & Bogdán 2010; Di Stefano 2010; Woods & Gilfanov 2013), with the conclusion that SD progenitors cannot produce the dominant fraction of type Ia SNe. On the other hand, constraints on the SN Ia delay-time distribution (DTD, i. e. the SN rate at time τ following a hypothetical brief star formation event) from various methods converge to a power-law shape $\propto \tau^{-1}$ (Maoz & Mannucci 2012), which is generally expected (from the physics of gravitational waves) in the DD scenario. It is fair, however, to stress that although progress is being made, no clear consensus has emerged yet.

5.2. Life after death: Evolution of SNRs

I now proceed to describe the formation and evolution of the *remnants* of SNe. A brief history of the development of SNR models is given in Ballet (2003). In both types of SN, the outer debris layers are ejected with large velocities (tens of thousands of km s^{-1}), much larger than the sound speed in the ambient gas. As a result, a shock wave develops and propagates ahead of the ejecta (also called the *blast wave*), which sweeps up, compresses, and heats the ambient medium. The shocked ambient medium pushes back on the ejecta, driving a *reverse shock* backwards into the ejecta¹⁵. The shocked ejecta are separated from the shocked ambient medium by a *contact discontinuity*. This early stage is called the **ejecta-dominated phase**: The mass of swept-up material is smaller than the mass of the ejecta, and the two shocks travels at

¹³Heavier nuclei are also produced by neutron capture, during the helium burning and subsequent stages (the so-called “*s*-process”).

¹⁴And following the prediction of Hoyle & Fowler (1960), this nuclear runaway will explode the star.

¹⁵In the observer's frame, however, the reverse shock radius is still increasing

essentially uniform velocity (in the observer’s frame), hence this phase is sometimes called “free expansion” phase. To estimate the duration of this phase, one can compute the time t_{ED} at which the swept-up mass is equal to the ejecta mass M_{EJ} , assuming (to the lowest order) a constant velocity V_{EJ} for the ejecta. This gives:

$$t_{ED} = V_{EJ}^{-1} \left(\frac{3 M_{EJ}}{4\pi\rho_0} \right)^{1/3} \quad (5.1)$$

which for most parameters ($V_{EJ} \sim 10000 - 15000 \text{ km s}^{-1}$, $M_{EJ} \sim 1 - 30 M_{\odot}$, $\rho_0 \sim 0.1 - 1 \text{ g cm}^{-3}$) is less than 1000 yr, i. e. only the youngest SNRs are in the ejecta-dominated phase.

Once the swept-up mass becomes larger than the mass of the ejecta, the outer shock decelerates. Still, the radiative losses are negligible, so that the expansion remains adiabatic. There, the behaviour of the remnant can be described by the Sedov (or Sedov-Taylor) self-similar solution. This is the **Sedov phase**, sometimes called “adiabatic phase”, although the expansion in the earlier ejecta-dominated is also adiabatic. This considers that the energy of the explosion E_0 is deposited in a medium of uniform (mass) density ρ_0 . The propagation of the blast wave is much faster than the local sound speed (or alternatively, the pressure of the ambient gas is negligible in comparison with the pressure behind the shock wave), i. e. the Rankine-Hugoniot relations (Eqs. 3.11 to 3.13) apply. From dimensionality arguments, it can be shown (Sedov 1946a,b)¹⁶ that the shock radius r_s will only depend on E_0 and ρ_0 , and will evolve with time t as:

$$r_s = \zeta \left(\frac{E_0}{\rho_0} \right)^{1/5} t^{2/5} \stackrel{\gamma=5/3}{=} 1.17 \left(\frac{E_0}{\rho_0} \right)^{1/5} t^{2/5}, \quad (5.2)$$

with ζ obtained after solving for the radial profiles (e. g. Ballet 2003). The time derivative gives the shock velocity v_s in that phase, or alternatively the temperature (Eq. 3.14). The Sedov model is appealing, since various quantities can be derived from the measured X-ray flux and temperature. Given the assumption of the Sedov model, it should be valid after a time t_{ED} or a few t_{ED} . For a detailed analytical and numerical description of the transitions between the two phases, see Truelove & McKee (1999).

As more and more ambient medium is engulfed by the expanding blast wave, the shock velocity, and therefore post-shock temperature, decreases. This cooler material loses more energy, because the recombining material is able to efficiently radiate away energy in UV and optical lines (Cox & Daltabuit 1971). This last phase is called the **radiative phase**. Shocks are radiative for velocity slower than $\sim 200 \text{ km s}^{-1}$, at which point hardly any X-rays are emitted (Eq. 3.15). The transition to the last phase takes place at (Ballet 2003):

$$t > t_{rad} = 2.4 \times 10^3 \left(\frac{n_0}{1 \text{ cm}^{-3}} \right)^{-4/7} \left(\frac{E_0}{10^{51} \text{ erg s}^{-1}} \right)^{3/14} \text{ yr}. \quad (5.3)$$

After which the dynamical evolution enters a pressure-driven stage ($r_s \propto t^{2/7}$) and finally a momentum-conserving stage ($r_s \propto t^{1/4}$, see Cioffi et al. 1988). At these latest stages, the SNR merges with the ISM. Since SNRs well in the radiative phase are no longer X-ray sources, they are not encountered in this thesis. However, some parts of the SNRs studied can be radiative. It is also clear from Eqs. (5.1) and (5.3) that most of X-ray-emitting SNRs are in the Sedov phase.

Perhaps the most important modification to the idealised hydrodynamical picture I just described is induced by particle acceleration. SNR shocks are prime candidate sites to accelerate cosmic-rays by diffusive shock acceleration (Bell 1978a,b; Blandford & Ostriker 1978, see also reviews of Drury 1983 and Blasi 2013). Indeed, the non-thermal X-ray emission detected in some SNRs establishes that electrons are accelerated up to 10^{14} eV (e. g. Koyama et al. 1995). Particles with TeV energies have been subsequently directly detected from SNRs (Aharonian et al. 2004), while γ -ray observations revealed the

¹⁶I could not access the original papers; as cited in Sedov’s later textbook (1959). See also Zel’dovich & Raizer (1967)

pion-decay process characteristic to the presence of high-energy protons (Ackermann et al. 2013). The main modification to the SNR evolution is that there will be a non-thermal pressure P_{NT} contribution from cosmic-rays in the post-shock pressure. Furthermore, a fraction of accelerated particles may escape the system, and the jump conditions (Eqs. 3.8 to 3.10) must be rewritten. This leads to higher compression ratios χ (Berezhko & Ellison 1999) than in the purely thermal case ($\chi = 4$ for $\gamma = 5/3$). Another consequence is the lower post-shock temperature: If we quantify this as $w \equiv P_{NT}/P_{\text{total}}$, then Eq. 3.14 becomes (Vink 2012):

$$kT_s = (1 - w) \frac{1}{\chi} \left(1 - \frac{1}{\chi} \right) \mu v_s^2. \quad (5.4)$$

When both velocity and post-shock temperature are available, the efficiency of cosmic-ray acceleration can be measured. For instance, Helder et al. (2009) found a high efficiency ($> 50\%$) in the Galactic SNR RCW 86). A few SNR models incorporate the back-reaction of energetic particles (see Decourchelle et al. 2000; Ferrand et al. 2010, 2012, 2014, and references therein)

5.3. Impact on the ISM

The tremendous amount of energy released by supernovae cannot go unnoticed by the surrounding medium. As a matter of fact SNe and their remnants are the dominant source of energy and turbulence for most of the ISM, (Mac Low & Klessen 2004). Part of that energy is carried by the cosmic rays accelerated at the shock front of SNRs, giving an energy density of $1\text{--}2 \text{ eV cm}^{-3}$ (or up to $1/3$ of the total ISM energy density, Webber 1998). More generally, stellar feedback, of which SNe are a major component (in addition to the ionising radiation and winds from massive stars), is an essential ingredient of galaxy evolution models (Dobbs et al. 2011; Scannapieco et al. 2012; Henriques et al. 2013). SNRs are also the recycling centres that return metals back in the ISM. As such, they are driving the chemical evolution of galaxies (e. g. Pagel 2001), and their inclusion in models is needed to satisfactorily reproduce the abundances observed in galaxies (Yates et al. 2013) and in the hot gas of galaxy clusters (Kapferer et al. 2006).

At smaller scales, SNRs are responsible for the morphology of the ISM. Their progenitors (for CC-SNRs) blow bubbles, and (all types of) SNe carve the surrounding medium as their remnants expand. The correlated actions of several SNe and multiple episodes of star formation results in the (very) large structures that are superbubbles and supergiant shells (Chu 2008). This affects the morphological appearance of the ISM at most wavelengths/ For instance, the structures carved by SNRs are seen as holes in HI maps (Meaburn 1980; Kim et al. 1999), while the shells of SBs and SGSs are bright in optical lines (Dunne et al. 2001; Book et al. 2008).

5.4. Observations of SNRs

Because of the strong interaction of SNRs with their surrounding, it is not surprising that they produce detectable features across most of, if not all the electromagnetic spectrum. The identification of SNRs is best done by combining several signatures¹⁷. The detection of at least two of these signatures is usually needed to classify with certainty a source as an SNR:

- **Extended non-thermal radio emission**, that is characteristic of synchrotron radiation. This is emitted by electrons in the magnetic fields compressed and amplified by the SNR shocks. Consequently, SNRs have a shell morphology in radio, following the outer boundary of the expansion. The typical radio spectral index α (using $S \propto \nu^\alpha$, where S is the flux density and ν the frequency) is about -0.5 ,

¹⁷Historically, SNRs were first identified in radio and optical, before the advent of X-ray observations. An history of early SNR X-ray astrophysics is given by Robert Petre in Trümper & Hasinger (2008, Chap. 17)

although α can have a wide range of values depending on environmental factors and the evolutionary state of the remnant (Filipovic et al. 1998).

- **Optical line emission characteristic of shock excitation:** SNRs have no optical continuum (or only a minor synchrotron contribution) but strong line emission, in particular $H\alpha$, $[\text{N II}]$, $[\text{S II}]$, and $[\text{O III}]$. An efficient observational criterion is the $[\text{S II}]/H\alpha$ ratio. In photo-ionised regions (e. g. H II regions), sulphur is brought to ionisation stages higher than S^+ and the ratio is small. By contrast, SNRs will create regions of lower ionisation and higher density behind the shocks which emit strongly in the collisionally excited $[\text{S II}]$ line. A widely used threshold is $[\text{S II}]/H\alpha > 0.4$, as derived from Galactic and LMC SNRs (e. g. Mathewson & Clarke 1973; Fesen et al. 1985). Note that this threshold is valid for the LMC which has a lower (roughly half) abundance of sulphur compared to in the Milky Way (where the strength of the $[\text{S II}]$ line is generally similar or larger than that of the $H\alpha$ line). Detection of high-velocity gas ($\Delta V > 100 \text{ km s}^{-1}$) can also sometimes be used to confirm an SNR nature, though it is often absent (Chu 1997).
- **Extended thermal X-ray emission:** The ISM and SN ejecta engulfed by shocks are heated to X-ray emitting temperatures (Sect. 3.4). The low density of the ISM justifies the use of the coronal approximation, and consequently the X-ray spectrum is thermal in nature, with many ionic lines on top of a Bremsstrahlung continuum, and in many cases non-equilibrium ionisation (following the description of Sect. 3.3). X-ray observations are a very powerful tool to study SNRs, because at the typical electron temperatures of SNR shocks ($kT \sim 0.2 - 5 \text{ keV}$), all astrophysically abundant elements (mostly O, Ne, Mg, Si, S, Ar, Ca, and Fe, but also C, N, and Ni) have emission lines in the 0.3 – 10 keV range accessible to X-ray instruments. Furthermore, the hot plasmas are optically thin and thus allow for straightforward spectroscopy (no radiation transfer). Coupled with SNR models (even simple ones), one can obtain important information about the evolutionary state, ambient density, and elemental composition of SNRs. The main drawback is that soft X-rays (below 2 keV) are sensitive to absorption, which can often mask SNRs in the Galaxy, where foreground column densities are high (in excess of several 10^{22} cm^{-2}).

SNRs are also observed at other wavelengths. They can emit **infrared** (IR) light, chiefly in forbidden lines, rotational/vibrational lines of molecular hydrogen, emission in polycyclic aromatic hydrocarbon (PAH) bands, and thermal continuum emission from dust collisionally heated by shock waves (e. g. Seok et al. 2013, and references therein) and/or by stellar-radiation reprocessing. Infrared synchrotron emission is only expected in pulsar wind nebulae, for instance in the Crab (Temim et al. 2006). Polycyclic aromatic hydrocarbons are thought to be destroyed by shocks with velocities higher than 100 km s^{-1} and should not survive for more than a thousand years in a tenuous hot gas (Micelotta et al. 2010a,b). However, PAH features have been detected in Galactic SNRs (Andersen et al. 2011), where shock velocities are rather low owing to interactions with a molecular cloud environment, and even in the strong shocks of the young LMC remnant N132D (Tappe et al. 2006). LMC SNRs were discovered in IR with the *Infrared Astronomical Satellite* (Graham et al. 1987; Schwering 1989). More recent surveys with *Spitzer* and *Akari* allowed more extensive studies (Williams et al. 2006b,a; Seok et al. 2008, 2013). Observations with *Herschel* allowed to push observations of SNRs in the submillimetre domain ($\lambda \gtrsim 100 \mu\text{m}$), revealing sputtering of dust by SNR shocks (Lakićević et al. 2015).

Highly ionised species present in SNRs can emit **ultraviolet** lines. Blair et al. (2006) observed LMC SNRs (even more than in X-rays, observations of Galactic SNRs are plagued by absorption) with the *Far Ultraviolet Spectroscopic Explorer* (*FUSE*, covering the range 900 – 1200 Å). They detected O VI and C III lines from 15 objects, bringing the total number of UV-detected SNRs in the LMC to 22.

SNRs are even seen in **high energy γ -rays** (above 100 MeV). The dominant production mechanism is hadronic, i. e. nuclear collisions leading to pion production and subsequent γ -emitting decay (see e. g. Drury et al. 1994, in addition to a leptonic component, from Bremsstrahlung and inverse Compton scattering

of energetic electrons). γ -ray emission is enhanced for SNRs interacting with molecular clouds, which offer dense targets for energetic nuclei (Aharonian et al. 1994). Galactic SNRs were detected in the GeV domain with EGRET (Sturmer & Dermer 1995; Esposito et al. 1996) and later with Fermi (e. g. Abdo et al. 2009), which detected the characteristic pion-decay signature (Ackermann et al. 2013). In the TeV domain, detections mainly originate from H.E.S.S. (Aharonian et al. 2004, 2006). For a census of high-energy observations of Galactic SNRs, see Ferrand & Safi-Harb (2012). In the LMC, however, only one TeV source is known, the pulsar wind nebula in N157B (Komin et al. 2012).

5.5. Typing SNRs

The two flavours of SNe deposit a similar amount of energy in the ISM, producing remnants which are harder to type the older they are. The most secure typing methods are the study of SN optical light echoes (Rest et al. 2005, 2008; *infrared* light echoes can be used to probe the ISM dust, see e.g. Vogt et al. 2012), the association with a neutron star/pulsar wind nebula, or the measurement of the nucleosynthesis products in the ejecta (e. g. Hughes et al. 1995). In the latter case, one uses the ability of X-ray observations to access chemical composition. If shock-heated ejecta have a measurable contribution to the X-ray spectrum, then it is usually straightforward to retrieve the type of SN progenitor, because the nucleosynthesis pattern of CC and thermonuclear SNRs are markedly different (Woosley & Weaver 1995; Iwamoto et al. 1999). Core-collapse SNe inject large amounts of oxygen and other α -elements (Ne, Mg, and Si), while type Ia SNe produce mostly iron (but also Si and S; I naturally emphasise the discussion on elements that can be observed in X-rays). The situation in the Milky Way is complicated by absorption, which can mask the main lines of O, Ne, Mg, and Fe; the typing based on abundance ratios involving Si, S, and trace elements (Ar, Ca) is more complex (see e. g. Rakowski et al. 2006).

The methods described above are best suited to relatively young remnants ($\lesssim 5000$ yr), leaving a significant fraction of the SNR population untyped. However, several *evolved* SNRs have been discovered (in X-rays) in the Magellanic Clouds with an iron-rich, centrally bright emission (Nishiuchi et al. 2001; Hendrick et al. 2003; van der Heyden et al. 2004; Seward et al. 2006; Borkowski et al. 2006a), naturally leading to their classification as type Ia remnants. In addition, studies of the X-ray and infrared morphologies of SNRs (Lopez et al. 2009; Peters et al. 2013) suggest that, as a class, type Ia and CC SNRs have distinct symmetries: type Ia remnants are more spherical and mirror symmetric than the CC SNRs.

Optical spectroscopy is another method to type the SN progenitor¹⁸. In some cases the fast-moving ejecta are detected in optical lines with highly elevated abundances of oxygen. Following a similar argument to X-ray spectroscopy, those so-called *oxygen-rich SNRs* have massive star progenitors. See for instance Lasker (1978), Chevalier & Kirshner (1979), Morse et al. (1995), and references therein. On the contrary, some SNRs have prominent Balmer lines of hydrogen, but absent or weak [S II] and [O III] lines. These include the remnants of historical type Ia SNe (SN 1006 and Tycho's SN). The Balmer-dominated optical spectra are interpreted as non-radiative shocks overtaking (partially) neutral gas (Chevalier & Raymond 1978; Chevalier et al. 1980). A type Ia SN progenitor is consistent with the presence of neutral gas, as massive stars would completely ionise their surrounding. A sample of optically bright Balmer-dominated SNRs was detected in the LMC by Tuohy et al. (1982). By analogy with SN 1006 and Tycho's SNR, they suggested that these were type Ia SNRs as well, a classification later confirmed (mostly through X-ray observations, Hughes et al. 1995).

Finally, clues to the type of remnants are provided by the study of the stellar population around the SNRs. High-mass stars (i.e. CC-SN progenitors) are rarely formed in isolation but cluster in OB associations. Chu & Kennicutt (1988) used this method to tentatively type all LMC remnants known at the time. With the availability of the SFH map of the LMC (Harris & Zaritsky 2009), derived from resolved stellar populations, it is now possible to study the connection between remnants and the age of their parent populations.

¹⁸For historical reasons, this was the first method available

[Badenes et al. \(2009\)](#) performed such a study on (young) SNRs having secure type Ia or CC classifications. As expected, given the short lifetimes of massive progenitors, they found that all CC SNRs in their sample had SFHs dominated by recent peaks of star formation rate. This appears to be *necessary*, but not *sufficient*. Indeed, type Ia SNRs can also be found in star-forming regions, as they showed for N103B (see [Hughes et al. 1995](#); [Lewis et al. 2003](#); [Yamaguchi et al. 2014](#), for strong arguments supporting the type Ia classification) or for SNR 0104–72.3 in the SMC ([Lee et al. 2011](#)). On the other hand, the type Ia SNRs of the (limited) sample of [Badenes et al. \(2009\)](#) are associated with a variety of environments, and future similar studies will provide more insights. I investigate the local SFHs of all the LMC SNRs in Sect. [11.4](#).

Part II.

Material and Methods

6. Technical description of XMM-Newton

6.1. Spacecraft and operations

Most of the results of this thesis rely on data obtained by the *XMM-Newton* space observatory. Key aspects of this mission are reviewed in this Chapter, whilst all details are explained in [Jansen et al. \(2001\)](#) and [Lumb et al. \(2012\)](#).

The *XMM-Newton* space observatory was launched on 1999 December 10 by an Ariane-V. It is a cornerstone mission of the European Space Agency Horizon 2000 programme, initiated in the early 1980's. With a mass of 4 tonne and a length of 10 m, it remains one of the largest scientific satellite ever launched. A sketch of *XMM-Newton* is shown in Fig. 6.1 (top left). The 6.8 m-long carbon-fibre telescope tube connects the Mirror Support Platform, which carries the three X-ray mirrors, Optical Monitor, and star trackers, to the Focal Plane Assembly hosting the spectrometer and imaging detectors.

The observatory was placed in a 48 hours highly eccentric orbit. Altitude originally ranged from 114 000 km at apogee to 7000 km at perigee ([Jansen et al. 2001](#)). Such an orbit allows passive cooling of the X-ray cameras between temperatures of $-100\text{ }^{\circ}\text{C}$ and $-80\text{ }^{\circ}\text{C}$. However, the spacecraft enters the radiation belt for a fraction of the orbit, limiting operations to altitudes larger than 60 000 km. Note that due to several perturbations, the *XMM-Newton* orbit changes with time¹⁹.

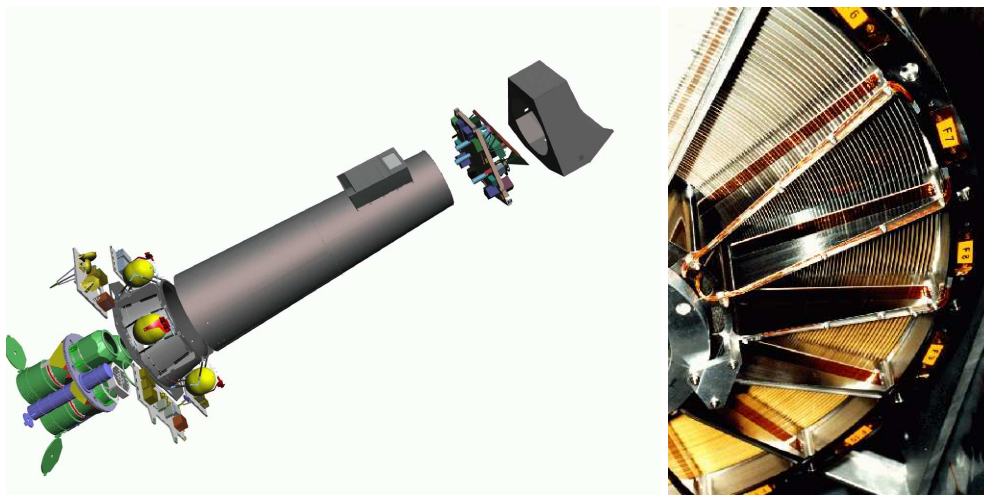


FIGURE 6.1 – *Left*: Sketch of *XMM-Newton*, showing from left to right: X-ray mirrors (green) and Optical Monitor (blue); electronic boards with propellant tanks (yellow) and thrusters (red); carbon-fibre telescope tube; Focal Plane Platform, with cameras and radiators. (Image courtesy of Dornier Satellitensysteme GmbH.) *Right*: A close-up view of the mirrors shells mounted on the spider wheel. (Photo courtesy of D. de Chambure, XMM-Newton Project, ESA/ESTEC.)

¹⁹See *XMM-Newton* Users Handbook, Issue 2.11, 2013 (ESA: XMM-Newton SOC).

6.2. Telescopes

XMM-Newton carries three identical X-ray telescopes, each consisting of 58 gold-coated nested Wolter-I mirrors (see Sect. 2.2) with a focal length of 7.5 m. The innermost mirrors have a diameter of 306 mm and a thickness of 0.47 mm. The thickness increases to 1.07 mm for the outer mirror shells, which have a 700 mm diameter. The mirrors were manufactured using a replication process: A gold layer is first transferred on a super-polished mandrel, before the nickel shell of the mirror is electroformed on the gold layer (de Chambure et al. 1998). The mandrels are made out of double conical aluminium blocks, coated with nickel. They are then shaped and polished to achieve a surface roughness better than 4 Å.

The mirror modules are encased between ancillary elements: in front, the visible and X-ray light baffles that reduce stray light; behind, an electron deflector and (for two out of three telescopes) the Reflection Grating Assembly which deflects about half of the X-ray light on a secondary focus, for use with the Reflection Grating Spectrometer (RGS).

The design for the telescopes was chosen to maximise the collecting area. Indeed, XMM-Newton remains the most sensitive X-ray observatory fifteen years after launch, with an effective area of 1500 cm² (per telescope) at 1 keV. At the same time it offers a satisfactory angular resolution of ~15'' (Half-Energy Width), as measured both on-ground and in-orbit. Finally, the field of view of each telescope is ~30' in diameter.

6.3. EPIC instruments

Three CCD imaging cameras are placed at the focal points of each of the X-ray telescopes. Two of them have Metal Oxide Semi-conductor (MOS) CCD arrays and the third uses pn-CCDs. Together, they form the European Photon Imaging Camera (EPIC). I briefly review their properties and performances in this Section. This work does not make use of the spectrometers onboard XMM-Newton (the RGS instrument, den Herder et al. 2001) and consequently I do not describe them.

6.3.1. The EPIC-pn camera

The EPIC-pn camera (Strüder et al. 2001) consists of a monolithic 6 × 6 cm² wafer with 12 pn-CCD back-illuminated chips arranged in four quadrants. Each chip has 150 μm × 150 μm pixels arranged in 200 rows and 64 columns. The pixel size on the sky is 4.1'', providing adequate sampling of the PSF. The majority of the field-of-view (97 %) is covered by the pn camera.

Various read-out modes exist for the camera. In the most-commonly used full-frame (FF) mode, the short frame time of 73.3 ms provides both a good time resolution and a high pile-up limit. Windowed or “timing” (i. e. non-imaging) modes can accommodate for (very) bright source observations with time resolution as short as 0.03 ms.

EPIC-pn is the most sensitive imaging camera to date (see effective area curve on Fig. 6.2, left). It has a modest spectral resolution, from 111 eV (FWHM) at 1 keV and 162 eV at 6 keV (early-phase in-flight calibration, Strüder et al. 2001). Mostly due to radiation damage, the energy resolution degrades²⁰ at a rate of ~2.5 eV yr⁻¹.

6.3.2. The EPIC-MOS cameras

The EPIC-MOS cameras (Turner et al. 2001, hereafter MOS1 and MOS2) both consist of seven MOS-type CCDs with 600×600 pixels, each 40 μm square (1.1''). As opposed to the pn camera, pixel columns are not

²⁰XMM-Newton calibration technical note XMM-SOC-CAL-TN-0018, v3.3

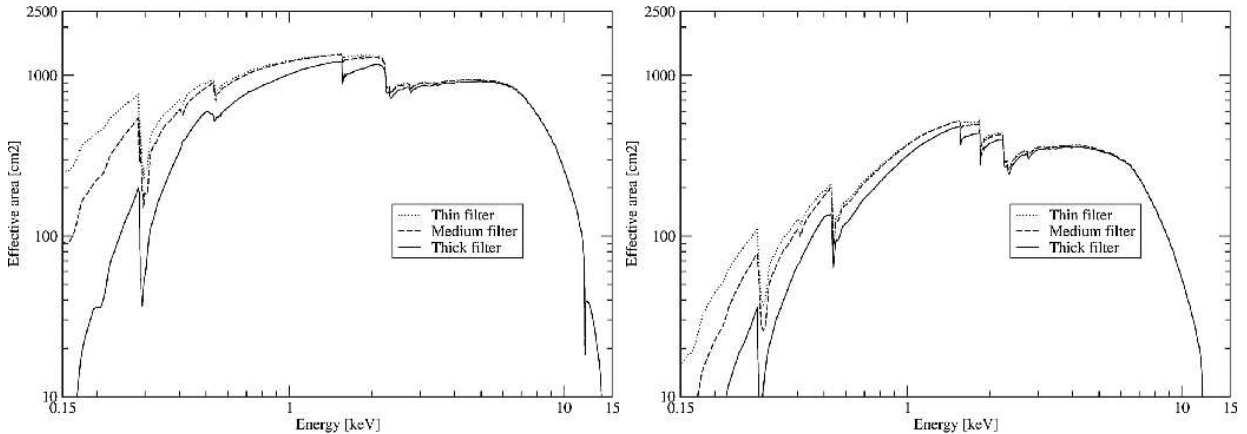


FIGURE 6.2 – Effective areas of EPIC-pn (left) and MOS (right) in full-frame modes, for different optical blocking filters.

read-out in parallel, resulting in a longer integration time of 2.6 s, limiting the time resolution. As for pn, windowed or timing modes can be used to read out only a fraction of the CCDs.

The telescopes focusing X-rays on the MOS cameras are equipped with the gratings of the RGS, such that about 44 % of the incident flux reaches the MOS CCDs. Consequently, the effective area of EPIC-MOS is less than that of pn (Fig. 6.2). However, the two MOS cameras are superior to pn in terms of energy resolution: at 1 keV, the FWHM resolution is only 80 eV. At 6 keV the resolution is ~ 150 eV, close to the Fano limit. No significant degradation of these performances has been observed since 2002.

The only failure to date to the MOS instruments (and to the whole EPIC system) has been the loss of one outer CCD (MOS1 CCD-6) in March 2005, most likely due to a micro-meteorite impact (Abbey et al. 2006). A very similar event in December 2012, having probably the same origin, resulted in the loss of another MOS1 chip (CCD3) and an increased noise level in the neighbouring CCD4. However, the overall effect of these events is limited, since only 28 % of the MOS1 geometrical area is affected. In turn, MOS1 only contains ~ 22 % of the total effective area of the whole EPIC instrument. The performances and the quality of the calibration remain thus extremely high after 15 years in the harsh condition of space, a truly EPIC achievement.

6.4. Instrumental background

The signal recorded in an XMM-Newton observation comprises many components, which can be separated in three main groups: the X-ray emission of the target of the observation, an astrophysical X-ray background (hereafter AXB, i. e. X-rays from any source located *in projection* near the target), and an instrumental background. Here only the latter is presented. The properties of the AXB and the spectral analysis method used are described in Sect. 8.

The instrumental background of the EPIC consists of three components. The first is an **electronic noise**, in the form of hot pixels/columns or read-out noise. In the case of EPIC-pn, the read-out noise increases dramatically below energies of $\lesssim 300$ eV, especially if double-pixel events are used.

The second component is the **particle-induced background**, the spectrum of which includes both a continuum and many lines. The *continuum part* is due to the quiescent particle background (QPB). Cosmic rays deposit a large amount of energy ($\gg 10$ keV) in many adjacent pixels and are easy to distinguish from valid X-ray events. However, the unrejected fraction of direct and Compton-scattered cosmic rays produces a remaining continuum with a rather flat spectrum and a rate of 0.021 ± 0.0022 events $\text{cm}^{-2} \text{s}^{-1}$ for the MOS

cameras, and about twice as much for pn (Lumb et al. 2002). The continuum is both chip-, position-, and time-dependent (at least for MOS where it has been extensively studied, see Kuntz & Snowden 2008). These variations have to be taken into account in the spectral analysis. The *line part* of the particle background is composed of many X-ray fluorescence lines produced by the interaction of high-energy particles with the material surrounding the detectors (Al, Ni, Cu, etc.). Due to this origin the fluorescence line component varies with time. This component is highly position-dependent, mirroring the distribution of the camera material around the detectors (Lumb et al. 2002; Freyberg et al. 2004; Kuntz & Snowden 2008). EPIC is capable of looking at itself !

The third component is the so-called **soft proton contamination** (SPC). Low-energy protons, accelerated in the Earth magnetosphere and focused by the X-ray telescopes onto the detectors, produce events that cannot be distinguished from genuine X-ray events. The soft proton flux has a highly time-variable, “flaring” nature. At times of the strongest flares, most of the data are unusable anyway (except in the case of a very bright target). But soft proton flares can occur on longer time scales, at lower amplitudes. These time intervals are typically used for science, though they include a small but potentially important contamination by soft protons (hence the term “SPC”). The flaring spectrum was found by Kuntz & Snowden (2008) to be rather flat, with a small roll-off at high energy. The same authors showed that the stronger the flare, the flatter (i. e. harder) the SPC spectrum.

7. XMM-Newton observations and data reduction

7.1. Covering the LMC

FOLLOWING the tradition for new X-ray instruments to observe the Large Magellanic Cloud (Sect. 4.3.1), XMM-Newton has been often (and continues to be) pointed at our nearest neighbour galaxy. It started already with the “first light” image of the observatory, of the 30 Doradus region (Dennerl et al. 2001). Since then, about 200 observations of the LMC were performed. In many cases, one specific object is placed at the focus of the telescopes. All kinds of objects are surveyed, including X-ray binaries (e. g. LMC X-1, Hanke et al. 2010), SSSs (such as CAL 83, Paerels et al. 2001), many previously-known and newly-found SNRs (Sect. 11), and superbubbles (for instance N51D, Yamaguchi et al. 2010). Some fields are observed several times, yielding very deep exposures. For instance, the SNR N132D is used as a calibration source and regularly observed; also SN 1987A is frequently monitored (Sect. 9). In these two regions, the combined exposure reaches 10^6 s. Besides regular observations, the so-called “target of opportunity” (ToO) observations can be triggered to observe a transient source in a particular state. X-ray binaries in outburst are the most relevant and common cases of ToO in the LMC. The identification of their outbursts are made with other satellites, mostly *Swift* (for example Vasilopoulos et al. 2013), but also *Integral* (e. g. Sturm et al. 2012b).

In recent years, several programmes for observations of the LMC were proposed in which I was or became involved. This includes for instance XMM-Newton observations of SNR candidates selected from the ROSAT catalogue. This programme was initiated in XMM-Newton’s Announcement of Opportunity 9 (AO-9) and reconducted since then, providing confirmation of one or two new SNRs each year (those are analysed in Sect. 10 and Sect. 11). The most ambitious project was the survey of the LMC, proposed as a Very Large Programme (VLP) for XMM-Newton (PI: Frank Haberl). The survey comprises 70 pointings chosen to fill the gaps between all existing observations. This provides a contiguous field in the central region of the LMC, a strategy similar to the XMM-Newton survey of the SMC (Haberl et al. 2012b; Sturm 2012; Sturm et al. 2013). Because the LMC is larger and closer, even the 70 observations of the survey and the archival data still cover only about half of the total extent of the galaxy. Due to the large number of required observations, the survey was performed over several AOs, starting in AO10 (2011-2012) in priority C. In AO11 all fields were accepted with priority B, and most observations of the survey were conducted in 2012. Nine fields, blighted by high background, were re-observed during AO12 and AO13 to reach an homogenous depth across all the survey field.

7.2. Data reduction

The processing of all available XMM-Newton data in the LMC region, and those of the VLP survey in particular, was done with the data analysis pipeline developed in our research group over several years. This pipeline was already used for the surveys of M31 (Pietsch et al. 2005; Stiele et al. 2011) and M33 (Pietsch et al. 2004; Misanovic et al. 2006). It was then enhanced for the analysis of the SMC survey by Richard Sturm (2012). The analysis pipeline is similar in essence to that used for the XMM-Newton Serendipitous Source Catalogue Watson et al. (2009), with the advantage of a better spatial accuracy (thanks to astrometric boresight corrections), and dedicated source screenings and cross-identifications.

The pipeline is a collection of tasks from the XMM-Newton Science Analysis Software²¹, specifically designed for the observatory and provided by ESA. The tasks are organised in bash scripts, together with other tools, in particular the FITS-file manipulation tasks of the FTOOLS package²² (Blackburn 1995). Starting from the raw data, organised in observation data files (ODFs), the pipeline performs all the necessary tasks to obtain clean event lists. Those are tables with one row per event, including all relevant information (detector position, energy channel, time of arrival, pattern, flags, etc.)²³. From the event lists, images, spectra, or time series can be extracted. They are also used for source detection. I summarise the important steps of the pipeline in the next paragraphs.

Preparing the data: To point to the Current Calibration Files (CCFs) corresponding to each observation, a CCF index file (CIF) is created with the SAS task `cifbuild`. Then, using the task `odfingest`, the ODF summary file is extended with data extracted from the instrument housekeeping datasets. The instrument mode is also determined based on the CIF.

Creating event lists: The meta-tasks `epchain` and `emchain` produce EPIC-pn and MOS event lists, respectively, performing all necessary tasks. Raw events are first extracted from each exposure and CCD chip. Bad pixels are flagged. In the case of EPIC-pn, the task `epreject` corrects shifts in the energy scale of some pixels induced by high-energy particles hitting the detector while the offset map is calculated. Raw events are then assigned pattern and detector position information. EPIC-pn events are corrected for gain variation and charge transfer inefficiency (CTI). The calibrated events are (tangentially) projected on the sky using the task `attcalc` and an attitude history file (AHF), which records the attitude of the spacecraft during the observation. The AHF is created by the task `athkgen` that is automatically ran before the main chain (unless the AHF already exists). EPIC-pn event times are randomised within their read-out frame. Finally, event lists from all CCDs are merged in the final list by `evlistcomb`.

Time filtering: Times that are useful for analysis are known as good time intervals (GTIs), and the SAS tasks use GTI files containing the start and end times of GTIs. Standard GTIs are created prior to running the chain to identify the times when the instrument is in nominal state (based on the housekeeping parameters). In addition, periods of high background must be filtered out. The pipeline identifies the background-GTIs as times when the count rate in the (7–15) keV is below a threshold of 8 cts ks⁻¹ arcmin⁻² and 2.5 cts ks⁻¹ arcmin⁻² for EPIC-pn and EPIC-MOS, respectively. Soft proton flares affect all detectors, so only the GTIs *common* to pn and MOS are used. When one instrument starts earlier or last longer, this interval is added to the GTIs.

Images creation: The pipeline then produces images from the calibrated, cleaned, and background-filtered event lists. The image pixels have a size of 2'' × 2''. All single to quadruple-pixel (PATTERN = 0 to 12) events with FLAG = 0 from the MOS detectors are used. From the pn detector single and double-pixel events (PATTERN = 0 to 4) with (FLAG && 0xf0000) = 0 (including events next to bad pixels or bad columns) are used. Below 500 eV, only single-pixel events are selected to avoid the higher detector noise contribution from the double-pixel events. Exposure maps taking into account the telescope vignetting (which is energy-dependent) are created with the task `eexppmap`. Images and exposure maps are extracted in the standard XMM-Newton energy bands (Table 7.1) for all three cameras.

EPIC records photons not only during the integration time, but also during CCD read-out. These are out-of-time (OoT) events, which are assigned a wrong detector column and wrong CTI-correction (and thus a wrong energy). They also produce streaks running from bright sources to the edges of the detector. The OoT

²¹SAS, <http://xmm.esac.esa.int/sas/>

²²<http://heasarc.gsfc.nasa.gov/ftools/>

²³In all LMC observations, a total of 442 884 600 events were recorded (counting only those in the calibrated event lists).

fraction f_{OoT} is a function of the integration-to-read-out time ratio and therefore is different for every mode of pn and MOS. In the MOS camera, the charge of pixels in the exposed area are first (quickly) transferred to a storage area, shielded from the sky; from there there are read-out, while a subsequent integration start in the exposed area. Therefore, f_{OoT} is much smaller for MOS than for pn. OoT images are created from the EPIC-pn OoT event lists, scaled by the corresponding f_{OoT} ²⁴, and subtracted from the images. MOS and pn images are then merged, smoothed with a 10'' full width at half maximum (FWHM) Gaussian kernel, and finally divided by the vignetted exposure maps.

TABLE 7.1 – Energy bands used for X-ray images

Name	E_{\min}	E_{\max}
Standard–1	0.2	0.5
Standard–2	0.5	1
Standard–3	1	2
Standard–4	2	4.5
Standard–5	4.5	12
SNR–soft	0.3	0.7
SNR–medium	0.7	1.1
SNR–hard	1.1	4.2

Notes. The “standard” bands are used by the pipeline for all observations in the LMC field. The “SNR” bands are tailored for the objects with thermal spectra.

Detector-background images are also created, by using XMM-Newton filter wheel closed (hereafter FWC) data, obtained with the detectors shielded from astrophysical and soft-proton backgrounds by a 1.05 mm-thick aluminium filter. FWC data are collected several times per year, and the merged event lists of these observations are made available by the calibration working group²⁵. The detector corners are always shielded from the X-ray telescopes, and the count rate in the corners is used to estimate the contribution of the instrumental background f_{FWC} to the science image. The FWC image is scaled by f_{FWC} and subtracted from the science image.

Source detection: X-ray source detection is performed simultaneously to images in all five energy bands of all three instruments with the SAS meta-task `edetectchain`. This task is a script that first searches for point sources using a sliding box detection method (`eboxdetect` in “local detection mode”). Sources detected in this first run are then removed from the input images by `esplinemap` which creates smooth background maps by fitting 2-D splines. A second run of `eboxdetect` (in “map detection mode”) searches for sources,

this time using the background from the maps produced by `esplinemap`. The resulting list is used as input for `emldetect`, which performs a maximum likelihood PSF-fitting to determine the parameters (e. g. position and source counts) of each source. This thesis is mainly concerned with SNRs, i. e. extended sources. However, detecting point sources is highly desirable: it allows me to excise unrelated point sources from spectral extraction regions and to look for central compact objects or pulsar wind nebulae inside SNRs.

Extension for SNRs: I extended the pipeline with several scripts for the analysis of the SNRs in the LMC (although they are useful for any extended sources). The *spectral* analysis is described in Sect. 8. For imaging purposes, all observations of an SNR are combined to produce an image centered on the source. The smoothing of the images (using the SAS task `asmooth`) is performed both in constant and adaptive mode. In the latter, the task calculates a library of Gaussian kernels such that the resulting images reached a minimum (Poissonian) signal-to-noise ratio of 5 everywhere. Regions of good statistics (e. g. bright sources) will be smoothed with a 10'' FWHM kernel (the chosen minimum value), whereas fainter regions (diffuse emission, rims of the field of view) will be smoothed with wider kernels. I selected the (minimum) kernel size for (adaptive) smoothing manually depending on the available data and brightness of the SNR under investigation. Moderately-bright and faint SNRs (i. e. most of the sample) have smoothing kernel sizes of

²⁴Values taken from the XMM-Newton Users Handbook.

²⁵http://xmm2.esac.esa.int/external/xmm_sw_cal/background/filter_closed/

$\gtrsim 10''$ or $\gtrsim 20''$. The few brightest objects and SNRs in very deep fields (e. g. the field around SNR 1987A, see Sect. 9) only need shallow smoothing (kernels $\gtrsim 3''$ or $\gtrsim 6''$).

The standard bands of the pipeline are not the best suited for SNRs, which show thermal emission concentrated between 0.5 keV and 2 keV. In addition, lines and line complexes from different elements are well separated in this range. Therefore, I produced images in a set of energy bands tailored to the thermal spectrum of SNRs (Table 7.1). A soft band from 0.3 keV to 0.7 keV includes strong lines from oxygen; a medium band from 0.7 keV to 1.1 keV comprises Fe L-shell lines as well as Ne He α and Ly α lines; and a hard band (1.1 – 4.2 keV) which includes lines from Mg, Si, S, Ca, Ar, and possibly non-thermal continuum. Thus, the composite images of SNRs provide a visual evaluation of their temperature: evolved objects with a relatively cool plasma ($0.2 \text{ keV} \lesssim kT \lesssim 0.4 \text{ keV}$) are most prominent in the soft band, those with higher temperatures ($0.4 \text{ keV} \lesssim kT \lesssim 1 \text{ keV}$) in the medium band. Only (young) SNRs with a much hotter component or a non-thermal continuum will have significant emission in the hard band as well.

8. Method of X-ray analysis for extended sources

THE OBJECTS this thesis is concerned with are SNRs, i. e. *extended* X-ray sources. Furthermore, many of these remnants have a low surface-brightness. Consequently, the analysis of their spectra is more challenging. A careful treatment of the background, both instrumental and astrophysical, is utterly important in order to obtain meaningful fits and extract the purest possible information from the source. It is not desirable to simply subtract a background spectrum extracted from a nearby region, because of the different responses and background contributions associated to different regions, and because of the resulting loss in the statistical quality of the source spectrum. An alternative method, which I developed and used, is to extract a nearby background spectrum, define a (physically-motivated) model for the background and simultaneously fit the source and background spectra. This Chapter explains the method in detail.

8.1. Spectral extraction

Because of the telescope vignetting, the effective area is not constant across the extent of SNRs. To take this into account, all spectra (source and background) are extracted from *vignetting-weighted* event lists. These are produced as the first step of the analysis with the SAS task `evigweight`. It assigns a weight to each event of energy E_j at detector coordinates $(detx_j, dety_j)$, which is the inverse of the ratio of the effective area at that position to the central effective area (at the same energy):

$$w_j = \frac{A_{0,0}(E_j)}{A_{detx_j, dety_j}(E_j)} \quad (8.1)$$

The corrected event lists are equivalent to that obtained with a flat instrument. For spectral analysis, a flat response file with the on-axis effective area must then be used.

8.2. Modelling the instrumental background

I described the instrumental background of XMM-Newton in Sect. 6.4. It will be present in all observations and is position-dependent. Its contribution will be relatively higher in spectra of sources with low surface brightness and must be taken into account, i. e. modelled. To do so, I use the FWC data (Sect. 7.2). Several hundreds of kilosecond worth of data are now available, providing a good knowledge of the spectrum of the instrumental background. As part of his PhD thesis, Richard Sturm (2012) developed an empirical model of the EPIC-pn FWC data. This includes an exponential decay (modified by a spline function), a power law, and a combination of Gaussian lines to account for the electronic noise, QPB, and instrumental lines, respectively. In addition, two smeared absorption edges to the continuum are included.

I extended his work and developed a similar model for the EPIC-MOS FWC spectra. This allows to analyse jointly the pn and MOS spectra of LMC SNRs (Sect. 11.2) and take advantage of the better spectral resolution of MOS. There is no low-energy noise as for EPIC-pn, so no exponential decay function is needed. I obtained satisfactory results with a broken power law for the continuum, leaving the slope of the two segments as well as the energy of the break free. A smeared absorption edge around $E \approx 0.53$ keV (K edge of oxygen) improved the fit and was included. A set of Gaussian are used to model the fluorescence lines. The materials of the MOS and pn cameras are different, and so is the observed fluorescence line pattern.

Both have a strong Al K line at 1.49 keV. MOS background also features a strong Si K line at 1.74 keV, as opposed to pn, where the strongest line is Cu K at 8.05 keV. Other lines from Au, Cr, Mn, Zn, Cu, Fe, and Ni are detected (Lumb et al. 2002; Kuntz & Snowden 2008) and included in the MOS detector background model.

8.3. Modelling the astrophysical background

The AXB can usually be modelled with four or less components (Snowden et al. 2008; Kuntz & Snowden 2010). The soft part of the AXB ($E \lesssim 2$ keV) has mostly a thermal emission spectrum and originates from various regions/hot plasmas. The Local Hot Bubble (LHB) is a region in the solar neighbourhood filled with million-degree plasma ($kT \approx 85$ eV, Henley & Shelton 2008). This component was modelled with an unabsorbed APEC model. Emission from the Galactic halo comprises a cool ($kT \sim 0.1$ keV) and warm ($kT \sim 0.25$ keV) thermal component. Since the cool component is mostly absorbed by the foreground Galactic absorbing column, I did not include it in the AXB model to keep it as simple as possible. For the warm component I used an absorbed APEC model.

Above 2 keV, the background is mostly from the cosmic X-ray background (CXB), a superposition of unresolved distant objects, in other words AGN. This component has an absorbed power-law spectrum, with a photon index fixed at $\Gamma = 1.46$ (Chen et al. 1997). To account for the non-uniformity of this component, the normalisation is a free parameter in my background model.

The foreground Galactic absorption is reproduced by the photoelectric absorption model *phabs* in XSPEC, using the cross-sections from Balucinska-Church & McCammon (1992). The foreground column density $N_{H \text{ Gal}}$ at the location of each analysed source is taken (and fixed) from the HI maps of Dickey & Lockman (1990, available online on the HEASARC pages²⁶).

8.4. Simultaneous fitting

For the analysis of one extended source, two different regions are defined:

- a source spectrum extraction region (hereafter SRC region), and
- a background spectrum extraction region (hereafter BG region).

Two spectra are extracted per instrument (pn, MOS1, and MOS2) from each region, one from the event list of the science observation, the second from the FWC data. The FWC spectra must be extracted at the same *detector* position as in the science observation, because of the strong position-dependency of the instrumental background for both pn and MOS (Sect. 6.4 and references therein). The SRC and BG regions are best defined in World Coordinates System (WCS, i. e. sky position²⁷). Therefore, I first project the FWC data at the same sky position than the science observation, using its attitude history file and the SAS task `attcalc`. I can then use the same extraction regions to select FWC spectra.

I applied the same screening and filtering criteria used for the science data to the FWC data, including the vignetting correction with `evigweight`. Formally, the instrumental background is *not* subjected to vignetting, which is an effect of the telescope on *photons*. However, by applying a vignetting correction to the science data, one assigns weights to genuine X-ray events as well as to particle background events, since one cannot *a priori* distinguish the two type of events. Therefore, one needs to vignetting-correct the FWC data to make sure that the FWC spectra, used for the modelling of the instrumental background contribution to the science data, have been processed in the same way as the latter. At a given position

²⁶<http://heasarc.gsfc.nasa.gov/cgi-bin/Tools/w3nh/w3nh.pl>

²⁷This is more practical, in particular when several observations of a source with different pointings exist.

on the detector, `evigweight` will assign heavier weights to photons with higher energies, an effect that can be easily accounted for in the background model. To do so, I added a spline function to the pn and MOS instrumental background models. This reproduces the effect of the vignetting correction, which “overweights” events above 5 keV, if they have been recorded at significant off-axis angles.

The four spectra are fitted simultaneously. The instrumental background model is constrained by the FWC data, and included (with tied parameters) in the spectra from the science observation. The science spectrum in the BG region therefore allows the parameters of the AXB to be determined. It is assumed that the temperature of the thermal components and the surface brightness of the thermal and non-thermal components do not vary significantly between the SRC and BG regions. Thus, the appropriate temperature and normalisation parameters are linked. All background components are then accounted for, and one can explore the intrinsic emission from the source using several emission models (Sect. 10 & 11.2).

Part III.

Results and discussion

9. The X-ray evolution of SNR 1987A

9.1. Introduction

SN 1987A was discovered in the LMC on 23 February 1987. It has been extensively studied ever since and is exceptional in many ways. It is the nearest supernova in almost 400 years²⁸. The SN was promptly classified as type II. The detection of a burst of neutrinos by two Earth-based experiments (Hirata et al. 1987; Bionta et al. 1987) confirmed the theory that type II SNe result from the collapse of a stellar core into a neutron star, with most of the energy (10^{53} erg) released through neutrinos.

The progenitor star was identified in pre-explosion plates to be SK -69 202 (from the catalogue of Sanduleak 1970), a 12th magnitude B3 I supergiant star of about $20 M_{\odot}$, i. e. not a red supergiant as expected. The SN was unusually dim, with a maximum luminosity 2.5 mag fainter (i. e. a factor of ten) than typical for type II SNe, a consequence of the compactness of the blue supergiant progenitor.

SN 1987A was detected surprisingly early (a few months) at high energies, with the Japanese satellite *Ginga* (in the 6 keV – 20 keV band, Dotani et al. 1987) and the Soviet Mir-Kvant instrument (from 20 keV to 300 keV, Sunyaev et al. 1987). Since the expanding shell was X-ray thick at this time, the observed hard X-ray photons were likely γ -rays from the radioactive decay of ^{56}Ni and ^{56}Co , Compton-scattered down in the hard X-ray band.

Optical imaging revealed the presence of three rings (Crotts et al. 1989; Burrows et al. 1995). Two rings form a bipolar hourglass-shaped nebula; the third one, brighter and closer to the SN site, is known as the “Equatorial Ring” (hereafter ER). This structure is likely to have been formed by the interaction between the stellar winds emitted by the progenitor star during its red supergiant and blue supergiant phases (e.g. Chevalier & Dwarkadas 1995), although a binary merger model might be favoured (Morris & Podsiadlowski 2007, 2009). As the explosion blast wave propagates and interacts with the circumstellar medium (CSM), soft X-rays are produced. Careful monitoring of the X-ray light curve allows to probe the complex CSM structure around the SN progenitor and constrain pre-explosion evolution models.

Contrary to hard X-rays, early observations (August 1987) in the soft band (0.2 keV – 2.1 keV) with a sounding rocket resulted in a non-detection, with an upper limit of 1.5×10^{36} erg s⁻¹ (Aschenbach et al. 1987). The “first-light” observations of ROSAT towards 30 Doradus yielded an upper limit of 2.5×10^{34} erg s⁻¹ (Trümper et al. 1991). Only from April 1991 onwards was a soft X-ray signal detected (Beuermann et al. 1994). The early evolution followed with ROSAT revealed a slow but steady increase (Hasinger et al. 1996).

The next-generation observatories (*Chandra*, *XMM-Newton*, *Suzaku*) have naturally targeted SN 1987A on many occasions. In particular, the *Chandra* monitoring in the first half of the 2000s had the highest cadence. With these data, Park et al. (2005) reported a dramatic upturn of the soft X-ray light curve, about 6200 days after the explosion (i. e. late 2003), transitioning from a linear to exponential rise. This is interpreted as the beginning of the interaction of the blast wave with the main body of the ER, as supported

²⁸In the historical records, there are four certain Galactic SNe after AD 1000: SN 1604 (Kepler’s SN), SN 1572 (Tycho’s SN), SN 1054 (Crab nebula), SN 1006, and one likely in 1181 (progenitor of 3C58) (Clark & Stephenson 1977; Stephenson & Green 2002). The identification of Flamsteed’s star (AD 1680) as the progenitor of Cas A is seriously questioned (Broughton 1979; Kamper 1980; Stephenson & Green 2002). The lack of historical records also suggest than the second youngest SNRs in the LMC (0509–675) cannot be from much later than the beginning of the 17th century (see discussion in Badenes et al. 2008). Finally, the youngest Galactic SNR G1.9+0.3 has an age $\lesssim 150$ years (Reynolds et al. 2008; Green et al. 2008) but its location near the tremendously-absorbed Galactic center precluded its detection.

TABLE 9.1 – Details of the XMM-Newton EPIC-pn observations of SNR 1987A

ObsId	Obs. start date	Age ^(a) (days)	Filter	Total / filtered exp. time ^(b) (ks)
0406840301	2007 Jan 17	7267	Medium	106.9 / 81.9
0506220101	2008 Jan 11	7626	Medium	109.4 / 91.0
0556350101	2009 Jan 30	8013	Medium	100.0 / 84.0
0601200101	2009 Dec 12	8328	Medium	89.9 / 89.8
0650420101	2010 Dec 12	8693	Medium	64.0 / 61.7
0671080101	2011 Dec 02	9048	Medium	80.6 / 70.5
0690510101 ^(c)	2012 Dec 11	9423	Medium	68.0 / 68.0

Notes. ^(a) Number of days since the explosion of SN 1987A. ^(b) Total and useful (filtered) exposure times, after removal of high background intervals. ^(c) Not included in Maggi et al. (2012b).

by the simultaneous brightening of optical hot spots along all the ER (Gröningsson et al. 2008)²⁹. Similar conclusions were reached by Haberl et al. (2006) using the first XMM-Newton observations and re-analysis of Chandra data.

It is expected that after the forward shock overcame the main body of the ER, the X-ray light curve will flatten and then turn-over. The soft X-rays are therefore a probe of the ER. Dewey et al. (2012, hereafter D12) present simple hydrodynamic models that reproduce the soft and hard X-ray light curves. The models show the soft X-ray flux behaviour for both the case where the forward shock has left the ER and the case where the ER is still being shocked (the “thin” and “thick” cases in their Figure 12).

Since 2007, a more frequent XMM-Newton monitoring was performed. I had the great chance to use these data to contribute to the research on SN 1987A after its 25th birthday³⁰. I used the superior capabilities of the EPIC-pn camera, focusing first on the X-ray light curve and its rapid evolution since 2006. I also examined the spectrum around 6.4 keV – 6.7 keV to assess the presence, properties, and evolution of the Fe K lines, which are detected unambiguously for the first time. This work was published in a Letter to *Astronomy & Astrophysics* (Maggi et al. 2012b). Note that the identifier “SNR 1987A” is used throughout this work: the source is now clearly in the *remnant* stage rather than the *supernova* stage, as the emission is dominated by radiation from shock-heated CSM/ejecta, as typical in (older) remnants.

9.2. Observations and data reduction

I used data of the almost yearly XMM-Newton monitoring of SNR 1987A (PI: F. Haberl), from January 2007 to December 2012. The high-resolution Reflection Grating Spectrometer (RGS) data taken up to January 2009 are presented in Sturm et al. (2010). I homogeneously (re-)analysed all observations from 2007 to 2012, four of which had not been published so far³¹. I mainly used data from the EPIC-pn camera operated in full-frame mode with medium filter. Details of the observations are listed in Table 9.1. All the observations were processed with the SAS version 11.0.1. I extracted spectra from a circular region centred on the source, with a radius of 25″. The use of spatially-integrated spectra is dictated by the small radius of the source (still less than 1″, Helder et al. 2013), which is completely unresolved by XMM-Newton.

²⁹See also the iconic *HST* images at <http://hubblesite.org/newscenter/archive/releases/2007/10/>.

³⁰Or shall I say 25th deathday ?

³¹The last observations was not included in Maggi et al. (2012b).

Only *Chandra* is able to resolve the source, using complex deconvolution techniques (Burrows et al. 2000; Racusin et al. 2009). Even *Chandra* studies rely on spatially-integrated spectra. The background spectra were extracted from a nearby point-source-free region common to all observations. Only single-pixel events (PATTERN = 0) from the pn detector were selected. I rebinned the spectra with a minimum of 20 counts per bin in order to allow the use of the χ^2 -statistic. Non-rebinned spectra were used with the C-statistic (Cash 1979) for the study of Fe K lines, because of the limited photon statistics above 6 keV. The spectral fitting package XSPEC (Arnaud 1996) version 12.7.0u was used to perform the spectral analysis.

9.3. The spectra of SNR 1987A

9.3.1. Spectral model

I fit the EPIC-pn spectra of SNR 1987 with a three-component plane-parallel shock model (called vps shock in XSPEC, where the prefix “v” indicates that abundances can vary), using `neivers` 2.0. This is the same model as the one used by D12 for *Chandra* and *XMM-Newton* spectra, with a fixed-temperature component ($kT = 1.15$ keV), although I did not use a Gaussian smoothing. This model gives slightly better fits than when using a two-component model (e. g. Park et al. 2004; Heng et al. 2008). The high- and low-temperature components are believed to originate from the interaction of the shocks with uniform material and denser clumps in the ER, respectively (D12). Another interpretation is that the high-temperature component comes from plasma shocked a second time by a reflected shock (Zhekov et al. 2006).

For elemental abundances, I followed the same procedure as in Haberl et al. (2006): N, O, Ne, Mg, Si, S, and Fe abundances were allowed to vary but were the same for all observations, whereas the He, C, Ar, Ca, and Ni abundances were fixed. The systemic velocity of SNR 1987A (286 km s^{-1} , e. g. Gröningsson et al. 2008) was taken into account by choosing the redshift accordingly.

For the absorption of the source emission, two photoelectric absorption components were included, one with $N_{H \text{ Gal}} = 0.6 \times 10^{21} \text{ cm}^{-2}$ (fixed) for the Galactic foreground absorption (Dickey & Lockman 1990) and another one with $N_{H \text{ LMC}}$ (free in the fit) for the LMC. Metal abundances for the second absorption component are fixed to the average metallicity in the LMC (i. e., half the solar values, Russell & Dopita 1992). All spectra share the same $N_{H \text{ LMC}}$.

I simultaneously fitted the first six spectra using energies between 0.2 keV and 10 keV. The last observation, not included in Maggi et al. (2012b), was analysed later on using the same workflow. For consistency with the detection of Fe K lines, I included an additional (Gaussian) line to the model for the spectra obtained after 2007. The central energies and widths of the lines were fixed to the values found in the detailed analysis of the lines (see below). Only the normalisation of each line was left free.

9.3.2. Spectral evolution

The fit was satisfactory, with $\chi^2 = 5114.2$ for 4109 degrees of freedom. Detailed spectral fits were not the focus of the study published in Maggi et al. (2012b). For the sake of completeness, however, I include in this thesis all spectral results of observations from 2007 to 2012. The best-fit parameters are listed in Table 9.2 and their evolution vs. time are plotted in Fig. 9.1. In summary, the spectral results are the following :

- The best-fit $N_{H \text{ LMC}}$ was $3.18^{(+0.07)}_{(-0.13)} \times 10^{21} \text{ cm}^{-2}$, corresponding to a total absorption column of $3.7 \times 10^{21} \text{ cm}^{-2}$, somewhat higher than found using the grating instruments aboard *Chandra* and *XMM-Newton* (Sturm et al. 2010; Zhekov et al. 2006).
- The abundance pattern (Table 9.2) is in line with the one reported by Sturm et al. (2010) and D12.
- The temperature of the cool component slowly but steadily increased from 0.35 keV to 0.44 keV, while its normalisation remained stable since 2009.

- The temperature of the hot component is always in excess of 3.5 keV, and its normalisation increased after 2009.
- The emission measure of the mid-temperature component (kT fixed at 1.15 keV) shows the largest and most stable increase.
- The ionisation age does show an increasing trend, although this parameter has relatively large uncertainties.

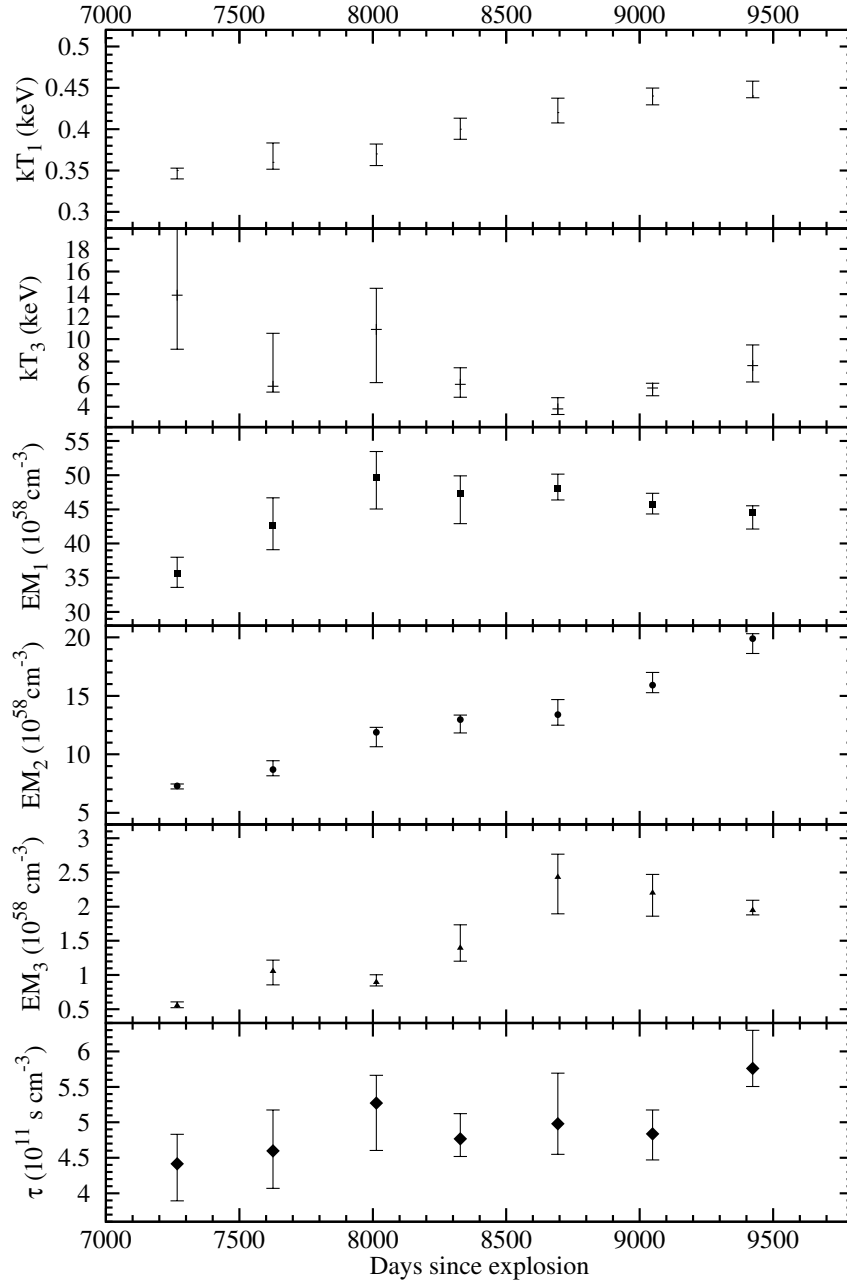


FIGURE 9.1 – Evolution of the best-fit spectral parameters of SNR 1987A between and 2012. From top to bottom: kT of the low-temperature and high-temperature component; Emission measures $EM = \int n_e n_H dV$ of the low-, mid-, and high-temperature components; ionisation age τ . All values and uncertainties are listed in Table 9.2.

TABLE 9.2 – Spectral results, abundances, fluxes, and Fe K line properties of SNR 1987A

Epoch	Age (days)	low- kT component		1.15 keV component	high- kT component		ionisation age (10^{11} s cm $^{-3}$)	
		kT (keV)	EM (10^{58} cm $^{-3}$)	EM (10^{58} cm $^{-3}$)	kT (keV)	EM (10^{58} cm $^{-3}$)		
2007 Jan	7267	0.35±0.01	35.69 $^{+2.34}_{-2.07}$	7.31 $^{+0.17}_{-0.27}$	13.89 $^{+7.11}_{-4.80}$	0.55 $^{+0.05}_{-0.03}$	4.42 $^{+0.41}_{-0.56}$	
2008 Jan	7626	0.36 $^{+0.02}_{-0.01}$	42.63 $^{+4.09}_{-3.51}$	7.80 $^{+}_{-0.37}$	5.82 $^{+4.69}_{-0.52}$	1.06 $^{+0.15}_{-0.20}$	4.60 $^{+0.57}_{-0.53}$	
2009 Jan	8013	0.37±0.01	49.66 $^{+3.82}_{-4.57}$	11.89 $^{+0.42}_{-1.24}$	10.86 $^{+3.64}_{-4.71}$	0.90 $^{+0.02}_{-0.05}$	5.27 $^{+0.39}_{-0.67}$	
2009 Dec	8328	0.40±0.01	47.29 $^{+2.64}_{-4.37}$	12.97 $^{+0.40}_{-1.14}$	5.98 $^{+1.47}_{-1.14}$	1.40 $^{+0.34}_{-0.19}$	4.77 $^{+0.26}_{-0.25}$	
2010 Dec	8693	0.42 $^{+0.02}_{-0.01}$	48.13 $^{+2.03}_{-1.73}$	13.40 $^{+1.28}_{-0.90}$	3.80 $^{+0.99}_{-0.49}$	2.43 $^{+0.34}_{-0.53}$	4.98 $^{+0.71}_{-0.43}$	
2011 Dec	9048	0.44 $^{+0.02}_{-0.01}$	45.72 $^{+1.66}_{-1.38}$	15.92 $^{1.10+}_{-0.63}$	5.66 $^{+0.41}_{-0.70}$	2.20 $^{+0.27}_{-0.34}$	4.84 $^{+0.33}_{-0.37}$	
2012 Dec	9423	0.44 $^{+0.02}_{-0.01}$	44.56 $^{+0.99}_{-2.41}$	19.90 $^{+0.44}_{-1.26}$	7.66 $^{+1.81}_{-0.86}$	1.95 $^{+0.15}_{-0.07}$	5.76 $^{+0.54}_{-0.26}$	
	N	O	Ne	Mg	Si	S	Fe	
	1.35±0.06	0.08±0.01	0.29±0.01	0.26±0.01	0.51±0.01	0.48±0.02	0.24±0.01	
Epoch	Age (days)	Flux (0.5–2 keV) (10^{-13} erg s $^{-1}$ cm $^{-2}$)	Flux (3–10 keV)	\dot{F}_X (%)	E_{line} (keV)	σ -width (eV)	Flux (10^{-6} ph cm $^{-2}$ s $^{-1}$)	EW (eV)
2007 Jan	7267	33.51 $^{+0.46}_{-0.49}$	4.09 $^{+0.86}_{-1.71}$	—	—	—	—	—
2008 Jan	7626	43.34 $^{+0.56}_{-0.57}$	5.22 $^{+0.67}_{-1.54}$	29.8	6.58 $^{+0.05}_{-0.07}$	46 (< 146)	1.07 $^{+0.57}_{-0.46}$	174
2009 Jan	8013	52.77 $^{+0.71}_{-0.64}$	6.31 $^{+0.76}_{-1.86}$	20.5	6.55 $^{+0.15}_{-0.14}$	125 (< 433)	0.94 $^{+1.50}_{-0.65}$	169
2009 Dec	8328	59.04 $^{+0.66}_{-0.69}$	7.42 $^{+0.89}_{-2.37}$	13.8	6.63 $^{+0.11}_{-0.09}$	229 (< 424)	2.64 $^{+1.69}_{-1.78}$	432
2010 Dec	8693	65.90 $^{+1.08}_{-1.17}$	8.16 $^{+0.96}_{-2.24}$	11.6	6.61 $^{+0.06}_{-0.06}$	105 (< 227)	2.51 $^{+1.39}_{-0.99}$	344
2011 Dec	9048	70.69 $^{+0.71}_{-0.76}$	11.31 $^{+1.08}_{-2.16}$	7.5	6.61 $^{+0.06}_{-0.06}$	83 (< 178)	2.08 $^{+1.01}_{-0.86}$	238
2012 Dec	9423	74.60 $^{+0.79}_{-0.87}$	11.65 $^{+1.22}_{-2.33}$	5.4	6.78 $^{+0.06}_{-0.05}$	84 (< 155)	2.11 $^{+0.97}_{-0.85}$	230

Notes. Top panel: best-fit values and 90 % C. L. uncertainties for the parameters of the three-components spectral model described in Sect. 9.3.1, in spectra obtained between 2007 and 2012. Middle panel: Best-fit abundances relative to the solar values as listed in Wilms et al. (2000). Bottom panel: Fluxes and Fe K line properties. Columns (3) and (4) list the soft and hard X-ray fluxes with 3σ errors (99.73 % C.L.). Column (5) gives the increase rate of the flux (in %) since previous measurement, normalised to one year. Columns (6) to (9) give the central energy, σ -width, total photon flux and equivalent width (EW) of the Gaussian used to characterise the Fe K feature in the spectra of SNR 1987A (with 90 % C. L. uncertainties).

9.4. X-ray light curve

I measured the soft (0.5 keV – 2 keV) and hard (3 keV – 10 keV) fluxes at all epochs, using the XSPEC flux command. The results with 3σ uncertainties (99.73 % confidence level, C. L.) are listed in Table 9.2. As is customary for SNR 1987A, I give *absorbed* fluxes, so comparisons between various observatories are easier (because they do not depend on the column densities obtained from the fit). The fluxes up to January 2009 are fully consistent with the results from Heng et al. (2008) and Sturm et al. (2010), which used the same data.

I included these results and the unpublished data point of 2012 in the X-ray light curve shown in Fig. 9.2. Older XMM-*Newton* fluxes are taken from Haberl et al. (2006). I show the *Chandra* measurements reported first in Park et al. (2011) and then in Helder et al. (2013). I also add the results from Suzaku observations (Sturm et al. 2009). Within their respective errors, XMM-*Newton*, *Chandra*, and Suzaku measured soft and hard X-ray fluxes that agree very well. Park et al. (2011), using the ACIS calibration available at that time, stated that the soft X-ray flux from SNR 1987A has been nearly constant after day ~ 8000 . Obviously XMM-*Newton* observed a source that was *not* constant, although one does observe a mild flattening of the light curve. The increase rates of the soft X-ray flux (Table 9.2) vary from one year to another, showing that the evolution of the X-ray flux is not smooth. One should therefore be cautious when claiming a steepening or flattening of the light curve and wait for a longer baseline.

The discrepancy between *Chandra* and XMM-*Newton* measurements after day 8000 is reconciled by Helder et al. (2013), using the revised *Chandra* calibration. They conclude that the apparent break in the soft X-ray light curve (Park et al. 2011) was mainly due to build-up of contamination on the ACIS optical blocking filters.

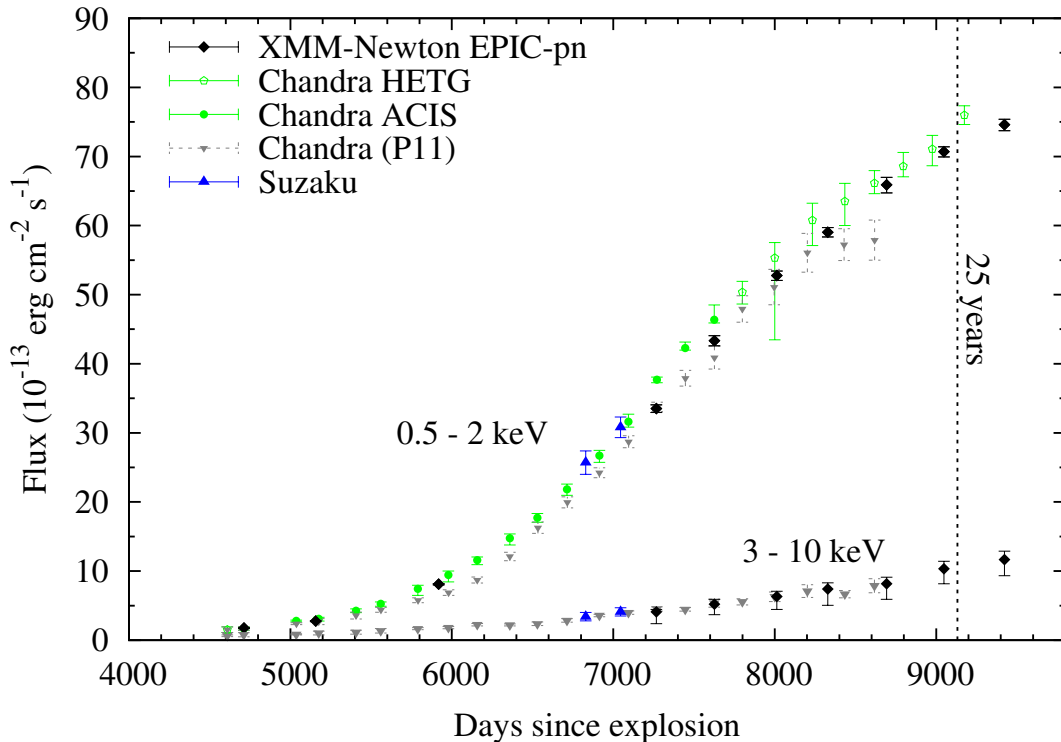


FIGURE 9.2 – Light curve of SNR 1987A in the soft and hard X-ray ranges. XMM-*Newton* data points (black diamonds) after day 7000 are given with 99.73 % C. L. error bars. Updated *Chandra* measurements (with 68 % C. L. errors, Helder et al. 2013) and those based on the older calibration (with 90 % C. L. errors, Park et al. 2011) are shown in green and grey, respectively. Suzaku measurements (Sturm et al. 2009, blue triangles) are also shown.

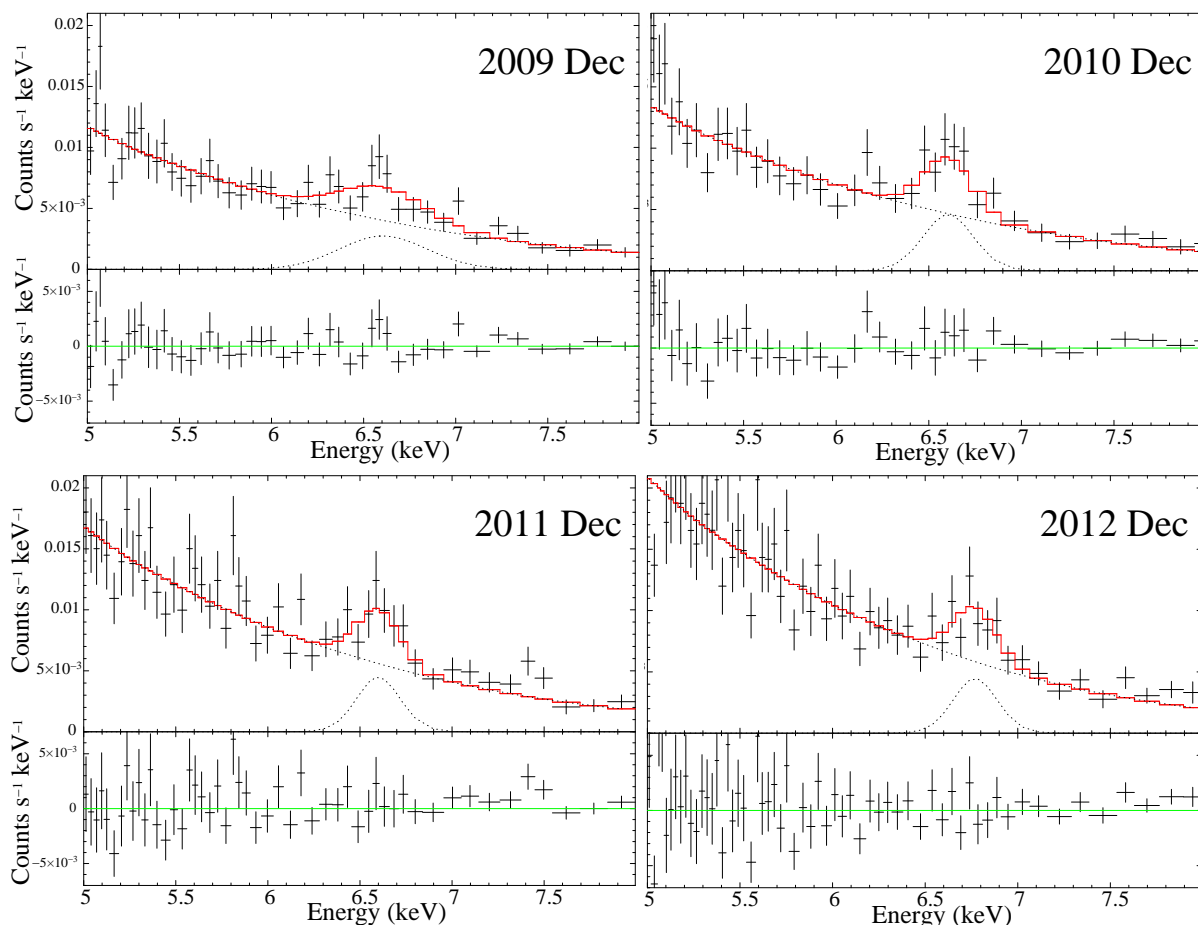


FIGURE 9.3 – EPIC-pn spectra of SNR 1987A in the 5 keV – 8 keV range, showing the Fe K lines at four recent epochs. The model used (red) is the sum of two components: a Bremsstrahlung continuum and a Gaussian, shown by dotted lines. The bottom panels show the fit residuals. All panels have the same scale. For plotting purpose only, adjacent bins are rebinned in order to have a significant ($\geq 5\sigma$) detection in each rebinned channel. The feature seen at ~ 7.4 keV in the 2011 spectrum is an instrumental artefact and not an Ni K line.

9.5. Fe K lines

The superior high-energy effective area of *XMM-Newton* (~ 900 cm² at 6.4 keV vs. ~ 200 cm² for *Chandra*) allows the study of Fe K lines with the EPIC cameras at energies between 6.4 and 6.7 keV, i. e. out of the range covered by RGS³². Heng et al. (2008) note a possible detection of an Fe K α line in the spectrum obtained in 2007, but the insufficient statistics precluded a more detailed analysis. In the co-added spectra from 2007 to January 2009, Sturm et al. (2010) identified a line at 6.57 ± 0.08 keV.

I analysed the presence and properties of Fe K lines in all the monitoring observations (Table 9.1). I fit the non-rebinned spectra with a Bremsstrahlung continuum and a Gaussian line, making use of the C-statistic to take the limited number of counts in each bin into account. I performed *F-tests* to evaluate the significance of the line in each observation: I found a detection more than 3σ significant in the data from 2008 and 2011, and more than 4σ significant in the spectra from December 2009 and 2010. The January 2009 observation, having a slightly shorter exposure due to longer high background activity periods, still yields a 2σ detection. I found only a marginal (1σ) detection in the 2007 spectrum, in agreement with previous studies.

³²By combining several years worth of *Chandra*'s High Energy Transmission Grating data (~ 500 ks), it is possible to detect (at low significance) Fe K lines (Dan Dewey, personal communication).

I display the lines in the four most recent spectra from 2009 to 2012 in Fig. 9.3. The plasma temperatures of the Bremsstrahlung continua range from $kT = 2.75$ keV to 3 keV, and the emission measures follow the increasing trend of the hard X-ray flux. Line properties are given in Table 9.2 for all observations except the one from 2007.

No evolution of the line central energy is found within the uncertainties, but the spectra suffer from limited statistics at high energy. The centroid energy of the Fe K line complex depends on the ionisation stages of iron present, increasing from 6.4 keV for Fe II, to 6.7 keV for Fe XXV (Makishima 1986; Kallman et al. 2004, and Sect. 3.3.3). The spectral resolution is only ~ 160 eV (Strüder et al. 2001), so the contributions from various Fe ions present in the X-ray emitting plasma cannot be resolved. Therefore, the large measured widths of the lines in our spectra are most likely due to a sum of lines (which might be Doppler-broadened) from several Fe ions, convolved with the instrumental response of the camera. The weighted average of the emission-line centroids (6.60 ± 0.01 keV) and the typical widths (~ 100 eV) indicate the presence of ionisation stages from Fe XVII to Fe XXIV. This is consistent with the detection of lines from Fe XVII to Fe XX in the RGS spectra (Sturm et al. 2010), and the detection of an Fe XXII–Fe XXIII blend in the *Chandra* High Energy Transmission Grating spectra (Dewey et al. 2008).

The flux in the iron line indicates an increase around day 8000, and a decrease afterwards. However, given the large (statistical) errors in the flux measurements, the possibility that the flux of the line remained constant in the past three years cannot be excluded. Since the hard continuum steadily increased during that period of time, the equivalent width of the line decreased in the last observations (Table 9.2).

9.6. Discussion

The monitoring campaign with *XMM-Newton* since 2007 is ideally suited to follow the evolution of SNR 1987A: (i) the same instrument setting (observing mode, filter, read-out time) is used, (ii) the spectra are extracted from the same regions, and (iii) the same model is used for all the spectra. The high throughput of *XMM-Newton* results in the high statistical quality of the spectra. This allows high-confidence flux measurements with relatively small errors which are free of cross-calibration problems due to different observing modes.

The resulting light curve shows a continuous increase in the soft X-ray flux of SNR 1987A, indicating that no turn-over has been reached yet and that the blast wave is still propagating into dense regions of the ER. To further constrain the thickness of the ER, given the continuous increase in the soft X-ray flux, Maggi et al. (2012b) used the “ $2 \times 1D$ ” hydrodynamical model from D12. The recent *XMM-Newton* and *Chandra* measurements point towards a thickness of at least 4.5×10^{16} cm (3000 AU) for the ER, and each year of continued flux increase requires an additional ER thickness of $\sim 0.53 \times 10^{16}$ cm (350 AU).

The high-energy collective power of *XMM-Newton* allowed the detection and characterisation of the Fe K lines from SNR 1987A. I found that the energies and the widths of the lines imply the presence of a collection of ionisation stages for iron. To investigate which model component is most responsible for the Fe K lines, I used the best-fit three-shock model (switching off the Gaussian line) and using the NEI version 1.1, as it includes low ionisation stages (below He-like ions), which allows the whole range of energy between 6.4 keV and 6.7 keV to be probed as a function of kT and τ (see Fig. 3 in Furuzawa et al. 2009). As expected, one finds that only the high-temperature component significantly contributes to the hard continuum and the line. When including emission from ions with lower ionisation than Fe XV, the shapes and fluxes of the lines from the high-temperature component (Fig. 9.4) fail to reproduce the data. There is need for lower ionisation stages to explain the excess observed at ~ 6.55 keV. This points to the presence of shocked material with shorter ionisation ages τ . In the framework of the hydrodynamics-based model from D12, one finds that the main contribution to the Fe K emission therefore comes from the out-of-plane material (“H II region”), which has a temperature and ionisation age that produces emission in the 6.55 keV – 6.61 keV range. Another possibility for the low-energy emission (~ 6.4 keV) is fluorescence

from near-neutral Fe, including Fe in the unshocked ejecta. Material in the dense ER clumps, on the other hand, has a temperature that is too low to significantly contribute to the line.

Following the evolution of the Fe K line fluxes and centroid energies is crucial to constraining their origin. Next-generation instrumentation, such as the X-ray calorimeter aboard Astro-H (Takahashi et al. 2012) or the X-IFU of Athena (Barret et al. 2013), will be able to resolve lines from different Fe ions, thus providing even deeper physical insights.

The calibration issues encountered by the *Chandra* team show how important it is to use *both* observatories to monitor such an important source. To follow the evolution of the light curve and of the iron lines, subsequent observations of SNR 1987A with *XMM-Newton* are highly desirable.

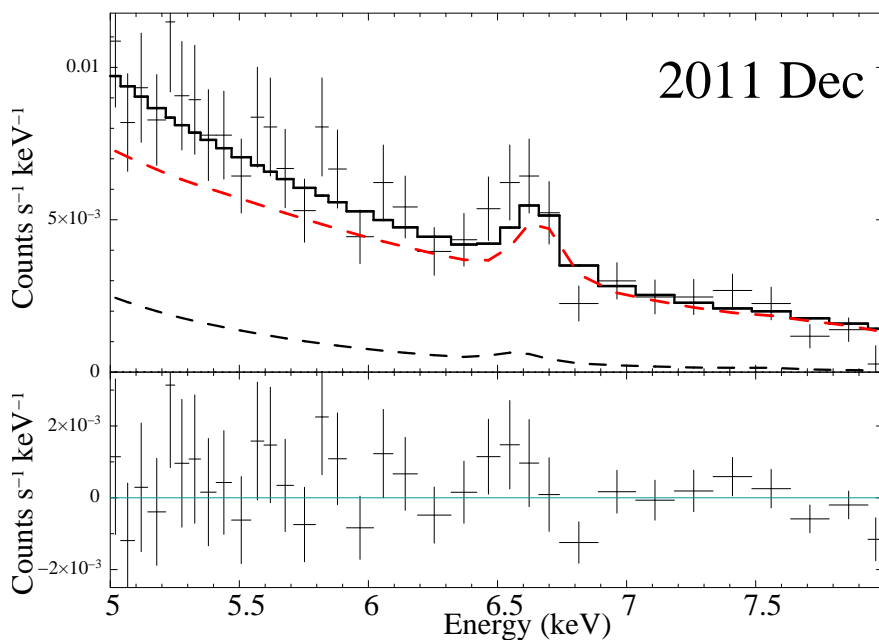


FIGURE 9.4 – Details of the Fe K lines region of the spectrum from December 2011. The model used is the three-shock components model described in Sect. 9.3, including emission from Fe below He-like ions and without a Gaussian line. The “hot” component (red dashed line) dominates the continuum and line spectrum but does not account for an emission excess around 6.55 keV.

10. Study of individual supernova remnants

OVER the course of my thesis, numerous new LMC SNRs have been revealed. Most were found serendipitously in the XMM-*Newton* survey fields (Sect. 7.1), even though some might have been known as SNR candidates (e. g. DEM L205 and MCSNR J0508–6902) beforehand. XMM-*Newton* data were used to investigate the morphological and spectral features of the remnants. X-ray observations were supplemented with optical, infrared, and radio-continuum data to provide a holistic view of the remnants. The new SNRs are presented in three sections: DEM L205, identified in the first survey observations, is analysed in Sect. 10.1. The discovery of three iron-rich SNRs is described in Sect. 10.2, and two remnants with unusual morphology are presented in Sect. 10.3.

For the naming of SNRs in the Magellanic Clouds, I made use of the acronym “MCSNR”, which was pre-registered to the International Astronomical Union by R. Williams et al., who maintain the Magellanic Cloud Supernova Remnants online database³³. This ensures a more consistent and general naming system. Indeed, some old remnants were named after nearby H II regions (e. g. LHA 120-N103B), others with B1950 coordinates, resulting in an inconsistent and confusing nomenclature. Therefore, all SNRs are assigned the identifier “MCSNR JHHMM+DDMM”, although I also retained the old “common names” from the literature for easy cross-identifications.

10.1. Confirmation of the supernova remnant status of DEM L205

The very first pointing of the XMM-*Newton* survey of the LMC covered DEM L205, an object in the giant H II complex LHA 120-N51 (presented in Fig. 10.1) classified as a “possible SNR” Davies, Elliott, & Meaburn (1976). Using the new X-ray observations, archival optical and infrared data, and new radio-continuum observations analysed by collaborators, I conducted an analysis that confirmed the SNR nature of the source and estimated some of its parameters. This study was published in Maggi et al. (2012a).

10.1.1. Observations and data reduction

10.1.1. A. X-rays

DEM L205 was in the field of view of a 28 ks observation (ObsId 0671010101, the first of the XMM-*Newton* survey of the LMC) carried out on 19 December 2011. The EPIC cameras operating in full-frame mode were used as the prime instruments. After the screening of high background-activity intervals, the useful exposure times for pn and MOS detectors were ~ 20 and 22 ks, respectively. An archival XMM-*Newton* observation (ObsId 0071940101, pointing at the LMC SB N 51D) includes the object in the field of view, at a larger off-axis angle. None of the EPIC cameras covered the remnant to its full extent. I used data from this observation only for the purpose of imaging but not spectrometry. This yields a longer exposure time, particularly in the western part of the remnant, which is covered by all cameras in both observations. In Table 10.1 I list the details of the observations. I created adaptively smoothed, vignetting-corrected, and detector-background-subtracted images in the standard XMM-*Newton* energy bands (see Table 3 in Watson et al. 2009) for all three cameras, before merging MOS and pn data.

³³MCSNR, <http://www.mcsnr.org/Default.aspx>

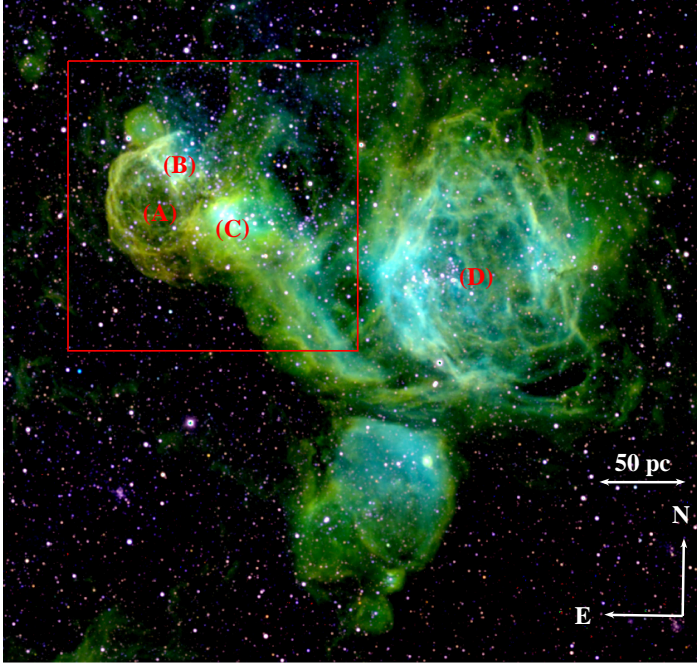


FIGURE 10.1 – The giant H II complex LHA 120-N 51 in the light of [S II] (red), H α (green), and [O III] (blue), all data from MCELS. The red box delineates the area shown in Fig. 10.2. Noticeable substructures are: DEM L205 (A), the SNR candidate analysed in this Section; N51A (B) and N51C (C, also named DEM L201), two H II regions also seen in the radio and the IR; the SB N51D, or DEM L192, in (D).

TABLE 10.1 – XMM-*Newton* observations of DEM L205

ObsId	Obs. start date	Central Coordinates		Filter ^(a) pn/M1/M2	exposure time (ks) ^(b)			Off-axis angle ^(c)
		RA (J2000) DEC (J2000)			pn	M1	M2	
0671010101	2011 Dec 19	05 ^h 29 ^m 55.7 ^s –67° 26′ 14″		T/M/M	20.1	21.7	21.7	8.8
0071940101	2001 Oct 31	05 ^h 26 ^m 04.9 ^s –67° 27′ 21″		T/T/T	26.8	31.2	31.2	13.7

Notes. ^(a) T: Thin ; M: Medium. ^(b) Performed duration (total) and useful (filtered) exposure times, after removal of high background intervals. ^(c) Angle in arcmin between the centre of the pn detector and the centre of the X-ray source (as defined in Sect. 10.1.2. A).

10.1.1. B. Other wavelengths

DEM L205 was observed in radio with the Australia Telescope Compact Array (ATCA) on the 15 and 16 November 2011 at wavelengths of 3 cm and 6 cm (9000 MHz and 5500 MHz), using the array configuration EW367. Baselines formed with the sixth antenna were excluded, leaving the remaining five antennae to be arranged in a compact configuration. The observations were carried out in the so-called snap-shot mode, totalling ~50 min of integration over a 12 h period. The source PKS B1934–638 was used for primary (flux) calibration and the source PKS B0530–727 was used for secondary (phase) calibration. The phase calibrator was observed for a period of 2 min every half our during the observations. The 6 cm observations were merged with those from Dickel et al. (2005, 2010). In addition, use is made of the 36 cm Molonglo Synthesis Telescope (MOST) unpublished mosaic image as described by Mills et al. (1984) and an unpublished 20 cm mosaic image from Hughes et al. (2007). Beam sizes were 46.4″ × 43.0″ for the 36 and 20 cm images. The 6 cm image beam size was 41.8″ × 28.5″, with a position angle of 49.6° (eastwards of north).

To study the remnant candidate in optical emission lines, I used the MCELS (Sect. 4.2). All MCELS data

covering the object were flux-calibrated and combined with a pixel size of $2'' \times 2''$. The [S II] and H α images were stellar continuum-subtracted to produce a map of [S II]/H α . The X-ray composite image and [S II]/H α contours from these data are shown in Fig. 10.2. In addition, I used an unpublished higher-resolution H α image in Fig. 10.7 (pixel size of $1'' \times 1''$), which was obtained as part of the ongoing MCELS2 program with the MOSAIC II camera on the Blanco 4-m telescope at the CTIO³⁴.

To study the IR emission of the source and its environment, I retrieved the *Spitzer* IRAC and MIPS mosaiced, flux-calibrated (in units of MJy sr⁻¹) images processed by the SAGE team (Meixner et al. 2006, Sect. 4.2). The pixel sizes are 0.6'' for all IRAC wavelengths and 2.49'' and 4.8'' for 24 μ m and 70 μ m MIPS data, respectively.

10.1.2. Data analysis and results

10.1.2. A. X-ray images

I created composite images, using the energy ranges 0.2 keV – 1 keV for the red component, 1 keV – 2 keV for the green, 2 keV – 4.5 keV for the blue. The X-ray image is shown in Fig. 10.2. In addition to soft diffuse emission and many point sources, an extended soft source is clearly seen. This source correlates with the positions of DEM L205 and of the ROSAT PSPC source [HP99] 534 (Haberl & Pietsch 1999a). The images alone already show that the source has hardly any emission above 1 keV.

The X-ray emission can be clearly delineated by an ellipse centred at RA = 05^h 28^m 05^s and DEC = $-67^\circ 27' 20''$, with a position angle of 30° (eastwards of north, see Fig. 10.2). The major and minor axes have sizes of 5.4' and 4.4', respectively. At a distance of 50 kpc, this corresponds to an extent of ~ 79 pc \times 64 pc. Note that the eastern and southern boundaries of the X-ray emission are more clearly defined than the western and northern ones. I discuss this issue in Sect. 10.1.3. C.

10.1.2. B. X-ray spectra

Fitting method: I created a vignetting-weighted event list to take into account the effective area variation across the source extent (see Sect. 8). The spectrum was extracted from a circular region with a radius of 3' and the same centre as the ellipse defined above. A nearby region of the same size, free of diffuse emission, was used to extract a background spectrum. Point sources were excluded from the extraction regions. Spectra were rebinned with a minimum of 30 counts per bin to allow the use of the χ^2 -statistic. The spectral-fitting package XSPEC (Arnaud 1996) version 12.7.0u was used to perform the spectral analysis.

The background and source spectra were modelled simultaneously, following the method and background model described in Sect. 8. A soft proton contamination (SPC) term was also included. The SPC was modelled by a power-law *not* convolved with the instrumental response, which is appropriate for photons but not for protons (Kuntz & Snowden 2008).

Three models were used for the emission of the remnant: a CIE model (APEC), a non-equilibrium ionisation (NEI) plane-parallel shock model (vpshock Borkowski et al. 2001), and a Sedov model (Borkowski et al. 2001). The mean and post-shock electron temperature (T_s and T_{es} , respectively) in the Sedov model were constrained to be the same, because of little or no variations in the best-fit parameters and the χ^2 with $\beta = T_{es}/T_s$ between 0 (by taking $T_{es} = 0.01$ keV, the minimal value in the Sedov model implemented in XSPEC) and 1. This is a reasonable assumption, since old remnants should be close to ion-electron temperature equilibrium.

When fitted to the source region spectrum, the normalisations of the X-ray background components were allowed to vary, but their *ratios* were constrained to be the same as in the background region. I found 5% or smaller variations between the normalisations of the background components of the two regions (which are shown by the dashed lines in Fig. 10.3). Because the background spectrum was extracted from the

³⁴The reduced image was shared by Dr. Robert Gruendl

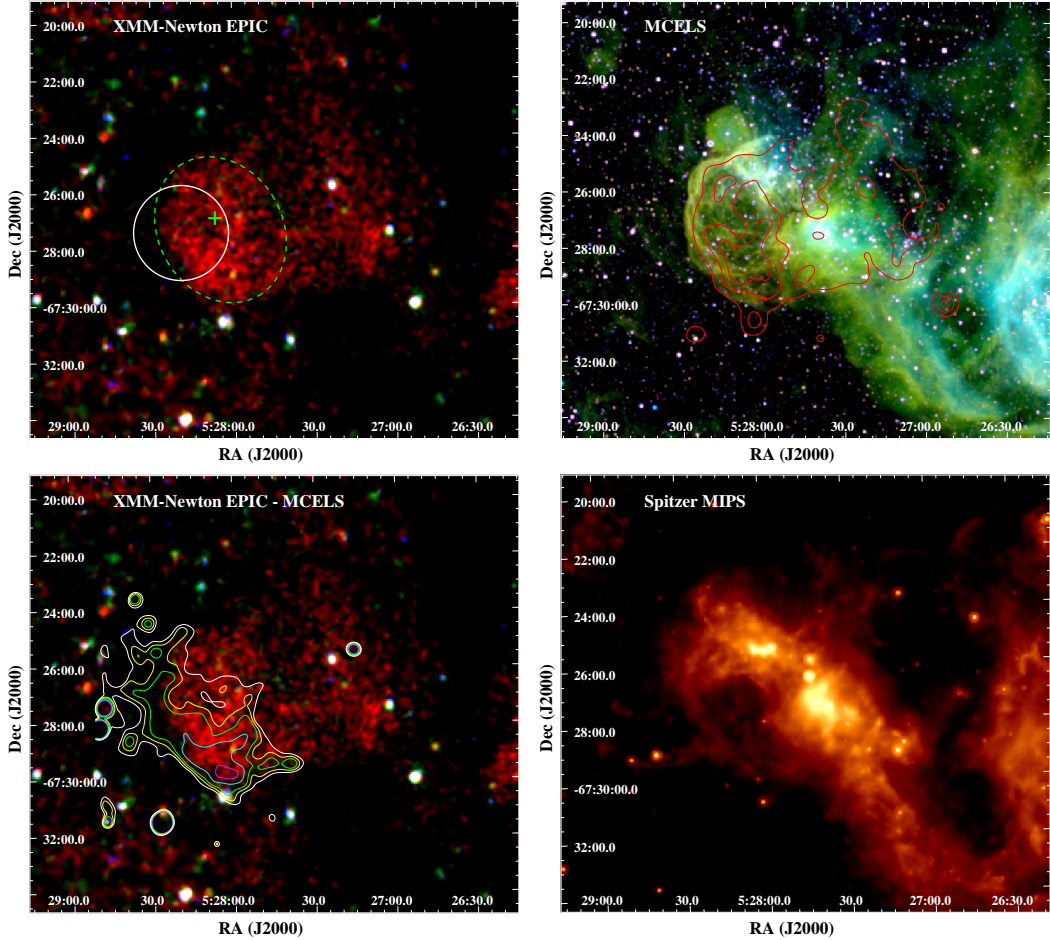


FIGURE 10.2 – A multicolour view of DEM L205. *Top left*: X-ray colour image of the remnant, combining all EPIC cameras. Data from two overlapping observations are combined and smoothed. The red, green, and blue components are soft, medium, and hard X-rays, as defined in the text. The white circle is the 90 % confidence error of the [HP99] 534 position and the green cross is the central position of DEM L205. The green dashed ellipse encompasses the X-ray emission and is used to define the nominal centre and extent of the remnant. *Top right*: The same region of the sky in the light of [S II] (red), $H\alpha$ (green), and [O III] (blue), where all data are from the MCELS. The soft X-ray contours from the top left image are overlaid. *Bottom left*: Same EPIC image as above but with [S II]-to- $H\alpha$ ratio contours from MCELS data. Levels are (inwards) 0.4, 0.45, 0.5, 0.6, and 0.7. *Bottom right*: The remnant as seen at $24\ \mu\text{m}$ by *Spitzer* MIPS. Optical and IR images are displayed logarithmically.

same observation (that is, at the same time period) and at a similar position and off-axis angle as the source spectrum, the SPC contribution was not expected to vary much (Kuntz & Snowden 2008). The validity of this assumption was checked *a posteriori* by looking at the data above 3 keV. I therefore used the same SPC parameters for the background and source spectra.

To account for the absorption of the source emission, I included two photoelectric absorption components, one with a column density $N_{H\text{ Gal}}$ for the Galactic absorption and another one with $N_{H\text{ LMC}}$ for the LMC. Except for O and Fe, which were allowed to vary, the metal abundances for the source emission models were fixed to the average metallicity in the LMC (*i.e.*, half the solar values, Russell & Dopita 1992), because the observations were not deep enough to permit abundance measurements and because high-resolution spectroscopic data were unavailable.

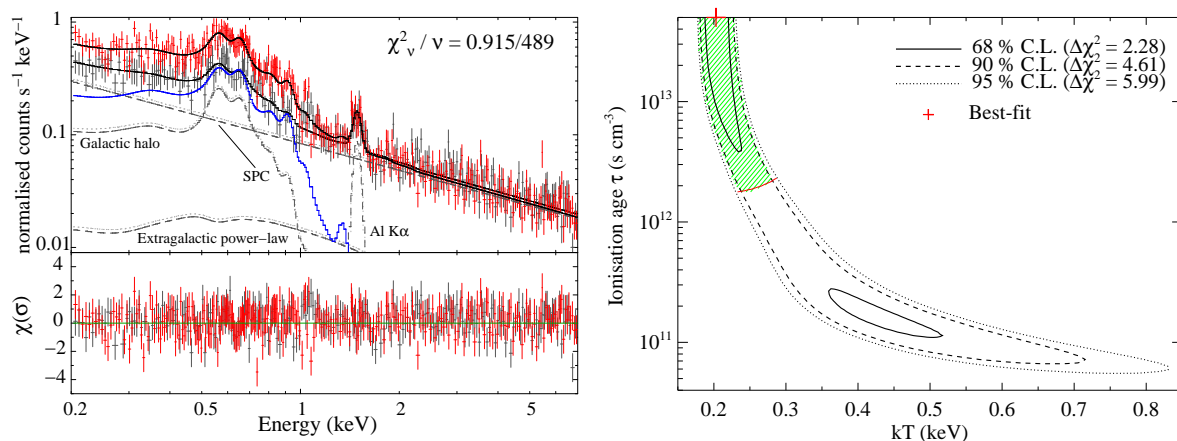


FIGURE 10.3 – *Left*: EPIC-pn spectrum of DEM L205. The spectra in the background and source regions (grey and red data points, respectively) are modelled simultaneously. The background model components are shown by the dashed lines and labelled. The Sedov model used for the remnant is shown by the blue solid line. Residuals are shown in the lower panel in terms of σ .

Right: The $kT - \tau$ parameter plane for the Sedov model. The 68, 90, and 95 % CL contours are shown by the solid, dashed, and dotted black lines, respectively. The formal best-fit, occurring at the upper limit of the ionisation ages of the XSPEC model ($5 \times 10^{13} \text{ s cm}^{-3}$) is marked by the red plus sign. The red line shows the 99 % CL lower contour of emission measure obtained with the APEC model. The green hatching indicates the region where $\Delta\chi^2 < 4.61$ and EM is in the 99 % CL range of the APEC model (see Sect. 10.1.2. B).

Spectral results: I fitted the data between 0.2 keV and 7 keV. I extended the fit down to low energies to constrain the parameters of the Local Hot Bubble (LHB) component, which has a low plasma temperature ($kT \lesssim 0.1 \text{ keV}$). The data above 2 keV, where the Galactic components hardly contribute, were necessary to constrain the non-thermal extragalactic emission and the SPC (Kuntz & Snowden 2010).

The quality of the data statistics was too low to place strong constraints on the foreground hydrogen absorption column. The best fit value for $N_{H \text{ Gal}}$ was $5.3 \times 10^{20} \text{ cm}^{-2}$ (using the APEC component), with a 90 % confidence interval from 3 to $10 \times 10^{20} \text{ cm}^{-2}$. I therefore fixed it at $5.9 \times 10^{20} \text{ cm}^{-2}$ (based on the HI measurement of Dickey & Lockman 1990). I found that the best-fit intrinsic LMC column density value tended to 0, with a 90 % confidence upper limit of $3.9 \times 10^{20} \text{ cm}^{-2}$ (using the APEC component), and then fixed $N_{H \text{ LMC}}$ to 0. Even though the best-fit temperature of the Local Hot Bubble derived (85 eV) agrees well with the results of Henley & Shelton (2008), the errors are large because this component contributes only to a small number of energy bins. The significance of the LHB component was less than 10 % (using a standard F-test), and I removed this component from the final analysis. The power-law component was also faint but more than 99.99 % significant.

I achieved good fits and obtained significant constraints on the source parameters. The reduced χ^2 were between 0.91 and 0.92. The plasma temperatures (kT between 0.2 keV and 0.3 keV) are consistent for all models. They are similar to temperatures found in other large SNRs (e.g. Williams et al. 2004; Klimek et al. 2010). The unabsorbed X-ray luminosity of the Sedov model is $1.43 \times 10^{35} \text{ erg s}^{-1}$ in the range 0.2 keV – 5 keV, whilst the other models yield similar values. More than 90 % of the energy is released below 0.9 keV.

The best-fit values with 90 % confidence levels (CL) errors are listed in Table 10.2. The spectrum fitted by the best-fit Sedov model is shown in Fig. 10.3 (left). The ionisation timescales were large (more than $10^{12} \text{ s cm}^{-3}$), which indicates quasi-equilibrium. In this regime, kT and τ are degenerate, because the spectra hardly change when increasing kT and decreasing τ . This effect is shown in Fig 10.3 (right). However, the emission measure (EM), which is a function of the volume of emitting plasma and densities, *does not* depend on the model used, provided the column density is the same. With the help of the 99 % CL range of

TABLE 10.2 – X-ray spectral results for DEM L205

Background model best-fit parameters							
Model	$N_{H \text{ Gal}}^{(a)}$ (10^{20} cm^{-2})	kT_{Halo} (eV)	$EM_{\text{Halo}}^{(b)}$ (10^{57} cm^{-3})	$\Gamma_{\text{XRB}}^{(a)}$	A_{XRB}	Γ_{SPC}	A_{SPC}
vaptec	5.9	201_{-9}^{+20}	$5.2_{-0.8}^{+0.8}$	1.46	$2.68_{-1.3}^{+1.4}$	$0.78_{-0.06}^{+0.05}$	$8.48_{-0.9}^{+0.9}$
vpshock	5.9	203_{-12}^{+15}	$5.1_{-0.8}^{+0.7}$	1.46	$2.39_{-1.5}^{+1.1}$	$0.79_{-0.06}^{+0.05}$	$8.69_{-1.0}^{+1.0}$
vsedov	5.9	205_{-12}^{+13}	$5.0_{-0.5}^{+0.6}$	1.46	$2.02_{-0.7}^{+1.4}$	$0.79_{-0.02}^{+0.03}$	$8.93_{-0.4}^{+0.4}$

Source model best-fit parameters							
Model	$N_{H \text{ LMC}}^{(a)}$ (10^{20} cm^{-2})	kT (eV)	τ ($10^{12} \text{ s cm}^{-3}$)	EM (10^{57} cm^{-3})	$12 + \log(\text{O}/\text{H})$	$12 + \log(\text{Fe}/\text{H})$	χ^2 / dof
vaptec	0	251_{-18}^{+18}	—	$20.6_{-3.0}^{+3.0}$	$8.22_{-0.11}^{+0.10}$	$6.57_{-0.33}^{+0.25}$	452.96 / 490
vpshock	0	257_{-33}^{+60}	4.21 (> 1.02)	22.0	$8.10_{-0.11}^{+0.11}$	$6.86_{-0.31}^{+0.27}$	446.09 / 489
vsedov	0	203_{-20}^{+72}	50.0 (> 1.90)	24.5	$8.16_{-0.10}^{+0.12}$	$6.84_{-0.30}^{+0.25}$	447.44 / 489

Notes. The top panel lists the best-fit parameters of the background model and the bottom panel shows the parameters of the source models (details are in Sect. 10.1.2. B). Errors are given at the 90 % confidence level. I required the emission measures of the vpshock and vsedov models to be in the 99 % CL range of EM obtained with the vaptec model (see text), and this gave the range of errors for kT and τ of the vpshock and vsedov models. Γ_i and A_i are the spectral indices and normalisations of the power-law component i , where i is either the X-ray background (XRB) or soft proton contamination (SPC). A_{XRB} is given in 10^{-5} photons $\text{keV}^{-1} \text{ cm}^{-2} \text{ s}^{-1}$ at 1 keV and A_{SPC} in units of 10^{-2} photons $\text{keV}^{-1} \text{ cm}^{-2} \text{ s}^{-1}$. The χ^2 and associated degrees of freedom (dof) are also listed. ^(a) Fixed parameter (see text for details). ^(b) Emission measure $EM = \int n_e n_H dV$.

EM obtained using the APEC model ($16.0 - 25.4 \times 10^{57} \text{ cm}^{-3}$), which does not have the $kT - \tau$ degeneracy problem, I obtained additional constraints on kT and τ .

The O and Fe abundances are (about 0.2 dex) lower than those in Russell & Dopita (1992) but consistent with the results found by Hughes et al. (1998) in other LMC SNRs. The abundances found for DEM L205 match well those reported in the nearby (13' or ~ 190 pc in projection) LMC SB N 51D (Yamaguchi et al. 2010).

10.1.2. C. Radio morphology

To assess the morphology of the source, I overlaid the radio contours on the XMM-Newton image. Weak, extended ring-like emission correlates with the eastern side of the X-ray remnant and is most prominent, as expected, at 36 cm, but only marginally detected at higher frequencies (Fig. 10.4). It is difficult to classify the morphology of this SNR at radio wavelengths because it lies in a crowded field. The surrounding radio emission is dominated in the north by LHA 120-N 51A, which is classified as an H II region (Filipovic et al. 1998) and also correlates with the small molecular cloud [FKM2008] LMC N J0528–6726 (Fukui et al. 2008), and in the west by the H II region LHA 120-N 51C.

If one assumes that the analysable region of the 36 cm image (Fig. 10.4, left) is typical of the rest of the remnant's structure, the SNR would have a typical ring morphology. Nevertheless, with the present resolution, one cannot easily estimate the total flux density of this SNR at any radio frequency. However, note the steep drop (across the eastern side of the ring) in flux density at higher frequencies, which results in a nearly completely dissipated remnant as seen at 6 cm (Fig. 10.4, right).

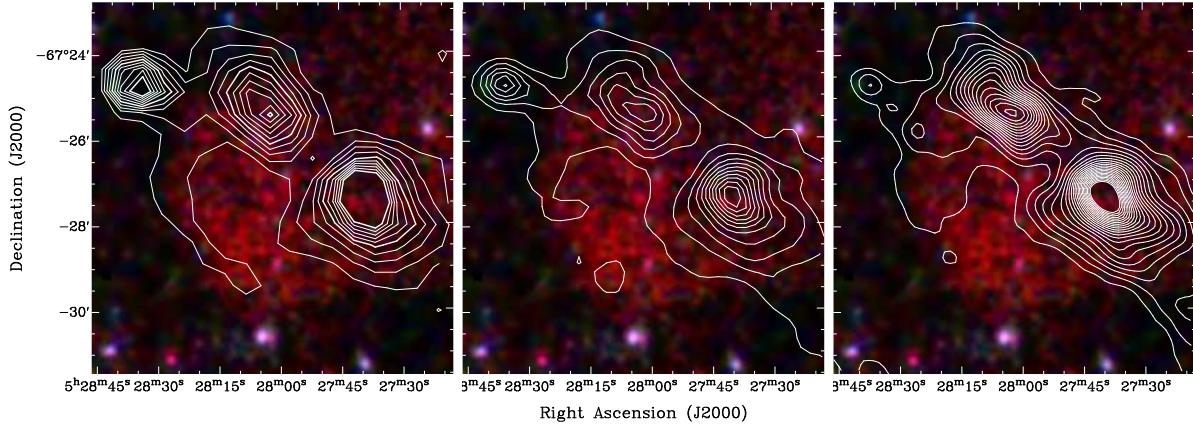


FIGURE 10.4 – Radio contours of DEM L205 overlaid on the X-ray image. *Left*: 36 cm contours from 5 to 50σ with 5σ steps ($\sigma = 0.4$ mJy/beam). *Middle*: 20 cm contours from 3 to 23σ with 2σ steps ($\sigma = 1.3$ mJy/beam). *Right*: 6 cm contours from 3 to 200σ with 9σ steps ($\sigma = 0.1$ mJy/beam). Beam sizes are $40'' \times 40''$ for the 36 cm and 20 cm images, and $41.8'' \times 28.5''$ at 6 cm. Note that the portion of the sky shown is smaller than in Fig. 10.2.

10.1.2. D. Radio spectral energy distribution

We were unable to compile a global spectral index for the remnant because a large portion of DEM L205 cannot be analysed at radio wavelengths (as described above). However, a spectral index map (Fig. 10.5) shows the change in flux density from 36 cm to 6 cm. The map was formed by reprocessing all observations to a common $u - v$ range, and then fitting $S \propto \nu^\alpha$ pixel by pixel using all three images simultaneously. The areas of the SNR that are uncontaminated by strong sources have spectral indices between -0.7 and -0.9 , which is steeper but close to the typical SNR radio-continuum spectral index of $\alpha \sim -0.5$. The uncertainties in the determination of the background emission are likely to cause a bias toward steeper spectral indices. I also point out that the bright point source seen in the north-east (mainly at 36 cm) is most likely a background galaxy or an active galactic nucleus (AGN).

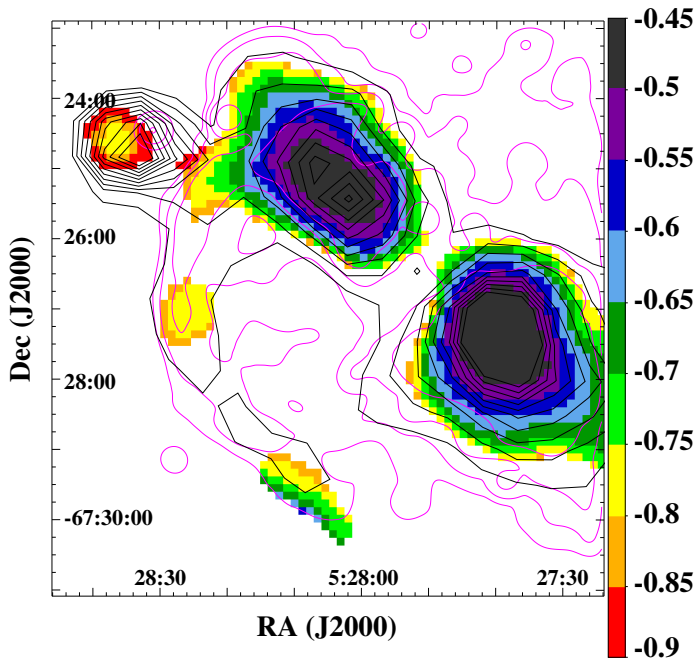


FIGURE 10.5 – Spectral index map of DEM L205 between wavelength of 36 cm, 20 cm, and 6 cm, covering the same field as Fig 10.4. The sidebar gives the spectral index α . The 36 cm contours (black) are overlaid, with the same levels as in Fig. 10.4. The $H\alpha$ structures (Figs. 10.1 & 10.2) are sketched by the magenta contours.

10.1.2. E. Infrared flux measurement

The IR data suffer from the same crowding issues as the radio-continuum data. The IR emission in the SNR region (see Figure 10.6) is dominated by the two H II regions seen in radio, whose positions are shown in the 8 μm images (Fig 10.6, left). However, at 24 μm , an arc of shell-like emission is seen in the eastern and south-eastern regions of the remnant (outlined in Fig 10.6, middle) at the same position of the 36 cm emission. I used the optical and X-ray emission contours to constrain the region at 24 μm that can be truly associated with the SNR and found that this arc tightly follows the H α and X-ray morphologies. I integrated the 24 μm surface brightness in this region (in white in Fig. 10.6, middle) and found a flux density of $F_{24} = 660$ mJy.

To calibrate my method of flux density measurement and estimate the uncertainties, I derived the 24 μm flux densities of the LMC SNRs N132D, N23, N49B, B0453–68.5, and DEM L71, and compared them to the values published in Borkowski et al. (2006b) and Williams et al. (2006a). I was able to reproduce these authors' values, but with rather large error ranges ($\sim 30\%$), chiefly because of uncertainties in the definition of the integration region. The two aforementioned studies integrated the flux density only in limited areas of the SNRs, and the integration regions are not explicitly defined in their papers. In the case of DEM L205 it is also difficult to define the area of IR emission from the SNR only, so I believe these 30% error ranges are a reasonable estimate of the error in the flux density measurement. The systematic uncertainties in the flux calibration of the *Spitzer* images are small in comparison and can be neglected. In particular, given that the thickness of the region in the plane of the sky is $20'' - 25''$, only a small aperture correction would be needed (at least at 24 μm).

The 70 μm image (Fig 10.6, right) shows that DEM L205 has the same morphology as at 24 μm , but with lower resolution, hence the confusion is even higher. Simply using the same region as for F_{24} , I found a flux density of $F_{70} = 3.4$ Jy, with similarly large errors. I discuss the origin of the IR emission in Sect. 10.1.3. A.

In the IRAC wavebands, no significant shell-like emission is detected. I tentatively identified two arcs at 8 μm (marked in cyan on Fig 10.6, left) that could originate from the interaction of the shock with higher densities towards the H II regions. The two arcs are also present at 5.8 μm (not shown) but neither at 4.5 μm nor 3.6 μm , where only point sources are seen.

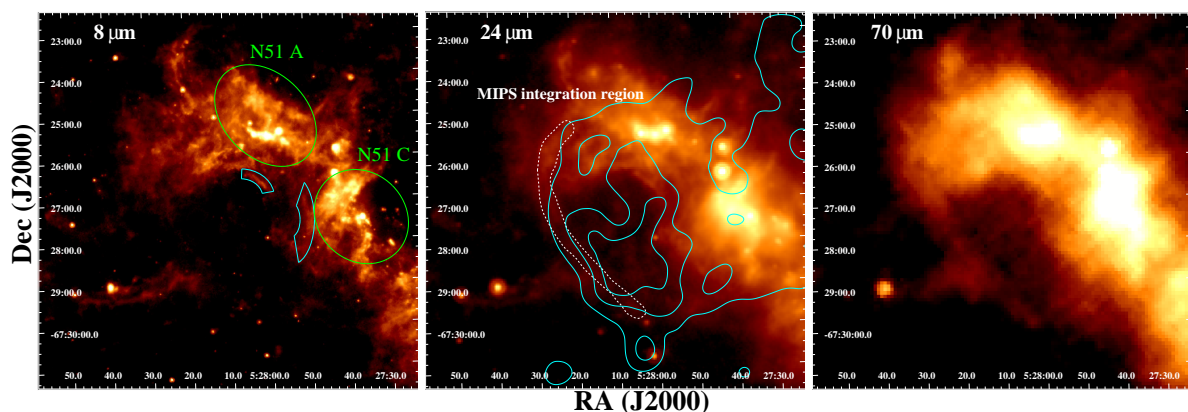


FIGURE 10.6 – *Spitzer* images of DEM L205 at 8, 24, and 70 μm (from left to right). All images show a similar portion of the sky as the radio images and are displayed logarithmically. The green ellipses on the 8 μm image show the positions of the two H II regions seen in the 36 cm image, and the cyan arcs indicate the 8 μm emission possibly associated with the SNR. The white dashed line shown in the 24 μm image marks the region where I measured the flux densities at 24 μm and 70 μm (Sect. 10.1.2. E). Soft X-ray contours are overlaid in cyan.

10.1.3. Discussion

DEM L205 exhibits all the classical SNR signatures, and is therefore confirmed as a *new supernova remnant*. On the basis of the J2000 X-ray position, DEM L205 is thus called MCSNR J0528–6727 in the catalogue of LMC remnants. In the following sections, I take advantage of the multi-wavelength observations of the remnant and discuss the origin of the IR emission (the various processes that can occur in SNRs to emit IR light have been introduced in Sect. 5.4), derive some physical properties of the remnant, compare the morphology at all observed wavelengths and discuss the environment in which the SN exploded, and analyse the star formation activity around the SNR.

10.1.3.A. Origin of the IR emission

No significant emission from DEM L205 was detected in the IRAC wavebands (which have been chosen to include the main PAH features), with the possible exception of the two $8\ \mu\text{m}$ and $5.8\ \mu\text{m}$ arcs (Fig. 10.6, left) in the direction of the neighbouring H II regions (in the north and west). This means that PAHs have been efficiently destroyed. The absence of IR spectroscopic observations precludes further interpretation.

The presence of H α emission shows that hydrogen is not in the molecular phase, hence rotational/vibrational line contribution is negligible. The emission in the $24\ \mu\text{m}$ and $70\ \mu\text{m}$ wavebands should then be dominated either by dust or ionic forbidden lines. Ionic lines in the $24\ \mu\text{m}$ filter bandpass are [S I] $25.2\ \mu\text{m}$, [Fe II] $24.50\ \mu\text{m}$ and $25.99\ \mu\text{m}$, [Fe III] $22.95\ \mu\text{m}$, and [O IV] $25.91\ \mu\text{m}$. [S I] emission is not expected because of the prominent [S II] optical emission, showing that S⁺ is the primary ionisation stage of sulphur. The morphological similarities between the MIR and X-ray emission lead to the interpretation that one mainly observes the thermal continuum of dust. The correlation with $70\ \mu\text{m}$ supports this scenario, and the 70-to- $24\ \mu\text{m}$ ratio (~ 5.2) is consistent with a dust temperature of 50 K – 80 K (Williams et al. 2006a).

In the northern part of the arc of $24\ \mu\text{m}$ emission (encompassed by the white dashed line in Fig. 10.6, middle), the MIR emission is slightly ahead of the shock (delineated by the X-ray emission), whereas it correlates tightly with the shock in the rest of the arc. This morphology and the presence of the OB association LH 63 (see Fig. 10.7, right) indicates that stellar radiation dominates the heating of the dust in the north. In the southern part, shock waves could play a more significant role in heating the dust.

The lack of spectroscopic data prevent us from establishing the precise contribution of dust vs. O and Fe lines. Because of these limitations and the confusion with the background, and because only part of the SNR is detected at IR wavelengths, I did not attempt to derive a dust mass. Consequently, no dust-to-gas ratio (using the swept-up gas mass estimate from X-ray observations) and dust destruction percentage can be given.

10.1.3.B. Properties of DEM L205 derived from the X-ray observations

From the X-ray spectral analysis, several physical properties of the remnant can be derived: electron and hydrogen densities n_e and n_H , dynamical and ionisation ages t_{dyn} and t_i , swept-up mass M , and initial explosion energy E_0 . I used a system of equations adapted from van der Heyden et al. (2004), given by:

$$n_e = \frac{1}{f} \sqrt{r_e \frac{EM}{V}} \quad (\text{cm}^{-3}) \quad (10.1) \quad n_H = n_e / r_e \quad (\text{cm}^{-3}) \quad (10.2)$$

$$t_{\text{dyn}} = 1.3 \times 10^{-16} \frac{R}{\sqrt{kT_s}} \quad (\text{yr}) \quad (10.3) \quad t_i = 3.17 \times 10^{-8} \frac{\tau}{n_e} \quad (\text{yr}) \quad (10.4)$$

$$M = 5 \times 10^{-34} m_p r_m n_e f^2 V \quad (M_\odot) \quad (10.5) \quad E_0 = 2.64 \times 10^{-8} kT_s R^3 n_H \quad (\text{erg}), \quad (10.6)$$

where EM is the emission measure ($= n_e n_H V$) in cm^{-3} , kT_s is the shock temperature in keV, and τ is the ionisation timescale in s cm^{-3} . These parameters are determined by the spectral fitting. In addition, R is the radius of the X-ray remnant in cm (using the semi-major axis of 39.5 pc, see Sect. 10.1.2. A), V is the volume ($4\pi/3 \times R^3$) assuming spherical symmetry (as discussed below), m_p is the proton mass in g, r_m is the total number of baryons per hydrogen atom ($= n_m/n_H$), and r_e is the number of electrons per hydrogen atom ($= n_e/n_H$). Assuming a plasma with 0.5 solar metal abundances, as done in the spectral fitting, one has $r_m \approx 1.40$ and $r_e \approx 1.20$ (for full ionisation). Finally, f is a filling factor to correct for any departure from spherical symmetry, as inferred from the X-ray morphology. f is defined as $\sqrt{V_t/V}$, where V_t is the true X-ray emitting (ellipsoidal) volume. Adopting the semi-minor axis of the X-ray emitting ellipse (32 pc) as the second semi-principal axis, f is in the range 0.81 – 0.90, with the third semi-principal axis being between 32 pc and 39.5 pc.

The properties are listed in Table 10.3, using f in this range and EM in the range defined in Sect. 10.1.2. B. The large amount (from 400 M_\odot to 460 M_\odot) of swept-up gas justifies *a posteriori* that the SNR is indeed well-established in the Sedov phase. Because the remnant is old, the plasma is close to or in collisional ionisation equilibrium, as indicated by either the acceptable fit of the APEC model or the large ionisation timescale τ , for which only a lower limit is found. Thus, the spectrum changes very slowly with time and τ is no longer a sensitive age indicator (van der Heyden et al. 2004). This explains why t_i is unrealistically long (> 770 kyr, from Eqs. 10.1 and 10.4) and unreliable.

TABLE 10.3 – Physical properties of DEM L205.

n_e (10^{-2} cm^{-3})	n_H	t_{dyn} (10^3 yr)	M (M_\odot)	E_0 (10^{51} erg)
5.6 – 7.8	4.7 – 6.5	35^{+2}_{-5}	400 – 460	0.52 – 0.77

10.1.3. C. Multi-wavelength morphology

In Fig. 10.2, we see an X-ray remnant with a slightly elongated shape and a maximal extent of 79 pc. Therefore, DEM L205 ranks amongst the largest known in the LMC (Badenes et al. 2010), consistent with its fairly advanced evolutionary stage, and is comparable to e. g. SNRs described in Cajko et al. (2009); Klimek et al. (2010); Grondin et al. (2012). The optical emission-line images (Figs. 10.2 and 10.7) show the shell-like structure of DEM L205 coinciding with the boundary of the X-ray emission from the remnant. Dunne et al. (2001) classified the shell as a superbubble (SB), interpreting the morphology of DEM L205 as a blister blown by the OB association LH 63 (see text below and Fig. 10.7, right). They measured a mild expansion velocity of $\sim 70 \text{ km s}^{-1}$ for the $H\alpha$ shell, which is typical of SBs. Supernova remnants exhibit higher expansion velocities ($\gtrsim 100 \text{ km s}^{-1}$), although this is not a necessary condition (Chu 1997).

On the basis of the low densities ($< 0.1 \text{ cm}^{-3}$) derived from the X-ray spectral analysis, I conclude that the supernova exploded inside the blister, producing the bright X-ray emission in the interior of the SB. The SNR shocks reaching the inner edge of the bubble might then have produced non-thermal radio emission, and the observed morphology at 36 cm is consistent with this picture.

The remnant is located in a complex environment. In the north and west, we detected two H II regions and a strip of dust and gas extending down towards the south-west. The H II regions also show bright IR emission, mainly from dust heated by stellar radiation, and bright (thermal) radio-continuum emission (Figs. 10.4 & 10.6). The [S II]-to- $H\alpha$ ratio is higher in the south of the remnant, indicating that the diffuse optical emission there is caused by the SNR shocks. In addition, the lower ratio in the north and west parts of the remnant is most likely due to photoionisation by the massive stars (bringing sulphur to ionisation stages higher than S^+) from the same OB associations that power the H II regions and produced the SB in which the supernova exploded. I therefore propose that the SNR and the H II regions are physically connected.

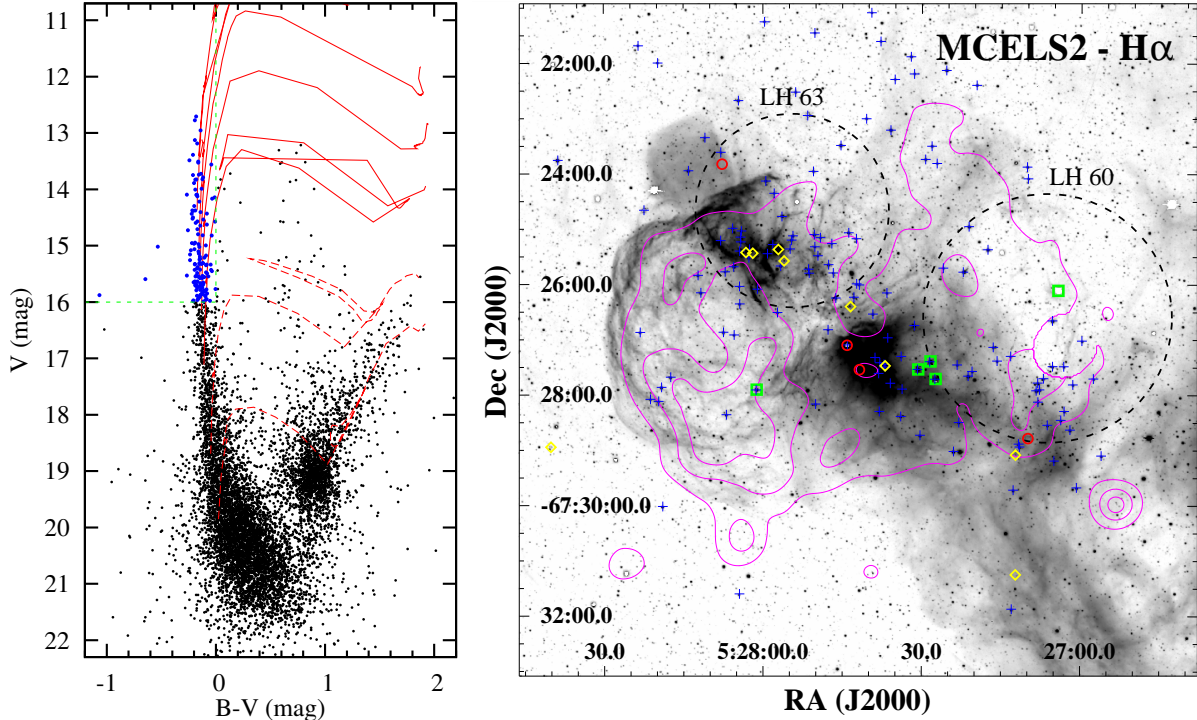


FIGURE 10.7 – *Left*: Colour-magnitude diagram (CMD) of the MCPS stars (Zaritsky et al. 2004) within 100 pc ($\sim 6.9'$) of the central position of DEM L205. Geneva stellar evolution tracks (Lejeune & Schaerer 2001) are shown as red lines, for metallicity of $0.4 Z_{\odot}$ and initial masses of $3, 5 M_{\odot}$ (dashed lines) and $10, 15, 20, 25,$ and $40 M_{\odot}$ (solid lines), from bottom to top. The green dashed line shows the criteria used to identify the OB stars ($V < 16$ and $B - V < 0$). Stars satisfying these criteria are shown as blue dots.

Right: MCELS2 $H\alpha$ image of the SNR, with the soft X-ray contours in magenta. The blue plus signs show the positions of the OB candidates identified in the CMD and green squares identify Sanduleak OB stars. The black dashed circles encompass the nearby OB associations 60 and 63 from Lucke & Hodge (1970). Positions of definite (yellow diamond) and probable (red circle) YSOs from Gruendl & Chu (2009) are also shown.

Furthermore, whilst the X-ray surface brightness falls abruptly across the eastern and southern boundaries of the remnant, much weaker emission is detected in the north and west, right at the positions of the $H\text{II}$ regions seen at all other wavelengths (Figs. 10.2, 10.4, and 10.6). This indicates that the remnant is *behind* the $H\text{II}$ regions. The absorption column density is higher in the north and west, suppressing the X-ray emission and giving rise to the observed asymmetrical, irregular shape in these regions. The ellipse defined in Sect. 10.1.2. A is probably an oversimplification of the actual morphology of the X-ray emitting region. The remnant may have a more spherical shape, with some parts masked by the $H\text{II}$ regions.

Soft and faint diffuse X-ray emission is also detected on the other side of the dust/gas strip. The diffuse X-ray emission is enclosed by very sharp and faint $H\alpha$ filaments (Figs. 10.2 and 10.7). The presence of the OB association LH 60 suggests that another stellar-wind-blown SB in which a SN had exploded is observed. The faintness of the X-ray and optical emission precludes further analysis. There, note that the $[\text{S II}]$ -to- $H\alpha$ ratio is less than 0.4. However, it cannot be used in that case because of the presence of massive stars from the OB association.

10.1.3. D. Past and present star formation activity around the SNR

To investigate the star content around the remnant, I used the MCPS catalogue of [Zaritsky et al. \(2004\)](#) and constructed the colour-magnitude diagram (CMD) of the $\sim 20\,000$ stars lying within 100 pc (6.9') of the remnant's centre. The CMD (Fig. 10.7, left) shows a prominent upper main-sequence branch. I added stellar evolutionary tracks of [Lejeune & Schaerer \(2001\)](#), for $Z = 0.4 Z_{\odot}$ and initial masses from $3 M_{\odot}$ to $40 M_{\odot}$, assuming a distance modulus of 18.49 and extinction $A_V = 0.5$ (the average extinction for “hot” stars, [Zaritsky et al. 2004](#)). I used the criteria of $V < 16$ and $B - V < 0$ to identify OB stars, and found 142 of them in the sample (shown in a $H\alpha$ image in Fig. 10.7, right). Using $V < 15$ or 14 instead of 16 would give 86 and 20 stars, respectively.

I also looked for nearby OB associations in [Lucke & Hodge \(1970\)](#) and OB stars in the catalogue of [Sanduleak \(1970\)](#). Contamination by Galactic stars was monitored by performing a cross-correlation with Tycho-2 stars ([Høg et al. 2000](#)). Five Sanduleak stars are in this region, four of them having a match in the MCPS catalogue, with the selection criteria. The “missed” Sanduleak star is a VV Cepheid (a binary with a red component), which thus possibly explains why these criteria were not satisfied. Two OB associations (LH 60 and 63) lie close to the remnant ($\sim 6'$ and $3'$, respectively), and their extent indeed contain many OB stars from the MCPS catalogue.

[Harris & Zaritsky \(2008\)](#) performed a spatially resolved analysis of the SFH of the “Constellation III” region, and DEM L205 was included in their study (the “E00” cell in their Fig. 2). They identified that a very strong peak in the star formation rate occurred in the region of the remnant 10 Myr ago, and that little star formation activity had occurred prior to this burst.

The rich content of high-mass stars and the recent peak in SFH around the remnant strongly suggest that a core-collapse supernova has formed DEM L205. It is however impossible to completely rule out a type Ia event. Considering at face value that most of the stars were formed in the SFR peak 10 Myr ago, I estimated a lower limit for the mass of the SN progenitor of $20 M_{\odot}$, because less massive stars have a lifetime longer than 10 Myr ([Meynet et al. 1994](#)). I cannot estimate an upper limit, because the progenitor might have formed more recently (the region is still actively forming stars, see below).

I searched for nearby young stellar objects (YSOs) to assess the possibility of SNR-triggered star formation, as in [Desai et al. \(2010\)](#). Using the YSOs from the catalogue of [Gruendl & Chu \(2009\)](#), I report an SNR–molecular cloud–YSOs association around DEM L205: the positions of young stars are shown in the $H\alpha$ image (Fig. 10.7, right). Four YSOs lie in the H_{II} region/molecular cloud in the north, and are closely aligned with the X-ray emission rim. In addition, four YSOs lie in the western H_{II} region, significantly beyond the remnant's emission but correlated with the diffuse X-ray emission from the SB around LH 60. Two additional YSOs are aligned with the south-western edge of the SB.

Given the contraction timescale for the intermediate to massive YSOs (10^6 yr to 10^5 yr, [Bernasconi & Maeder 1996](#)), the shocks from the remnant cannot have triggered the formation of the YSOs already present. These YSOs are more likely to have formed by interactions with winds and ionisation fronts from the local massive stars, as illustrated by the alignment of young stars along the rim of the adjacent SB. The remnant will be able to trigger star formation in the future, when the shocks have slowed down to below 45 km s^{-1} ([Vanhala & Cameron 1998](#)). By this time, however, the neighbouring massive stars will also have triggered further star formation. It is therefore difficult to assess the exact triggering agent of star formation, as [Desai et al. \(2010\)](#) pointed out, in particular in such a complex environment.

10.1.4. Summary

The first observation of the LMC survey with *XMM-Newton* included the SNR candidate DEM L205 in the field of view. In combination with unpublished radio-continuum data and archival optical and IR observations, all classical SNR signatures are found, namely :

- extended X-ray emission
- optical emission with a shell-like morphology and an enhanced [S II]-to- $H\alpha$ ratio
- non-thermal and extended radio-continuum emission.

The source is also detected in the IR where predominantly thermal emission from dust is observed. One can therefore definitely confirm this object as a supernova remnant. A core-collapse supernova origin is favored, in light of the recent burst of star formation and the presence of many massive stars in the close vicinity of the remnant. In that interpretation, a lower limit of about $20 M_{\odot}$ is placed on the mass of the progenitor. The SN exploded in a SB, thus expanding in a low density medium. With a size of $\sim 79 \times 64$ pc, DEM L205 is one of the largest SNRs known in the LMC. Given the low plasma temperature ($kT \sim 0.2$ keV – 0.3 keV), I derived a dynamical age of about 35 kyr.

10.2. New iron-rich SNRs : The most evolved remnants of type Ia supernovae

IN THIS section, I describe the discovery, analysis, and properties of three new SNRs, which share the properties of being *iron-rich*, as revealed by their X-ray spectra. They are members of a growing class of Magellanic remnants which show centrally-peaked X-ray emission highly enriched in iron. This establishes their type Ia (thermonuclear) SN origin. MCSNR J0508–6902 was identified with ROSAT as an SNR candidate. XMM-Newton was used in combination with new radio and optical observations to study in details the remnant. Results were published in Bozzetto, Kavanagh, Maggi, et al. (2014, hereafter BKM14). I have been involved in the analysis of X-ray data and the discussion of the results reproduced here. The two other sources are MCSNR J0508–6830 and MCSNR J0511–6759. They were discovered in the survey observations. I conducted the study of the objects which was published in Maggi, Haberl, Kavanagh, et al. (2014, hereafter MHK14). I emphasise here my original contributions, mostly the X-ray analysis and discussion. The radio and optical data (observations and analysis) were mainly contributed by my co-authors. I reproduce here some of these results for the sake of completeness, whilst details of the observations and analysis can be found in the original publications.

10.2.1. Source identification and observations

X-rays : MCSNR J0508–6902 was selected as a bona-fide SNR candidate from the PSPC catalogue of LMC sources (HP99), based on its spatial extent and extent likelihood, hardness ratios, and non-variability. The source had the identifier [HP99] 791 and was proposed for XMM-Newton observations in AO9 (PI: Sasaki, 2009). The observation was blighted by very high background, but an extended X-ray source was indeed found and confirmed the SNR nature. The last pointing of the LMC survey was therefore set to cover [HP99] 791 and yield the required exposure time. On the other hand, MCSNR J0508–6830 and MCSNR J0511–6759 were serendipitously discovered during the LMC survey³⁵. They matched the criteria for SNR candidates described in Sect. 5. Details of the observations are summarised in Table 10.7 (p. 84).

To designate the sources I used the identifier “MCSNR JHHMM+DDMM”. I chose to introduce the names of the objects from the start of the discussion to allow an easier description of the analysis. For the same reason I will here and after simply call them “remnants” (and no longer “candidates”). Firm evidence for their classification as SNR is presented in Sect. 10.2.3.

Radio : For the study of MCSNR J0508–6830 and MCSNR J0511–6759 in MHK14, archival data from various radio surveys were used, particularly the 4800 MHz survey by Dickel et al. (2010) and the 1370 MHz survey by Hughes et al. (2007). Both surveys used the ATCA in fairly compact configurations to produce half-power beamwidths of 35'' and 45'', respectively. Data at both frequencies from a survey using the 64-m Parkes telescope (Haynes et al. 1991; Filipovic et al. 1995) were included in the imaging to improve the sensitivity to the smooth emission from these extended regions.

In the case of MCSNR J0508–6902, the same new ATCA observations as for DEM L205 (Sect. 10.1, Maggi et al. 2012a) were used, again in combination with archival MOST and ATCA data.

Optical : I used data from the MCELS (Sect. 4.2). All observations covering MCSNR J0508–6830 and MCSNR J0511–6759 were combined, flux-calibrated, and smoothed with a 2'' Gaussian. The corresponding continuum images were subtracted, thereby removing (most of) the stellar contribution and revealing the faint diffuse emission in its full extent. The continuum-subtracted images were prepared by Sean Points. I then produced a $[S II]/H\alpha$ ratio map. To avoid noise where the pixel values in either bands

³⁵The faint ROSAT source [HP99] 606 is in close proximity to MCSNR J0511–6759 but was not classified, even as a candidate SNR, due to the very limited data available

were low or negative (due to over-subtraction of the continuum, particularly around stars), I set the ratio to 0 for these pixels. From this map I could investigate possible strong $[\text{S II}]/\text{H}\alpha$ ratios, which are indicative of shock excitation. I used a conservative criterion of 0.6 to identify regions where the ratio is clearly enhanced. The $[\text{S II}]/\text{H}\alpha$ map is used in Figs. 10.8 & 10.9, and the results described in Sect. 10.2.3. A.

For MCSNR J0508–6902, I used the (non-continuum-subtracted) MCELS data to image the object in $[\text{S II}]$, $\text{H}\alpha$, and $[\text{O III}]$. In addition, we used the deep arcsecond-resolution $\text{H}\alpha$ image from the photographic survey with the UK Schmidt telescope (UKST) by Reid & Parker (2006) with matching SR (short “broad-band” red image), and spectroscopy (in the red part of the spectrum) using the multi-object fibre spectrograph AAOmega 2dF on the Anglo-Australian Telescope (AAT). Details of the photographic and spectroscopic observations are given in BKM14. In Fig. 10.11 I show the $\text{H}\alpha$ quotient image ($\text{H}\alpha$ divided by SR) with the position of the 2dF fibres.

Infrared : I used *Spitzer* data from the SAGE survey to assess possible emission from MCSNR J0508–6830 and MCSNR J0511–6759, and study their surrounding cold environments. I essentially used MIPS data at $24\ \mu\text{m}$ from the mosaiced, flux-calibrated images processed by the SAGE team.

10.2.2. Data analysis

I reduced the *XMM-Newton* observations with the method described in Sect. 7, creating adaptively smoothed, vignetting-corrected, and detector-background-subtracted images in the “SNRs” energy bands. Data from all EPIC detectors were merged.

I extracted energy spectra from vignetting-corrected event lists (Sect. 8). In the case of MCSNR J0508–6830 and MCSNR J0511–6759, the extraction regions were circles including all the X-ray emission. I extracted background spectra from adjacent regions, which were chosen to be at a similar off-axis angle and on the same CCD chip as the source. However, MCSNR J0508–6830 was located on more than one chip, possibly leading to systematic uncertainties in computing response functions. Point sources detected in the extraction regions were excised.

Because of the morphology of MCSNR J0508–6902, which shows striking differences between the soft- and medium-band emission (Sect. 10.2.3. A), spectra were extracted from two regions : *i*) the central region, defined to enclose the 0.7 keV – 1.1 keV band contours with an ellipse ($\sim 2.8' \times \sim 1.6'$), and *ii*) a “shell” region, using a $\sim 5'$ diameter circle, excluding the central extraction region. Since MCSNR J0508–6902 was observed on-axis, the background spectrum was taken from a source and diffuse emission-free region further off-axis than the remnant. The instrumental background variation is taken into account in the spectral modelling (Sect. 8). Only the survey observation of MCSNR J0508–6902 (Obs. ID 0690752001) is considered for the spectral analysis. The only ~ 9 ks of data from Obs. ID 0651880201 add little to our analysis (the faint shell of the remnant is not even detected in images from this observation). Furthermore, the flare-filtered event lists are still heavily contaminated by SPC.

For all sources, only EPIC-pn spectra were used for the spectral analysis because all three remnants are very faint in the MOS-only images. The spectra were rebinned using the FTOOLS `grppha` to have a minimum of 25 counts per bin. XSPEC version 12.8.0u was utilised for the spectral analysis. I followed the method and used the background model described in Sect. 8 to simultaneously model the source emission and the (instrumental + X-ray) background. The foreground Galactic absorption was fixed to the values derived from the H I map of Dickey & Lockman (1990) at the position of each object. Guided by the results of the spectral analysis, I used several emission models for the remnants, starting with single-temperature models assuming either collisional ionisation equilibrium (CIE) or non-equilibrium ionisation (NEI) (as described later, see (Sect. 10.2.3. B & 10.2.3. C).

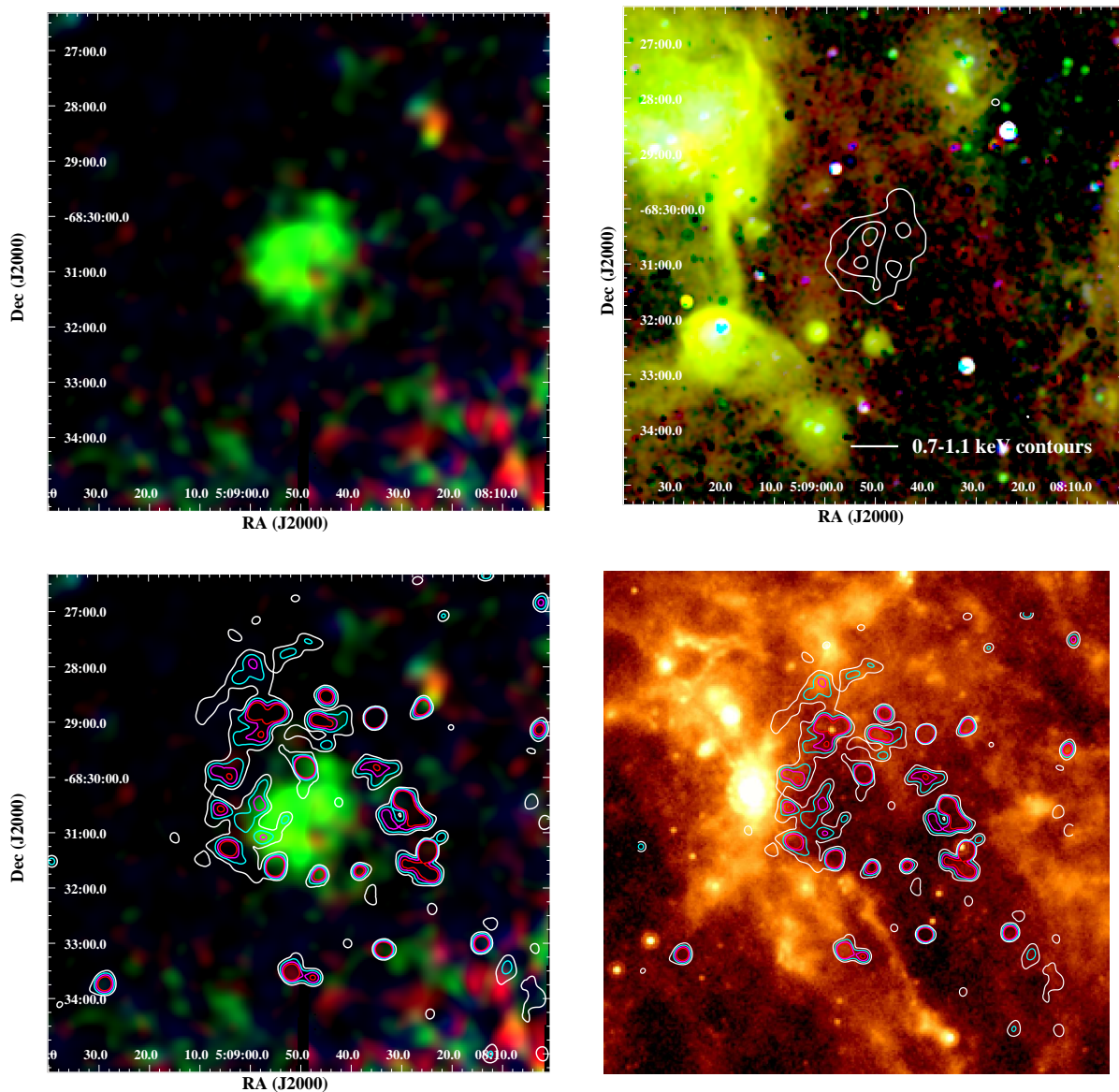


FIGURE 10.8 – A multicolour view of MCSNR J0508–6830. *Top left*: X-ray colour image of the remnant, combining the data from all EPIC cameras. The red, green, and blue components are soft, medium, and hard X-rays. *Top right*: The same region of the sky in the light of [S II] (red), $H\alpha$ (green), and [O III] (blue), where all data are from the MCELS. The X-ray contours from the medium band are overlaid. *Bottom left*: Same EPIC image as above but with [S II]-to- $H\alpha$ ratio contours from MCELS data. Levels are at 0.6, 0.8, 1.0, and 1.2 in white, cyan, magenta, and red, respectively. *Bottom right*: The remnant as seen at $24\ \mu\text{m}$, with the same [S II]-to- $H\alpha$ ratio contours as on the left.

10.2.3. Results

10.2.3. A. Multi-wavelength morphology

MCSNR J0508–6830: Images of the object at various wavelengths are shown in Fig. 10.8. This remnant is the faintest source of this sample. It emits X-rays chiefly in the medium band (0.7 keV – 1.1 keV), with little or no flux in the softer and harder bands, respectively. This suggests the predominance of iron emission and is explored in greater detail in the spectral analysis (Sect. 10.2.3. B).

To estimate the size and nominal centre of the X-ray remnant I fit an ellipse to the 0.7 keV – 1.1 keV contours. The outer contour was chosen to be 0.26 times the amplitude (peak intensity minus average background intensity). This would enclose 90 % of the flux of a Gaussian-distributed profile. Size uncertainties were estimated by changing the outer contours by $\pm 10\%$ of the total amplitude and then re-computing the size of the ellipse. I found a nominal centre of RA = $05^{\text{h}} 08^{\text{m}} 49.5^{\text{s}}$, DEC = $-68^{\circ} 30^{\text{m}} 41^{\text{s}}$, a semi-major and semi-minor axis of $1.15'$ and $0.90'$, respectively, and a position angle (PA) of 40° west of north. The uncertainty is $0.1'$ in each direction. At the assumed distance of the LMC, this gives an extent of MCSNR J0508–6830 of $16.7(\pm 1.5) \text{ pc} \times 13.1(\pm 1.5) \text{ pc}$.

Whilst there is no obvious association in the MCELS images to the X-ray emission, one does detect very faint [S II] emission, which encircles the remnant seen in X-rays almost completely, except in the south (Fig. 10.8, top right). At the position of the [S II] shell there is no contribution from $H\alpha$, which is only emitted by the nearby, most likely unrelated, H II regions. Therefore, this shell and its location around the central X-ray emission appears more clearly in the X-ray image vs. [S II]/ $H\alpha$ contours (Fig. 10.8, bottom left). The [S II] shell is twice as large as the X-ray-emitting region (semi-axes of about $1.9' \times 2.0'$). I discuss this morphology in light of the spectral results and in comparison with other SNRs in Sect. 10.2.4.

MCSNR J0508–6830 is not obvious on the radio images but we do see the nearby H II region to the northeast and curving around to the north and southeast as shown in the optical images. The lack of association of radio emission with the faint [S II] shell or bright X-ray central region indicates the faintness of the SNR at radio frequencies and/or the insufficient sensitivity of the current radio surveys.

In the infrared, there is no evident emission from the remnant. Most of the diffuse emission of that region (Fig. 10.8, bottom right) can be associated to the nearby H II regions seen in radio and in the optical.

MCSNR J0511–6759: A multicolour view of MCSNR J0511–6759 is shown in Fig. 10.9. The X-ray colour of this source is very similar to MCSNR J0508–6830, in the sense that the 0.7 keV – 1.1 keV band totally dominates the X-ray emission. The morphology is roughly spherical, so I adjusted a circle on the intensity map to derive the position of the centre: RA = $05^{\text{h}} 11^{\text{m}} 10.7^{\text{s}}$, DEC = $-67^{\circ} 59^{\text{m}} 07^{\text{s}}$. To measure the size and associated uncertainty for the source, I extracted intensity profiles intersecting the remnant's centre, at ten different position angles. I measured the extent at which the intensity falls below 0.26 times the amplitude (the same criterion as for MCSNR J0508–6830 can be applied as well for this remnant as they have similar morphologies). I repeated this measurement for each PA, before computing the mean and standard deviation of the ten measurements. I obtained a radius of $0.93' \pm 0.09'$, corresponding to a physical size of $13.5(\pm 1.3) \text{ pc}$.

In the continuum-subtracted [S II] images one can see faint diffuse emission at the position of MCSNR J0511–6759. This optical emission has a roughly circular morphology, encasing the bright X-ray emission. It appears slightly limb-brightened, indicating a shell morphology, and its extent is $\sim 3.8' \times 3.6'$, i.e. larger than the X-ray emission. $H\alpha$ emission is seen at the same location, albeit even fainter, whilst $[\text{O III}]\lambda 5007 \text{ \AA}$ is completely absent. Despite the faintness of this optical emission, its shell-like morphology and its strong [S II]/ $H\alpha$ ratio (in excess of 0.6 and reaching 1.5) allows to secure the association of the optical emission to the X-rays, and to clearly discriminate the remnant from the ambient optical emission, e.g. from the H II region DEM L89 (Davies et al. 1976) located $\sim 8'$ to the north-west.

In addition, note the presence of a small knot of X-ray emission, $\sim 1.7'$ towards the east, *outside* of the main X-ray-emitting region. Its morphology is different from that of a point source, and its colour/hardness ratios are very similar to that of the bulk of the X-ray emission. Furthermore, it is located at the eastern tip of the diffuse optical emission described above, suggesting that the knot is likely to belong to the remnant, possibly being a clump of X-ray emitting ejecta (“schrappnel”).

MCSNR J0511–6759 was too faint to be detected in the various radio surveys of the LMC. The diffuse infrared emission (at $24 \mu\text{m}$) around the remnant is very moderate. A weak filament is found to correlate with the south-eastern part of the [S II] shell, suggesting a physical association with MCSNR J0511–6759. I discuss a possible origin of this emission in Sect. 10.2.4.

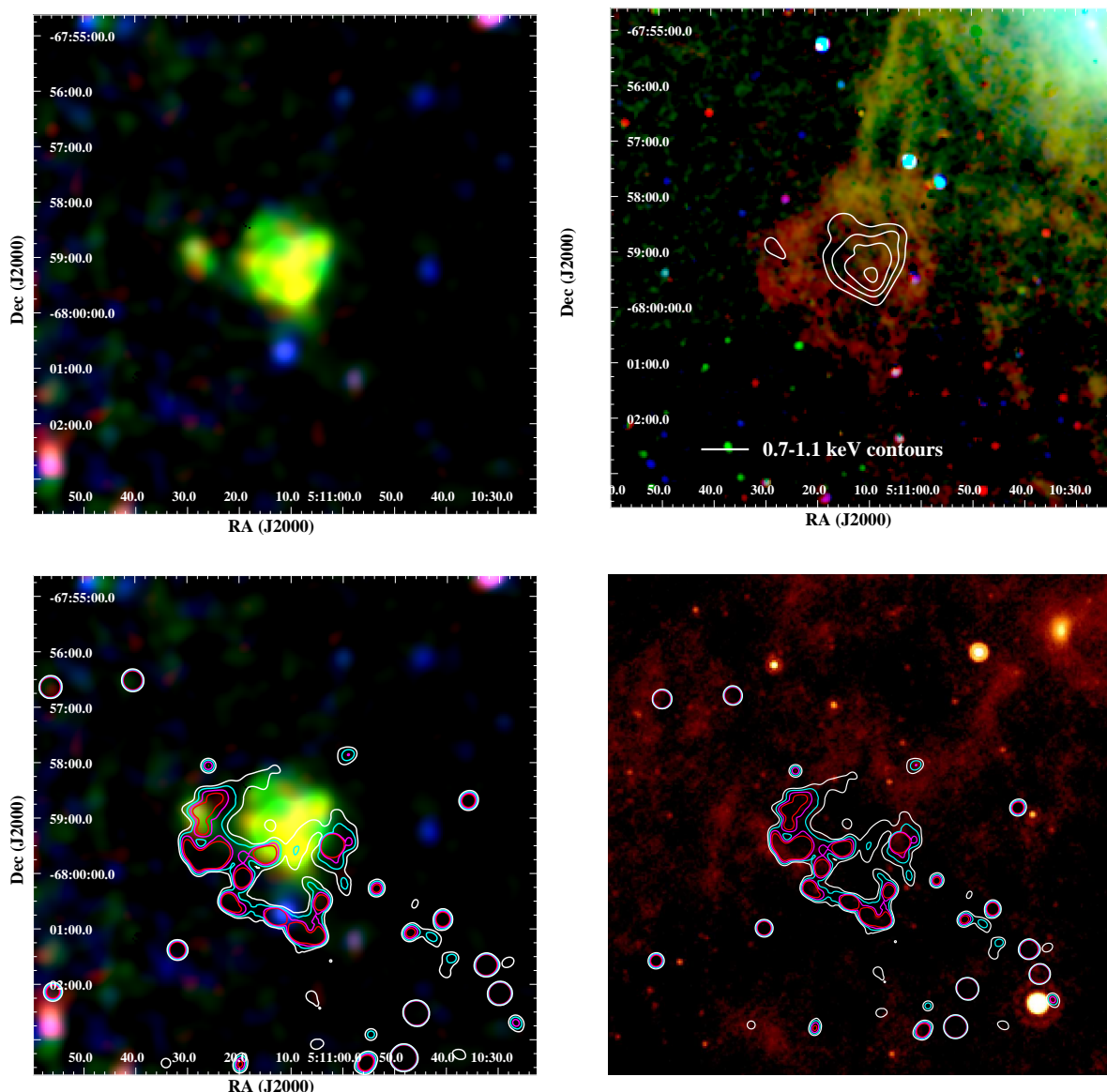


FIGURE 10.9 – Same as Fig. 10.8 for MCSNR J0511–6759.

MCSNR J0508–6902: This remnant has a clear association at radio frequencies (Fig. 10.10, bottom row) and exhibits a filled-in shell morphology (in particular at 20 cm) centred at RA = $05^{\text{h}} 08^{\text{m}} 33.7^{\text{s}}$, DEC = $-69^{\circ} 02^{\text{m}} 33^{\text{s}}$. The emission at 36 cm and 20 cm is fairly uniform across the remnant with lib brightening in the south-east. At shorter wavelength (6 cm, not shown) only the south-eastern emission remains while all emission is lost at 3 cm. The radio spectral index is measured from datasets including zero-spacing observations as $\alpha = -0.62 \pm 0.34$, from which an average equipartition field of $\sim 28 \mu\text{G}$ is estimated (BKM14). This value cannot be confirmed by Farady rotation measurements, since no polarisation is detected from the remnant.

All optical lines from the MCELS data ([S II], $\text{H}\alpha$, and [O III]) are detected from the remnant (Fig. 10.10, top right). The [O III] emission fits within the confine of the radio emission along the south-eastern limb of the remnant and extends in the northern region to complete the ellipse ring structure of the remnant. On the other hand, $\text{H}\alpha$ and [S II] are mostly detected in the north-western region and show little association with

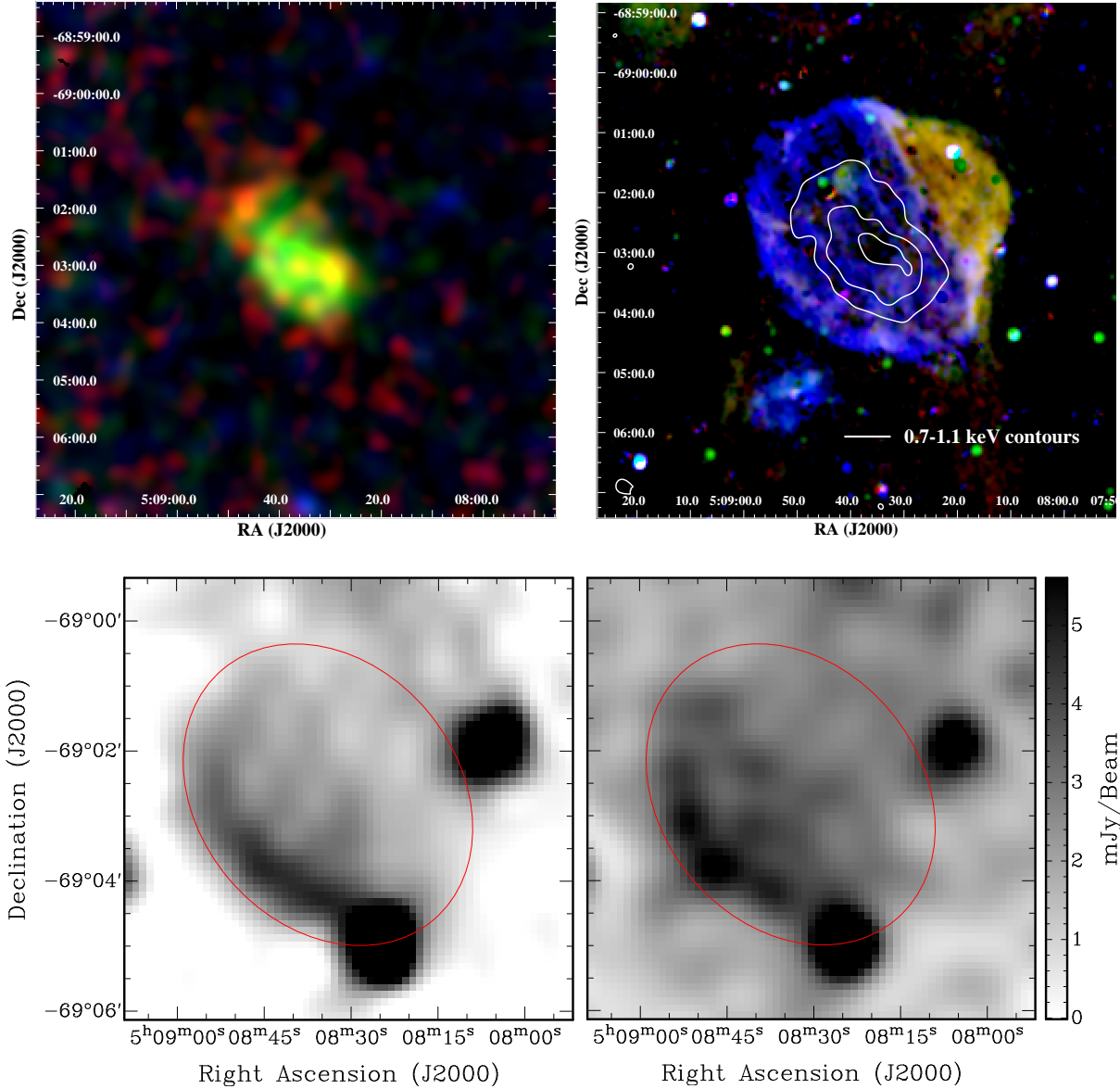


FIGURE 10.10 – *Top row*: X-ray colour image (left) of MCSNR J0508–6902 and MCELS image (right) with medium band X-ray contours overlaid.

Bottom row: Radio-continuum image of the remnant at 36 cm (843 MHz, left) and 20 cm (1400 MHz, right). The overlaid ellipse indicates the optical association for this SNR. The side bar quantifies the total intensity in mJy per beam. (Radio images prepared by Luke Bozzetto.)

the radio emission. The $H\alpha$ and $[S\ II]$ emission is also stronger than $[O\ III]$. This morphology is reminiscent of that of the LMC SNR J0453–6829 (Haberl et al. 2012a).

Thanks to the higher resolution of the deep UKST $H\alpha$ image, it is possible to see a complete optical shell which follows the radio emission in the east (Fig. 10.11). Strong $H\alpha$ and $[S\ II]$ lines are detected in the 2dF spectra taken from various regions along the optical shell (see BKM14), including the faint optical filament in the east. The high $[S\ II]/H\alpha$ ratios, ranging from 0.6 to 1.29, reveal the shock-excitation origin of the optical emission, an expected signature of a SNR.

The X-ray morphology (Fig. 10.10, top left) is remarkable: faint and soft X-ray emission following the 20 cm radio-continuum emission is detected, filling out the shell of the remnant. The X-ray emission in the 0.7 keV – 1.1 keV band is brighter and encased within the radio and optical emission, making its central location evident. The central region has a size comparable to the emission in the same medium band of MCSNR J0508–6830 and MCSNR J0511–6759, although it is slightly elongated ($\sim 2.8' \times \sim 1.6'$). Combining radio, optical, and X-ray images, one can deduce an extent of the object of $304'' \times 234''$ ($\pm 4''$), or $74 \text{ pc} \times 57 \text{ pc}$ ($\pm 1 \text{ pc}$). This places the remnant amongst the 20 % largest SNRs in the LMC (Badenes, Maoz, & Draine 2010).

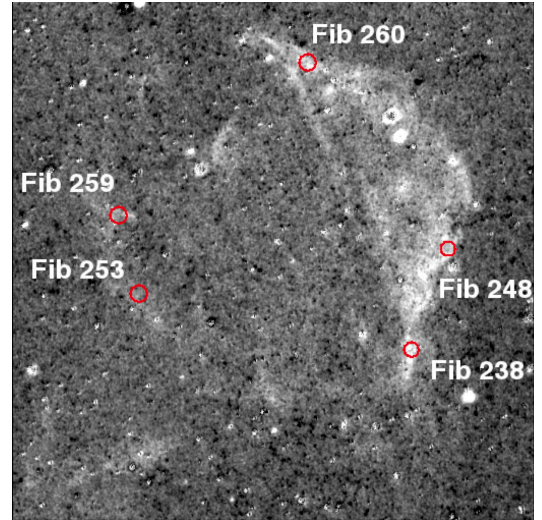


FIGURE 10.11 – $H\alpha$ quotient image taken from the data of Reid & Parker (2006). The positions of the 2dF fibres for the optical spectroscopy are indicated.

10.2.3. B. X-ray spectroscopy

MCSNR J0508–6830: The X-ray spectrum of this remnant is shown in Fig. 10.12 (left). The most striking feature is the large Fe L-shell bump ($\sim 0.7 \text{ keV}$ to $\sim 0.9 \text{ keV}$) which dominates the X-ray emission.

Despite the faintness of the source, I could obtain meaningful best-fit parameters and uncertainty ranges with the simple spectral models. The results are listed in Table 10.6 (p. 83). The best fits were obtained for temperatures of about 0.6 keV – 0.7 keV and a low absorption, consistent with $N_H \sim 0 \text{ cm}^{-2}$ (90 % C.L. upper limit of $1.8 \times 10^{21} \text{ cm}^{-2}$). For low N_H values ($\lesssim 10^{21} \text{ cm}^{-2}$), absorption effects are small and mostly affect photons below 0.5 keV; since the source shows no significant emission below this energy, N_H cannot be efficiently constrained. I fixed the LMC N_H to 0 cm^{-2} for the rest of the analysis, stressing that this does not influence the results presented below. No significant effects of non-equilibrium ionisation were detected: the ionisation age was close to the upper limit available in the *vpshock* model.

The fits greatly improved when the Fe abundance was let free, and improved marginally if O abundance was free as well. The O abundance tended towards 0, but was essentially unconstrained (upper limit of ~ 20 times the solar value). This happens because at the best-fit temperature ($\sim 0.6 \text{ keV}$), which is set by the shape of the iron L-shell bump, the oxygen emissivity is relatively low. I therefore cannot well constrain this parameter. The Fe abundance was found to be greatly in excess of the average LMC value, or even solar value. The upper limit of $\text{Fe}/\text{Fe}_\odot$ is very high or unconstrained because of the degeneracy between this parameter and the normalisation of the *vapec* (or *vpshock*) component. Indeed, since iron is almost the only contributor to the spectrum, the fitting procedure cannot distinguish between a higher iron abundance and lower emission measure, or *vice-versa*. The low contribution of oxygen to the spectrum and predominance of iron is investigated further in a multi-component plasma analysis (Sect. 10.2.3. C).

MCSNR J0511–6759: The X-ray spectrum of this remnant (Fig. 10.12, right) resembles that of MCSNR J0508–6830, as expected from their morphological and X-ray colour similarities. It is also dominated by an Fe L-shell bump and has an even lower contribution from oxygen lines.

The best-fit *vapec* and *vpshock* models are obtained for plasma temperatures of 0.64 keV and 0.56 keV, respectively (see Table 10.6). Initial trial fits were made with a free LMC absorption column. They consistently returned 0 cm^{-2} as the best-fit value for N_H , although the 90 % C.L. upper limit of $2.1 \times 10^{21} \text{ cm}^{-2}$ for N_H is quite high. In the rest of the analysis I fixed N_H to 0 cm^{-2} (see the caveat on N_H presented above for MCSNR J0508–6830).

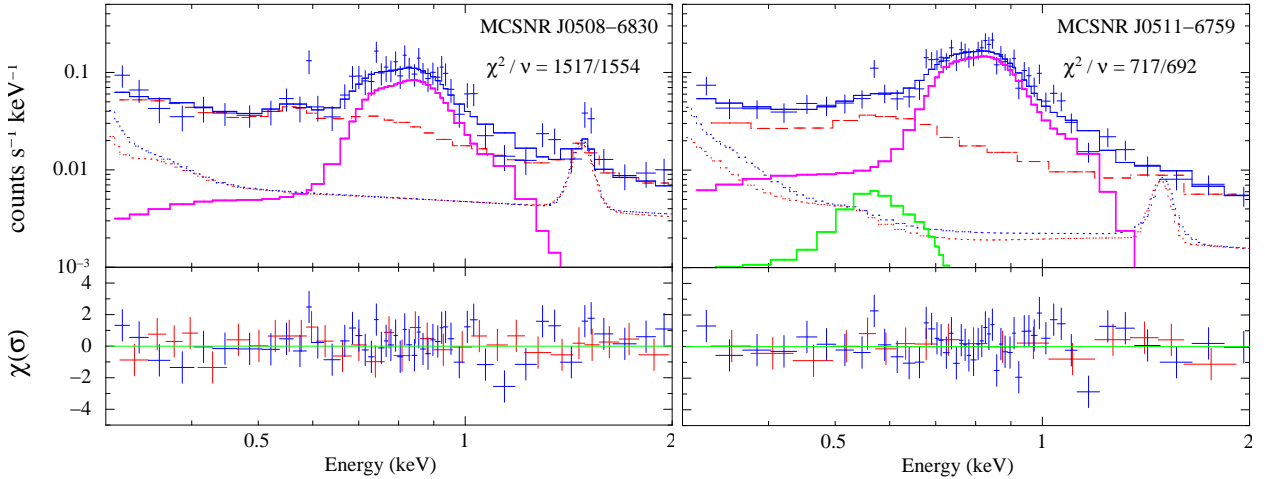


FIGURE 10.12 – X-ray spectra of the MCSNR J0508–6830 (left) and MCSNR J0511–6759 (right). Data extracted from the source region are shown by blue data points, with the total (source+background) model as the solid blue line. The red and blue dash-dotted lines show the instrumental background model measured in the background and source extraction regions, respectively. The X-ray+instrumental background model is shown by the dashed red line. For clarity I do not show the data points from the background extraction region but only the residuals of the fit (red points in the lower panels).

Again, no oxygen was formally required, whilst an Fe abundance greatly in excess of the solar value was needed. For the same reason as for MCSNR J0508–6830 I investigated the iron-rich nature of the source with a multi-component plasma analysis (Sect. 10.2.3.C).

The ionisation age τ in the plane-parallel shock model was high (best-fit value of $8.7 \times 10^{11} \text{ s cm}^{-3}$). Its high 90 % C.L. lower limit ($1.6 \times 10^{11} \text{ s cm}^{-3}$) and its unconstrained upper limit suggests that the X-ray emitting plasma in MCSNR J0511–6759 is close to or at collisional ionisation equilibrium.

MCSNR J0508–6902 : The spectral analysis of this remnant was done in two steps. *i)* The shell spectrum was first modelled alone. *ii)* The best-fit model of the shell was included in the analysis of the central region spectrum, to account for the shell emission seen in projection.

i) Initial shell fits with the *vsedov* model resulted in best-fitting values for kT_s and kT_{es} (the mean and post-shock electron temperature, respectively) to be equal within their 90 % confidence interval and thus were constrained to be the same, as done for DEM L205 (see Sect. 10.1). Due to the relatively poor count statistics, metal abundances for the shell emission were fixed at their average LMC values (≈ 0.5 solar, Russell & Dopita 1992). With a reduced $\chi^2_v = 1.21$, the *vsedov* model provides an acceptable fit to the shell spectrum. The LMC column density tended to zero in all fits, with a 90 % C.L. upper limit of $8 \times 10^{20} \text{ cm}^{-2}$. LMC N_H was fixed to 0 cm^{-2} in the rest of the analysis. The best-fit temperature is $kT_s = kT_{es} = 0.41 \left(\begin{smallmatrix} +0.05 \\ -0.06 \end{smallmatrix} \right) \text{ keV}$, a value consistent with other large LMC SNRs (e. g. Williams et al. 2004; Grondin et al. 2012) as well as the (similarly looking, see Sect. 10.2.4) SNRs DEM L238 and DEM L249 (Borkowski et al. 2006a). The high ionisation age indicates that the plasma is in ionisation equilibrium. The absorption-corrected X-ray luminosity of the shell is $L_X = 4.5 \times 10^{34} \text{ erg s}^{-1}$ between 0.3 keV and 5 keV. This also includes the shell emission in the central region (see below). The spectrum of the shell is shown in Fig. 10.13 (left) with the best-fit Sedov model (parameters listed in Table 10.6).

Using the fit results one can further estimate physical parameters using the Sedov self-similar model (Sect. 5) and the strong shock approximation (Sect. 3). From the X-ray temperature and eq. 3.14, the shock velocity is $v_s = 572(\pm 36) \text{ km s}^{-1}$. The similarity solution $v_s = (2R)/(5t_{\text{dyn}})$ yields a range in dynamical age t_{dyn} of 20 kyr – 25 kyr.

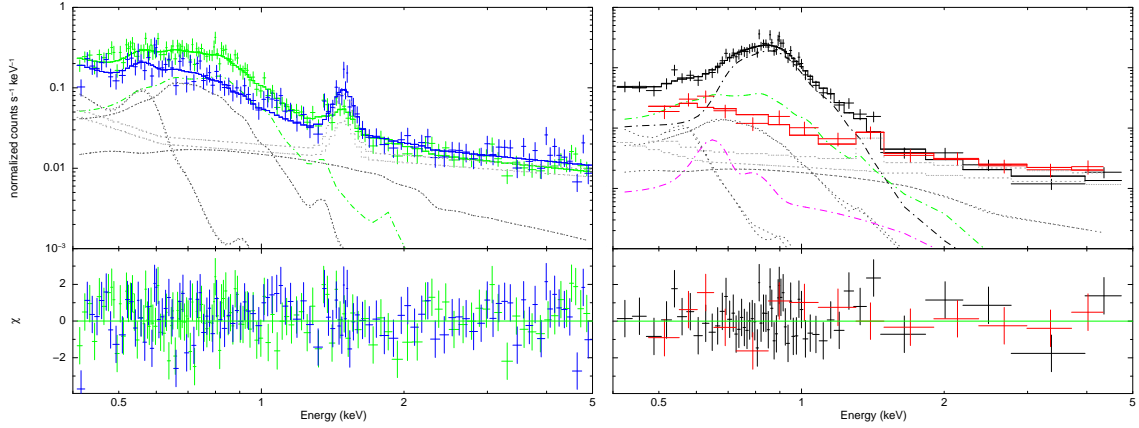


FIGURE 10.13 – X-ray spectrum of MCSNR J0508–6902, extracted from the shell (left) and central region (right) and associated backgrounds. The shell spectrum is shown by the green points, the shell background in blue, the central spectrum in black, and the central background in red. The best-fit model for each spectrum (described in Sects. 10.2.3.B & 10.2.3.C) is represented by the solid lines of matching colour. The light grey and dark grey dotted lines indicate the particle-induced and astrophysical background components, respectively. In both panels the shell emission is represented by the green dash-dotted line. The black and magenta dash-dotted lines in the central spectrum show the pure Fe and pure O component, respectively. (Figures prepared by Dr. Patrick Kavanagh.)

The normalisation of the *vsedov* model is proportional to the volume emission measure $\int n_e n_H dV$, which can be rewritten as a function of the pre-shock ambient hydrogen density $n_{H,0}$:

$$\text{EM} = \left(\frac{n_e}{n_H}\right) n_{H,0}^2 \frac{4\pi}{3} R_s^3 \int_0^1 3 \left(\frac{\rho(r)}{\rho_0}\right)^2 r^2 dr \quad (10.7)$$

where R_s is the shock radius and r the normalised radius (R/R_s). To evaluate the integral one can use the approximation of Kahn (1975) for the normalised mass distribution in the Sedov model (his equation 7.19); numerical integration then gives ≈ 2.07 . MCSNR J0508–6902 is not spherically symmetric since the semi-major and semi-minor axes are 37 pc and 28.5 pc, respectively. Taking these semi-major and semi-minor axes as the first and second semi-principal axes of an ellipsoid and assuming that the third semi-principal axis is in the range 28.5 pc – 37 pc, I determine the volume (V) limits for the remnant and their corresponding effective shock radii (R_{seff}) to be $(3.7 - 4.8) \times 10^{60} \text{ cm}^3$ and 31.1 pc – 33.9 pc, respectively. With these values, the best-fit EM (Table 10.6), and $n_e/n_H \approx 1.2$ (for a fully ionised, 0.5 Z_\odot plasma), eq. 10.7 yields $n_{H,0} = (1.5 - 2.8) \times 10^{-2} \text{ cm}^{-3}$. Since the pre-shock density of nuclei is given as $n_0 \approx 1.1 n_{H,0}$, it follows that $n_0 = (1.7 - 3.1) \times 10^{-2} \text{ cm}^{-3}$. That is, the SNR is expanding into a fairly rarefied environment.

One can then estimate the mass swept-up by the SNR shock as $M = (4\pi/3) R_s^3 1.4 m_p n_0 = (32 - 62) M_\odot$. Finally, the explosion energy is given by $E_0 = 1.4 m_p n_0 R_s^5 / 2.02 t_{\text{dyn}}^2$, yielding $E_0 = (0.37 - 0.75) \times 10^{51} \text{ erg}$. The physical properties of MCSNR J0508–6902 are summarised in Table 10.4.

ii) The shell contribution to the central region spectrum was considered by including the shell best-fit model of Table 10.6. I fixed all the shell parameters except the normalisation. Doing so, I determine that 13% to 28% of the total shell emission contributes to the central spectrum. In Fig. 10.13 (right) I show the X-ray spectrum from the central region. On top of the shell emission (green dot-dashed line), there is a prominent Fe L-shell bump ($\sim 0.7 \text{ keV}$ to $\sim 0.9 \text{ keV}$), very much like in MCSNR J0508–6830 and MCSNR J0511–6759.

TABLE 10.4 – Physical properties of MCSNR J0508–6902 derived from the Sedov model.

n_0 (10^{-2} cm^{-3})	v_s km s^{-1}	t_{dyn} (10^3 yr)	M (M_\odot)	E_0 (10^{51} erg)
1.7 – 3.1	572 ± 36	20 – 25	32 – 62	0.37 – 0.75

Initially fitting the interior emission with a CIE model at LMC abundances resulted in a very poor fit (reduced $\chi^2 > 2$). Large residuals remained around 0.9 keV due to Fe L-shell emission lines. Allowing the Fe abundance to vary resolve most that issue. A best-fit (reduced $\chi^2 = 1.08$) is obtained for $kT = 0.76 \pm 0.03$ keV and the iron abundance $Z_{\text{Fe}} > 2.01 Z_{\odot}$. The lower limit of Z_{Fe} is already four times higher than the average LMC value, clearly indicating an iron-enrichment of the central X-ray emitting plasma. When freed, other metal abundances such as oxygen did not improve the fits and were poorly constrained.

10.2.3. C. Multi-component plasma fits

The X-ray emission of the three new remnants presently described is dominated by iron, with a possible minimal contribution from oxygen. To investigate this further, I modelled these sources with a multi-component plasma, each component representing emission from a single element. This approach has been used in the past and allows, under some assumptions, to calculate the mass of the supernova nucleosynthesis products (e.g. Hughes et al. 2003; Kosenko et al. 2010).

As initial spectral fits showed (Sect. 10.2.3. B), the interior plasma is likely to be in CIE. Upon trying NEI models, I obtained only high ionisation age $\sim 10^{13}$ s cm^{-3} , suggestive indeed of a plasma in CIE. Consequently, I later only used *vap*ec models. The abundance of each element in its respective component was set to 10^9 the solar values, thus making sure I approximate a pure-metal component. Only plasmas composed of Fe and O needed to be included in the fit. The temperature of the oxygen plasma (kT_{O}) was not well constrained, given the very small contribution of this element. Therefore, I tied the temperature of this component to that of the Fe component. This is expected if these two elements are co-spatial. I also tried fits with kT_{O} fixed at the peak emissivity temperature of the strongest oxygen lines in the 0.3 keV – 1 keV range (i.e. $kT_{\text{O}} = 0.17$ keV). This turned out to have very little influence on the results, which I give in Table 10.5. The fits returned a zero normalisation of the oxygen component in both MCSNR J0508–6830 and MCSNR J0511–6759, showing the minimal contribution of O in the emission of these two remnants, as expected from the spectral analyses described above. The normalisation of the oxygen component in MCSNR J0508–6902 is consistent with 0 at the 90 % confidence level, but is formally non-zero.

The normalisation of each component is proportional to the emission measure EM_X (given in terms of $n_e n_H V$ for each component X). Therefore, given a knowledge of the number ratios n_X/n_H and n_e/n_X for an element X , I can derive the **mass** M_X of that element produced by the supernova using :

$$M_X = \sqrt{\frac{V_X \text{EM} (n_X/n_H)}{(n_e/n_X)}} m_U A_X \quad (10.8)$$

(e.g. Kosenko et al. 2010), where m_U is the atomic mass unit. A_X is the atomic mass of element X and V_X the volume it occupies. For MCSNR J0511–6759 I assumed a spherical morphology with a radius of 13.5 pc (Sect. 10.2.3. A), and therefore $V_X = 3 \times 10^{59}$ cm^3 . The volume of MCSNR J0508–6830 is derived assuming an ellipsoidal morphology, with semi-major and minor axes of 16.7 pc and 13.1 pc. As a third semi-axis I took the average of the two others (i.e. 14.9 pc), yielding $V_X = 4 \times 10^{59}$ cm^3 . The same assumption is made for MCSNR J0508–6902, which gives $V_X = 4.6 \times 10^{59}$ cm^3 . These two volumes would be 13% higher or lower in the case of an oblate or prolate morphology, respectively.

The main uncertainty for estimating M_X is in the ratio of electron-to-ion n_e/n_X . I follow the prescription of Hughes et al. (2003) and consider two limiting cases. In the first one (case I) the emission originates purely from ejecta, without admixture from hydrogen. Considering that Fe dominates the ejecta, with only minimal contribution from oxygen to the pool of electrons, this means n_e/n_{Fe} is only set by the average ionisation state of iron. At this temperature I take $n_e/n_{\text{Fe}} = 18.3$ (Shull & van Steenberg 1982). The second physically plausible case (case II) assumes that a similar mass of H has been mixed with the iron ejecta. Therefore, there are 56 H atoms (contributing each with one electron) per Fe atom, and n_e/n_{Fe} is 74.3. I give the best-fit parameters and the derived iron mass in both cases in Table 10.5.

TABLE 10.5 – Results of the multi-component plasma fits for the iron-rich SNRs.

Fit parameter	J0508–6830	J0508–6902	J0511–6759
$kT_{\text{Fe,O}}$ (keV)	0.71 ± 0.06	0.78 ± 0.03	$0.65^{+0.06}_{-0.03}$
$\text{EM}_{\text{Fe}} \times n_{\text{Fe}}/n_{\text{H}}$ (10^{57} cm^{-3})	0.8 ± 0.1	2.1 ± 0.1	1.5 ± 0.1
$\text{EM}_{\text{O}} \times n_{\text{O}}/n_{\text{H}}$ (10^{57} cm^{-3})	$0 (< 0.7)$	$0.6 (< 2.0)$	$0 (< 0.8)$
χ^2/ν	1516.99/1554	66.49/64	717.46/692
V (10^{59} cm^3)	4	4.6	3
M_{Fe} (M_{\odot} , case I)	1.03 ± 0.08	1.78 ± 0.06	1.19 ± 0.05
M_{Fe} (M_{\odot} , case II)	0.51 ± 0.04	0.88 ± 0.03	0.59 ± 0.03

Notes. The derived mass of iron is given for two level of H admixture in the ejecta, as described in Sect. 10.2.3.C.

10.2.4. Discussion

The SNRs described in this section are remarkable in their morphological and chemical structure. They are particularly notable due to the centrally located iron-rich plasma, which betrays their type Ia SN origin. They join the sample of MC SNRs with a faint, soft X-ray shell containing iron-rich hot gas (possibly) in collisional equilibrium. See Sect. 11.3.2, where I discussed these sources in a broader context, comparing them with all other type Ia SNRs. The central location of most of the X-ray emission is reminiscent of the mixed-morphology SNRs classification (MMSNRs, [Rho & Petre 1998](#); [Lazendic & Slane 2006](#)), which has been applied only to Galactic remnants. The MMSNRs are usually close to, and interacting with, a molecular cloud environment, showing OH masers. It means that the MMSNRs very likely have massive progenitors and are not type Ia SNRs, as opposed to the three SNRs described here.

They are likely more evolved versions of the very similar remnants DEM L238 and DEM L249. Indeed, the shell emission of MCSNR J0508–6902 is fainter compared to that of its central iron-rich plasma. The age derived from the Sedov model also point to a remnant older than DEM L238 and DEM L249 ([Borkowski et al. 2006a](#)). On the other hand, the main difference with MCSNR J0508–6830 and MCSNR J0511–6759 is the absence in the data of a detected X-ray shell, whilst very dim [S II] emission still indicates the locations of the furthest advance of the SN blast wave. This echoes other cases in the SMC, namely DEM S128, IKT 5, and IKT 25 ([van der Heyden et al. 2004](#)). The faint sulphur emission and lack of soft X-rays from the shells of MCSNR J0508–6830 and MCSNR J0511–6759 indicate that they reached the point when radiative cooling caused the shells to become either too cool to emit X-rays, or too faint to be detected in the data available. Another possibility is a compositional difference, with Fe in centre and more normal composition outside which would make for a high emissivity contrast at a given thermal pressure. If the temperature in the shell is that low, one might expect [O IV] emission at $25.9 \mu\text{m}$. The detection of faint filament in the MIPS image, at the south-eastern rim of the [S II] shell of MCSNR J0511–6759, lends support to that scenario.

As discussed in [Borkowski et al. \(2006a\)](#), the long ionisation ages of the iron-rich central plasma is puzzling given the type Ia classification of these remnants, because it requires higher densities in the centre than expected from standard type Ia SN models. This claim is so far limited by the low statistics available. Indeed, if the emission is mostly from a single element, and possibly dominated by a single ion (e. g. Fe XVII), it is hard to determine simultaneously kT and τ , because fits are driven to CIE (large τ) at the peak emissivity temperature of the dominating species. Deeper observations at higher spectral resolution will allow to verify this claim. A possibility for the origin of the long central ionisation ages could be in pre-explosion effects of the progenitor on its circumstellar medium (CSM). Several type Ia progenitor candidates are relatively massive (main-sequence) stars ($\sim 3.5 - 8 M_{\odot}$), capable of producing denser CSM, via ejection of their stellar envelope prior to the SN event.

TABLE 10.6 – X-ray spectral results for new LMC SNRs discovered in the XMM-Newton survey.

Model	N_H Gal (10^{20} cm $^{-2}$)	N_H LMC (10^{20} cm $^{-2}$)	kT (keV)	τ (10^{12} s cm $^{-3}$)	EM (10^{57} cm $^{-3}$)	O/H	Fe/H	χ^2 / dof	$L_X^{(a)}$ (10^{34} erg s $^{-1}$)
MCSNR J0508–6830									
<i>vap</i> ec (LMC abund.)	6.4	0.6 (< 18)	$0.66^{+0.06}_{-0.08}$	—	$1.14^{+0.4}_{-0.2}$	0.46	0.63	1508.92 / 1554	1.29
<i>vap</i> ec (free abund.)	6.4	0	$0.71^{+0.06}_{-0.07}$	—	$0.001^{+0.7}_{-0.0004}$	0	> 1.1 ^(b)	1488.34 / 1554	0.90
<i>vpsh</i> ock (free abund.)	6.4	0	$0.60^{+0.11}_{-0.05}$	2.75 (> 0.47)	$0.28^{+1.8}_{-0.24}$	0	$4.12^{+11.21}_{-2.46}$	1519.42 / 1553	0.93
MCSNR J0511–6759									
<i>vap</i> ec (LMC abund.)	5.8	0 (< 21)	$0.62^{+0.05}_{-0.04}$	—	1.9 ± 0.2	0.46	0.63	732.85 / 693	2.16
<i>vap</i> ec (free abund.)	5.8	0	$0.65^{+0.05}_{-0.04}$	—	$0.12^{+0.8}_{-0.10}$	0	$11.4^{+96.8}_{-6.7}$	707.52 / 692	1.56
<i>vpsh</i> ock (free abund.)	5.8	0	$0.57^{+0.06}_{-0.05}$	0.75 (> 0.18)	$0.60^{+0.68}_{-0.53}$	0	$3.19^{+3.41}_{-1.78}$	700.96 / 691	1.74
MCSNR J0508–6902 (shell emission)									
<i>vsed</i> ov (LMC abund.)	7	0 (< 8)	$0.41^{+0.05}_{-0.06}$	$2.70^{+6.92}_{-1.73}$	$4.75^{+2.47}_{-2.21}$	0.46	0.63	267.08/219	4.5
MCSNR J0514–6840									
<i>vap</i> ec (LMC abund.)	5.9	0 (< 0.13)	0.19 ± 0.01	—	10.2 ± 0.7	0.46	0.63	8041.68 / 7960	3.42
<i>vap</i> ec (free abund.)	5.9	$0.6^{+0.3}_{-0.2}$	0.19 ± 0.01	—	$17.8^{+1.6}_{-1.5}$	$0.30^{+0.04}_{-0.03}$	$0.36^{+0.26}_{-0.20}$	7979.80 / 7958	3.81
<i>vpsh</i> ock (free abund.)	5.9	0 (< 0.09)	0.30 ± 0.01	$0.26^{+0.06}_{-0.05}$	5.1 ± 0.3	0.28 ± 0.03	$0.38^{+0.13}_{-0.11}$	8005.27 / 7957	4.01
<i>vsed</i> ov (free abund.)	5.9	0 (< 0.07)	$0.18 - 0.25$ ^(d)	$0.3 - 6$ ^(d)	$5.11 - 11.2$	0.36 ± 0.05	0.34 ± 0.10	7975.11/7958	4.21
MCSNR J0517–6759									
<i>2vap</i> ec (LMC abund.):									
Cool component	5.8	3.5	< 0.14	—	112^{+72}_{-90}	0.46	0.63	2558.92 / 2547	0.47
Hot component	5.8	0	$0.59^{+0.05}_{-0.04}$	—	$1.85^{+0.16}_{-0.20}$				1.96

Notes. Best-fit parameters of the various source models (details are in Sect. 10.2.3. B). Uncertainties are given at the 90 % confidence level. Parameters with no uncertainties were frozen. The abundances of O and Fe are given relative to the solar values as listed in Wilms et al. (2000). The χ^2 and associated degrees of freedom (dof) are also listed. ^(a) Absorbed luminosity in the 0.3 keV – 5 keV band. ^(b) 3σ lower limit.

TABLE 10.7 – XMM-Newton log for observations of new SNRs discovered in the LMC survey.

MCSNR	Observation ID	Obs. start date	Exposure time (ks) ^(a)		Off-axis angle ^(b)
			pn	M1/M2	
J0508–6830	0690742401	2012 Sep 09	26.0	27.2	10.9
J0511–6759	0690742201	2012 Aug 06	25.1	28.9	7.9
J0508–6902	0651880201	2010 May 02	8.7	10.0	on-axis
	0690752001	2012 Sep 22	24.9	26.5	on-axis
J0514–6840	0690742601	2012 Aug 12	27.3	28.0	10.0
	0690742701	2012 Nov 09	29.5	33.6	13.4
J0517–6759	0690741101	2012 Jun 25	24.6	26.2	4.1

Notes. ^(a) Exposure times after removal of high background intervals. ^(b) Angle in arcmin between the aiming point of the observations and the centre of the X-ray source (as defined in Sect. 10.2.3. A).

10.3. MCSNR J0514–6840 and J0517–6759: the role of the environment in shaping supernova remnants

THIS SECTION reports on two additional SNRs unveiled by observations of the *XMM-Newton* survey. Even though they display some features in other parts of the EM spectrum (in particular optical emission lines), the X-ray emission allows a secure classification. At all wavelengths at which they are detected, the local environment plays a key role in their observational appearance. I also present evidence that one of these remnant is close to and interacting with a molecular cloud, suggesting a massive progenitor. The results below were first published in [BKM14](#). Note that most of the description of the data and analysis are the same as for MCSNR J0508–6830 and MCSNR J0511–6759 (previous section).

10.3.1. Source identification and observations

The two remnants described in this section were covered by the *XMM-Newton* survey and identified as bona-fide SNRs according to the criteria described in Sect. 5. Details of the X-ray observations are summarised in Table 10.7. The exact same set of multiwavelength data as for MCSNR J0508–6830 and MCSNR J0511–6759 was used, namely ATCA and Parkes observations at radio wavelengths; continuum-subtracted MCELS images for the study of optical emission lines; and *Spitzer*'s MIPS image (at 24 μm) in the infrared. Keeping the nomenclature consistent, I hereafter refer to the sources as MCSNR J0514–6840 and MCSNR J0517–6759, based on their position.

10.3.2. Data analysis

The X-ray data were treated in exactly the same way as described in Sects. 8 & 10.2. In the case of MCSNR J0514–6840, two observations included the source in the field of view, and I merged images from the two datasets together. I used a circular extraction region centred on the remnant to select vignetting-weighted single- and double-pixel events and build its energy spectrum. Because of the unusual, roughly triangular morphology of MCSNR J0517–6759 (see Sect. 10.3.3. A), I manually defined a polygonal region following this remnant's X-ray emission. Background spectra were extracted from adjacent regions. Detected point sources were excluded from the extraction regions. As for MCSNR J0508–6830 and MCSNR J0511–6759, only EPIC-pn spectra were useful, and I disregarded the MOS spectra.

10.3.3. Results

10.3.3. A. Multi-wavelength morphology

MCSNR J0514–6840: A multiwavelength view of the remnant is shown in Fig. 10.14. In X-rays, this source exhibits a rather soft colour, being dominated by emission in the 0.3 keV – 0.7 keV band. Globally, the morphology is spherically symmetric, although the southern limb is slightly brighter than the northern one. A darker lane also appears to separate the two halves along the east-west equator. Analysis of the X-ray spectrum provides clues to the origin of these features (Sect. 10.3.3. B). The position and size of the remnant were obtained from the X-ray image in the same fashion as for MCSNR J0511–6759. I found a centre located at RA = 05^h 14^m 15.5^s, DEC = –68° 40^m 14^s, and a radius of 1.83' \pm 0.12', i.e. 26.5(\pm 1.7) pc.

Optical emission is present, correlating with the southern edge of the X-ray shell (Fig. 10.14, top right). Both H α and [S II] lines are detected in emission: though the [S II]/H α ratio map is still noisy due to the very low diffuse emission of that region, the ratio at the position of the remnant is clearly in excess of 0.6 (Fig. 10.14, bottom left), indicative of shock-excitation. In addition, [O III] emission is present, outlining the edges of the H α and [S II]-emitting regions. The strong [O III] emission suggests partially radiative shocks: when the shock age τ is decreased, the strength of the [O III] line (relative to Balmer lines) increases, whilst

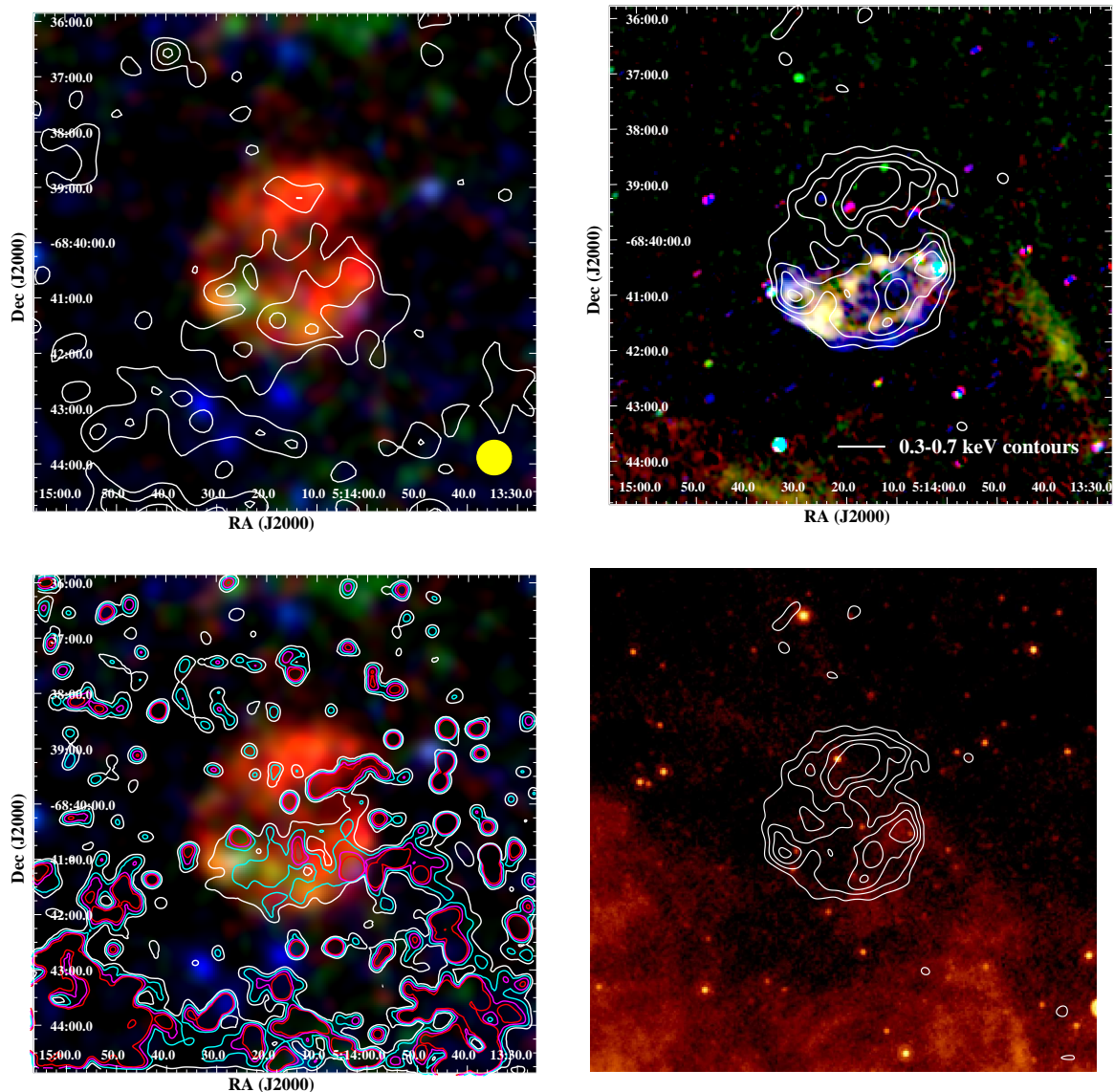


FIGURE 10.14 – Same as Fig. 10.8 for MCSNR J0514–6840. On the XMM-Newton image (top left) the 4800 MHz contours are shown in white. Levels are at 1.5, 2, 2.5, and 3 mJy beam⁻¹. The yellow disc in the lower right corner indicates the half-power beamwidth of 35". The X-ray contours used on the optical image (top right) are from the soft X-ray image. On the MIPS image (bottom right) the X-ray contours are used to locate the position of the remnant, rather than [S II]/H α .

that of [S II] decreases (e. g. [Dopita et al. 2012](#), and references therein). The location of the strong [O III] emission probably traces regions with lower densities and/or shocked more recently.

MCSNR J0514–6840 is clearly detected at radio frequencies. At 4800 MHz, it looks somewhat like the optical line images with the brightest emission on the southern side (see contours on Fig. 10.14, top right). The X-ray image has a more circular outline. The 1370 MHz radio image also seems to have a rather sharp north-south gradient across the whole image near the top of the SNR. The integrated radio flux densities of this SNR are quite uncertain due to the low intensity emission and the relatively high r.m.s. noise surrounding this remnant in the radio images. Consequently, it is difficult to obtain an accurate spectral index. However, we estimate that between $\nu = 843$ MHz and $\nu = 4800$ MHz the remnant has a rather flat

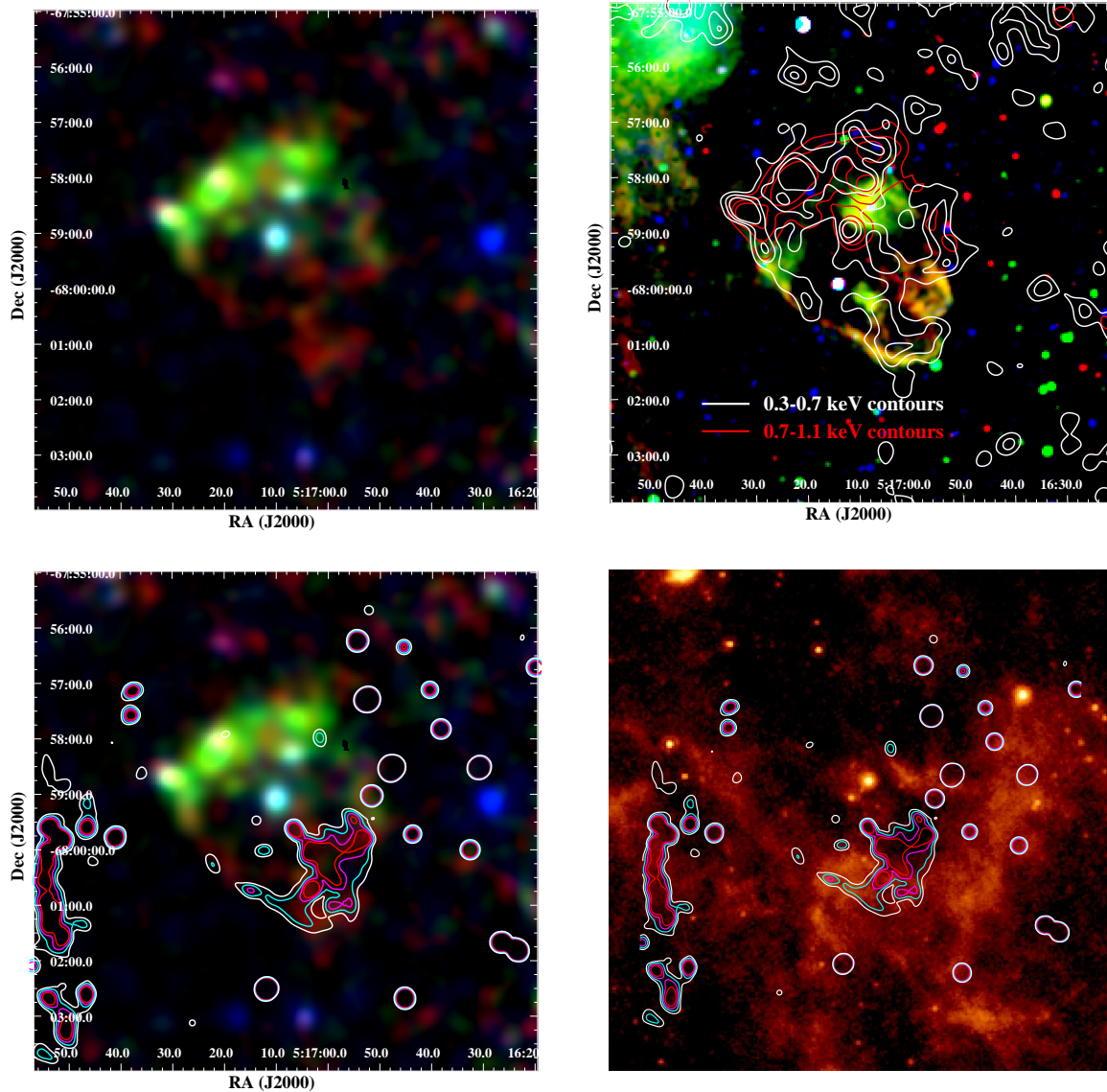


FIGURE 10.15 – Same as Fig. 10.8 for MCSNR J0517–6759. On the optical image (top right) I show the soft band X-ray contours in white and the medium band X-ray contours in red.

spectrum with a spectral index α between -0.5 and 0 . The flatter radio-continuum spectrum is indicative of an older remnant.

There is no infrared emission that can be clearly linked to the remnant. Bright diffuse emission is seen towards the south of the remnant (Fig. 10.14, bottom right), indicating a denser/dustier environment in that direction. I explore this further in Sect. 10.3.4.

MCSNR J0517–6759: The source exhibits a rather atypical morphology in X-rays, that can be described as “triangular” (Fig. 10.15). It is elongated along the NE–SW axis with a largest extent of $\sim 5.4'$ (78.3 pc). The NE side of the triangle is brighter than the rest of the remnant and extends $\sim 3.5'$ (50.8 pc) along the SE–NW direction. This NE “bar” includes all the flux in the medium energy band, whilst the fainter SW “tip” appears softer. As nominal location of the remnant I took the incentre of the triangle delineating the X-ray emission, which yields RA = $05^{\text{h}} 17^{\text{m}} 10.2^{\text{s}}$, DEC = $-67^{\circ} 59^{\text{m}} 03^{\text{s}}$.

[S II] and H α lines are detected in the SW of the remnant, closely following the “tip” of the X-ray emission, with strong [S II]/H α ratios (0.6–1.2, see Fig. 10.15 bottom left). The brighter and harder X-ray “bar” lacks such optical emission. [O III] line emission is not observed anywhere in this remnant.

The presence of an X-ray point source close to the geometrical centre of MCSNR J0517–6759 is evident in the image (Fig. 10.15). I identified an infrared/optical counterpart 2.4'' away from the X-ray source, i.e. well consistent with the typical position uncertainty of XMM-Newton. The counterpart is identified as SAGE J051710.30-675900.9 in the *Spitzer* catalogue of the LMC (Meixner et al. 2006). Based on its mid-IR colours, it was classified as an active galactic nucleus (AGN) candidate by Kozłowski & Kochanek (2009). Kozłowski et al. (2013) later on spectroscopically confirmed the source as a $z = 0.427$ AGN. Therefore, I conclude that the central point source in MCSNR J0517–6759 is a background AGN rather than a compact stellar remnant. I discuss later the morphology in greater detail (Sect. 10.3.4), in light of the X-ray spectroscopy results (Sect. 10.3.3. B).

The radio image of MCSNR J0517–6759 only shows weak, compact emission from the central point source, consistent with the AGN classification discussed just above. Bright diffuse 24 μm emission is observed at the south-west of MCSNR J0517–6759. Infrared light intrinsically emitted by the remnant is however likely to be masked by the emission of a nearby molecular cloud (as described below). Besides this, two weak filaments outline the eastern and western rims of the remnant. They are presented and discussed in greater detail in Sect. 10.3.4.

10.3.3. B. X-ray spectroscopy

MCSNR J0514–6840: Spectra from the two observations of the source were fit simultaneously. The parameters of the SNR component in both spectra were tied together. The astrophysical background components also shared the same parameters, allowing only for a constant factor between the two sets of spectra. Only the (detector position-dependent) instrumental background and (time-dependent) SPC components had different parameters for each observation.

From the first fits using one-temperature CIE and NEI models, good results were obtained for relatively soft temperatures of 0.2 keV – 0.4 keV, depending on the model used (see Table 10.6). Using a Sedov model resulted in a minor statistical improvement, but allows to estimate physical properties averaged over the remnant (as done below). When O and Fe abundances were let free to vary, the fits improved significantly (e.g. $\chi^2/\nu = 7979.80/7958$ instead of $\chi^2/\nu = 8041.68/7960$). However, the best-fit values for O/O $_{\odot}$ and Fe/Fe $_{\odot}$ were both only reduced by a factor of ~ 0.6 compared to the value given in Russell & Dopita (1992), being rather consistent with those from Hughes et al. (1998), whilst the ratio O/Fe remained well within the uncertainties of the LMC ISM value given in the two latter references. This indicates that the SN ejecta have no significant contribution to the X-ray spectrum, which is dominated by the swept-up ISM. This justifies *a posteriori* that the remnant is indeed well in the Sedov phase. It also means that no typing of the SN progenitor can be achieved through the spectral analysis.

I show the X-ray spectrum fitted with the Sedov model in Fig. 10.16. The formal best-fit parameters with this model are listed in Table 10.6. The best-fit temperature is rather low and the ionisation age rather high ($\sim 2 \times 10^{12}$ s cm $^{-3}$). These two parameters are however relatively poorly constrained. I investigated the kT vs. τ parameter space: equally acceptable fits are allowed both for low temperatures (~ 0.2 keV) with high ionisation ages ($\sim 2 \times 10^{12}$ s cm $^{-3}$), and for higher temperatures (~ 0.25 keV – 0.3 keV) with lower ionisation ages (a few 10^{11} s cm $^{-3}$). This degeneracy is explained to some extent to the statistics available: only lines from a limited set of elements (O, Fe, and possibly Ne) are detected and can be used to constrain those parameters. Another contributor is possibly that the assumption of the Sedov model of a uniform ambient medium does not hold, resulting in asymmetric evolution and varying plasma conditions. The presence of such an inhomogeneous ISM is supported by the optical image, as only the southern edge of the remnant emits lines; as for the X-ray image, the remnant is (marginally) brighter in the southern half.

Guided by the morphology of MCSNR J0514–6840 (Sect. 10.3.3. A, Fig. 10.14), I extracted spectra from

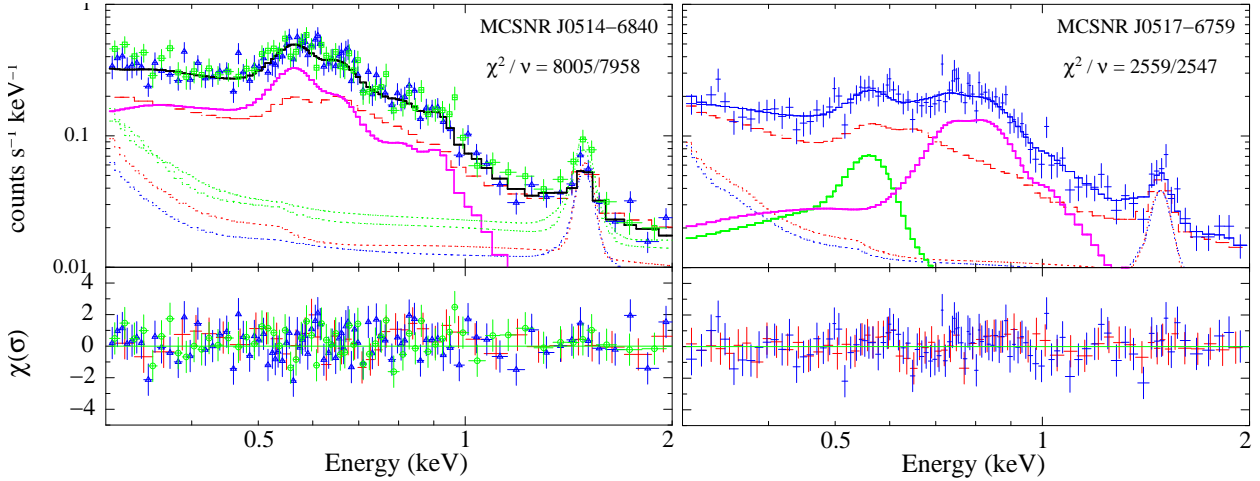


FIGURE 10.16 – X-ray spectra of the MCSNR J0514–6840 (left) and MCSNR J0517–6759 (right). Same colour coding as in Fig. 10.12. For MCSNR J0514–6840, spectra from two overlapping observations are shown by the green squares and blue triangles. The thick magenta lines show the source emission component. For MCSNR J0517–6759, the two components of the best-fit model are shown by the green and magenta solid lines (see text for details).

the southern and northern halves, in order to look for possible plasma properties or column density (or both) variations across the remnant. In all this analysis, I assumed that the ISM have a homogeneous chemical composition and fixed abundances at their best-fit values. I divided the SNR along the “dark lane” that crosses the remnant’s equator. First using CIE models, I could constrain the temperature and N_H of both spectra, despite the degraded statistics. I found that they had similar temperature (0.18 keV – 0.22 keV), but that N_H was significantly higher in the south than in the north ($\sim 1.3 \times 10^{21} \text{ cm}^{-2}$ vs. $\sim 0.3 \times 10^{21} \text{ cm}^{-2}$). Using either the *vpshock* or Sedov model, I found (roughly five times) higher ionisation ages in the south spectrum as compared to the north, which is again an indication of an inhomogeneous ISM. More specifically, it indicates a density gradient increasing southwards. I interpret these results as environmental effects in Sect. 10.3.4.

Assuming the Sedov self-similar solution for MCSNR J0514–6840, I used the same equations as in Sect. 10.2.3.B to calculate its properties. Given the issues discussed in the paragraph above, there are concerns that this model, which assumes a spherical symmetry and homogeneous ISM, might yield incorrect results. However, using the best-fit parameters from the integrated spectrum as a measure of the properties averaged over the remnant, I can still obtain rough but useful estimates of important numbers (e.g. age, density, etc...). Alternatively, I can compute the physical properties of the remnant with parameters derived when fitting the north and south spectra, and use these as limiting cases.

TABLE 10.8 – Physical properties of MCSNR J0514–6840 derived from the Sedov model.

n_0 (10^{-2} cm^{-3})	v_s km s $^{-1}$	t_{dyn} (10^3 yr)	M (M_\odot)	E_0 (10^{51} erg)
3 – 5	390 – 470	22 – 27	90 – 150	0.2 – 0.5

is $t_{\text{dyn}} = (22 - 27) \text{ kyr}$. The flatter radio-continuum spectrum is consistent with this quite advanced age. The explosion energy, given by $E_0 = 1.4m_p n_0 R_S^5 / 2.02t_{\text{dyn}}^2$, is $E_0 = (0.2 - 0.5) \times 10^{51} \text{ erg}$. The physical properties of MCSNR J0514–6840 are summarised in Table 10.3.3.B.

From eq. 10.7 and given the radius R_S of 26.5 pc for the remnant, I obtain pre-shock densities $n_{H,0} = (0.03 - 0.05) \text{ cm}^{-3}$, using the integrated spectrum. I can then estimate the mass swept-up by the SNR shock as $M = (90 - 150) M_\odot$. Under the strong shock conditions, the shock velocity is estimated to $v_S = (390 - 470) \text{ km s}^{-1}$ (eq. 3.14) and therefore the dynamical age

MCSNR J0517–6759: I started by analysing the integrated spectrum of MCSNR J0517–6759, excluding only the central background AGN. An initial fit with a one-temperature CIE model (*vapec*) with LMC abundances failed to reproduce the spectrum, as indicated by strong residuals. Namely, the “best-fit” model, with $kT \sim 0.5$ keV, could reproduce the Fe L-shell emission (between 0.7 keV and 1.1 keV) but underpredicted the data around 0.5 keV – 0.6 keV (dominated by K lines of O VII) whilst predicting too much flux at 0.6 keV – 0.7 keV (dominated by the O VIII Lyman series). In other words, the temperature constrained by the Fe emission is too high for oxygen. This issue could neither be resolved by using an NEI model, nor by changing the O/Fe abundance balance, because at $kT \sim 0.5$ keV oxygen is mostly in the H-like ionisation stage (Shull & van Steenberg 1982), and simply increasing the O abundance would overproduce ~ 0.65 keV emission even more.

Driven by this result and by the morphological analysis of the source (Sect. 10.3.3. A), I concluded that a two-temperature model was required. I used two *vapec* models with distinct temperatures and absorption columns, but both with LMC abundances. This time I obtained satisfactory fits, with no systematic residuals. The integrated spectrum fitted with this model is shown in Fig. 10.16 (right). Best-fits were obtained with a “hot” ($kT_{\text{hot}} \sim 0.6$ keV) and “cool” ($kT_{\text{cool}} \sim 0.1$ keV) component. The hot component models the Fe and O VIII emission, whilst the low-temperature component accounts for the extra O VII emission. Although the absorption was poorly determined, the “cool” component required a significantly higher N_H ($0.6\text{--}8.3 \times 10^{21} \text{ cm}^{-2}$) than the “hot” one, which returned a zero best fit-value with an upper limit of $1.7 \times 10^{21} \text{ cm}^{-2}$. I chose to fix the absorption for the “hot” component to 0 cm^{-2} , whilst for the low-temperature component I fixed the N_H to $3.5 \times 10^{21} \text{ cm}^{-2}$, as measured from the HI map of Kim et al. (2003). I give the best-fit parameters of this model and the luminosity of both components in Table 10.6.

I then proceeded to apply this model to spectra extracted from various regions of the SNR, namely from the NE “bar” and the SW “tip” (Fig. 10.15). Only normalisations and temperatures of the two components were allowed to change. The best-fit temperatures from the NE and SW spectra were the same as in the integrated spectrum. As expected from the images, I found that $\sim 80\%$ of the flux of the “hot” component originates from the NE “bar”, and $\gtrsim 90\%$ of the “cool” emission is in the SW tip. Scenarios for the origin of this peculiar morphological and spectral features are presented in the Discussion below.

10.3.4. Discussion

MCSNR J0514–6840 displays a subtle variation of X-ray colour along its north-south axis (Fig. 10.14), being harder towards the south. The X-ray spectral analysis in Sect. 10.3.3. B strongly suggests that this is a foreground extinction effect by a varying absorption column density. The higher N_H of the southern half suppresses more soft X-ray flux than in the northern half, resulting in the observed colour gradient.

Direct evidence for the north-south density gradient can be found at longer wavelengths, e.g. in the HI map of Kim et al. (2003, Fig. 10.17). The Spitzer MIPS $24 \mu\text{m}$ image of the neighbourhood of the remnant (Fig. 10.14), which traces cold dust, also shows a dustier environment towards the south. It is reasonable to postulate that the X-ray dark lane seen across the remnant is also a consequence of foreground absorption, although the obscuring structure falls below the spatial resolution of the HI map.

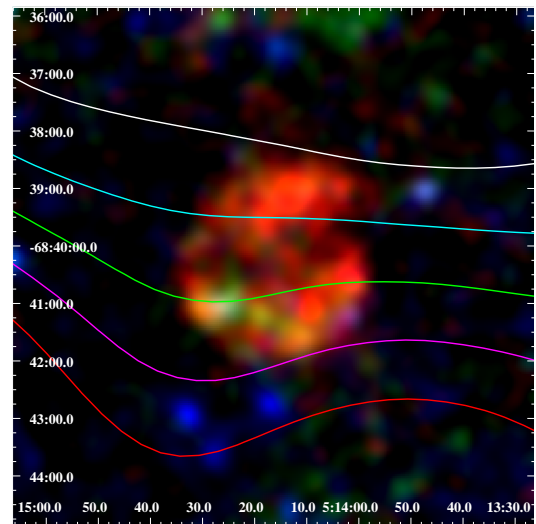


FIGURE 10.17 – X-ray image of MCSNR J0514–6840 overlaid with HI column density contours. Levels shown are 1.5, 1.75, 2.0, 2.25, and 2.5, in units of 10^{21} cm^{-2} , increasing from north to south.

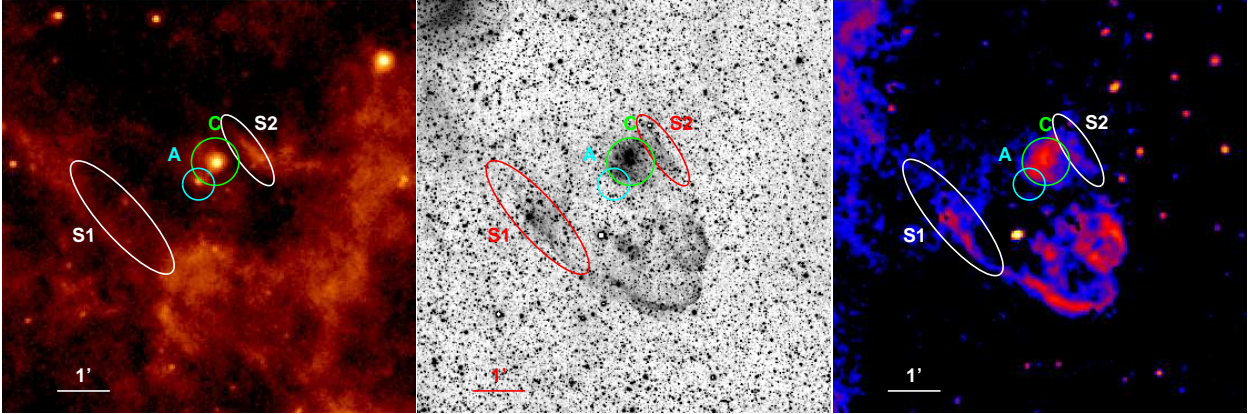


FIGURE 10.18 – Annotated view of MCSNR J0517–6759, as seen at 24 μm (left) and in the lines of $\text{H}\alpha$ (middle) and $[\text{S II}]$ (right). The $\text{H}\alpha$ image has been taken with the Blanco 4-m telescope and has a pixel size of $0.27'' \times 0.27''$ (no continuum has been subtracted). The ellipses (“S1” and “S2”) mark faint filaments (see Sect 10.3.4 for details). The green circle (“C”) shows an unrelated compact H II region, and the cyan circle (“A”, left image) marks the background AGN detected in X-rays and in the mid-IR.

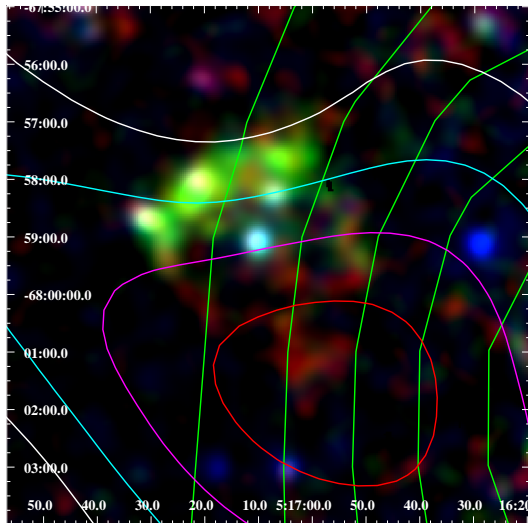


FIGURE 10.19 – Same as Fig. 10.17 for MCSNR J0517–6759, with CO contours from the NANTEN survey added in green. The HI levels shown are 2.0, 2.25, 2.5, and 2.75 (in units of 10^{21} cm^{-2}), in white, cyan, magenta, and red, respectively. CO contours are from 1σ to 5σ , in steps of 1σ ($\approx 0.4 \text{ K km s}^{-1}$), and increase westwards.

optical arc in the SW to the X-ray ridge in the NE. 24 μm emission is also seen in these filaments, possibly originating from compressed, heated dust in the pre-shock region. Since the temperature is so low (almost too cool to emit X-rays), line emission by $[\text{O IV}]$ (at 25.9 μm) is also likely contributing to the MIPS data. Only the X-ray ridge remains not enclosed by longer wavelength emission.

MCSNR J0517–6759 exhibits a more dramatic asymmetry: a cool ($\sim 0.1 \text{ keV}$) X-ray shell is seen in the SW, correlating with relatively bright $\text{H}\alpha$ and $[\text{S II}]$ emission. In the NE, we see a “ridge” of X-ray emission with higher temperature ($\sim 0.6 \text{ keV}$) and little to no co-spatial optical emission.

To provide a better view of the remnant’s emission at various wavelengths, I show in Fig. 10.18 an annotated triptych of MCSNR J0517–6759 as seen at 24 μm and in $\text{H}\alpha$ and $[\text{S II}]$ lines. Mid-IR point sources within the remnant are the background AGN discussed in Sect 10.3.3. A (cyan circle “A” in Fig. 10.18) and a $B = 14.75 \text{ mag}$ star identified as 2MASS J05170629-6758401 (Zaritsky et al. 2004; Skrutskie et al. 2006). The star is likely to simply lie in projection within MCSNR J0517–6759 and to be unrelated to the remnant. However, the ionising radiation of 2MASS J05170629-6758401 is responsible for the compact H II region around the star that is seen in optical lines (green circle “C” in Fig. 10.18) and might hide actual SNR emission. In spite of these interlopers, it is possible to see faint filaments in optical lines, identified by the “S1” and “S2” ellipses in Fig. 10.18, which connect the bright

Again, I conclude that the asymmetry is essentially governed by the inhomogeneous ISM. Several tracers indicate a much denser ISM towards the SW of the remnant, namely :

1. atomic hydrogen (Kim et al. 2003), see contours on Fig. 10.19.
2. CO emission : MCSNR J0517–6759 is located at the NE boundary of the giant molecular cloud (GMC) [FKM2008] LMC N J0516-6807 (Fukui et al. 2008, green contours on Fig. 10.19). However, the NANTEN survey only has moderate resolution (beam size of $2.6'$), and the object is not covered by the MAGMA survey of the LMC (Wong et al. 2011), which has a higher angular resolution ($\sim 45''$). The green contours on Fig. 10.19 are somewhat misleading, as the brightest part of the GMC (i.e. where most of the molecular material resides) is really towards the SW, in the same direction as the elongation of the SNR.
3. Cold dust : Mid-IR emission ($24 \mu\text{m}$) outlines the outer part of the GMC, as can be seen in Fig. 10.18 (left panel), SW of the remnant.

As Lopez (2014) shows, SNRs interacting with molecular clouds are the most elliptical (or elongated) remnants. In the presence of high density inclusions, the SNR blast wave is slowed, and consequently the remnant loses its spherical structure or intrinsic (a)symmetries early in its evolution. MCSNR J0517–6759 perfectly exemplifies the key role of environment on shaping the morphology of evolved SNRs.

The evolution of SNRs expanding in a non-uniform ISM has been investigated by several authors in numerical simulations (e.g. Dohm-Palmer & Jones 1996; Hnatyk & Petruk 1999; Orlando et al. 2009), pointing to the asymmetries that develop along the density gradient. However, these studies dealt with much younger SNRs than MCSNR J0517–6759. In particular, Hnatyk & Petruk (1999) showed the strong X-ray surface brightness contrast that can be produced by density gradients. The brightest emission is expected from the densest region, as L_X scales with the square of the density. This effect likely contributes to the slightly brighter emission in the south of MCSNR J0514–6840, but the *opposite* trend is seen in the case of MCSNR J0517–6759, which shows brighter emission from the lower density region. This can be interpreted as a later-time evolution effect : The *interaction* of the blast wave with the much denser ISM in the SW caused the shock to cool down quickly and to become radiative, leading to a lower level of X-ray emission. The X-rays emitted are also softer and more easily absorbed (especially since N_H is larger in the SW), further reducing the observed X-ray flux. This scenario also explains the stronger optical emission in the SW.

The low-temperature component in the SW is seen essentially as a line complex at $0.5 \text{ keV} - 0.6 \text{ keV}$. There could be charge exchange (CX) emission contribution to that line complex, instead of a purely thermal emission. CX X-ray emission in SNRs has been detected in the Cygnus Loop and Puppis A remnants (Katsuda et al. 2011, 2012). The fraction of CX to the X-ray emission can be enhanced if the hot gas is interacting with denser, neutral gas, as I suggest for MCSNR J0517–6759. However, the data available allow neither to rule out the presence, nor to constrain the contribution of CX to the X-ray emission of the cool SW shell.

The NE part of the blast wave, on the other hand, expands in a more tenuous environment and is seen as the X-ray ridge. The higher shock temperature (or expansion velocity) in the lower density region is consistent with the results of Dohm-Palmer & Jones (1996). As a consequence of the bi-lateral velocity structure, the apparent centre of the remnant shifts away from the actual explosion site, towards the lower-density region. The shifts predicted by Dohm-Palmer & Jones are up to 20% of the apparent radius. The SN that created MCSNR J0517–6759 should conversely have exploded south-west of the apparent geometrical centre, i. e. more embedded within the molecular cloud [FKM2008] LMC N J0516-6807.

An alternative explanation might be that the SNR shock broke out into the lower-density medium in the NE, as suggested for e.g. N11L and N86 (Williams et al. 1999b). However, the higher temperature of the plasma in the breakout region and the current lack of detected optical filaments “streaming” ahead of

the breakout are at odds with this scenario. It is also possible that MCSNR J0517–6759 is similar to e. g. DEM L238, DEM L249, or MCSNR J0508–6902 (Borkowski et al. 2006a, Sect. 10.2): the X-ray “ridge” is actually at the centre of the SNR shell but only the SW part of the shell remained detectable. Unless deeper data are available, any scenario will remain highly speculative and I favour the simpler scenario of “asymmetric evolution” described above.

Analysis of the local stellar environment and SFH (method described in Sect. 11.4) shows that MCSNR J0517–6759 is in a region dominated by a burst of recent (12 Myr) star formation, which favours a core-collapse SN origin. The asymmetric/elongated morphology, likely originating from the interaction with a molecular cloud, with which the remnant is associated, is consistent with this type (Lopez 2014).

11. On the X-ray properties of the rich population of LMC supernova remnants

S ECTION 10 PRESENTED the discovery and study of several new supernova remnants, adding to a substantially large sample of SNRs in the LMC. Analysing this sample as a *population* rather than focusing on individual objects can provide insights on numerous astrophysical processes, such as galactic chemical enrichment, the role of SNRs in feedback and star formation, and the progenitors of SNe.

In this final chapter, I first compile a sample of LMC SNRs (Sect. 11.1). I then analyse the X-ray spectra of all SNRs for which *XMM-Newton* data are available (Sect. 11.2). This allows to characterise the global spectral properties of the sample, search for emission from Fe K or from SN ejecta, and measure the chemical abundance of the ISM gas phase in the LMC. I discuss the specific evolution of SNRs of both types in Sect. 11.3. I apply a new method to tentatively type the complete sample in Sect. 11.4, before discussing the ratio of CC to Ia SNR thus obtained. The X-ray luminosity function of SNRs is compared for galaxies in the Local Group (Sect. 11.5). Finally, I show the (pseudo-) 3D distribution of SNRs in the LMC (Sect. 11.6).

11.1. Compiling a complete sample of LMC SNRs

Obtaining a complete and clean census of LMC remnants is a complex task, for several reasons :

- *Classification* : different authors may use different criteria to classify an object as a definite SNR.
- *Literature size* : with the exception of the early works, the discovery of most new objects was reported in separate papers, building up a vast literature.
- *Nomenclature* : an additional problem related to the previous point is the inconsistencies in the naming convention for LMC SNRs. The common names of many remnants used in the literature, especially those discovered first, are an unruly collection of various surveys and catalogs in specific wavelengths. Some are referred to after the H II complex within which they are located (e. g. “SNR in N44” for MCSNR J0523–6753), or worse, a nearby H II region (e. g. DEM L109 for MCSNR J0513–6912, though the former is most likely unrelated to the remnant). Other names use B1950 coordinates, with little to no consistency in the coordinates convention. Consequently, some objects were mistakenly listed twice in SNR compilations (Sect. 11.1.2).

To bypass these shortcomings, I performed a complete literature survey to build a list of LMC SNRs, combining all papers that either *i*) report the discovery or classification of one or more SNRs, *ii*) give a list of LMC SNRs, or *iii*) present new candidates (Sect. 11.1.1). The list is then cleaned (Sect. 11.1.2) from the wrongly identified or misclassified objects. Unconfirmed candidates, particularly in lights of new X-ray observations, are also removed. This list is used to study the global spectral properties of LMC SNRs (Sect. 11.2), the relation with local star formation history (Sect. 11.4), and the SNR X-ray luminosity function and size distribution (Sect. 11.5).

11.1.1. Literature survey

The first extragalactic supernova remnants were found in the LMC in the 1960s. Combining Parkes observations with H α photographs, Mathewson & Healey (1963)³⁶ first identified N49 as an SNR, to which Westerlund & Mathewson (1966) soon added N63A and N132D. Less than ten years later, Mathewson & Clarke, using the same method, had already discovered 12 new SNRs³⁷. The survey with *Einstein* allowed Long et al. (1981) to list 26 SNRs detected in X-rays, confirming many previously suggested candidates (based on optical or radio data). Mathewson et al. (1983) provided a catalogue of 25 SNRs with radio, optical, and X-ray results. With more observations, Mathewson et al. (1984, 1985) increased the size of the sample to 32.

In the 1990s, several new SNRs were discovered with ROSAT pointed observations (Chu et al. 1993, 2000; Smith et al. 1994), sometimes aided by optical spectroscopy (Chu et al. 1995b, 1997). Since then, about twenty new remnants were discovered or confirmed in a collection of papers. Some discoveries stemmed from new radio observations (e. g. Bozzetto et al. 2012a,b; de Horta et al. 2012). The majority, though, used XMM-*Newton* observations, either of optically-selected candidates (Klimek et al. 2010), ROSAT-selected candidates (Grondin et al. 2012; Bozzetto et al. 2014; Whelan et al. 2014), or serendipitous discoveries during the LMC survey (Maggi et al. 2012a, 2014; Kavanagh et al. 2015).

Several groups compiled lists of SNRs in the (Large) Magellanic Cloud(s), the purpose being to analyse some of their global properties. Williams et al. (1999a) were the first to compile a sample of all known LMC SNRs at that time, in order to study their X-ray morphology. They showed ROSAT images for 31 out of their list of 37 SNRs. Blair et al. (2006, hereafter BGS06) compiled a sample of 39 SNRs in the LMC which was observed with the *Far Ultraviolet Spectroscopic Explorer (FUSE)* satellite. The goal was to study UV emission from SNRs, in particular in the light of highly ionised oxygen (O VI λ 1032). A sample of 52 confirmed and 20 candidates radio-selected SNRs was observed spectroscopically in Payne et al. (2008), but the exact list was not given. Instead, they reported the results for the 25 objects which were detected. Desai et al. (2010) studied the triggering of star formation by SNRs. To that end, they examined the young stellar objects and molecular clouds associated to LMC SNRs. Their census resulted in a list of 45 objects. On the other hand, a total of 54 SNRs was used by Badenes et al. (2010, hereafter BMD10) to study their size distribution. The difference stems from their including objects from unpublished sources (i. e. online catalogues). Seok et al. (2008, 2013) combined *AKARI* and *Spitzer* observatories to survey the infrared emission of LMC SNRs. They presented a list of 47 SNRs, warning that some sources in BMD10 still needed confirmation.

11.1.2. Cleaning the sample: Objects not included

To build the final list of LMC SNRs, I combined objects from the older catalogues (Mathewson & Clarke 1973; Long et al. 1981; Mathewson et al. 1983, 1984, 1985) with those reported in individual studies since then. I also included all sources present in the various compilations described in the previous Section. After removing all multiple occurrences of the same object, I “cleaned” the sample, searching for *i*) misclassification: the object is something else than an SNR, e. g. a superbubble; *ii*) unconfirmed candidate: new data obtained since the classification as an SNR/candidate argue against this interpretation; *iii*) misidentification: spurious source due to confusion (of the coordinates or nomenclature) in the literature. Below, I describe the objects erroneously classified as SNRs or candidates and the evidence motivating the decision. These objects are listed in Table 11.1 and were not included in the final sample.

³⁶B. E. Westerlund was also co-author.

³⁷Counting the two distinct shells they identified in N135 (the remnants to be known as DEM L316A and DEM L316B) and including the two objects in the 30 Doradus region that they identified as candidates.

[BGS2006b] J0449–693: This object was observed in the UV by [Blair et al. \(2006\)](#) and in optical by [Payne et al. \(2008\)](#), although the latter used a different location, further to the south-east than the former. None of these studies gave conclusive evidence of an SNR nature (no UV lines detected, moderate $[S II]/H\alpha$ ratio). [Klimek et al. \(2010\)](#) used MCELS and XMM-Newton to identify the true SNR in that region, that they named SNR0449–6921, now registered as [BMD2010] SNR J0449.3–6920 in Simbad. The X-ray emission originates from an optical shell clearly distinct from the position given for [BGS2006b] J0449–693. In [Badenes et al. \(2010\)](#), both sources are listed, although only [BMD2010] SNR J0449.3–6920 (SNR0449–6921) is the true source. This is an example of a misidentification due to coordinates confusion.

LHA 120–N 185: [Blair et al. \(2006\)](#) observed but could not detect UV emission from this source (that they incorrectly listed as SNR 0453-672). It was not included in the compilations from [Desai et al. \(2010\)](#) and [Seok et al. \(2013\)](#). Only [Badenes et al. \(2010\)](#) classified the source as an SNR. X-ray emission detected, surrounded by the large, bright optical shell N 185. However, the nature of the source remains uncertain. Most likely, N 185 is actually a superbubble, and not the remnant of a single supernova ([Zhang et al. 2014;](#) [Reyes-Iturbide et al. 2014](#)).

SNR J051327–691119: This source is located north-westwards of SNR B0513–692 (which has the name MCSNR J0513–6912 in my list). [Bojičić et al. \(2007\)](#) present the optical and radio observations of this region, identifying the large ($4.1' \times 3.3'$) shell of MCSNR J0513–6912. They detected a strong unresolved radio source at its north-western edge, that they classified as an unrelated H II region or background galaxy (GH 6–2, see references in [Bojičić et al. 2007](#)).

In addition, they observed a faint optical shell seen in both MCELS $[S II]$ and AAO/UKST deep $H\alpha$ images. Follow-up optical spectroscopy revealed distinct, higher $[S II]/H\alpha$ ratios from this faint shell, prompting ([Bojičić et al. 2007](#)) to classify this shell as a new candidate SNR, J051327–691119. This region was covered by the XMM-Newton survey, revealing in details the X-ray emission of MCSNR J0513–6912 (Sect. 11.2). On the other hand, the candidate J051327–691119 lacks any X-ray feature. The small extent of the source ($40''$ diameter in $H\alpha$) would suggest a young, X-ray bright SNR, easily detectable in observations of the XMM-Newton survey. With only weak optical evidence, a confused field in the radio, and a stringent non-detection in X-rays, one is forced to conclude that J051327–691119 is *not* an SNR.

LHA 120–N 204: It is only listed as an SNR in the compilation of [Badenes et al. \(2010\)](#). It was selected from the observations of [Payne et al. \(2008\)](#) where it appeared for the first time in the literature. Therefore it was selected from radio catalogues. The “SNR” lies within the large (diameter of $14'$) optical shell N 204, although a size of $1'$ was given in [Payne et al. \(2008\)](#). The field 61 of the XMM-Newton survey covered this region, detecting no extended X-ray emission. With the small size of this source, bright emission is expected. Instead, an X-ray point source is detected in projection in N 204, which correlates with a mid-IR selected AGN (MQS J052749.08–703641.7, [Kozłowski et al. 2012](#)). The background AGN is most likely the origin of the radio emission which led to the misclassification of the target as an SNR candidate.

[BMD2010] SNR J0529.1–6833: The classification as an SNR candidate (in the MCSNR online database) stems from the detection of radio emission correlating with the large optical shell DEM L203. This object is however in the compilation of “confirmed” SNRs of [Badenes et al. \(2010\)](#). Again, X-ray observations can shed light on the nature of the source. DEM L203 has no X-ray counterpart in the ROSAT catalogue. More importantly, XMM-Newton covered the object on three occasions during the LMC survey. Combining ~ 35 ks of EPIC data, only unrelated large-scale diffuse emission is detected, without any correlation with the optical shell, as shown in Fig. 11.1. A very old age, as indicated by the large extent, might explain the lack of X-ray emission, although XMM-Newton can and did detect the largest SNRs, such as MCSNR J0450–7050 ($5.7'$ diameter, [Cajko et al. 2009](#)) or J0506–6541 ($6.8'$ [Klimek et al.](#)

2010). Furthermore, the MCELS image reveals no clear enhanced [S II] emission, and the source was not spectroscopically observed by Payne et al. (2008). In light of this and the absence of X-ray emission, I do not confirm the classification of this object as an SNR and did not include it in the final sample.

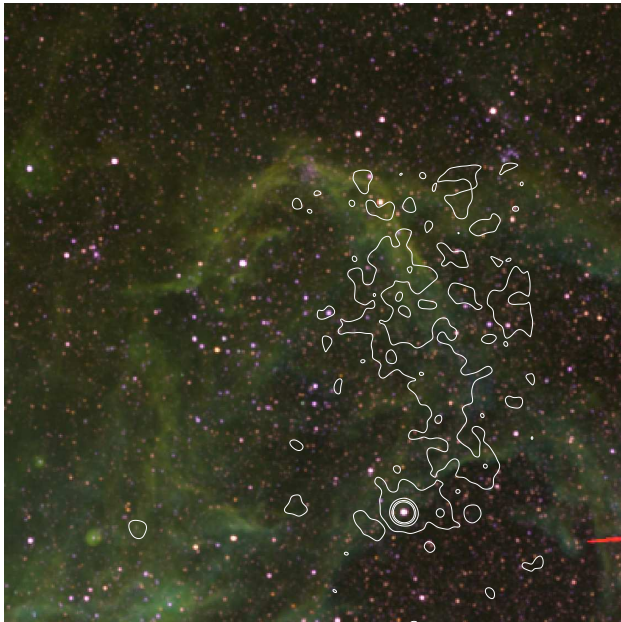


FIGURE 11.1 – The rejected SNR candidate in DEM L203 in optical lines ([S II] (red), H α (green), and [O III] (blue), data from MCELS), with soft X-ray contours (from XMM-Newton) overlaid in white. The image spans 20' across. The bright star seen in X-rays (lower right corner) is the Galactic star HD 269602.

RX J0533.5–6855: Lowry et al. (2004) used ROSAT to study the X-ray diffuse emission around the point source RX J053335–6854.9 (referenced as RX J0533.5–6855 in Simbad) and concluded that the X-ray arc seen was a large SNR candidate; they classified the X-ray point source as a dwarf M2-M3 star in the Solar neighbourhood. This region was covered in the XMM-Newton survey. The diffuse emission detected with ROSAT is found to be part of larger scale structures from the hot phase of the LMC ISM. There is *no* large SNR around RX J0533.5–6855.

30 DOR C: This is the well-known large shell seen in X-rays with a non-thermal spectrum (Bamba et al. 2004; Kavanagh et al. 2015). Its nature as a superbubble rather than a standard SNR was already recognised by Mathewson et al. (1985). It was however listed as an SNR in Blair et al. (2006, with the identifier [BGS2006b] J0536–692) and Badenes et al. (2010, as [BMD2010] SNR J0536.2–6912). Interestingly, there *is* an SNR (in projection) in 30 DOR C (MCSNR J0536–6913, Kavanagh et al. 2015), but it was revealed only later and is most likely distinct from the non-thermal shell.

SNR B0538–69.3: The first classification as an SNR dates back to Mathewson et al. (1984), based on radio and weak optical evidence. Badenes et al. (2010) included that source with the wrong J2000 coordinates. Blair et al. (2006) used the correct position but did not detect UV emission from the object. B0538–69.3 is unusually bright in radio (Miroslav Filipović, personal communication) considering the general lack of X-ray and optical emission. Mathewson et al. (1984) noted that the absence of X-ray emission might be due to the high N_H towards this region of the LMC. However, other SNRs are found in that region (e. g. MCSNR J0536–6913, DEM L299, the Honeycomb nebula), so a negative results with XMM-Newton argues against the source being an SNR.

TABLE 11.1 – LMC objects erroneously classified as SNRs or candidates, not included in the final sample.

Name	Alternative name	Category	Ref. code
[BGS2006b] J0449–693	B0450–6927	Wrong identification	BGS06
LHA 120–N 185	N185	Wrong classification (superbubble)	PWF08
SNR J051327–691119	DEM L109	Unconfirmed candidate	BFP07
LHA 120–N 204	B0528–7038	Wrong identification	PWF08
[BMD2010] SNR J0529.1–6833	DEM L203	Unconfirmed candidate	BMD10
RX J0533.5–6855	X-ray arc around RX J053335–6854.9	Unconfirmed candidate	LCG04
30 DOR C	[BGS2006b] J0536–692	Wrong classification (superbubble)	MFT85
SNR B0538–69.3	[BGS2006b] J0538–693	Unlikely	MFD84

Notes. See text in Sect. 11.1.2 for a description of each object. Reference codes: (MFD84) Mathewson et al. (1984); (MFT85) Mathewson et al. (1985); (LCG04) Lowry et al. (2004); (BGS06) Blair et al. (2006); (BFW07) Bojčić et al. (2007); (PFW08) Payne et al. (2008); (BMD10) Badenes et al. (2010).

11.1.3. The final sample

My compilation results in a list of 59 definite SNRs. In Table A.1 (p. 160) I list the final sample of LMC SNRs used in this thesis. Basic information is given for each object: MCSNR identifier and old name (see Sect. 10), position, X-ray data available, and reference. In addition, I added columns with X-ray results: X-ray luminosity (Sect. 11.2 and 11.5), size, and N_H fraction (Sect. 11.6). Finally, I give for each SNR the values of the two metrics used to assess the local stellar environment described in Sect. 11.4.1. See text in Appendix A for detailed description of each column.

This work focuses on the X-ray emission of LMC SNRs. Therefore, there are only confirmed SNRs in the final sample (no candidate), although some have been confirmed during my PhD thesis, by me and collaborators (e. g. MCSNR J0512–6707, J0536–6913). The resulting list provides the cleanest, most complete sample of SNRs in the LMC, *as far as X-rays are concerned*: XMM-Newton observations exist for 51 SNRs. Out of the eight objects without XMM-Newton data available, three were covered with *Chandra*, and two only by ROSAT. Only three objects have not any X-ray information available (yet), though their radio and optical properties warrant their classifications as SNR. In Sect. 11.5 and Sect. IV, I discuss the total number of LMC SNRs and the overall completeness of the sample

11.2. The X-ray spectra of LMC SNRs

THE X-RAY spectrum of an SNR encrypts precious information about the temperature, ionisation state, and chemical composition of the plasma. This, in turn, provides clues to the evolutionary state of the remnant, ambient density (of the inter- or circum-stellar medium), age, explosion energy, and the type of supernova progenitor. The distribution of these parameters, the impact of the environment (position in the LMC, local SFH) on them, and their interrelations (e. g. temperature vs. size/age, luminosity vs. ambient density) are valuable information to understand the evolution of SNRs and their role in the hydrodynamical and chemical evolution of galaxies.

The (Large) Magellanic Cloud population is ideal for such a study. As seen in Sect. 11.1, the sample of known LMC SNRs is large (about 60 objects and growing), relatively complete, and many (X-rays) observations are available. *A contrario* in our Milky Way, the absorption, distance uncertainties, and lack of sky coverage preclude a similarly clean work. In more distant galaxies (e. g. M31, M33), the current angular resolution and sensitivity make the identification and analysis of SNRs arduous, limiting these studies to the brightest objects

However, the X-ray spectral analyses of LMC SNRs are presented in a wide collection of individual papers with little consistency in

- the instruments: Spectra have been studied with many observatories, from A to X (ASCA to XMM-Newton), using various instruments and settings. Simply comparing the results from various instruments can introduce cross-calibration uncertainties;
- the spectral models: The model used to account for the X-ray emission of a particular remnant depends first on the level of details needed/allowed by the available data. For instance, a single-temperature CIE model with fixed abundances might have provided satisfactory fits to the ROSAT spectrum of a remnant, but deep XMM-Newton observations could reveal elevated abundances for some elements, or require a second component with a higher temperature. Then, some authors do not explore a wide range of possible models (e. g. CIE vs. NEI, single ionisation age vs. ionisation age distribution). Furthermore, there are differences even in the same class of models, since they use different atomic databases (which also improve with time) and codes to simulate spectra;
- the analysis methods: There are almost as many ways to analyse SNRs as there are research groups investigating them, particularly in the way that the background is dealt with. Sometimes, the background is simply ignored or subtracted³⁸; in other cases, the instrumental background is estimated/measured, subtracted, and the source and astrophysical background are modelled simultaneously; finally, as I did in Sect. 10, the source can be modelled simultaneously with the astrophysical *and* instrumental background components. This prevents a direct comparison of the parameters and their error bars, because the various methods have different systematic uncertainties.

Finally, several known SNRs were observed for the first time with modern X-ray instrumentation during the LMC survey and their spectral properties are as yet unpublished. Because of these limitations, it is not feasible to study the spectral properties of the whole population of LMC remnants with a mere survey of the available literature. Instead, **I performed a systematic and homogeneous X-ray spectral analysis of all LMC SNRs for which XMM-Newton EPIC data are available.**

11.2.1. Extraction of the spectra

The first step of the analysis is to extract spectra for each SNR of the sample, as well as corresponding background spectra from nearby regions (using the same observation). To that end, a source spectrum

³⁸For bright objects, or cases with very high signal-to-noise, this simple approach is usually sufficient.

extraction region (the SRC region) and a background spectrum extraction region (the BG region) must be defined. Due to the spread in morphology and size of the SNRs, unequal properties of their background (diffuse emission and point source crowding), and their varying location on the EPIC detectors, SRC and BG regions cannot be created automatically.

Therefore, I manually defined extraction regions for each SNR. For the SRC region, the constraint was simply to include all the remnant’s emission and exclude unrelated point sources that might be located in projection (as in the case of e. g. MCSNR J0517–6759, see Sect. 10.3.3. B). I used the contours taken from the X-ray image, combining all observations of each remnant, to identify the boundaries of the SNR emission. If the morphology of the object requires it, an arbitrary shape (polygonal region) is used instead of a circle or ellipse.

The BG regions are chosen from different locations on the pn and MOS detectors if needed, in order to be on the same CCD chip as (most of) the SNR emission. In most cases where the remnant was the target of the observation (i. e. was observed on-axis), the same BG region defined for pn can also be used for MOS data, because of the chip configuration of the latter with one central chip and six peripheral chips. Detected point sources are also excluded from the BG regions.

Two examples are shown in Fig. 11.2. In the simple case (that of MCSNR J0519–6902), I used a circular SRC region and the same BG regions for all EPIC detectors. In the more complex case of MCSNR J0547–6943 (or DEM L316B), I used a polygonal SRC region; the BG region is narrower for pn than for MOS to fit on a single CCD chip. In addition to point sources, I excluded arc-shaped regions which are affected by instrumental artifacts (single-reflections from LMC X-1). Extraction regions for all LMC SNRs analysed in this work are shown in Appendix B. Instrumental background spectra were extracted from FWC data at the same detector position as the SRC and BG regions following the method described in Sect. 8.4.

11.2.2. Spectral analysis and models

The next step is naturally to analyse all the extracted EPIC spectra. Several configurations are possible, depending on the data present. The spectral analysis method, which simultaneously fits the instrumental and astrophysical background with the source emission, requires FWC data. This limits the use of MOS data in some cases, because FWC data for MOS are only available in full-frame mode. It also happens that the SNR is outside the MOS field of view (too far off-axis or on one of the damaged chips of MOS1, Sect. 6.3.2). In these cases only the pn spectrum is used for analysis. The contrary (only MOS spectra available) occurs in rare cases.

About 80% of the SNRs in the sample were observed only once. A few were observed twice in overlapping survey observations. The deep field centred on SNR 1987A contains four SNRs in total, and a plethora of XMM-Newton data are at hand for those (see Sect. 9). To keep the analysis the same for most sources, I restricted the number of observations analysed simultaneously to two for these two cases. When more are available, I selected the deepest two datasets (i. e. longest flare-filtered exposure times). Finally, N132D is a calibration target and frequently observed. It is however too bright for the full-frame mode; only Small Window and Large Window modes have been used and thus I only used the deepest pn dataset.

I followed the method outlined in Sect. 8 to analyse the spectra. I found however more efficient to first pre-fit the instrumental and astrophysical background of each SNR. I first fitted the (FWC + AXB) EPIC-pn spectra alone and FWC MOS spectra alone. The visual examination of the early background fits allows to identify problematic cases, e. g. MOS in “anomalous” state (Kuntz & Snowden 2008) or presence of a significant SPC (see note below). If the pre-fitting of the background components was satisfactory, their best-fit parameters were used as starting points in the final fit, which includes the SNR emission model. Doing so speeds up the process of analysing the SNR spectrum alone.

The model of the SNR emission was build iteratively, in increasing order of complexity. First, one-component models are tried, using either CIE (*vapec*) or NEI (*vpshock*) XSPEC models. I refer to these models as “1T” (one temperature). The elemental abundances are initially set to the values measured by

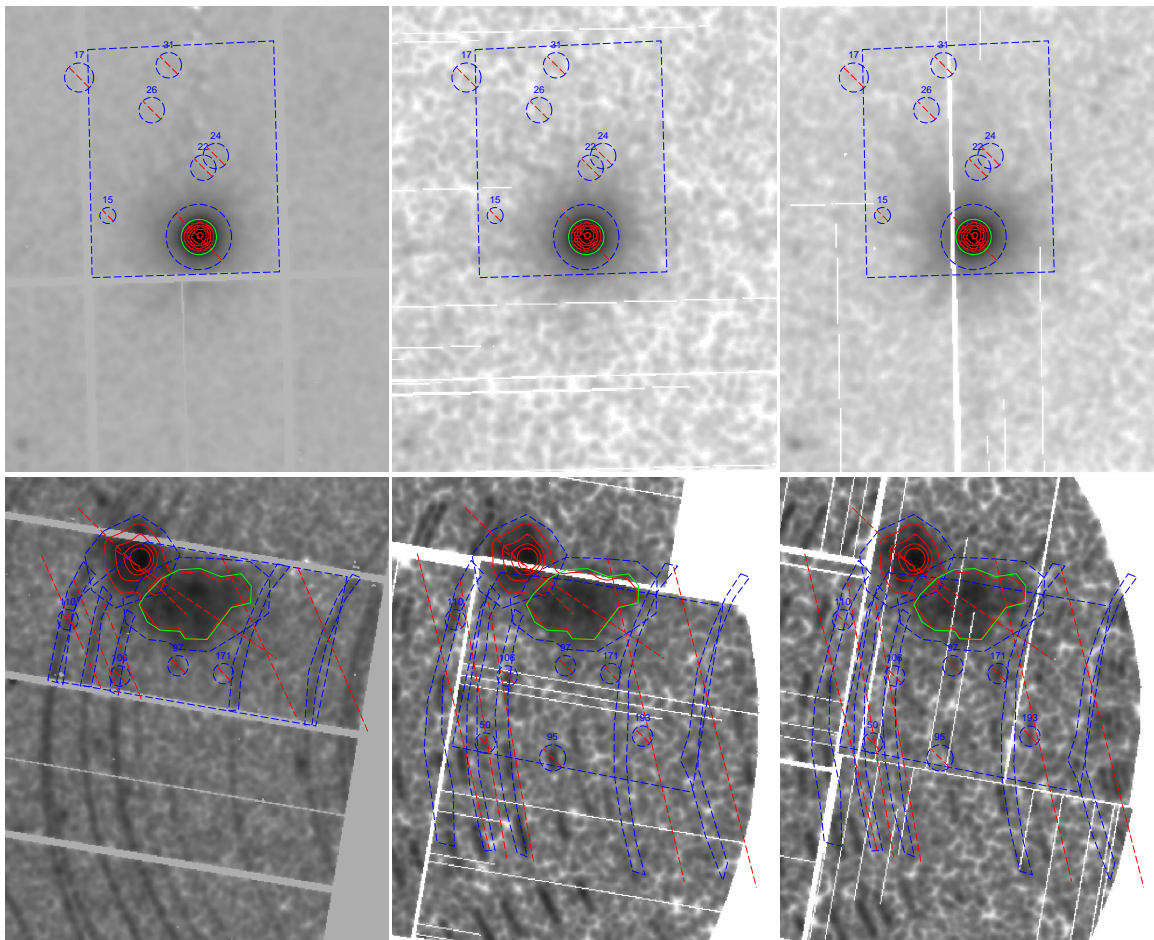


FIGURE 11.2 – *Top*: Extraction regions used to extract spectra of MCSNR J0519–6902 from EPIC pn, MOS1, and MOS2 detectors (left to right). For the scale, I recall that pn chips are 4.4′-wide. The X-ray contours (in red) are used to outline the boundary of the remnant emission and set the radius of the circular SRC region (in green). The BG regions are shown by the blue dashed rectangle. The barred blue circles show detected point sources and a “buffer” area around the SRC region. Those are excluded from the BG region.

Bottom: Same for MCSNR J0547–6943, outlined by the green polygonal region. The barred blue arcs are excluded to avoid single-reflections from LMC X-1.

Russell & Dopita (1992). Their abundance of silicon is highly uncertain, however, and therefore I use an initial value of half solar for Si. Analysis of the residuals and goodness-of-fit reveals if some elemental abundances need to be thawed. I evaluate the significance of the fit improvements (if any) with F-tests. A second component, again either CIE or NEI, is added if needed. Those are the “2T” SNRs. For several SNRs, the analysis of X-ray colour images already hints at the presence of two components, with e. g. a different temperature, N_H , or abundance pattern. This iterative process is done until a satisfactory fit is achieved, at which point 90 % C.L. errors are computed for all free parameters. More complicated models may be applied/needed for a handful of SNRs, particularly amongst the brightest ones. These cases are presented in Sect. 11.2.3. B.

Note: Cases with a problematic background Several situations can occur where the instrumental and X-ray backgrounds cannot be properly accounted for at first, hindering the analysis of the SNR emission.

- **Bad extraction region:** If the SNR is very bright, a background spectrum extracted too close to the SNR will include contamination from the telescope PSF wings. Alternatively, a nearby bright X-ray source can produce artifacts such as singly-reflected photons up to large angular distances ($\sim 1^\circ$). When this happens, I selected the background in another region better suited.
- **Anomalous MOS states:** The model for the instrumental background of the MOS detectors (Sect. 8) was developed for data obtained in the normal state; Kuntz & Snowden (2008) identified periods of “anomalous” background of EPIC-MOS. The instrumental background spectrum of this anomalous state is markedly stronger below 1 keV, which complicates the analysis of observations obtained during these epochs. If the SNR affected was faint, including the MOS data usually do not add much information, and only the pn spectrum was used. Conversely, if the SNR is bright, the error induced by fitting the anomalous spectra with the standard model is unimportant, because the source count rate is much higher than the instrumental background, and this issue can be discarded.
- **Soft proton contamination:** Observations affected by a strong SPC are easily identified by fitting the FWC and astrophysical backgrounds spectra together. Indeed, the background above 2 keV is almost purely instrumental. Therefore, a residual component at high energy in the background spectrum (extracted from science observation) that is not present in the FWC spectrum betrays the SPC. An extreme example is shown in Fig. 11.3. An extra component needs to be added to the X-ray background and SNR models to account for the SPC.

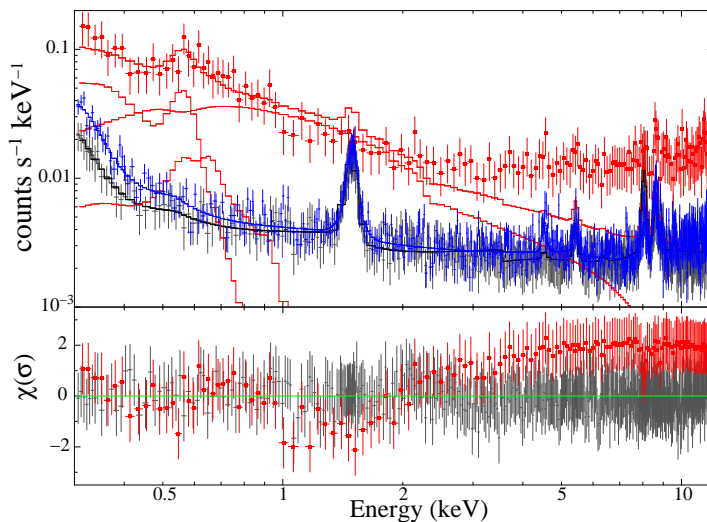


FIGURE 11.3 – Example of a strong soft proton contamination (SPC) affecting the spectral analysis of MCSNR J0529–6653 (ObsID 0700381101). The instrumental background, extracted from FWC data, is shown in the top panel in gray and blue. The spectrum extracted from the BG region is shown in red. The strong flat tail above 2 keV is the SPC, which the instrumental + AXB model cannot account for.

11.2.3. Results

11.2.3. A. General properties

Out of the sample of 59 SNRs and 51 with XMM-Newton data available, 45 are fitted with 1T or 2T models, while 6, amongst the brightest, are fit with more complex models (see Sect. 11.2.3. B). The results of the spectral analysis for the 1T/2T sample are given in the Appendix (Table A.2, p. 163). All relevant parameters are listed with their 90% C.L. uncertainties: The fitted LMC absorption column density (column 2), plasma temperature kT (3), ionisation age τ (4), emission measure EM (5), and abundances (6). When a second component is used, its parameters are given in columns (7) – (11). The quality of the fits are evaluated by the χ^2/ν of column (12), where ν is the number of degrees of freedom. The median reduced χ^2 is 1.16. 90% of the fitted objects have a reduced χ^2 less than 1.4.

In 32 cases, the SNR is fitted with, or the available data only require, a one component model. Amongst these, 9 do not show significant NEI effects and are fitted with a CIE model; in the 23 remaining objects, better fits are obtained with an NEI model. The plasma temperature for the “1T SNRs” clusters in the 0.25 keV – 0.45 keV range. The highest values of temperature (above 1 keV) are associated with the smallest ionisation ages. In at least some cases, this could be an artifact of the analysis due to insufficient data. The ionisation age τ of this sample is broadly distributed around a median value of $1.7 \times 10^{11} \text{ s cm}^{-3}$.

There are 13 SNRs in the 2T sample. Two objects are fitted with two CIE component models (MCSNR J0530–7008 and J0517–6759, see Sect. 10). The rest was fitted with two NEI components, although for three SNRs the ionisation age of one of the components was unconstrained and on the high end ($\tau \gtrsim 10^{13}$), indicating a plasma close to or in CIE. The median τ of the main component (i. e. that with higher emission measure) for the 2T sample is slightly higher ($5 - 7 \times 10^{11} \text{ s cm}^{-3}$) than that of the 1T sample, but low number statistics preclude a direct comparison. The temperature distribution is bimodal: one component has a median temperature of $kT = 0.31 \text{ keV}$, the second a higher median of 0.8 keV. In several cases the high- kT component also requires a different abundance pattern, revealing SN ejecta (Sect. 11.2.3. D).

For 9 SNRs, the data did not require or allow to fit elemental abundances. For a few cases, this happens because the spectrum is contaminated by a bright pulsar (N157B and MCSNR J0540–6920), or by LMC X-1 (MCSNR J0540–6944), and the thermal emission is not well separated by XMM-Newton. The other SNRs fitted with abundances from Russell & Dopita (1992, RD92 in Table A.2) are relatively faint. The limited available data therefore prevent the use of free abundances in the fits.

Oxygen and iron are the main contributors to the 0.5 keV – 2 keV X-ray emission for the relevant plasma temperatures. Consequently, they are the first elements for which abundances can be fitted. Out of the 45 1T/2T SNRs, 35 have at least free O and Fe abundances. Neon and magnesium also have prominent lines routinely detected below 2 keV, and their abundances were fitted in 33 and 30 SNRs, respectively. Silicon is detected and its abundance fitted, in 23 SNRs. This subset has a higher median temperature ($kT \sim 0.6 \text{ keV}$) than the whole sample, as expected. Indeed, Si emission becomes prominent for higher temperatures than, say, O, Ne, or Fe. While obvious and fitted in all the brightest SNRs, which are younger/hotter, lines of sulphur are not detected in most 1T/2T SNRs. Only a handful (MCSNR J0534–6955, J0547–7025, N63A) allow to fit the S abundances. All have plasma temperatures in excess of 0.8 keV. The fitted abundance patterns can be used to type of supernova progenitor, if ejecta are detected (Sect. 11.2.3. D), or to measure metallicity of the LMC ISM (Sect. 11.2.3. E).

11.2.3. B. The analysis of the brightest SNRs

For six of the brightest SNRs, the simple 1T/2T models approach was clearly insufficient to satisfactorily model the spectra. This is expected, because on the one hand, the exquisite statistical quality of these spectra imply that even a two-component model is not adequate to reproduce the complex multi-phase structure in these objects. On the other hand, the very young SNRs, in addition to a small ambient medium contribution, are dominated by ejecta. Because of stratification of the ejecta heated by the reverse shock, elements synthesised at different radii in the SN explosion can have distinct spectral properties.

All the “bright SNR” sample was observed in individual XMM-Newton and Chandra pointings. Detailed results are published in several papers (references are given below), with which my results were never at odd. Here, I used multi-temperature empirical models to reproduce the spatially integrated spectra. This allows *i*) to derive accurate X-ray fluxes, so that the luminosity function is complete at the bright end, *ii*) to measure the properties of the Fe K emission, if present (see Sect. 11.2.3. C), and *iii*) to obtain spectral properties (e. g. N_H , kT , τ) for statistical studies and comparison of their distributions for various sub-samples (Sect. 11.5). The adopted models are described below. The spectral parameters are given in Table A.3.

DEM L71 (MCSNR J0505–6753): DEM L71 is notoriously a type Ia SNR, owing to the detection of iron-rich ejecta (e. g. Hughes et al. 1995). van der Heyden et al. (2003) presented the XMM-Newton EPIC and

RGS results for this remnant, and [Hughes et al. \(2003\)](#) those obtained with *Chandra* observations. Different conditions are measured in the shell and central regions. It is then unsurprising that a 2T model as used for other SNRs did not produce acceptable fits. Instead, I obtained satisfactory results with three components: Two components (“Fe-low” and “Fe-high”) had Si, S, and Fe (the main nucleosynthesis products of Ia SNe) freed and common to the two components, while other metals were set to zero. These components account for the ejecta-rich emission, as well as the Si, S, and Fe contribution of the ISM. A third component, with O, Ne, and Mg abundances free and Si, S, Fe set to zero, accounts for the bulk of ISM emission.

In addition, Fe K emission is clearly detected, pointing to the presence of very hot ejecta ($kT > 2$ keV). The statistical weight of this feature remains small. Therefore, instead of adding another thermal component, I modelled the line with a Gaussian. The parameters of the Fe K line are used in comparison with other SNRs in Sect. 11.2.3.C. The ejecta components have best-fit temperatures of ~ 0.4 keV and ~ 0.9 keV (Table A.3). The ionisation age of the cooler component is twice that of the hotter one. The ISM component has a temperature of $kT = 0.46$ keV, the same as measured with *Chandra* ([Hughes et al. 2003](#)), and in between the two temperatures used for the shell emission by [van der Heyden et al. \(2003\)](#).

N103B (MCSNR J0509–6844): The spectrum of N103B is remarkable because of the numerous lines from highly ionised metals: Si XII and Si XIV S XV and (marginally) S XVI, Ar XVII, and Ca XIX. A strong Fe K blend is also detected. I fit the spectrum with the same three-temperature model as for DEM L71. One component had abundances fixed to RD92, accounting for the ISM emission. Two components with different kT and τ were used to reproduce the (dominating) ejecta emission. All relevant elements (O, Ne, Mg, Si, S, Ar, Ca, and Fe) were freed, but common to both components. A Gaussian was also included to fit the Fe K feature.

With this model, the spectrum of N103B is well reproduced across the whole 0.3 keV – 8 keV band. The results are comparable to those of [van der Heyden et al. \(2002\)](#), focusing on XMM-Newton data) and [Lewis et al. \(2003\)](#), with *Chandra*), especially regarding: *i*) the column density $N_H \sim 3 \times 10^{21}$ cm⁻²; *ii*) the presence of one high ionisation age component (at $kT \sim 0.7$ keV) and a hotter (1.6 keV) underionised component. Because the Fe K blend is modelled separately with a Gaussian, the fitted temperature of the hottest component is lower than in the previous references; *iii*) high abundances of S, Ar, and Ca.

N132D (MCSNR J0525–6938): [Behar et al. \(2001\)](#) presented the XMM-Newton observations of N132D from the Performance Verification programme. Results of the *Chandra* ACIS-S observations can be found in [Borkowski et al. \(2007\)](#). Both instruments spatially resolve the SNR into regions with different spectral properties. Therefore, though a three-temperature model can reproduce the main features of the spectrum (therefore allowing to measure accurately the integrated flux of the remnant), strong residual structures are seen between 0.5 keV and 1 keV, where the strongest variations are observed (lines of O, Ne, Fe).

The best fit is obtained with a cool (~ 0.5 keV) component with abundances close to the normal LMC values (i.e. it represents a blast wave component) that dominates the soft emission (below 1.5 keV). A second component with $kT \sim 1$ keV is characterised by enriched levels of O, Ne, and Mg, as well as a higher column density ($\sim 10^{22}$ cm⁻²). This component thus describes the bulk of the ejecta emission, and accounts for most of the Si and S emission. Finally, the presence of highly ionised iron is evident from the $kT = 6.67$ keV line ($K\alpha$ energy of Fe XXV). This indicates a third, very hot component (~ 5 keV). In this component only Fe, Ar, and Ca are included. The two latter elements improve the residuals around 3.1 keV (Ar XVII), and 3.9/4.1 keV (Ca XIX and Ca XX). These K lines were already mentioned in the early XMM-Newton results ([Behar et al. 2001](#)).

SNR 1987A (MCSNR J0535–6916): The observations, spectral modelling, and results for this remnant are presented in Sect. 9.

0519–69.0 (MCSNR J0519–6902): The SNR was observed early in the *Chandra* and *XMM-Newton* missions. In addition, the LMC survey covered the source, at an off-axis angle of $\sim 9'$, adding 23 ks and 27 ks to the existing (full-frame) 8 ks and 46 ks pn and MOS data, respectively. Spectra from the two observations were fitted simultaneously. 0519–69.0 exhibits strong lines of Si, S, Ar, and Ca, as well as prominent Fe L and K blends. To reproduce the spectra I used the multi-component approach of [Kosenko et al. \(2010\)](#), who extensively studied the *XMM-Newton* and *Chandra* data.

First, one NEI component with LMC abundances accounts for circumstellar/interstellar medium emission. Then, one NEI component for each (group of) element(s) having detected lines: oxygen, silicon and sulphur, argon and calcium, and iron. In the latter case two NEI components with distinct parameters are used, as the spectrum evidently includes both medium temperature and very hot iron. Due to the low count rate, and therefore statistical weight, of the Fe K blend, the hot iron component was driven to fit lower energy lines instead. To alleviate this issue I fitted the high-energy part of the spectrum separately with this component, then froze the best-fitting parameters in the global fits. Residuals around 0.72 keV (lines of Fe XVII) were fitted with an additional Gaussian line.

0509–67.5 (MCSNR J0509–6731): *XMM-Newton* observed the SNR for ≈ 40 ks in 2000, with pn operated in Large Window mode. This dataset is presented in [Kosenko et al. \(2008\)](#), while [Warren & Hughes \(2004\)](#) report the spectral and imaging analysis of a *Chandra* observation. Finally, [Badenes et al. \(2008\)](#) attempted to reproduce spectra from both instruments using a grid of hydrodynamical models and an X-ray emission code. Inconsistencies between pn and MOS spectra were found, with lines in the pn spectrum (red-)shifted relative to those in MOS spectra by about 1 %. This is likely a gain issue of the pn instrument. I discarded spectra from the MOS instruments, as they were operated in Small Window mode, for which no FWC data are available. To get the spectral model to match the observed energies of atomic lines, I freed the “redshift” parameter available in XSPEC models, which allows an *ad hoc* change of the energy scale. Satisfying results were obtained for a shift of ≈ 1 %, which is the measured pn/MOS discrepancy [Kosenko et al. \(2008\)](#).

As for J0519–6902, lines from heavy elements are prominent, and I used a multi-component model. Iron was included in two NEI components, one with a medium temperature (~ 1.4 keV) and a high-kT one (~ 11 keV) that reproduces the strong Fe K line. The latter component also includes calcium. Si, S, and Ar were grouped in another NEI component, and shared the same temperature and ionisation age. A last NEI component modelled the continuum+lines emission from the CSM/ISM. No Si, S, Ar, or Ca were included in this component. Even with this model, residuals remained around Fe lines (0.72 keV and 1.22 keV), which I fitted with two Gaussian lines.

11.2.3. C. Fe K emission from LMC SNRs

[Yamaguchi et al. \(2014\)](#) used *Suzaku* to systematically search for Fe K emission from Galactic and LMC SNRs. Fe $K\alpha$ emission was detected in 23 SNRs, including seven remnants in the LMC. Their essential finding is that the centroid energy of the Fe K emission, determined by the ionisation state of iron, is a powerful tool to discriminate between progenitor types. Indeed, the Fe K emission of type Ia remnants is significantly less ionised than in CC-SNRs. Furthermore, there is a positive correlation between the Fe $K\alpha$ line luminosity and centroid energy *within each progenitor group*.

Because the Fe K blend is a promising typing tool, I extended the search for Fe K emission of [Yamaguchi et al. \(2014\)](#) to all LMC SNRs observed with *XMM-Newton*. Compared to the *Suzaku* sample, the coverage is more complete (i. e. more SNRs observed) and more sensitive (the EPIC-pn effective area is slightly higher than that of *Suzaku*’s XIS, even combining all four detectors), and Fe K can potentially be detected from more SNRs.

In Table 11.2, I give the results for all LMC SNRs where Fe K emission is detected, ranked by increasing centroid energy. The *XMM-Newton* and *Suzaku* results are consistent within the uncertainties. Strikingly,

TABLE 11.2 – Fe K line properties of LMC SNRs

MCSNR	Alt. name	type	Energy centroid (eV)		Line flux (10^{42} ph s $^{-1}$)	
			XMM- <i>Newton</i>	<i>Suzaku</i>	XMM- <i>Newton</i>	<i>Suzaku</i>
J0509–6731	B0509–675	Ia	6432^{+29}_{-27}	6425^{+14}_{-15}	0.87 ± 0.21	0.96 ± 0.12
J0505–6753	DEM L71	Ia	6494 ± 58	—	$0.26^{+0.08}_{-0.09}$	—
J0509–6844	N103B	Ia	6514^{+31}_{-32}	6545 ± 6	5.10 ± 0.87	6.43 ± 0.30
J0519–6902	B0519–690	Ia	6543^{+28}_{-31}	6498^{+6}_{-8}	1.71 ± 0.45	2.78 ± 0.15
J0526–6605	N49	CC	—	6628^{+29}_{-26}	$< 4.75^{(a)}$	0.54 ± 0.12
J0536–6916	SNR 1987A ^(b)	CC	6635 ± 70	6646^{+55}_{-54}	0.64 ± 0.18	0.57 ± 0.24
J0535–6602	N63A	CC	6683^{+88}_{-99}	6647^{+16}_{-17}	$2.36^{+1.03}_{-1.08}$	2.57 ± 0.36
J0525–6938	N132D	CC	6685^{+15}_{-14}	6656 ± 9	4.58 ± 0.58	5.47 ± 0.51

Notes. *Suzaku* results are from Yamaguchi et al. (2014). ^(a) 3σ upper limit. ^(b) The quoted numbers are average values over the last six observations (see Sect. 9); the uncertainties are the RMS scatter.

I found Fe K emission undetected with *Suzaku* for only one source, DEM L71. Its line flux is smaller than from any other LMC remnant. Likely, this fact and the smaller effective area of XIS explain why it was undetected in the 100 ks-long *Suzaku* observation of the remnant (Hiroya Yamaguchi, personal communication). On the other hand, the second faintest Fe K line from LMC SNRs is found in N49. With XMM-*Newton* one does not formally detect the line. Including a Gaussian at the energy measured with *Suzaku*, the XMM-*Newton* spectrum allows a line flux an order of magnitude above that actually detected. This is only a statistical issue. Indeed, there are less than 10 ks of EPIC-pn data, which is no match to the 158 ks spent by *Suzaku* on N49 when detecting the Fe K line.

The properties of the Fe K emission from DEM L71 fit well with its type Ia nature. Furthermore, Yamaguchi et al. (2014, their Figure 1, right) used simple (one-dimensional) theoretical models of type Ia SNe exploding in uniform ambient media of various densities to predict the luminosity and energy of the line. Even with this simplistic approach, they are able to reproduce all the parameter space spanned by type Ia SNRs. In this context, the location of DEM L71 in the Fe K luminosity – energy diagram is well reproduced by a delayed-detonation model with a rather high explosion energy (1.4×10^{51} erg, DDTa in Badenes et al. 2003, 2005), in an ambient medium of density $\rho = 2 \times 10^{-24}$ g cm $^{-3}$, at age between 2000 yr and 5000 yr. This is in line with the measured density and age of DEM L71 (van der Heyden et al. 2003; Ghavamian et al. 2003). Furthermore, the DDTa model predicts a silicon-to-iron mass ratio of 0.08, close to that measured in X-rays (~ 0.15 , Hughes et al. 2003; van der Heyden et al. 2003). Since the hot, K α -emitting iron was previously overlooked, the $M_{\text{Si}}/M_{\text{Fe}}$ ratio should be even lower, closer to the prediction of the DDTa model.

The dearth of Fe K-emitting remnants, aside from the combined XMM-*Newton*/*Suzaku* sample (eight objects), is somehow expected. Indeed, most of the SNRs have plasma temperatures less than 1 keV (Sect. 11.2.3. A), which is too low to excite iron K-shell electrons, so that no emission is expected. Even if a spectrally-unresolved hot iron component exists in more LMC remnants, a further issue is detectability. The LMC SNRs of Yamaguchi et al. (2014) have hard X-ray (2 keV – 8 keV) luminosities above 10^{35} erg s $^{-1}$. There are only two other SNRs in the LMC above this level, MCSNR J0540–6920 and N157B, which are powered by a bright pulsar and pulsar wind nebula, respectively.

Despite these observational difficulties, it is very likely that the sample of LMC Fe K-emitting remnants (of Yamaguchi et al. 2014, plus DEM L71) is complete, because all young SNRs ($\lesssim 5000$ yr old) are now known and observed in X-rays. Translating the fraction of remnants with Fe K emission in the LMC ($\approx 13\%$) to the Galactic population (294 objects, Green 2014), we expect more than 40 such sources in

the Milky Way. This number is a lower limit, since fainter line fluxes than in the LMC can be reached. Yamaguchi et al. (2014) list 16 Galactic SNRs detected, out of 56 objects observed with *Suzaku* (Ferrand & Safi-Harb 2012, online database³⁹). About 80 more SNRs were observed and detected with *Chandra* or *XMM-Newton*, and 150 have not been covered in X-rays. A systematic analysis of all X-ray-detected SNRs and new/deeper observations of promising candidates with more sensitive instruments (e. g. *XMM-Newton* vs. *Chandra*, future missions such as Athena) will provide a better census of Fe K lines in SNRs. This will allow to type more remnants and to study the pre-SN evolution of their progenitors.

11.2.3. D. Detection of SN ejecta

When SN ejecta give an observable contribution to the X-ray emission of an SNR, the fitted abundances, or rather the fitted *abundance ratios*, will reflect the nucleosynthesis yields of either thermonuclear or CC SNe. To identify SNRs with detected ejecta and the origin thereof, I computed abundance ratios X/Fe , where X is O, Ne, Mg, or Si. The ratios are normalised with respect to $(X/Fe)_{LMC}$, the corresponding ratios with the LMC abundances. As CC-SNRs produce large amounts of light-Z elements and little iron, high $(X/Fe)/(X/Fe)_{LMC}$ ratios (in excess of one) indicate a massive star progenitor. On the contrary, the main product of thermonuclear SNe is iron, and ejecta in type Ia SNRs (if detected), are expected to have $(X/Fe)/(X/Fe)_{LMC} \ll 1$.

In Fig. 11.4, I show the abundance ratio diagrams of all SNRs with corresponding fitted abundances. The samples of SNRs with a secured CC or type Ia classification (as described in Sect. 11.3.1) are marked. Evidently, many of the known CC SNRs are located in regions of super-LMC X/Fe . The known type Ia SNRs are unsurprisingly in the $(X/Fe)/(X/Fe)_{LMC} \ll 1$ regions of the diagrams, because in most cases it is this very iron-enhancement that was used to classify them.

Several sources without previous classification are located in the high- and low-ratio regions of the diagrams. For typing purpose, I assign “high X/Fe ” and “low X/Fe ” flags to these objects, using the following scheme: For each element X , I plot the cumulative distribution of the ratio $(X/Fe)/(X/Fe)_{LMC}$. I then assign a “high X/Fe ” flag to an object if its ratio is above the 68th percentile ($\sim 1\sigma$) of the cumulative distribution. Symmetrically, a “low X/Fe ” flag is given if the ratio is below the 32th percentile. Since the uncertainties in the fitted abundances can be large, it is necessary to put a second constrain using the uncertainty of the ratio: A “high X/Fe ” flag is only given if the lower limit (i. e. ratio minus the uncertainty) is above the median of the cumulative distribution. For a “low X/Fe ” flag the upper limit must be below the median. This excludes all cases where the ratios are elevated (or much smaller than one) but highly uncertain. Though some of the criteria for “low X/Fe ” flags may seem high, the selected SNRs have actual ratios well below half the LMC average (well below 0.2 times the average for Mg). There are 23 SNRs in the 1T/2T sample with high or low abundance ratio flags, as listed in Table 11.4. These flags are used in Sect. 11.4 to help the typing of all LMC SNRs.

11.2.3. E. Metal abundances of the LMC ISM

When no SN ejecta is detected, the X-ray emission is dominated by the ISM swept-up by the SN blast wave. Therefore, the fitted abundances in these cases provide us with measurements of the chemical composition

TABLE 11.3 – Constraints used for the identification of ejecta in SNR spectra.

X	“high X/Fe ” flag		“low X/Fe ” flag	
	(1)	(2)	(1)	(3)
O	> 1.0	> 0.83	< 0.60	< 0.83
Ne	> 1.43	> 1.30	< 0.55	< 1.30
Mg	> 0.62	> 0.48	< 0.22	< 0.48
Si	> 2.70	> 1.60	< 1.30	< 1.60

Notes. (1) Constraints on the ratio $(X/Fe)/(X/Fe)_{LMC}$. (2) Constraints on the lower limit $(X/Fe)/(X/Fe)_{LMC} - \Delta(X/Fe)$. (3) Constraints on the upper limit $(X/Fe)/(X/Fe)_{LMC} + \Delta(X/Fe)$.

³⁹<http://www.physics.umanitoba.ca/snr/SNRcat/>

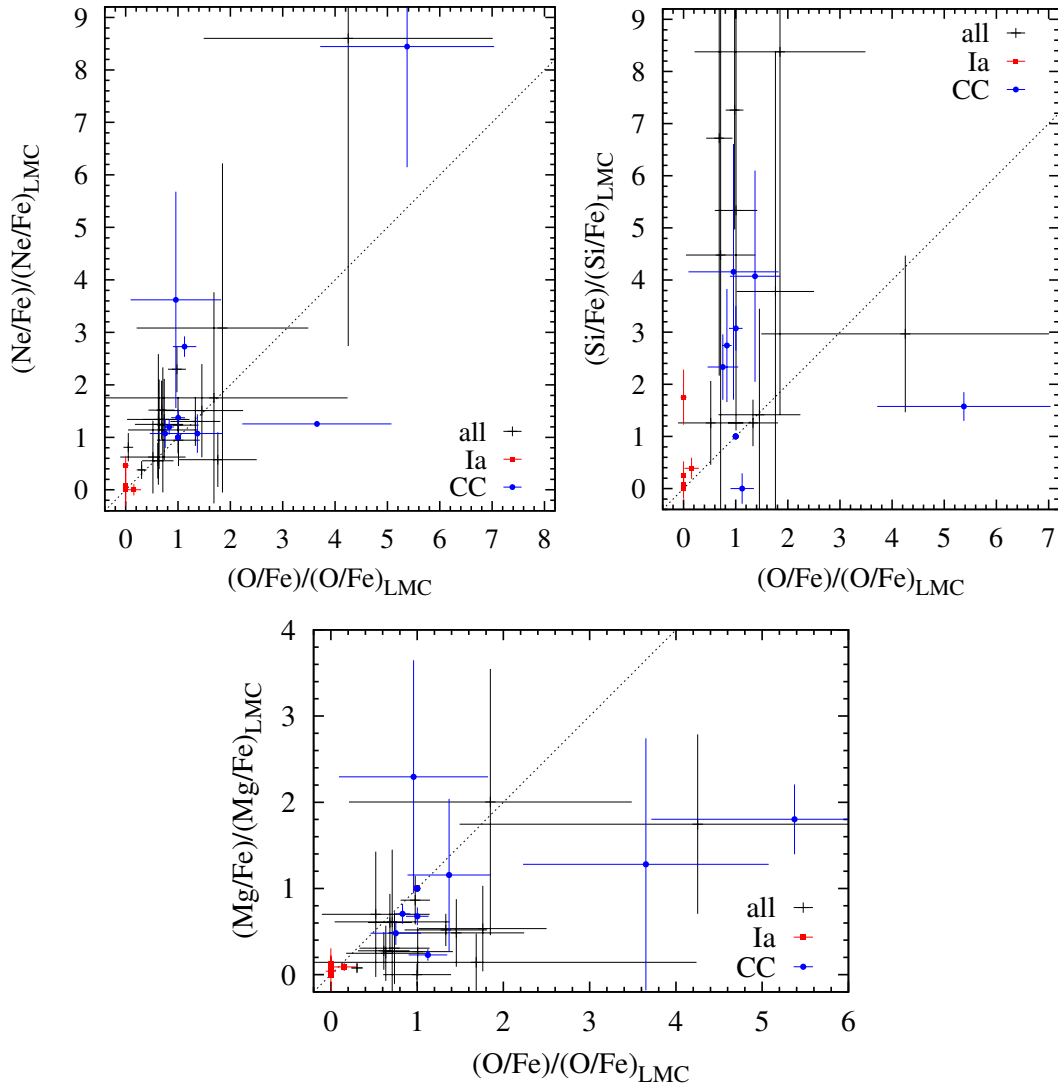


FIGURE 11.4 – Abundance ratio diagrams of LMC SNRs with fitted abundances. Sources firmly classified as type Ia or CC-SNRs are plotted in red and blue, respectively.

of the gas phase of the LMC ISM. [Russell & Dopita \(1992\)](#) and [Hughes et al. \(1998\)](#) have used samples of SNRs to obtain the abundance of some elements (using optical and X-ray observations, respectively), but the smaller sample of known SNRs and sensitivity of the X-ray instrument used (*ASCA*) at the time limited the number of SNRs eligible to measure LMC abundances.

I first selected all 1T/2T SNRs with fitted abundances but no high or low abundance ratios. To increase that sample, I included SNRs where some abundances are enhanced but others can still be used. E. g. for MCSNR J0453–6829, the spectrum is enhanced in Mg and Si, but the fitted values for O, Ne, and Fe, are still (assumed to be) reflecting the LMC ISM abundance. Furthermore, if the abundance of a given element is too uncertain, then the SNRs is not used to measure the average abundance of that element. This limits in particular the size of the SNR sample allowing the abundance of silicon to be measured.

In [Table 11.4](#) I give the list of SNRs used to measure the abundance of O, Ne, Mg, Si, and Fe, or a subset of these elements. The measured abundances for this sample are plotted relative to solar values in [Fig. 11.5](#). The final LMC abundances are obtained by taking the average values from all SNRs where an element is used; the errors given are the RMS scatter amongst the SNRs used. This method is similar to that of [Hughes](#)

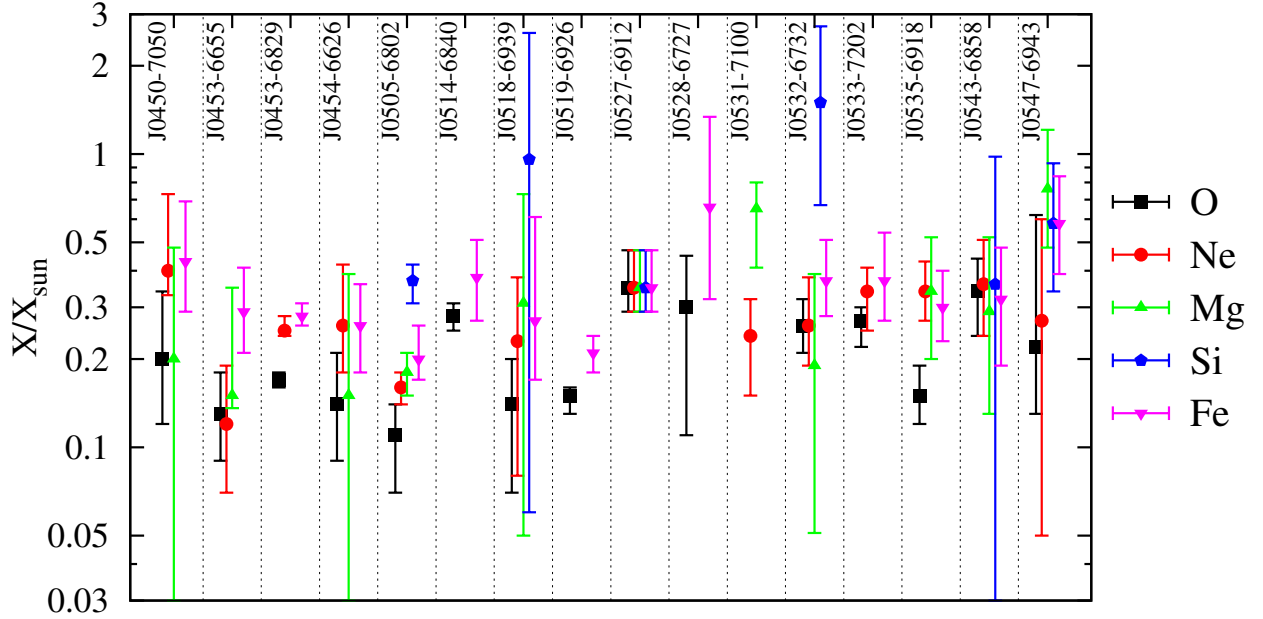


FIGURE 11.5 – LMC ISM abundances, relative to the solar values of Wilms et al. (2000), measured in a sample of 16 X-ray SNRs. The selection of the sample and the measurements of abundance are described in Sect. 11.2.3. E.

et al. (1998). Resulting abundances range from ~ 0.2 solar for oxygen to ~ 0.7 solar for silicon. The results are listed in Table 11.5. The absolute abundances, in the form $12 + \log(X/H)$ (by number), are given, in comparison with results from Russell & Dopita (1992) and Hughes et al. (1998). Abundances of Fe and Si measured with XMM-Newton are in good agreement with the results measured for (a different sample of) SNRs by Hughes et al. (1998). More recent studies of abundances in the LMC, using large samples of field stars (Cole et al. 2005; Pompéia et al. 2008; Lapenna et al. 2012; Van der Swaelmen et al. 2013), can be used to evaluate my results. The metallicity distributions $[\text{Fe}/\text{H}]^{40}$ peak at about -0.5 dex for most field star samples (Lapenna et al. 2012). The $[\text{Fe}/\text{H}]$ based on XMM-Newton SNRs ($-0.46_{-0.18}^{+0.13}$) matched that very well, indicating no metallicity difference between field stars and gas-phase ISM.

However, the abundances of light α -elements tend to be lower (by ~ 0.15 dex – 0.2 dex) compared to Hughes et al. (1998), although the results for Mg and Ne might still be reconciled given the larger uncertainties. Still, I measured a ratio $[\text{O}/\text{Fe}]$ of -0.21 while ASCA SNRs gave -0.06 . The likely explanation is two-fold. First, the α -elements abundance has an intrinsic scatter (about 0.05 dex – 0.08 dex at the relevant metallicity, Van der Swaelmen et al. 2013) that can partly explain the discrepancy. The second reason is the sample used by Hughes et al. (1998): six out of the seven SNRs they used are well-established CC-SNRs, including N132D, N49, N49B, in which regions enhanced in low-Z elements have been (since then) detected (this work, references in Sect. 11.3.1). The bias towards CC-SNRs, and the contribution of ejecta in the integrated spectra can explain the higher $[\text{O}/\text{Fe}]$ (or more generally $[\alpha/\text{Fe}]$) obtained by Hughes et al. (1998). On the other hand, the XMM-Newton sample used here is explicitly cleaned of SNRs with abnormal abundance patterns (i. e. those with ejecta detected), resulting in a purer sample better suited to the measurement of the ISM composition. However, this sample comprises SNRs fainter than used in previous studies, and the abundances thus obtained are consequently relatively uncertain.

The abundance pattern of metals should reflect the past history of chemical enrichment, and in particular the relative number of CC and Ia SNRs (hereafter $N_{\text{CC}}/N_{\text{Ia}}$), because their metal yields are markedly different

⁴⁰using the conventional notation: $[\text{X}/\text{Y}] = \log(\text{X}/\text{Y}) - \log(\text{X}/\text{Y})_{\odot}$.

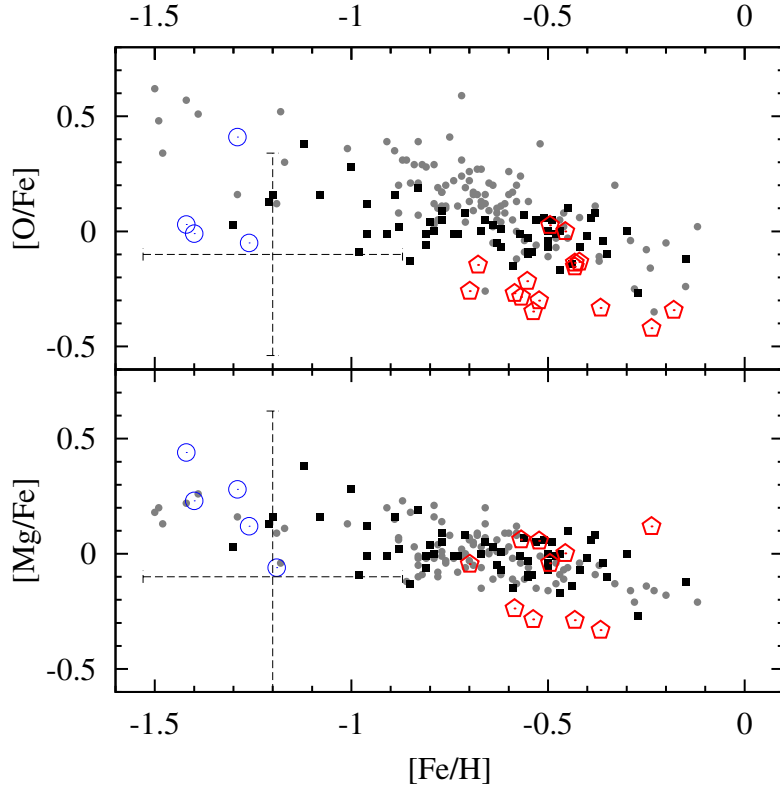


FIGURE 11.6 – $[\text{O}/\text{Fe}]$ and $[\text{Mg}/\text{Fe}]$ vs. $[\text{Fe}/\text{H}]$ diagrams for various LMC populations: Abundances measured in SNRs (ISM gas phase, this work) are shown with red pentagons. The crosses indicate median error bars. Blue open circles are the old globular clusters from Johnson et al. (2006, ages ~ 10 Gyr). Chemical abundances of Bar and disc stars are marked by black squares and grey dots, respectively (from Van der Swaelmen et al. 2013, ages $\gtrsim 1$ Gyr).

(Sect. 5). In Fig. 11.6 I show the $[\text{O}/\text{Fe}]$ and $[\text{Mg}/\text{Fe}]$ vs. $[\text{Fe}/\text{H}]$ diagrams. Abundances measured with SNRs (i. e. that of the ISM gas phase) are compared with that measured in older populations: old globular clusters from Johnson et al. (2006, ages ~ 10 Gyr) and Bar and disc field red giant stars from Van der Swaelmen et al. (2013, ages $\gtrsim 1$ Gyr). Although uncertainties from X-ray spectral fitting are substantial, there is a very clear trend for SNRs to be at higher metallicity ($[\text{Fe}/\text{H}]$) and lower $[\alpha/\text{Fe}]$ (in particular $[\text{O}/\text{Fe}]$). This reflects the continued enrichment by type Ia SNe in the last ~ 1 Gyr, which inject large amounts of Fe back in the ISM and drive younger populations towards the bottom right corner of the $[\alpha/\text{Fe}] - [\text{Fe}/\text{H}]$ diagrams. There are SNR-to-SNR variations in the abundances, but the metallicity scatter in the ISM gas phase is less than for field stars. In particular there is no metal-poor population ($[\text{Fe}/\text{H}] \lesssim -0.8$). I also checked that there is no clear correlation between location of an SNR in the $[\alpha/\text{Fe}] - [\text{Fe}/\text{H}]$ diagrams and the SFH around the SNR. For instance, SNRs with relatively high $[\alpha/\text{Fe}]$ are not necessarily in regions with increased recent SF, which would produce massive stars that release low- Z elements. Despite the uncertainties and the limited size of the sample, this lack of correlation likely indicates that SNe-produced elements are well mixed in the ISM. In other words, the ISM is quickly homogenised, at least at the spatial scales over which SFH is measured (~ 200 pc).

After LMC abundances were measured (e. g. Russell & Dopita 1992), Tsujimoto et al. (1995) found with chemical evolution models that the deficit of light α -elements of the MCs (i. e. lower $[\alpha/\text{Fe}]$ for a given $[\text{Fe}/\text{H}]$) compared to the Galaxy must be explained by a smaller $N_{\text{CC}}/N_{\text{Ia}}$ (more type Ia SNe). They measured a Galactic ratio of 6.7, but $N_{\text{CC}}/N_{\text{Ia}} \sim 4 - 5$ and ~ 3.3 for the LMC and SMC, respectively. My results for the LMC ISM abundance suggest an even lower ratio $N_{\text{CC}}/N_{\text{Ia}}$, because the deficit of light α -elements is wider than previously assumed by Tsujimoto et al. (1995). By tentatively typing all LMC remnants, I show in Sect. 11.4 that indeed $N_{\text{CC}}/N_{\text{Ia}}$ is particularly low, compared to previous measurements of the ratio in the LMC or inferred from galaxy cluster X-ray observations, and discuss likely explanations.

TABLE 11.4 – 1T/2T SNRs with detected ejecta (top part), and used for measurements of ISM composition (bottom part)

MCSNR	Old name	SN type	High X/Fe flags				Low X/Fe flags			
			O	Ne	Mg	Si	O	Ne	Mg	Si
J0453-6829	B0453-685	CC	—	—	Y	Y	—	—	—	—
J0506-6541	—		—	Y	—	—	—	—	—	—
J0506-7026	[HP99] 1139		—	—	—	—	Y	Y	Y	—
J0508-6830	—	Ia	—	—	—	—	Y	—	—	—
J0508-6902	[HP99] 791	Ia	—	—	—	—	Y	—	—	—
J0511-6759	—	Ia	—	—	—	—	Y	—	—	—
J0519-6926	B0520-694		—	Y	Y	Y	—	—	—	—
J0523-6753	N44		Y	Y	Y	—	—	—	—	—
J0525-6559	N49B	CC	—	Y	Y	Y	—	—	—	—
J0526-6605	N49	CC	Y	—	Y	Y	—	—	—	—
J0529-6653	DEM L214		Y	—	—	—	—	—	—	—
J0531-7100	N206		Y	—	—	Y	—	—	—	—
J0533-7202	1RXSJ053353.6-7204		—	—	—	—	—	—	Y	—
J0534-6955	B0534-699	Ia	—	—	—	—	Y	Y	Y	—
J0534-7033	DEM L238	Ia	—	—	—	—	Y	Y	Y	Y
J0535-6602	N63A	CC	Y	Y	—	—	—	—	—	Y
J0535-6918	Honeycomb		—	—	—	Y	—	—	—	—
J0536-6735	DEM L241	CC	Y	Y	Y	—	—	—	—	—
J0536-6913	B0536-6914	CC	Y	—	—	—	—	—	—	—
J0536-7039	DEM L249	Ia	—	—	—	—	Y	Y	Y	Y
J0537-6628	DEM L256		—	—	—	—	—	—	Y	—
J0547-6941	DEM L316A	Ia	—	—	—	—	Y	Y	Y	Y
J0547-7025	B0548-704	Ia	—	—	—	—	Y	Y	Y	—

		ISM abundance			
		O & Fe	Ne	Mg	Si
J0450-7050	B0450-709	Y	Y	Y	—
J0453-6655	N4	Y	Y	Y	—
J0453-6829	B0453-685	CC	Y	Y	—
J0454-6626	N11L		Y	Y	—
J0505-6802	N23	CC	Y	Y	Y
J0514-6840	—		Y	—	—
J0518-6939	N120		Y	Y	Y
J0519-6926	B0520-694		Y	—	—
J0527-6912	B0528-692		Y	Y	Y
J0528-6727	DEM L205		Y	—	—
J0531-7100	N206	CC	—	Y	—
J0532-6732	B0532-675		Y	Y	Y
J0533-7202	1RXSJ053353.6-7204		Y	Y	—
J0535-6918	Honeycomb		Y	Y	—
J0543-6858	DEM L299		Y	Y	Y
J0547-6943	DEM L316B		Y	Y	Y

Notes. The classification given (type Ia or core-collapse) is described in Sect. 11.3.1.

TABLE 11.5 – LMC abundances

Element	X/X_{\odot} (1)	N (2)	RMS (3)	$12 + \log(X/H)$	Hughes et al. (1998)	RD92
O	0.21	15	0.08	$8.01^{+0.14}_{-0.21}$	8.21 ± 0.07	8.35 ± 0.06
Ne	0.28	13	0.08	$7.39^{+0.11}_{-0.15}$	7.55 ± 0.08	7.61 ± 0.05
Mg	0.33	11	0.19	$6.92^{+0.20}_{-0.37}$	7.08 ± 0.07	7.47 ± 0.13
Si	0.69	6	0.42	$7.11^{+0.20}_{-0.41}$	7.04 ± 0.08	$7.81^{(a)}$
Fe	0.35	15	0.12	$6.97^{+0.13}_{-0.18}$	7.01 ± 0.11	7.23 ± 0.14

Notes. (1) Abundance relative to the solar value of [Wilms et al. \(2000\)](#). (2) Number of SNRs used to measure X/X_{\odot} . (3) RMS scatter amongst the N SNRs. ^(a) Silicon abundance was quoted as highly uncertain in [Russell & Dopita \(1992\)](#)

11.3. Phenomenology as function of SNR type

USING ALL possible typing methods, it is possible to firmly establish the SN origin for a sensible fraction of the LMC SNR sample. Doing so, I can study their evolution, look for similarities between SNR classes, or establish the main factors resulting in differences. Ways of deducing the type of SN explosion that created a given remnant were introduced in Sect. 5.5. I applied them to the SNR sample of Sect. 11.3.1, before discussing the properties of the type Ia and CC SNRs (Sect. 11.3.2 and 11.3.3).

11.3.1. Selection of SNRs with secured classifications

11.3.1. A. Type Ia SNRs

The spectacular case of MCSNR J0509–6731: One of the few SNRs less than a thousand years old, this object was first typed as a type Ia remnant by Tuohy et al. (1982) based on the Balmer-dominated optical spectrum. This classification was confirmed by the analysis of the ASCA spectrum, revealing ejecta emission rich in nucleosynthesis products of thermonuclear SNe (Hughes et al. 1995). Finally, light echoes from the SN, scattered off interstellar dust, were detected around four LMC SNRs (Rest et al. 2005). Optical spectroscopy of the light echoes of MCSNR J0509–6731 allowed Rest et al. (2008) to determine the SN spectral type as an overluminous 1991T-like SN Ia.

Balmer-dominated SNRs with X-ray-detected ejecta: Tuohy et al. (1982) also detected Balmer-dominated emission from MCSNR J0519–6902, J0505–6753 (DEM L71), and J0547–7025, concluding that they were produced by type Ia events. In the two former cases, the X-ray spectra clearly showed emission from the ejecta of thermonuclear SNe (Hughes et al. 1995, 2003; van der Heyden et al. 2003). For J0547–7025, the *Chandra* spectra revealed ejecta but the O/Fe ratio was not as decisive (Hendrick et al. 2003). Furthermore, this remnant was an outlier in Lopez et al. (2009, 2011), with a morphology more consistent with the sample of CC-SNRs. The observations of the XMM-*Newton* survey confirm the iron-rich nature of J0547–7025 (Table A.2), and therefore secure a type Ia classification consistent with the optical data.

Middle-aged to evolved iron-rich SNRs: Several remnants with ages exceeding 10^4 yr revealed iron-rich X-ray spectra (observed with XMM-*Newton* and *Chandra*) that betrayed their type Ia nature. MCSNR J0534–6955 was first identified as such with *Chandra* (Hendrick et al. 2003) and XMM-*Newton* observations give similar results (Table A.2). Slightly more evolved, MCSNR J0534–7033 and J0536–7039 (DEM L238 and L249, respectively) have a more pronounced separation of the shell and central iron-rich plasma (Borkowski et al. 2006a). The shell A of DEM L316 (MCSNR J0547–6941) has striking spectral differences to the very close neighbour MCSNR J0547–6943 (DEM L316B): the former is also mostly exhibiting Fe L-shell emission, which leads to the interpretation that it is another type Ia remnant (Nishiuchi et al. 2001; Williams & Chu 2005).

Then come the three iron-rich SNRs that I presented in Sect. 10.2. Finally, since the publications of those remnants in MHK14 and BKM14, me and collaborators obtained XMM-*Newton* follow-up observations of two remnants, which we classified as type Ia: *i*) MCSNR J0506–7026 was a ROSAT-selected candidate ([HP99] 1139), which revealed a remnant similar to DEM L238 and L249, about 17-21 kyr old and holding about $0.9 M_{\odot}$ - $1 M_{\odot}$ in the central region (Whelan et al. 2014, Table A.2); *ii*) MCSNR J0527–7104 was confirmed by our group in a multi-wavelength study (Kavanagh et al. 2013). A subsequent observation (performed 2014 May 31) revealed yet another iron-rich core (with an unusual morphology, see below), so that this source completes the (currently known) sample of LMC SNRs with a secured type Ia origin.

11.3.1. B. Core-collapse SNRs

Remnants hosting a compact object: Several neutron stars have been detected inside LMC SNRs, mostly powering a pulsar wind nebula (PWN). MCSNR J0540–6920 is the prototypical example: It hosts the pulsar PSR B0540–69 and is known as a twin of the Crab nebula (Kaaret et al. 2001). MCSNR J0537–6910 (N157B) is also dominated by a PWN around PSR J0537–6910 (Chen et al. 2006). Fainter, less obvious PWNe have been found in MCSNR J0453–6829 (Gaensler et al. 2003; Haberl et al. 2012a) and in MCSNR J0535–6602 (Williams et al. 2005). In the latter, the case for a PWN is not as strong; however, analysis of the X-ray morphology using a power-ratio method (Lopez et al. 2009) confirm the classification as CC-SNR.

Chandra observations (Hughes et al. 2006) of MCSNR J0505–6802 (N23) revealed, in addition to regions with enhanced O-group elements, a point source in the centre of the remnant that shows properties similar to compact central objects (CCOs) seen in other CC-SNRs, such as Cas A. Finally, a point source was detected in the “Head” of MCSNR J0536–6735 (DEM L241, see Bamba et al. 2006, and Fig. 11.9) using XMM-*Newton* observations and first classified as candidate PWN. With *Chandra* observations, Seward et al. (2012) could show that the source was not extended and identified the optical counterpart as an O5III(f) star. Based on this and the X-ray variability and spectrum, they concluded that the SNR was hosting an HMXB, akin to SXP1062 in the SMC (Hénault-Brunet et al. 2012).

Detection of the remains of massive star nucleosynthesis: MCSNR J0525–6938 (N132D), the brightest SNR in the LMC, belongs to the class of oxygen-rich remnants. Many clumps of X-ray emitting O-ejecta are detected in X-ray observations (Borkowski et al. 2007) and match the optical ejecta morphology seen by *Hubble*. Park et al. (2003b) have revealed a highly-enhanced Mg abundance and derived a large mass of Mg ejecta from MCSNR J0525–6559 (N49B), strongly suggesting a massive stellar progenitor. This classification is supported by the X-ray morphology of the remnant (Lopez et al. 2009).

The nearby MCSNR J0526–6605 (N49) is a more puzzling case. No compelling evidence for overabundant O or Fe is found, but Si- and S-rich ejecta features are detected by *Chandra* (Park et al. 2003a, 2012). These can be interpreted as explosive O-burning or incomplete Si-burning deep inside a CC SN explosion; however, the Si/S ejecta mass ratio favour a type Ia origin (Park et al. 2003a, 2012). The soft gamma-ray repeater SGR 0526-66 lies in projection in the remnant, favouring the CC-SNR scenario, although the physical association between the remnant and the SGR is uncertain (Gaensler et al. 2001; Kaplan et al. 2001). The best evidence to terminate the debate over the nature of N49 comes from the properties of its Fe K emission, which is clearly in the region occupied by CC-SNRs (Yamaguchi et al. 2014, Sect. 11.2.3. C). MCSNR J0535–6916 (N63A) is another case where ejecta features are detected but cannot yield a definite classification (Warren et al. 2003). As for N49, however, the Fe K emission allows to include N63A in the sample of secured CC-SNRs.

SNR 1987A: Last but not least comes the remnant with the most secured classification of all, as the SN itself was observed and its progenitor identified in pre-explosion images (see Sect. 9 and references therein).

The list of LMC remnants with secured CC and type Ia classifications is given in Table 11.6.

TABLE 11.6 – LMC remnants with a secured SN classification

MCSNR	Other name	Age (yr)	Evidence ^(a)	References ^(b)
Core-collapse SNRs				
J0536–6916	SNR 1987A	28	Historical	Maggi et al. (2012b)
J0540–6920	B0540–693	~1600	Pulsar	Kaaret et al. (2001)
J0525–6938	N132D	~3150	Ejecta, morphology	Borkowski et al. (2007)
J0535–6602	N63A	2000–5000	Ejecta, Fe K	Warren et al. (2003)
J0536–6913	—	2200–4900	Ejecta	Kavanagh et al. (2015)
J0505–6802	N23	~4600	Ejecta, CCO, morphology	Hughes et al. (2006)
J0526–6605	N49	~4800	Ejecta, SGR, Fe K	Park et al. (2012)
J0537–6910	N157B	~5000 ^(c)	PWN	Chen et al. (2006)
J0525–6559	N49B	~10000	Ejecta, morphology	Park et al. (2003b)
J0536–6735	DEM L241	> 10 ⁴ ^(c)	HMXB	Seward et al. (2012)
J0453–6829	B0453–685	12000–15000	PWN, morphology	Haberl et al. (2012a)
J0531–7100	N206	~25000	PWN candidate, morphology	Williams et al. (2005)
Type Ia SNRs				
J0509–6731	B0509–675	400±120	Light echo, ejecta Fe K, morphology	Rest et al. (2008)
J0509–6844	N103B	860	Ejecta, Fe K	Hughes et al. (1995)
J0519–6902	B0519–690	600±200	Ejecta, Fe K, morphology	Hughes et al. (1995)
J0505–6753	DEM L71	~4700	Ejecta, Fe K, morphology	Hughes et al. (1998, 2003)
J0547–7025	B0548–704	~7100	Ejecta	Hendrick et al. (2003) , this work
J0534–6955	B0534–699	~10000	Ejecta, morphology	Hendrick et al. (2003)
J0534–7033	DEM L238	~13500	Ejecta	Borkowski et al. (2006a)
J0536–7039	DEM L249	~15000 ^(c)	Ejecta	Borkowski et al. (2006a)
J0506–7026	[HP99] 1139	17000–21000	Ejecta	Whelan et al. (2014) , this work
J0508–6902	[HP99] 791	20000–25000	Ejecta	BKM14 , Sect. 10.2
J0527–7104	[HP99] 1234	~25000	Ejecta	Kavanagh et al. (2013) , this work
J0547–6941	DEM L316A	~27000 ^(c)	Ejecta	Williams & Chu (2005)
J0511–6759	—	~> 20000 ^(c)	Ejecta	MHK14 , Sect. 10.2
J0508–6830	—	~> 20000 ^(c)	Ejecta	MHK14 , Sect. 10.2

Notes. Ages for the first three type Ia SNRs are from light echo measurements ([Rest et al. 2005](#)).

^(a) Morphology: Typed from X-ray morphology by [Lopez et al. \(2009, 2011\)](#). Fe K: Typed from the properties of the Fe K emission by [Yamaguchi et al. \(2014\)](#), see also Sect. 11.2.3.C). CCO: Central compact object. PWN: Pulsar wind nebula. SGR: Soft gamma-ray repeater.

^(b) Because of the multiple studies on most remnants, the given references are “see [...] and references therein”.

^(c) Uncertain age.

11.3.2. Snapshots of type Ia SNRs life: A new evolutionary phase

X-ray images of all the type Ia SNRs listed in Table 11.6 are shown in Fig. 11.7. SNRs are arranged by increasing age (although it can be quite uncertain for some of the older objects). In Fig. 11.8, the corresponding sequence is seen in optical lines (data from MCELS). The sequence shows a strikingly contiguous evolution, considering that all images show unrelated objects. Several phases are readily observable:

- (I) **Ejecta-dominated phase in X-rays** for SNRs less than a thousand years old (Sect. 5.2). These remnants are only a few parsecs in radius. The images (with *Chandra*) reveal the clumpy structure of the X-ray emitting ejecta.
- (II) SNRs between 1000 and 10000 yr (early Sedov phase) with **well-defined limb-brightened X-ray shells around central emission**. The spectra of the shell have ISM abundances and mark the propagation of the blast wave in the ambient medium. Abundance measurements establish that the central regions are dominated by hot ejecta (chiefly iron), which produce prominent X-ray emission (similar surface brightness than the shell).
- (I)-(II) SNRs at $t < 10^4$ yr are **optically Balmer-dominated**: Almost exclusively $H\alpha$ is detected, which is interpreted as non-radiative fast shocks overtaking (partially) neutral gas (Chevalier & Raymond 1978; Chevalier et al. 1980, Sect. 5.5). This type of emission becomes fainter with time (e. g. B0548–704) and fades out after $\sim 10^4$ yr. SNR B0534–699 marks this optical transition, with only faint $H\alpha$ emission and wisps of [S II] along the northern limbs, indicating slower shocks.
- (III) Between roughly 1 and 2×10^4 yr (late Sedov phase), the **X-ray emission of the shell becomes fainter and softer**, but the iron-rich cores remain bright and hot ($0.6 \text{ keV} \lesssim kT \lesssim 0.9 \text{ keV}$). At the same time, optical emission resumes but is qualitatively different. In particular, the [O III] emission detected all around the shells marks the radiative cooling of the ISM overrun by slow shocks. This culminates in MCSNR J0508–6902, which also has the faintest shell detected. With these type Ia SNRs, we are therefore witnessing the transition of the shell into the radiative phase, as shocks are getting slower and slower, UV/optical lines are quickly cooling down the shell, and X-ray emission is fading out.
- (IV) Older SNRs are best seen in X-rays, because **the iron cores remain at X-ray emitting temperatures**. In optical lines, only weak features are found, such as the elliptical shell with enhanced [S II]/ $H\alpha$ around MCSNR J0527–7104 (Kavanagh et al. 2013). Only the shell of DEM L316A remains relatively bright in [S II] and $H\alpha$. This might be the last cooling stage of the swept-up ISM, which leaves only the very faint, “fossil” [S II] shells around the two oldest object of the sequence (J0511–6759 and J0508–6830, see Sect. 10.2.3. A)

This evolutionary interpretation is also supported by the (sparse) UV data available. In the early stages (up to DEM L71), the UV spectra are dominated by broad Lyman lines from fast non-radiative shocks (Ghavamian et al. 2007), the same shocks that produce the Balmer-dominated spectra in the optical. SNRs at the end of the Balmer-dominated phase (B0548–7104 and B0534–699) are not detected in the UV (Blair et al. 2006). The detection of UV lines resumes for older SNRs in the phase (III) described above. In DEM L238 and L249, Blair et al. (2006) reported the detection of C III $\lambda 977$ and O VI $\lambda 1032, 1038$ lines, which are the main coolant for plasma at $T \sim 0.8$ and 3.2×10^5 K, respectively (Cox & Daltabuit 1971). Together with their [O III] emission (main cooling line in the optical for $T \sim 10^5$ K) we see the radiative cooling behind the blast wave. The relative contribution of C III (vs. O VI) is higher in DEM L249 than in DEM L238, consistent with the former being slightly more evolved, and therefore having more cooler material than the latter. No UV observation of MCSNR J0506–7026 or J0508–6902 exist, but it is clear from the prominent [O III] shell of J0508–6902 that it is similar to DEM L238 and L249. Based on the smaller contribution of the shell in X-rays, I can predict that UV observations of J0508–6902 should reveal an even larger C III/O VI line ratio than in DEM L249, because most of the shell cooled down below 10^5 K. From phase (IV), only DEM L316A was observed in UV (the other SNRs were not known at the time of Blair et al. 2006). No emission was detected, indicating that most of the material is too cool to emit X-ray and UV light. It is likely to be the case for the other old SNRs as well, since their optical emission is qualitatively similar (only [S II] and $H\alpha$) but fainter.

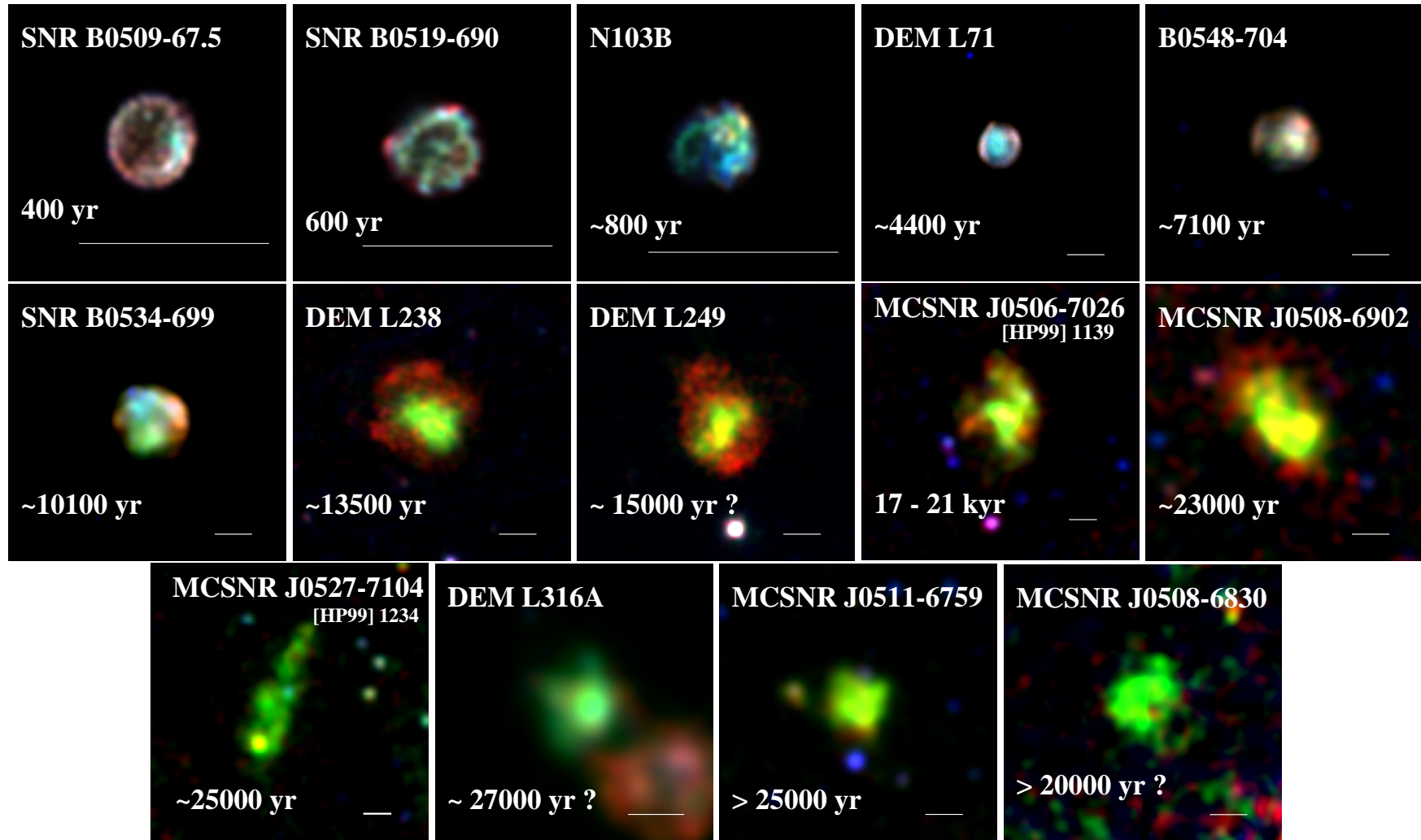


FIGURE 11.7 – Evolutionary sequence of well-established type Ia SNRs in the LMC (sample described in Sect. 11.3.1.A). For the three youngest objects, *Chandra* images are shown, using event files available from the *Chandra* SNR catalogue (see Sect. 11.5). For all others I show *XMM-Newton* images. For those, the red, green, and blue components are soft (0.3–0.7 keV), medium (0.7–1.1 keV), and hard (1.1–4.2 keV) X-rays. The medium band is dominated by Fe L-shell lines, and the iron-rich interiors, appearing greenish, are readily distinguished from the limbs (when existing) in evolved objects (second and third row). The white bars indicate the scale of 1'. The sequence is sorted by increasing age (references in Table 11.6). North is up and east is left.

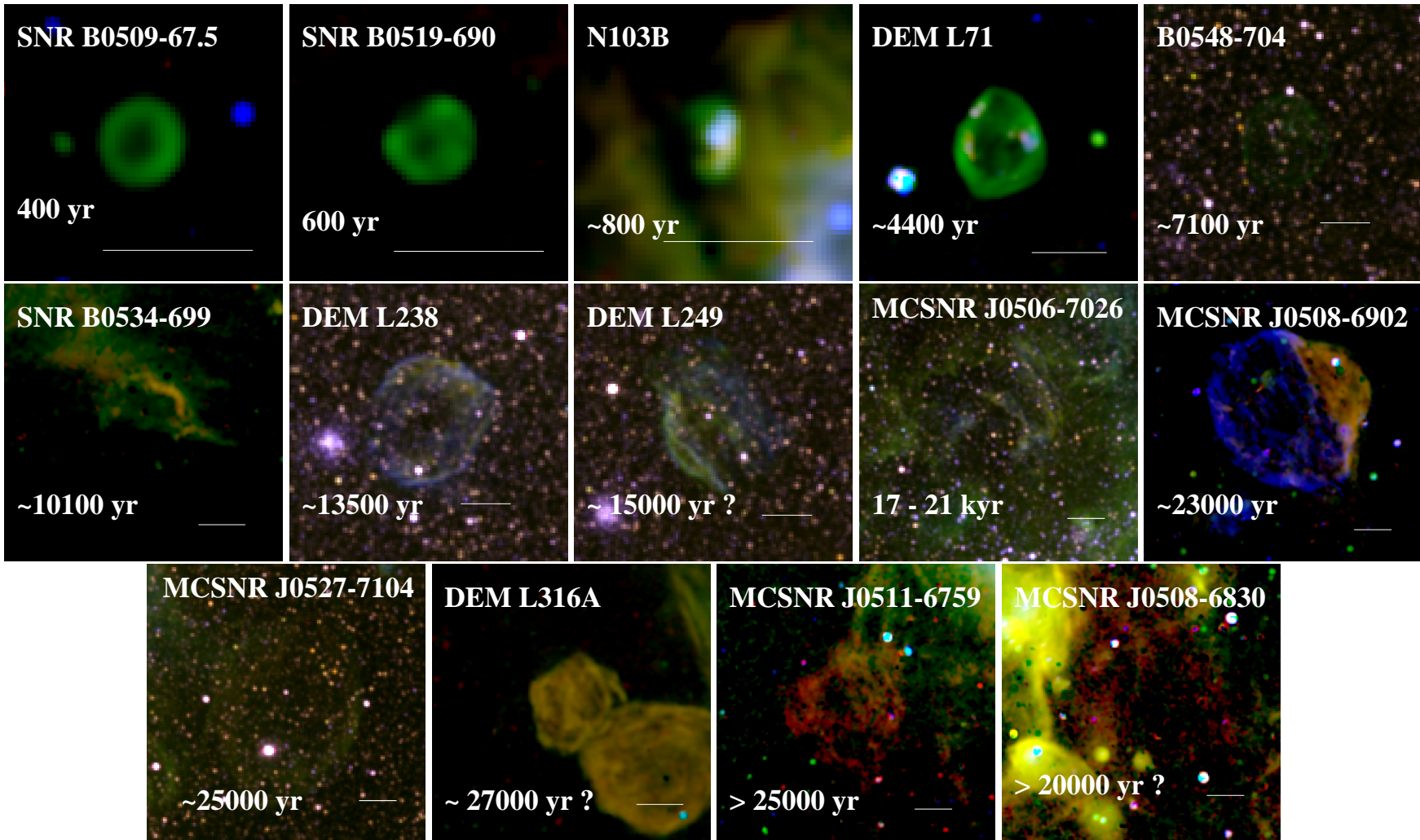


FIGURE 11.8 – Same as Fig. 11.7 but in the light of [S II] (red), H α (green), and [O III] (blue), where all data are from the MCELS. Continuum-subtracted images were used (prepared by Sean Points), except for five SNRs (where nearby stars are evident).

Before my PhD thesis, the only known old type Ia SNRs in the sequence of Fig. 11.7 was DEM L316A which appeared atypical at best, while the middle-aged SNRs DEM L238 and DEM L249 were potentially considered to originate from a distinct class of SN Ia (Borkowski et al. 2006a). **The five new type Ia SNRs added to the sample during my thesis provide the missing link in the evolutionary sequence. They also establish the existence of a previously overlooked phase in the life of SNRs,** where *i*) the outer blast wave is too slow to produce fresh X-ray emitting material; *ii*) the shocked shell has radiatively cooled down below X-ray and UV temperatures, but *iii*) the iron-rich ejecta in the central region are still hot. In this last phase, the remnants are most obvious in X-rays.

The reasons why iron cores remain hot are unclear, and could include heating at later times by (secondary) reverse shocks propagating within the ejecta. Thermal emission could be also hindered at the boundary of the ejecta, which is expanding in the low-density region excavated by the outer blast wave, leaving only the inefficient radiative cooling by iron lines and Bremsstrahlung.

Another puzzling feature is the morphological diversity of the iron cores at late times ($t \gtrsim 13500$ yr). All show departures from spherical symmetry. Many are elongated (in ellipsoids). MCSNR J0527–7104 is the extreme example. In that case and also for J0508–6902, the elongation runs along the same axis as the symmetry axis of the shell/blast wave, suggesting a common origin. On the other hand, no connection between the morphology of the cores and shells is apparent in DEM L238 and L249. In DEM L316A, the iron-rich emission is enhanced in the centre (see Williams & Chu 2005, for analysis of high-spatial resolution *Chandra* data). At the old end of the sequence, data are too shallow for a definite conclusion, although I noted in Sect. 10.2.3. A that J0508–6830 is likely elongated in the north-south direction, while a candidate ejecta shrapnel is visible at the east of the main emission of J0511–6759.

One final question is whether the remnants of the sequence in Fig. 11.7, in particular the evolved ones, are created by a special kind of type Ia SN (provided all Ia SNe are not strictly the same), as was initially suggested by Borkowski et al. (2006a). That question is inherently difficult to address because of the lack of a “control group”: If some evolved type Ia remnants exist without retaining hot ejecta, we will not be able to identify them as such, because other typing method (light echoes, Balmer-dominated optical spectra, Fe K line properties) are not applicable beyond 10000 yr. However, using a new method to tentatively type all LMC SNRs (in next section), I propose that 23^{+3}_{-4} SNRs (out of the *current* sample) are of type Ia. In other words, the SNRs shown in Fig. 11.7 represent at least half of all type Ia SNRs. If several classes of type Ia SN exist, then it is likely that those producing remnants with hot iron cores at late times are the rule rather than the exception.

11.3.3. The wide variety of core-collapse SNRs

In Fig. 11.9 I show XMM-*Newton* images of the CC SNRs from Table 11.6, again sorted by increasing age. In stark contrast to the type Ia SNRs of Fig. 11.7, no clear evolutionary trend emerges from this sequence. Core-collapse SNRs display more morphological and spectral variety than type Ia. The presence of a compact stellar remnant can profoundly modifies the appearance of the remnant: the young pulsar in MCSNR J0540–6920 dominates its X-ray emission. In J0537–6910 (N157B) the supersonic motion of the interior bright pulsar and its wind nebula result in the comet-shaped nebula Chen et al. (2006). A similar, elongated morphology is seen for DEM L241, except that instead of pulsar, the bright point source in an HMXB (Seward et al. 2012). In other cases (MCSNR J0453–6829, N23, N49), a stellar remnant is detected but has a very minute impact on the evolution of the SNR or its appearance. Some of the CC SNRs were typed as such based on the detection of ejecta emission. However, as opposed to the evolved type Ia SNRs, there are no mature CC SNR were the ejecta is dominating the emission.

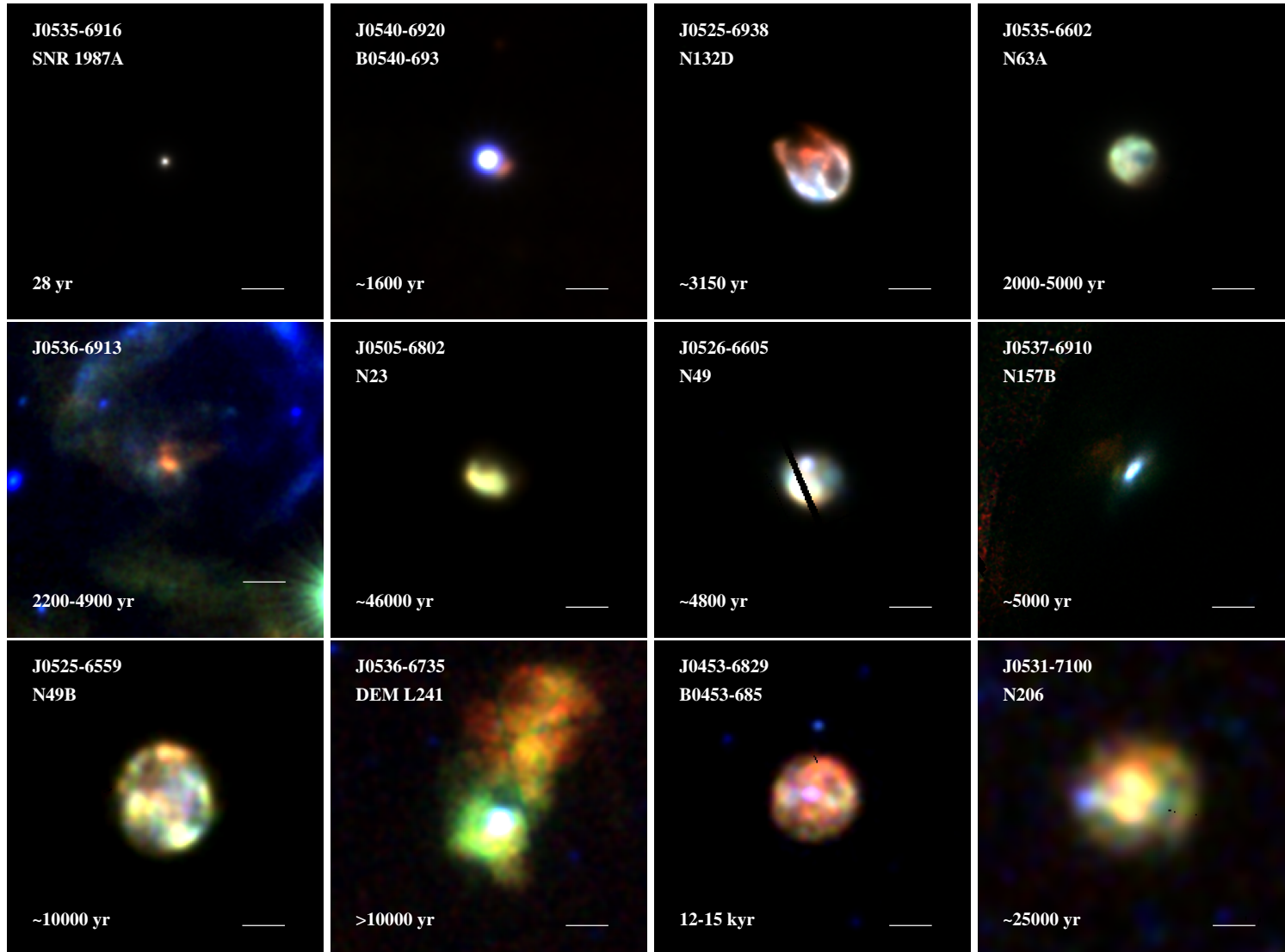


FIGURE 11.9 – Same as Fig. 11.7 for CC SNRs. Only XMM-Newton data are used. The white bar indicates the scale of $1'$, which is used for all images.

11.4. Measuring the ratio of CC to type Ia SNe using “SFH-typing”

ONLY A FRACTION of the LMC remnants has been given a secured classification. This “secured-type” sample is presented in Sect. 11.3.1 and listed in Table 11.6. Based on the local stellar environment of LMC SNRs, which is assessed as described in Sect. 11.4.1, I devised a method to tentatively type the rest of the sample. This method is calibrated with the “secured-type” sample and applied in Sect. 11.4.2. Finally, I discuss the measured ratio of CC to type Ia SNRs and its implications in Sect. 11.4.3.

11.4.1. Evaluating the local stellar environment

I devised two metrics to assess the local stellar environment of LMC SNRs. Both ultimately stem from the same set of data (the MCPS catalogue of Zaritsky et al. 2004). Although connected, they still measure two distinct properties and are therefore complementary, as I discuss below.

- **N_{OB} , the number of blue early-type stars in the immediate vicinity of the remnant:**

To obtain this number, I constructed a V vs. $(B - V)$ CMD of all stars within a 100 pc radius around each SNR. This value corresponds to the drift distance for a star of age 10^7 yr at a velocity of 10 km s^{-1} and was used by Chu & Kennicutt (1988). The upper main-sequence of stars in the LMC was identified by adding the stellar evolutionary tracks of Lejeune & Schaerer (2001), for $Z = 0.4 Z_{\odot}$ and initial masses from $3 M_{\odot}$ to $40 M_{\odot}$. I assumed a distance modulus of 18.49 and an extinction $A_V = 0.5$ (the average extinction for “hot” stars, Zaritsky et al. 2004). From there, I used the criteria of $V < 16$ and $B - V < 0$ to identify OB stars. This was used in Sect. 10.1 for DEM L205: In the resulting CMD (Fig. 10.7, page 69), a prominent upper-main sequence is obvious. The number of OB stars identified is in that case $N_{\text{OB}} = 142$. Another example (Fig. 11.10) shows the CMD of the region around MCSNR J0534–6955, devoid of young massive stars. For this remnant, N_{OB} is only 8.

- **$r = N_{\text{CC}}/N_{\text{Ia}}$, the ratio of CC SNe to thermonuclear SNe expected from the observed distribution of stellar ages in the neighbourhood of the remnants:**

This number is obtained via the spatially resolved SFH map of Harris & Zaritsky (2009, see Sect. 4.1.3). For each SNR I plot the SFR of the cell including the remnant as a function of lookback time and metallicity. Two example SFHs are shown in Fig. 11.11, corresponding to MCSNR J0528–6727 and MCSNR J0534–6955, for which CMDs are shown in Figs. 10.7 & 11.10 to exemplify the use of N_{OB} . They are strikingly different: The SFR around J0528–6727 soared in the last 20 Myr, when the numerous early-type stars in the vicinity of the remnant were formed. On the other hand, the star formation around J0534–6955 peaked (at a lower absolute rate) about 125 Myr ago and was shut down in the most recent 20 Myr.

Because stars might drift away from their birth place, one potentially important caveat is that the SFH of a cell hosting a SNR may be derived from stars having no physical connection with the SNR progenitor. For a detailed discussion on the relevance of local stellar populations to the study of progenitors, I point to Badenes et al. (2009). However, I stress that most of the information that can be gained from the study of the local

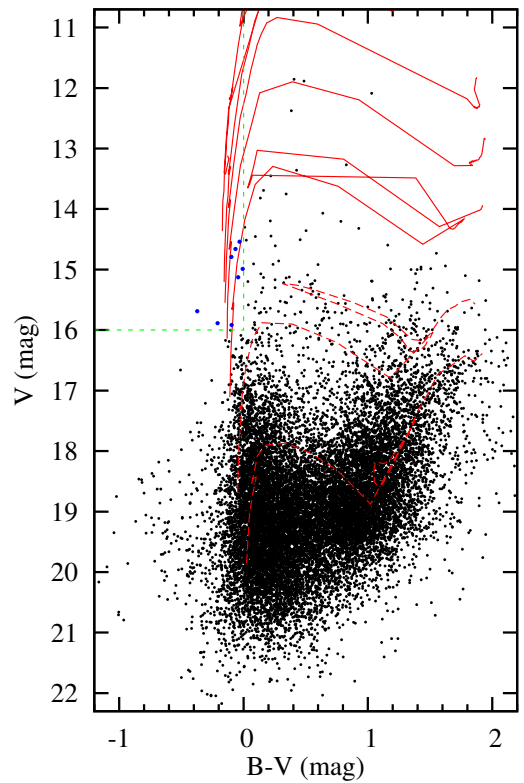


FIGURE 11.10 – CMD of the MCPS stars around MCSNR J0534–6955. Stellar evolution tracks (red) and selection criteria (green) as in Fig. 10.7.

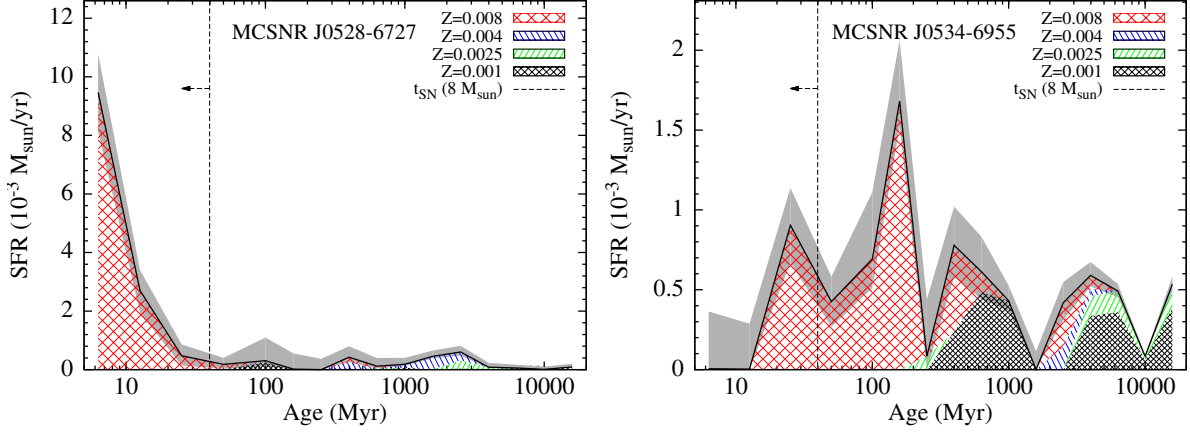


FIGURE 11.11 – Star formation history around MCSNR J0528–6727 (left) and J0534–6955 (right). Data are taken from [Harris & Zaritsky \(2009\)](#). The star formation rate in four metallicity bins are plotted against lookback time. The errors (combining all metallicities) are shown by the gray shading. The vertical dashed line at 40 Myr indicates the maximal lifetime of a CC SN progenitor. Note the changing vertical scale.

SFHs, in the context of typing remnants, is contained in the most recent time bins. Namely, the presence of recent star formation episode is a strong necessary (but not sufficient) condition to tentatively type a remnant as having a CC origin. Conversely, the lack of recent star-forming activity favours a thermonuclear origin.

To approach this question in a quantitative way, I did the following: I used the delay time distribution (DTD) $\Psi_i(\tau)$, the SN rate at time τ following a star formation event, measured by [Maoz & Badenes \(2010\)](#) in the Magellanic Clouds, with $i = 1, 2, \text{ and } 3$ designating the time intervals they used ($t < 35$ Myr, $35 \text{ Myr} < t < 330$ Myr, and $330 \text{ Myr} < t < 14$ Gyr, respectively). From timescale arguments it is reasonably assumed that Ψ_1 will correspond to the CC-SN rate, whilst Ψ_2 and Ψ_3 will be that of SNe Ia (regardless of their “prompt” or “delayed” nature). The SFR is integrated to obtain M_i , the stellar mass formed in each time interval. The SFH of [Harris & Zaritsky \(2009\)](#) is only given at $t = 25$ Myr and $t = 50$ Myr. To obtain M_1 , the mass formed at $t < 35$ Myr, I approximate $M(25 < t < 35)$ as half that formed between 25 Myr and 50 Myr (the second half is included in M_2). Likewise, I split the mass formed between $t = 250$ Myr and $t = 400$ Myr in two and include a half in both M_2 and M_3 .

Then, I compute $r = N_{\text{CC}}/N_{\text{Ia}}$ as the ratio of the *rates* of CC and Ia SNe, since the visibility times are the same for both types, i. e.:

$$r = \frac{\Psi_1 M_1}{\Psi_2 M_2 + \Psi_3 M_3} \quad (11.1)$$

Over the visibility time of a remnant — taking 100 kyr as a very conservative limit — the stars in the SFH cell including the remnant will not drift away. In other words, the distribution of stellar ages observed *now* is the same as that when the SN exploded. r is therefore a measure of the relative size of the pool of possible progenitors of both types. Using the same example SNRs as in Fig. 11.11, a value of $r = 9.0^{+1.9}_{-4.9}$ is obtained for J0528–6727⁴¹ while for J0534–6955 it is only $r = 1.2 \pm 0.1$.

⁴¹The uncertainty given for r solely includes that of the mass formed M_i , which is computed from uncertainties of the SFR given in [Harris & Zaritsky \(2009\)](#). The uncertainties on Ψ_2 and Ψ_3 are larger, but are the same for all SNRs in the sample, allowing to use r in a comparative fashion. I adopted $\Psi_2 = 0.26 \text{ SNe yr}^{-1} (10^{10} M_{\odot})^{-1}$ and $\Psi_3 < 0.0014 \text{ SNe yr}^{-1} (10^{10} M_{\odot})^{-1}$. Note that because Ψ_3 is an upper limit, r is formally a lower limit.

11.4.2. “SFH-typing” all LMC SNRs

I now proceed to give a tentative type to the whole sample of SNRs in the LMC, using N_{OB} and r . I assign two numbers called “Hint–CMD” and “Hint–SFH”, depending on the N_{OB} and r -value obtained for each SNR, respectively. The numbers range from 1 meaning “strongly favours a type Ia SN origin”, to 5 meaning “strongly favours a CC-SN origin”. I used the distribution of N_{OB} and r for the sample of “secured-type” SNR to establish the correspondence between their values and the hints.

This method is conceptually similar to that used by [Chu & Kennicutt \(1988\)](#), albeit with several improvements: Firstly, the sample in this work is twice the size of that available to [Chu & Kennicutt](#). Secondly, many (~ 25) SNRs have now a secured type (Sect. 11.3.1) and can be used to calibrate the method and evaluate the rate of erroneous classification. Then, the completeness of the census of early-type stars in the vicinity of the remnants is higher, owing to the use of the MCPS catalogue. Finally, the spatially-resolved SFH reconstruction was simply unavailable before [Harris & Zaritsky \(2009\)](#).

Calibration of the “SFH-typing”: The number of OB stars in the vicinity of the secured type Ia and CC SNRs is shown in Fig. 11.12. The two samples are rather well separated: The majority of type Ia SNRs have less than 20 early-type stars in their neighbourhood, while most of the CC-SNRs have $N_{\text{OB}} > 30$. The single major type Ia outlier is N103B ($N_{\text{OB}} = 99$), which is known to be in a region with a vigorous recent star formation activity (e.g. [Badenes et al. 2009](#)). MCSNR J0453–6829 is the only CC-SNRs to have a moderate N_{OB} (< 25). The choice of “Hint-CMD” is given in Table 11.7 to reflect this distribution: N_{OB} less than 5 (less than 35) strongly (moderately) favours a type Ia classification, while N_{OB} in excess of 80 (35) strongly (moderately) favours the CC-SN case.

Intuitively, any value $r > 1$ should favour a CC SN origin (conversely for a thermonuclear origin). However, an important caveat to interpret r is that the rates of [Maoz & Badenes \(2010\)](#), especially Ψ_2 and Ψ_3 , are quite uncertain, due to the still limited sample of SNRs. Specifically, Ψ_2 has a value that changes by a factor of four depending on the tracer used to constrain the SNR visibility time. To provide a better feeling on what r -value to expect in either case (and to decide where is the separation), I show the count distribution of secured type Ia and CC SNRs in the r -domain in Fig. 11.12. There is a stronger overlap of both types in the intermediate range ($2.2 \lesssim r \lesssim 3.5$) than with N_{OB} . However, the lower end ($r < 2.2$) still includes most of the type Ia SNRs, without contamination by the other type. N103B is again the only outlier at $r = 6.2$; above 3.4 only CC-SNRs are found. In view of this observed distribution, the ratio $r = N_{\text{CC}}/N_{\text{Ia}}$ still is a

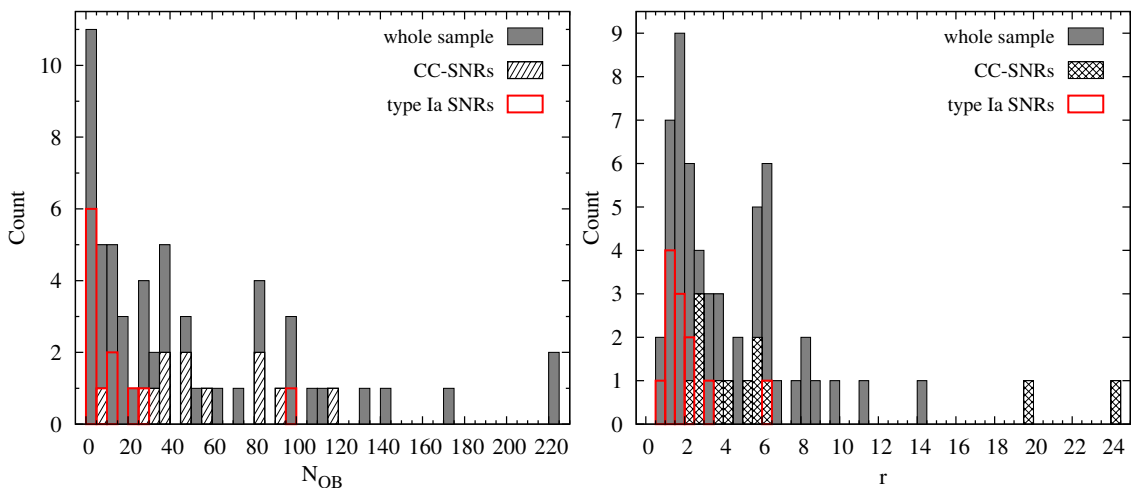
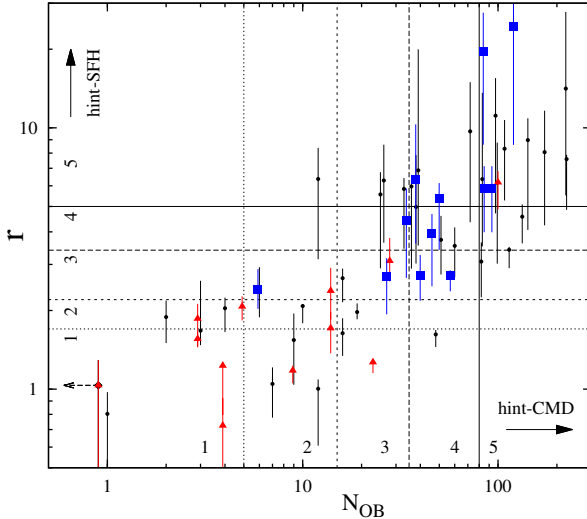


FIGURE 11.12 – Count distribution of LMC SNRs as function of N_{OB} and r (left and right, respectively). The distribution for the SNRs with a secured CC classification is shown with the hatched boxes; that for type Ia SNRs is outlined in red.

TABLE 11.7 – Criteria and “Hints” attributed to SNRs as function of N_{OB} and r .

Value	Hint-CMD	Hint-SFH	Meaning
1	$N_{\text{OB}} < 5$	$r < 1.7$	Strongly favours a type Ia SNR
2	$5 \leq N_{\text{OB}} < 15$	$1.7 < r < 2.2$	Moderately favours a type Ia SNR
3	$15 \leq N_{\text{OB}} < 35$	$2.2 < r < 3.4$	Undecided
4	$35 \leq N_{\text{OB}} < 80$	$3.4 < r < 5$	Moderately favours a CC-SNR
5	$80 \leq N_{\text{OB}}$	$5 < r$	Strongly favours a CC-SNR


FIGURE 11.13 – r – N_{OB} diagram of LMC SNRs. Secured Ia and CC SNRs are marked by red triangles and blue squares, respectively; the rest of the sample is shown with black dots. The arrow in the lower left corner indicate an SNR $N_{\text{OB}} = 0$. The regions corresponding to different “Hint-SFH” and “Hint-CMD” are marked by the gridding.

useful tool to assign a type to SNRs using the observed local SFH, and should be valid in a comparative and statistical sense. The “Hints-SFH” attributed to the sample based on r are listed in Table 11.7. r and N_{OB} are also displayed as scatter plot for secured Ia and CC SNRs (Fig. 11.13). There, the regions corresponding to different “Hints” are marked.

Caveat on the complementarity of N_{OB} and r : It is clear that the two metrics are connected. Both are based on the MCPS catalogue; the early-type stars detected in a cell drive the fitting of the most recent time bins in the SFH reconstruction of Harris & Zaritsky (2009). However, the r -value of a cell can be moderate even though N_{OB} is high, as evident from the scatter along the horizontal axis in Fig. 11.13. That is because r is a *relative* measure of the recent SFR compared to that at earlier epochs, while N_{OB} gives a measure of the *absolute* strength of the recent star formation. In the (high N_{OB} –moderate r) case, there are many available progenitors of both CC- and type Ia SN; these are typically cases where the classification is inconclusive.

Results for the whole sample: The count distributions for all LMC SNRs in the N_{OB} and r spaces are shown in Fig. 11.12, and as scatter plot in Fig. 11.13. They are similar, with larger numbers, to the distributions of the secured-type SNRs. About twenty remnants are in regions with a low number of early-type stars ($N_{\text{OB}} < 15$) and not dominated by recent SF ($r \lesssim 2$). There is a peak at $r \sim 6$ with a dozen remnants. Those are SNRs in star-forming regions which are widely spread across in the LMC. They are often associated with giant H II complexes (e. g. LHA-120 N4, N11, N44). The objects with extreme values for r ($\gtrsim 8$) also have the largest N_{OB} . Those are located in the two most intensively star-forming regions of the LMC: 30 Doradus, and the rim of the supergiant shell LMC 4 (which embeds the “Constellation III” region, Harris & Zaritsky 2008, 2009).

To combine the two “Hints” into one, I computed the arithmetic mean of Hint-CMD and Hint-SFH. The resulting “star-formation Hint” (Hint-SF) again range from 1 to 5. Its distribution for the whole sample and the secured-type SNRs is shown in Fig. 11.14. There are 19 remnants with $\text{Hint-SF} \leq 2$; they most likely all result from a type Ia SN. I call this sample “likely-Ia”. Likewise, the 28 objects above $\text{Hint-SF} \geq 4$ are probably most of the CC-SNR population. They form the “likely-CC” sample.

The single type Ia SNR contaminating the sample (N103B) allows to estimate a false-positive rate of 5 % – 10 %. The false-positive rate of the “likely-Ia” sample is probably lower: The massive stars formed at (roughly) the same time as the progenitor of a CC-SNR can hardly be missed by photometric survey, because they would form the bright end of the population.

There are 12 SNRs in between $2.5 \leq \text{Hint}_{\text{SF}} \leq 3.5$, for which the local stellar environment cannot be used to decisively type the origin; they form the “SFH-untyped” sample. Interestingly, two and five of these remnants can be classified from other indicators as type Ia (the iron-rich MCSNR J0508–6830 and DEM L71) or CC-SNRs (e. g. the oxygen-rich N132D or MCSNR J0453–6829, which hosts a PWN), respectively.

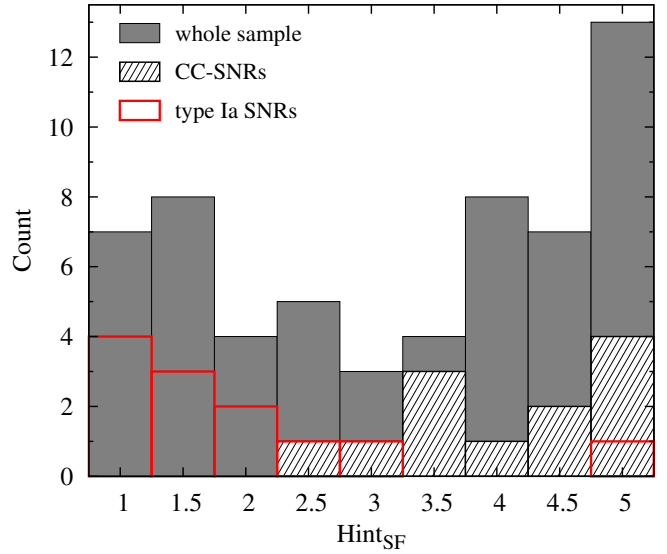


FIGURE 11.14 – Count distribution of the LMC SNRs as function of “Hint-SF”, combining N_{OB} and r (see text for details). Hatching and colours as in Fig. 11.12.

Including the spectral results for typing purpose The spectral analysis of Sect. 11.2 revealed the presence of ejecta-enhanced plasma in almost half of the sample (Tables 11.3 and A.3). One should take advantage of this for the typing of the remnant, in combination with the SFH-based method I just presented. I assign another number, “Hint-spec”, which depends on the high- or low-abundance flags of each SNR (Sect. 11.2.3.D). The numbers range from 1 (strongly favouring a type Ia origin) if “low X/Fe” flags are raised (i. e. the SNR is iron-rich), to 5 (strongly favouring a CC origin) when “high X/Fe” flags are raised (i. e. CC nucleosynthesis pattern is detected).

TABLE 11.8 – “Hint-spec” attributed to SNRs as function of spectral results.

Hint-spec	Criteria
1	at least three “low X/Fe” flags, no “high X/Fe” flag
1.5	two “low X/Fe” flags or low O/Fe, no “high X/Fe” flag
2	one “low X/Fe” flag (except O/Fe), no “high X/Fe” flag
2.5	low Si/Fe, no “high X/Fe” flag
3	ISM abundances, unfitted abundances, or no XMM-Newton data
3.5	high Si/Fe, no “low X/Fe” flag
4	one “high X/Fe” flag (except O/Fe), no “low X/Fe” flag
4.5	two “high X/Fe” flags or high O/Fe, no “low X/Fe” flag
5	at least three “high X/Fe” flags, no “low X/Fe” flag; pulsar/PWN detected

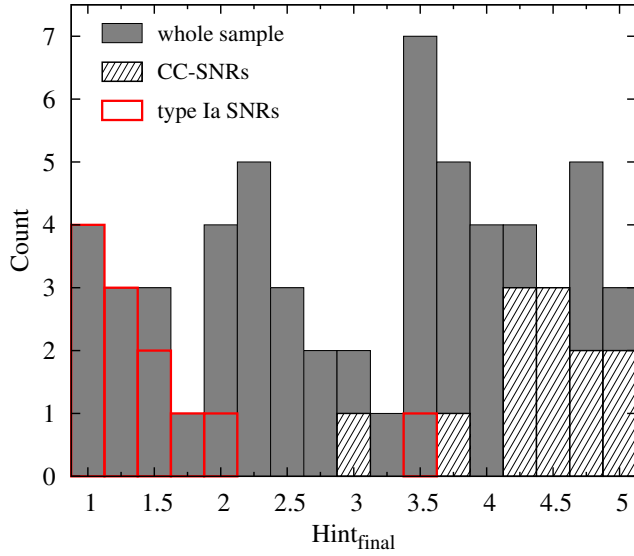


FIGURE 11.15 – Count distribution of the LMC SNRs as function of “Hint-final”, combining spectral and SFH information. Hatching and colours as in Fig. 11.12.

The choice of “Hint-spec” is given in Table 11.8. Note that a bigger impact is given to the low or high O/Fe ratio, as these elements are the most abundant. Therefore, this ratio is easier to fit, more reliable, and sometimes the only one available (e. g. for the new SNRs of Sect. 10.2). A value of 5 is also attributed to remnants where a pulsar/PWN is detected in the remnant. I combined “Hint-SF” and “Hint-spec” by taking their arithmetic mean. The distribution of the resulting “Hint-final” is shown in Fig. 11.15. The contamination (i. e. misclassification of N103B) is slightly alleviated, while a better separation of the “secured-type” SNRs is evident. There are 23 SNRs with “Hint-final” ≤ 2.5 which are likely of type Ia, and 31 SNRs where “Hint-final” ≥ 3.5 which are likely attributed to CC, although N103B (Hint-final=3.5) is still contaminating the sample. There are five sources with unconclusive “Hint-final”, including one secured-CC (N23).

11.4.3. Ratio of CC to type Ia SNe and implications

The observed number of SNRs of both types provides a measurement of the ratio of CC to type Ia SNe that exploded in the LMC over the last few 10^4 yr, i. e. very close to the current ratio of CC/Ia rates. Based on the “star formation Hint”, the numbers of SNRs in the “likely Ia” and “likely CC” samples translate in $N_{CC}/N_{Ia} = 1.47$ (28/19). Assuming all “SFH-untyped” SNRs which do not have a secured type are of type Ia then the ratio N_{CC}/N_{Ia} is 1.27 (33/26). Conversely, if the ‘SFH-untyped’ are all CC, the ratio is 1.81 (38/21). Even correcting for N103B, N_{CC}/N_{Ia} is conservatively in the range 1.2 to 1.8.

Including the spectral results (detection of ejecta in X-rays), we have a ratio $N_{CC}/N_{Ia} = 1.35$ (31/23). Correcting for N103B and N23 (with wrong and uncertain classifications), the ratio CC:Ia based on SFH and X-ray spectroscopy is between 1.11 (31/28) and 1.46 (35/24), depending on the type assigned to the remaining four objects. This range is compatible with that derived from the “SFH-typing” alone, albeit narrower because of the greater amount of information included in the calculation.

This ratio can be compared to two kinds of measurements: First, to the observed ratio of current rates, obtained from SNe search. For instance, Li et al. (2011b) measured a ratio of about 3:1 in a volume-limited sample. Second, to the ratio N_{CC}/N_{Ia} derived from ICM abundances. Galaxy clusters retain all the metals produced by SNe. The X-ray spectrum of the ICM reveals the elemental abundances, which are used to constrain the integrated numbers of CC and Ia SNe. From *Suzaku* observations of a small sample of clusters and groups of galaxies, Sato et al. (2007) estimated $N_{CC}/N_{Ia} \sim 3.5$ (ranging between 2 and 4, depending on the type Ia model used). With *XMM-Newton* and a larger cluster sample, de Plaa et al. (2007) measured a N_{CC}/N_{Ia} between 1.7 and 3.5, again depending on the adopted SN Ia models. However, none of the models explored could reproduce the Ar/Ca ratio. Lovisari et al. (2011) derived $N_{CC}/N_{Ia} \sim 1.5 - 3$. Therefore, **the current ratio of CC/Ia SNe in the LMC is significantly lower than that measured in local SNe surveys and in galaxy clusters.**

One possible caveat could be that we are missing CC-SNRs. For instance, SNe exploding in superbubbles (see references in Sect. 4.3.2.B) will not be directly recognised as SNRs. Wang & Helfand (1991) and Dunne et al. (2001) found a dozen SBs with an X-ray luminosity, measured with *Einstein* and ROSAT, brighter than theoretically expected for a wind-blown bubble, and possibly energised by interior SNRs. The

limited spatial resolution of the instruments used may result in *distinct* SNRs to have been overlooked and the X-ray emission of the SB overestimated (e. g. MCSNR J0523–6753, near the H II region/SB N44 in Wang & Helfand 1991, see also Jaskot et al. 2011). With a dozen extra CC SNRs, the ratio $N_{\text{CC}}/N_{\text{Ia}}$ is pushed to $\sim 1.5 - 2$. However, the number of type Ia SNRs currently known in the LMC is also expected to be below the actual number (see Sect. 11.5 for a discussion on sample completeness). Therefore, it is unlikely that the ratio $N_{\text{CC}}/N_{\text{Ia}}$ is significantly underestimated. Furthermore, the abundance pattern of the LMC, with its low $[\alpha/\text{Fe}]$ (Sect. 11.2.3. E), lends support to such a low $N_{\text{CC}}/N_{\text{Ia}}$. This should be lower than the value of $N_{\text{CC}}/N_{\text{Ia}} \sim 4 - 5$ estimated by Tsujimoto et al. (1995).

The low $N_{\text{CC}}/N_{\text{Ia}}$ ratio measured in the LMC therefore has to be a consequence of the different SFH of the Cloud compared to that in other nearby galaxies or galaxy clusters. The local SNe rates depend on the summed SFH of galaxies included in the SN surveys. The higher ratio measured by e. g. Li et al. (2011b) simply indicates that many star-forming galaxies are included in the local volume explored. The SFHs of galaxy clusters are relatively simple, with short episodes of star-formation at a redshift of $z \sim 3$ (Eisenhardt et al. 2008), so that the integrated numbers of type Ia and CC SNe inferred from X-ray observations correspond to the fractions of stars formed that end their lives as SN of either type.

In the LMC, star formation occurred during several episodes. In addition to many regions with recent or ongoing star formation where, unsurprisingly, the CC-SNRs are found (Sect. 11.6), the LMC had enhanced star formation episodes 100 Myr, 500 Myr, and 2 Gyr ago as well (Harris & Zaritsky 2009, Sect. 4.1.3). The SN Ia DTD follows fairly well a t^{-1} power law for delays $t > 1$ Gyr, and appear to keep increasing below 1 Gyr (for a review of SN Ia DTD measurements, see Maoz & Mannucci 2012). The majority of type Ia SNe explode within 2 Gyr after star-forming episodes. We are therefore coincidentally observing the LMC at a time when the rate of type Ia SN from the stellar populations formed 500 Myr to 2 Gyr ago is high. Integrated over an SNR lifetime (a few 10^4 yr), it results in the relatively large number of type Ia SNRs. It is not possible to use $N_{\text{CC}}/N_{\text{Ia}}$ to estimate η , the fraction of stars that eventually explode as Ia SNe (Maoz 2008), because of the complex SFH of the LMC: stars exploding now (as either SN types) were created at different epochs. Furthermore, η is also dependent on the initial mass function (IMF), over which one has little freedom, since the SFH-reconstruction already assumes a particular form (the Salpeter IMF).

There are no galaxy with which to compare the $N_{\text{CC}}/N_{\text{Ia}}$ of the LMC. In our own Milky Way, there remain too many untyped SNRs. More problematic are the distance uncertainties that prevent associating remnants to regions of star formation (e. g. spiral arms). In the Local Group (M31, M33) and beyond (e. g. M83 Dopita et al. 2010), the problem is again the lack of secured typing methods, and generally the absence of spatially-resolved SFH. The situation is likely to improve in the near future with more sensitive X-ray observatories (e. g. *Athena*), and large observing programmes of M31 and M33 with *Hubble* which allow to build SFH maps (so far, this was done in the few archival field available, Jennings et al. 2012, 2014). The SMC is the only obvious target remaining where a similar study can be currently performed, although the smaller sample of SNRs and inclination of the galaxy (and corresponding line-of-sight confusion) might complicate direct comparisons to the LMC.

11.5. X-ray luminosity function of SNRs in the Local Group

X-RAY LUMINOSITY FUNCTIONS (XLFs) are valuable tools for the study of X-ray sources and comparisons between populations. The XMM-Newton dataset is ideally suited to derive the XLF of LMC SNRs. Out of the 59 objects in the sample, XMM-Newton covered 51 of them, to which I fitted spectral models (Sect. 11.2). For all these, the X-ray fluxes in various bands are obtained from the best-fit models (Tables A.2 and A.3) with the XSPEC command `flux`. The final results are presented in the “broad” band, from 0.3 keV to 8 keV (the effect of including the high-energy part is very minor and discussed below).

Three SNRs have been covered with *Chandra* but not XMM-Newton: For MCSNR J0454–6713 (N9), I used the spectral results of Seward et al. (2006) to measure the flux. MCSNR J0459–7008 (N186D) was covered in the *Chandra* observation of the SB DEM L50. Jaskot et al. (2011) published the results from these data. I used their best-fit NEI model for the SNR emission, which is spatially resolved from the SB, to derive the X-ray flux. Finally for MCSNR J0550–6823, I used the spectral parameters given in the entry of the *Chandra* SNR catalogue⁴².

Two SNRs have neither XMM-Newton nor *Chandra* observations available, but were covered with ROSAT. Williams et al. (1999b) present a spectral analysis of MCSNR J0455–6839 (in N86). I obtained the X-ray flux of the SNR using their best-fit model. MCSNR J0448–6700 corresponds to the ROSAT PSPC source [HP99] 460, with a count rate of 1.41×10^{-2} cts s⁻¹. With the multi-mission count rate simulator WebPIMMS⁴³, I calculated the flux in several energy bands for various temperatures of an APEC model, assuming a total absorbing column $N_H = 7 \times 10^{20}$ cm⁻² towards the source and a mean abundance of 0.4 solar. The observed hardness ratios could be reproduced for $kT = 0.97$ keV. These spectral parameters and normalisation can be converted into fluxes in the same bands as used for the rest of the sample.

In total, 56 objects have well-defined X-ray fluxes and make it into the XLF. The adopted values are listed in Table A.1. Only three SNRs have no X-ray data available. The cumulative XLF is shown in Fig. 11.16. The L_X used is the observed value, uncorrected for (LMC) absorption, because the fitted column densities can be quite uncertain, in particular in the faint end. The sample spans almost four orders of magnitude in luminosity, from the brightest (N132D) at $L_X = 3.15 \times 10^{37}$ erg s⁻¹ down to $\sim 7 \times 10^{33}$ erg s⁻¹.

SNR XLF from other Local Group galaxies: The LMC XLF can be best compared to other Local Group galaxies such as M31, M33, and the SMC. Sasaki et al. (2012) studied M31 SNRs and candidates identified in the XMM-Newton Large Programme survey of the Andromeda galaxy (Stiele et al. 2011). They converted EPIC count rates into 0.35 keV – 2 keV luminosities assuming a thermal (APEC) spectrum with $kT = 0.2$ keV, $N_{H\text{ M31}} = 10^{21}$ cm⁻², and $N_{H\text{ MW}} = 0.7 \times 10^{21}$ cm⁻². The quoted values, however, are corrected for $N_{H\text{ MW}}$, while for the LMC I give the observed luminosities. For consistency with the LMC XLF, I re-included $N_{H\text{ MW}} = 0.7 \times 10^{21}$ cm⁻² in the results of Sasaki et al. (2012) and converted the luminosity in the 0.3 keV – 8 keV by scaling their L_X by 0.577 (a factor derived from simulating their assumed spectrum with and without $N_{H\text{ MW}}$). Note that the effect of the foreground absorption should be very minor, since $N_{H\text{ MW}}$ values are very similar in the directions of M31, M33, and the LMC ($5 - 7 \times 10^{21}$ cm⁻²). 26 objects were confirmed SNRs in Sasaki et al. (2012), and another 20 were candidate SNRs.

Long et al. (2010) present the most complete catalogue of M33 SNRs, based on the *Chandra* ACIS survey of M33 (ChASem33), which contains 82 detections (i. e. confirmed SNRs). They give L_X in the 0.35 keV – 2 keV band, converted from ACIS count rates, assuming a thermal plasma at 0.5 solar, $kT = 0.6$ keV, and total $N_H = 10^{21}$ cm⁻² (i. e. the spectrum found for the brightest source). I obtained the corresponding 0.3 keV – 8 keV luminosity by scaling up the values of Long et al. (2010) by 4 %.

Converting count rate to luminosity in different energy bands assuming a single temperature might affect the slope of the XLF. For instance, from a count rate in the 0.35 keV – 2 keV band, the luminosity in the

⁴²Maintained by Fred Seward: <http://hea-www.cfa.harvard.edu/ChandraSNR/index.html>

⁴³<http://heasarc.gsfc.nasa.gov/cgi-bin/Tools/w3pimms/w3pimms.pl>

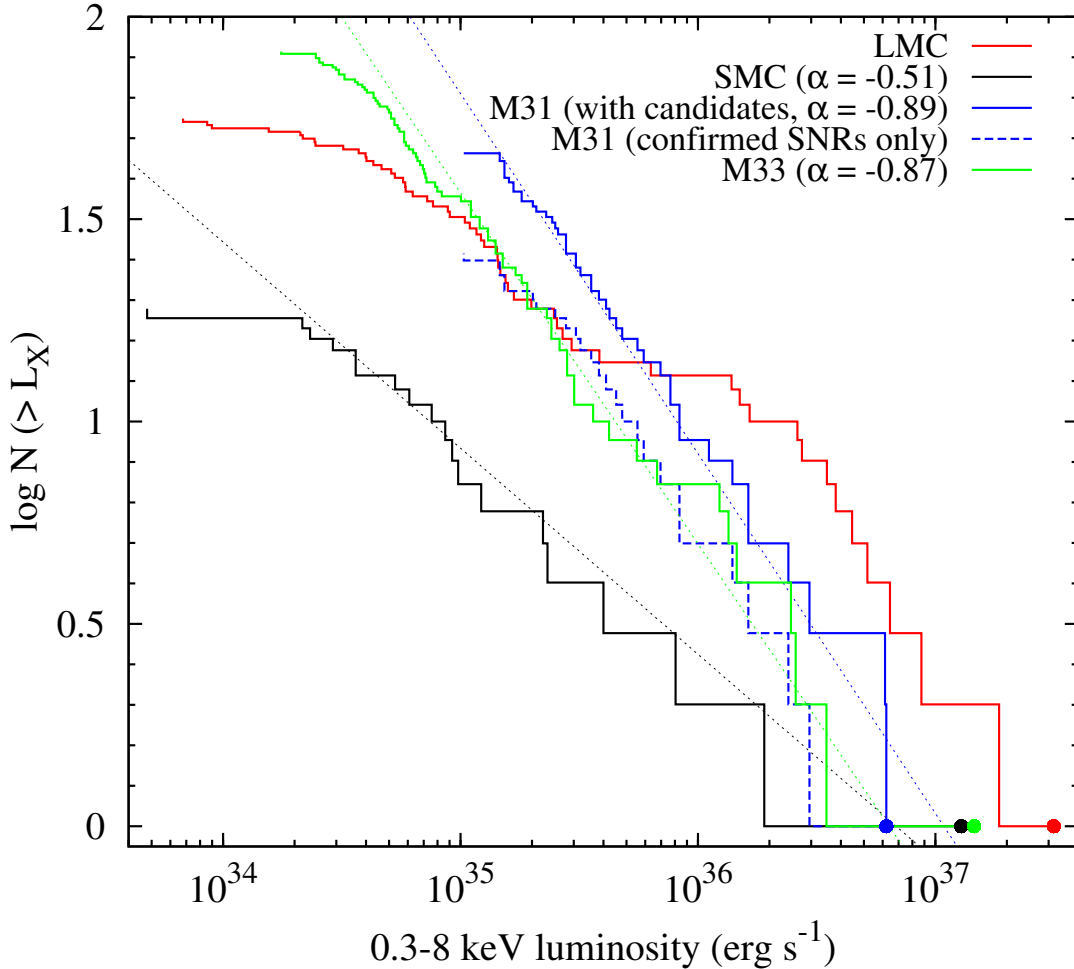


FIGURE 11.16 – Cumulative X-ray luminosity function of SNRs in Local Group galaxies. See text for details and references on how L_X was measured for each sample. The brightest SNR in each galaxy is marked by a dot. The dashed lines are nonlinear least-square fits of a power law ($N(> L_X) \propto L_X^\alpha$) for $L_X > 2 \times 10^{34} \text{ erg s}^{-1}$ (SMC), $10^{35} < L_X < 10^{36} \text{ erg s}^{-1}$ (M33), and for the full luminosity range of M31. Slopes α are given in the legend. These fits are only used to characterise the slopes and illustrate the differences between galaxies; they do not represent a physical fit of the population.

broad band is 25 % higher with $kT = 0.6 \text{ keV}$ than if it is 0.2 keV . The two studies have limited knowledge of the actual spectrum of each remnant, because the larger distances prohibit more complex spectral fits, and they have to assume a particular spectrum, regardless of luminosity. This is not the case in the LMC. I found a trend for brighter remnants to have higher plasma temperatures (Sect. 11.2.3. A). Quantitatively, the median temperatures are $kT = 0.31 \text{ keV}$ for luminosities less than $10^{35} \text{ erg s}^{-1}$, 0.55 keV between $10^{35} \text{ erg s}^{-1}$ and $10^{36} \text{ erg s}^{-1}$, and 0.8 keV above $10^{36} \text{ erg s}^{-1}$. The luminosities of M31 SNRs were given assuming $kT = 0.2 \text{ keV}$; I scaled the $0.3 \text{ keV} - 8 \text{ keV}$ luminosity up by 1.05, 1.20, and 1.35 for sources with $L_X < 10^{35}$, $10^{35} < L_X < 10^{36}$, and $L_X > 10^{36} \text{ erg s}^{-1}$, respectively. M33 SNRs were assumed to have a higher temperature (0.6 keV), which means that the luminosity of objects below $\sim 10^{35} \text{ erg s}^{-1}$ was overestimated by about 15 %, while for those above $10^{36} \text{ erg s}^{-1}$ it was underestimated by $\sim 8 \%$. Correcting for this effect ensures a meaningful comparison between M31, M33, and the LMC.

The SMC SNR population is comparatively smaller. [van der Heyden et al. \(2004\)](#) presented an X-ray spectral analysis of all SNRs in the SMC known at that time. I used their best-fit models to measure

the observed (i. e. absorbed) X-ray luminosity in the same 0.3 keV – 8 keV band⁴⁴, except for IKT 16. For this SNR I used results from Owen et al. (2011), which included more data from subsequent XMM-Newton observations. Three additional SNRs were covered with XMM-Newton; the results were published in Filipović et al. (2008), from which I borrowed the best-fit spectral models. The latter study also reported a new SNR, HFPK 334. For this one, I used the best-fit model from Crawford et al. (2014), which combined XMM-Newton and Chandra observations. Also included is the SNR XMMU J0056.5–7208 identified during the SMC survey (Haberl et al. 2012b; Sturm 2012). Finally, the Be/X-ray binary pulsar SXP 1062 was found to be associated to an SNR, of which it is most likely the progenitor (Hénault-Brunet et al. 2012). The thermal emission from the SNR was studied by Haberl et al. (2012c). This sample of 19 SMC SNRs is the most up to date.

Comparative study of SNR XLFs: The cumulative XLFs of M31 and M33 in the 0.3 keV – 8 keV band, corrected for the $kT - L_X$ trend, are shown along that of the SMC and LMC in Fig. 11.16. **In terms of depth**, the LMC XLF dominates. There is a single SNR at $L_X < 2 \times 10^{34}$ erg s⁻¹ in M33 and in the SMC, but the bright interior pulsar in the SMC case (SXP 1062) makes the measurement of the thermal emission luminosity uncertain. In contrast, there are eight SNRs with $L_X \lesssim 2 \times 10^{34}$ erg s⁻¹ in the LMC, of which seven were discovered or confirmed thanks to XMM-Newton observations.

In terms of number, the largest population so far is found in M33 (82 X-ray-confirmed SNRs), probably owing to the depth of the Chandra survey (using 100 ks pointings) and the favourable (face-on) orientation of M33. However, the population of M31 SNRs is larger than any other at $L_X \lesssim 5 \times 10^{35}$ erg s⁻¹ and is only limited by the depth of the survey ($\sim 10^{35}$ erg s⁻¹). The ratio of M31-to-M33 SNRs in the $10^{35} - 10^{36}$ erg s⁻¹ range is at most two, i. e. substantially smaller than the mass ratio of the galaxies (10–20, Corbelli 2003; Peñarrubia et al. 2014). This shows the effect of the higher (recent) SFR in M33 compared to M31 ($0.45 M_\odot \text{ yr}^{-1}$ vs. $0.27 M_\odot \text{ yr}^{-1}$, Verley et al. 2009; Tabatabaei & Berkhuijsen 2010) leading to a larger production of CC SNRs in M33. In the same luminosity range, the number of LMC SNRs is comparable to that in M33. This is expected because the LMC is only slightly less massive than M33. Furthermore, the recent SFR of the LMC is high, $0.3\text{--}0.4 M_\odot \text{ yr}^{-1}$ in the last 40 Myr (Fig. 4.1, Harris & Zaritsky 2009). This conspires with the high current type Ia SN rate (Sect. 11.4.3) to build up the large population of SNRs in the LMC. Finally, the “feather-weight” SMC (about ten times less massive than the LMC, Stanimirović et al. 2004; Harris & Zaritsky 2006) has a smaller, yet decent population of remnants, likely owing to its recent star formation activity ($0.08\text{--}0.3 M_\odot \text{ yr}^{-1}$, Harris & Zaritsky 2004).

In terms of shape, the XLF of M31 SNRs is the most uniform, following a power law ($N(> L_X) \propto L_X^{-\alpha}$) with $\alpha \sim -0.9$ down to $\sim 2 \times 10^{35}$ erg s⁻¹. This holds with or without including the candidates, which means that most are indeed bona-fide SNRs. The M33 remnants follow mostly the same distribution. There was a marginal indication that the M33 distribution was steeper than that of M31 (Sasaki et al. 2012), but this difference disappears once the $kT-L_X$ trend is taken into account. A small excess is seen above 5×10^{35} erg s⁻¹, as already noted by Sasaki et al. (2012). Towards the faint end, the M33 XLF flattens and diverges from the power law below 10^{35} erg s⁻¹, indicating incompleteness. Long et al. (2010) concluded that no SNR brighter than 4×10^{35} erg s⁻¹ was missed across the surveyed field. It is likely that they were over-conservative and that missing SNRs are only those which have luminosity below 10^{35} erg s⁻¹. The ChASem33 survey does not cover the total extent of the galaxy (Plucinsky et al. 2008), so a number of SNRs are also expected to be still absent from the XLF. In the SMC, although the population is limited to about 20 objects, the distribution is relatively uniform. The XLF is however flatter ($\alpha \sim -0.5$), which might indicate that SMC remnants evolve faster (and fade earlier) than in M31 and M33, due to a lower ISM density. The lower metallicity in the SMC (about 0.2 solar, Russell & Dopita 1992) also participates in the lower luminosities of the SMC SNR.

⁴⁴The luminosity given in van der Heyden et al. (2004), Table 3, for IKT 22 (1E0102–7219, the brightest SMC SNR) was mistyped. Instead of the 150×10^{27} W, it should read 1500×10^{27} W (1.5×10^{37} erg s⁻¹).

In contrast to the other galaxies, the luminosity function of SNRs in the LMC exhibits a complex behaviour and does not follow a smooth power-law distribution over most of the dynamical range. The most striking and robust result is the very prominent bright end of the LMC XLF. There are 13 SNRs with $L_X > 10^{36}$ erg s⁻¹, more than in M31 and M33. Amongst these, there are two SNRs hosting bright pulsars/PWNe and a harder non-thermal spectrum. Even restricting the XLF to the soft band or excluding these two objects, the population of bright LMC SNRs is still above the other ones. This bright population is not a clearly distinct group. In particular, it is not made up of remnants from only one SN type. There are four type Ia SNRs and nine CC-SNRs, so the N_{CC}/N_{Ia} ratio is higher than overall (Sect. 11.4.3), but not exceedingly so. Higher luminosities are expected from SNRs interacting with denser ISM. I compared the average LMC HI column density (from the map of Kim et al. 2003) around the position of remnants in various luminosity bins, but no trend could be found. However, the line-of-sight integrated column density might not be a good indicator of the ISM density *local* to the remnant, considering that the SNR could be in front of or behind the regions where most of the neutral hydrogen is (see Sect. 11.6).

A possible explanation for the population of bright SNRs in the LMC stems from its lower metallicity. Massive stars lose a considerable amount of mass in the form of winds (e. g. Kudritzki & Puls 2000). The stellar winds blow low-density cavities, bordered by dense shells, around the stars that eventually explode as (core-collapse) SNe. The interaction of the SN shocks with the modified CSM results in a different evolution compared to that in a constant-density ISM. Dwarkadas (2005, 2007, and references therein) explored the evolution of remnants in wind-blown cavities. It was shown that it critically depends on one parameter (coined Λ), the ratio of the mass of the dense shell to that of the ejected material. For low values ($\Lambda < 1$) the X-ray luminosity increases sharply when the shock reaches the dense shell early on ($t < 10^3$ yr). If instead the shell is more massive compared to the ejecta material, the shock propagates in the very low density of the (much larger) bubble, producing less X-ray emission. The increase of X-ray luminosity upon impact (after a few thousand years) is also smaller than in the low- Λ case (Dwarkadas 2005, his Figs. 7 and 12). The properties of the cavities around massive stars are determined by the mass loss rate \dot{M} during their various evolutionary stages. This in turn is affected by the elemental abundance (i. e. metallicity), because the main driving mechanism of stellar winds is the transfer of momentum from photons to the star atmospheric gas by line interactions⁴⁵ (Kudritzki & Puls 2000; Vink et al. 2001). By measuring mass-loss rates of early-type stars in the Galaxy, LMC, and SMC, Mokiem et al. (2007) could quantify the dependence of \dot{M} on the metallicity as $\dot{M} \propto Z^{0.83}$. It is therefore expected that in lower metallicity environment (e. g. LMC) massive stars explode in wind-blown cavities with lower Λ , and are more likely to produce X-ray bright remnants. It is important to note that in M33, which has a metallicity of about 0.4 solar (e. g. Blair & Kirshner 1985), the SNR XLF exhibits an excess of bright sources as in the LMC; in M31, the distribution shows no such effect. The very small number of remnants in the SMC, which has the lowest metallicity of that sample of galaxies (0.2 solar), prohibits conclusion regarding an excess of bright sources.

Finally, there are also four type Ia SNRs amongst the bright end of the population, to which the explanation discussed above does not apply. If I exclude these however, there is still an excess. Because they are prominently young (three are less than a thousand years old), it appears that the high current type Ia SN rate in the LMC (Sect. 11.4.3) will also contribute to a larger population of bright remnants.

Between $\sim 1 \times 10^{35}$ erg s⁻¹ and 5×10^{35} erg s⁻¹, where many SNRs reside (a third of the sample), the LMC XLF is comparable in shape to the M31 and M33 XLFs, with a power-law distribution (consistent with α between -1 and -0.8), and in number to M33 (M31 begins to have more sources below $\sim 8 \times 10^{35}$ erg s⁻¹). Towards the fainter end, the LMC XLF is again remarkable via its significant flattening. It is unlikely that this represents an overall flatter distribution (at least not as strongly as in the SMC), because it would imply that a lot of SNRs with $L_X \sim (5-8) \times 10^{35}$ erg s⁻¹ (thus easy to identify) have been missed. It is more plausible that the flattening of the XLF is almost exclusively due to incompleteness. The majority of the remnants at $L_X < 8 \times 10^{34}$ erg s⁻¹ (15/22) were identified/confirmed thanks to (pointed or serendipitous)

⁴⁵The product abundance \times ionisation fraction \times number of available lines for metals is comparable to that of hydrogen and helium.

XMM-Newton observations. Though many were already detected with ROSAT, the combination of the large effective area and resolution of XMM-Newton is usually needed to confirm the extent and thermal emission of candidates. Even with the VLP survey, the area of the LMC covered by XMM-Newton is less than 20 square degrees, i. e. only less than a third of the whole galaxy. Extending the covered fraction warrants to find the missing remnants. The M31 survey with XMM-Newton exemplifies how a full coverage results in a high completeness: the M31 SNR XLF is uniform down to the sensitivity limit of the survey, which fully covers the D_{25} ellipse of M31 (Sasaki et al. 2012). In contrast, the Chandra survey of M33 is focused on the inner part of the galaxy (Plucinsky et al. 2008): many fainter SNRs are found thanks to the deep observations and good angular resolution of Chandra, at the expense of missing the SNRs in the outskirts of the galaxy. In the LMC, the situation could easily be improved with more X-ray observations. I briefly discuss possible strategies in Sect. IV.

11.6. 3D spatial distribution

COMPARISON WITH OTHER WAVELENGTHS: The distribution of SNRs in the LMC is plotted on the HI column density map of Kim et al. (2003), showing the LMC gas disc (Fig. 11.17). The population exhibits correlations with neutral hydrogen structures. The most striking example is the many SNRs (a dozen) around the supergiant shell (SGS) LMC 4 (Meaburn 1980, SGS 11 in the notation of Kim et al. 1999). SGSs are formed by the combined action of multiple generations of massive star formation. Their expansions shock and sweep up the ISM, which can trigger further star formation along the SGS rims (Elmegreen 1998, and references therein). The impact of SGSs on star formation, particularly in the LMC, was demonstrated by Yamaguchi et al. (2001a,b). They found that the concentration of molecular clouds and young star clusters is enhanced by a factor of 1.5–2 near the SGS rims, and most of these clusters are on the side of the molecular clouds facing the interior of the SGSs. Book et al. (2009) added massive YSOs and H II regions/OB associations to the list of tracers of recent star formation that are well correlated with the shell peripheries.

Because (core-collapse) SNRs are themselves very good indicators of recent star formation, the distribution of many SNRs around the edge of LMC 4 is a further sign of the important role played by SGSs in triggering star formation. In turn, this could be used to look for *new* SNRs. The high number of remnants around LMC 4 is explained in part by the large size of the SGS (~ 1.2 kpc), but also by the good X-ray coverage (only two out of twelve SNRs around LMC 4 were not observed with XMM-Newton). Exploring SGSs less well studied, e. g. in the west and south-west regions of the LMC, is promising, as I discuss in the Outlooks (Sect. IV).

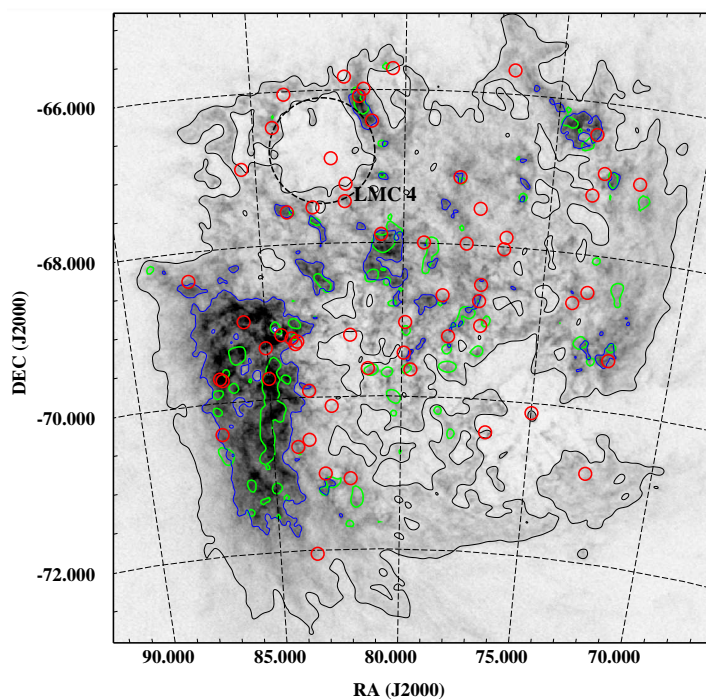


FIGURE 11.17 – Distribution of LMC SNRs (red circles) on the HI column density map of Kim et al. (2003), displayed on a linear scale ranging from 0 to $6 \times 10^{21} \text{ cm}^{-2}$. Black and blue contours indicate levels of 1 and $3 \times 10^{21} \text{ cm}^{-2}$, respectively. The green contours are the 3σ level (1.2 K km s^{-1}) of the velocity-integrated map of ^{12}CO ($J = 1 - 0$) from the NANTEN survey (Fukui et al. 2008). The position of the SGS LMC 4 is marked with a dashed black circle.

Another prominent HI feature is the density enhancement in the east that extends southwards into “arms B and E” (see Staveley-Smith et al. 2003, Fig. 1), which are interpreted as tidal features. Most of the SNRs in the south-east of the LMC are associated to the 30 Doradus complex (which itself might be a manifestation of tidal shear). Only a handful of sources are known in the regions of the B and E arms (and a single SNR is confirmed south of a declination of -71° , Bozzetto et al. 2013). The southern region of the LMC is poorly studied in X-rays, preventing conclusions regarding the dearth of SNRs observed there. However, it could be an interesting target for future studies (Sect. IV).

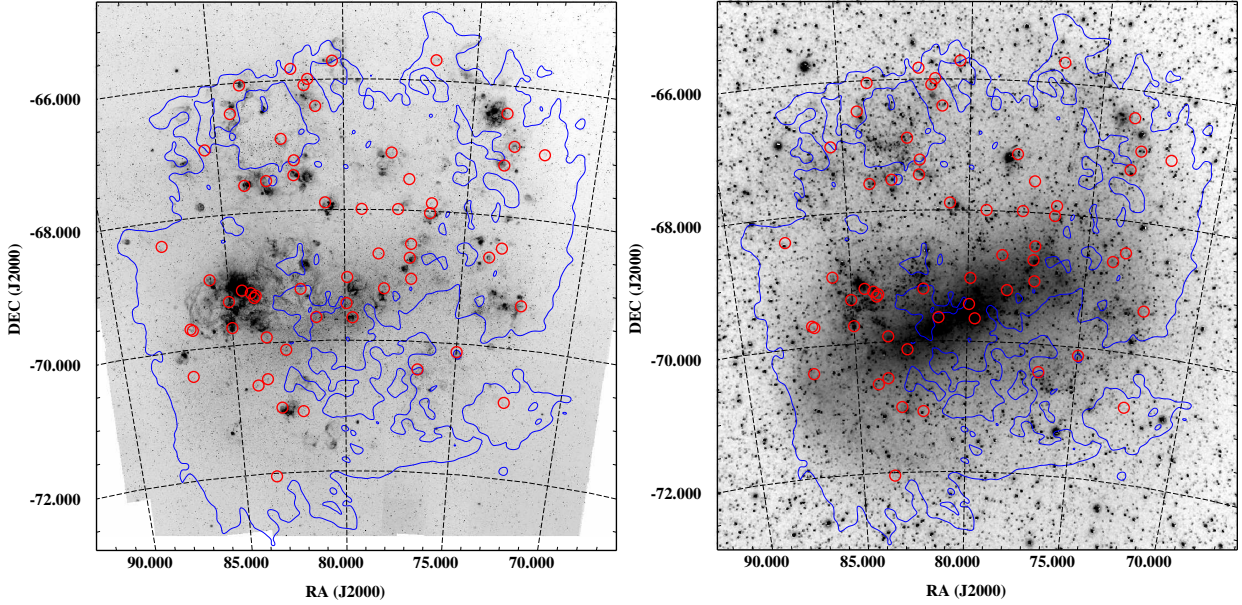


FIGURE 11.18 – *Left*: Location of LMC SNRs (red circles) on the MCELS $H\alpha$ mosaic, displayed logarithmically in grayscale. Blue contours outline a HI column density of $1 \times 10^{21} \text{ cm}^{-2}$ (see Fig. 11.17). *Right*: Same as left on a red continuum image from the SHASSA survey.

In Fig. 11.18, I show the position of SNRs relative to $H\alpha$ (left, MCELS data), and to a red continuum image from the SHASSA survey (Gaustad et al. 2001). The location of many SNRs near large H II regions, which trace regions of active star formation, is evident. This is the population of CC SNRs. On the other hand, many SNRs are not associated to $H\alpha$ emission, e. g. in the Bar, or south-east and north-west of it. These are likely the type Ia SNRs. They concentrate in regions of high stellar density (e. g. the Bar, as traced in the red continuum image) but are also present in more isolated, less active regions, where intermediate- and old-age stellar populations dominate.

Adding the third dimension: So far, I discussed the 2-D distribution of SNRs, projected on the sky. It is possible to gain a rudimentary sense of depth, by comparing the absorbing column density derived from X-ray observations (hereafter N_H^X), to the line-of-sight integrated HI column density, derived from 21 cm observations (hereafter $N_H^{21\text{cm}}$). I recall that N_H^X is an *equivalent* neutral hydrogen column density assuming a given chemical composition⁴⁶. The ratio $N_H^X/N_H^{21\text{cm}}$ (hereafter “ N_H fraction”) is a measurement of how deep an SNR is with respect to the HI structure. Interpreting the N_H fraction is made easier by the favourable orientation of the LMC. Neutral hydrogen is mainly distributed in a nearly circular disc at a moderate inclination angle (see Sect. 4), with a thickness of ~ 360 pc (Kim et al. 1999). Small N_H fractions ($\lesssim 0.3$, e. g. when N_H^X is consistent with zero) indicate that the SNR is well in front of the disc; intermediate values (0.3 to 0.8) are expected from sources within the disc; high fractions (0.8–1.2; a value of 1.23 is expected when including contributions of neutral and singly-ionised helium, Arabadjis & Bregman 1999) are associated to remnants on the far side, or behind, the disc. Values significantly above 1.2 are discussed below.

N_H^X is taken from the spectral results of Sect. 11.2. For the 1T/2T sample, the adopted value is simply that in Table A.2. Only two 2T remnants have two different absorption components: For MCSNR J0517–6759 I used the higher values. For MCSNR J0535–6602 (N63A), the highly absorbed component is ejecta-rich and has a lower EM; I therefore adopted the (lower) N_H of the ISM component, which is more representative.

⁴⁶X-rays are absorbed not only by HI, but also by molecular hydrogen, helium, and metals (Wilms et al. 2000).

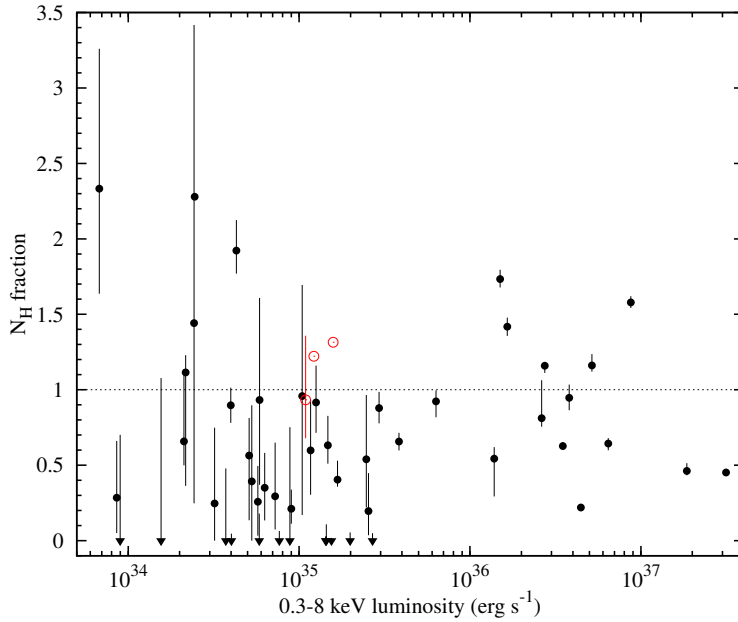


FIGURE 11.19 – N_H fraction = $N_H^X/N_H^{21\text{cm}}$ as function of broadband X-ray luminosity (see text for details). Downward pointing arrows indicate upper limits, for objects with N_H^X consistent with 0. SNRs covered with *Chandra* are shown in red.

For the brightest SNRs, I adopted the best-fit values of Table 9.2 (SNR 1987A) and Table A.3. For three SNRs with *Chandra* data only, I obtained N_H^X from the references given in Sect. 11.5. Five remaining SNRs have either no or only ROSAT data available, and are not used in this analysis.

$N_H^{21\text{cm}}$ is measured from the map of Kim et al. (2003), by averaging the column density around each SNR over a $5'$ radius (the resolution of the map is about 1 pc). I checked that using a smaller averaging radius, closer to the typical SNRs size, gave essentially the same results. I then computed the ratio, propagating only the uncertainties on N_H^X since they should dominate the error budget in most cases. N_H fractions are plotted against L_X in Fig. 11.19. No correlation is evident, as expected: L_X depends mostly on the evolutionary state of the remnant, while the depth within the LMC does not. At lower luminosities, however, there are more remnants with only upper limits on N_H^X (and thus on the N_H fraction). This likely stems from the difficulty of deriving N_H^X from limited X-ray statistics. For the same reason, the error bars are larger in the handful of cases below a few 10^{34} erg s^{-1} , and the sense of depth provided by the N_H fraction becomes blurry.

In Fig. 11.20, the N_H fraction is projected on the sky, on the same field of view as showed in Figs. 11.17 and 11.18. Remarkable LMC structures are labelled. In the Bar regions, SNRs are primarily on the near side (low N_H fraction). Some of these remnants must originate from the stellar population of the Bar. Therefore, this lends support to previous findings that the Bar is indeed “floating” (in front) of the disc (see references in Sect. 4.1.2). This method has the advantage that it does not need distance measurements of both disc and Bar objects; it directly gives locations *relative* to the disc. In the bulge model of Zaritsky (2004), SNRs in the Bar, but behind the disc⁴⁷, should have large N_H fractions, while some scatter should be found along the line of nodes, where the disc and bulge intersect. Unfortunately, there are too few SNRs known in the Bar region to adequately test this alternative model.

The remnants in the 30 Doradus region and directly south of it (MCSNR J0540–6920 and J0540–6944) are the most absorbed, both in absolute and relative terms (largest N_H^X and largest N_H fractions). From distance measurements with red clump stars, Koerwer (2009) found that 30 Dor was further away, although it was noted that this could be an effect of 30 Dor being next to the Bar floating in front of the disc. With my analysis it is confirmed that not only 30 Dor lies at a larger distance compared to neighbouring features, but is indeed *behind* the plane of the gas disc.

⁴⁷The obscuring effect by the disc on X-rays is moderate, not sufficient to mask SNRs as it does on stars in optical surveys.

Finally, it is striking from Figs 11.19 and 11.20 that a few SNRs have an N_H fraction in excess of 1.2, and up to 2.3. The extra absorption is likely to come from molecular hydrogen in front of the object (Arabadjis & Bregman 1999). I show in Fig. 11.17 CO contours from the NANTEN survey (Fukui et al. 2008). CO is used as a tracer of molecular hydrogen. In the east of the LMC there are large regions of molecular gas, following the peak density in HI. In most cases with large N_H fractions, I could find nearby (less than a few arcmin away in projection) CO clouds, using either the NANTEN catalogue or the higher resolution MAGMA survey (Fukui et al. 2008; Wong et al. 2011, respectively). I stress that this does not imply that the remnants and the molecular clouds are physically connected, but is usually merely a projection effect, with the remnant behind, and not interacting with the molecular cloud. This can happen, however, as exemplified by the case of MCSNR J0517–6759, where secondary evidence hints at a physical connection (Sect. 10.3).

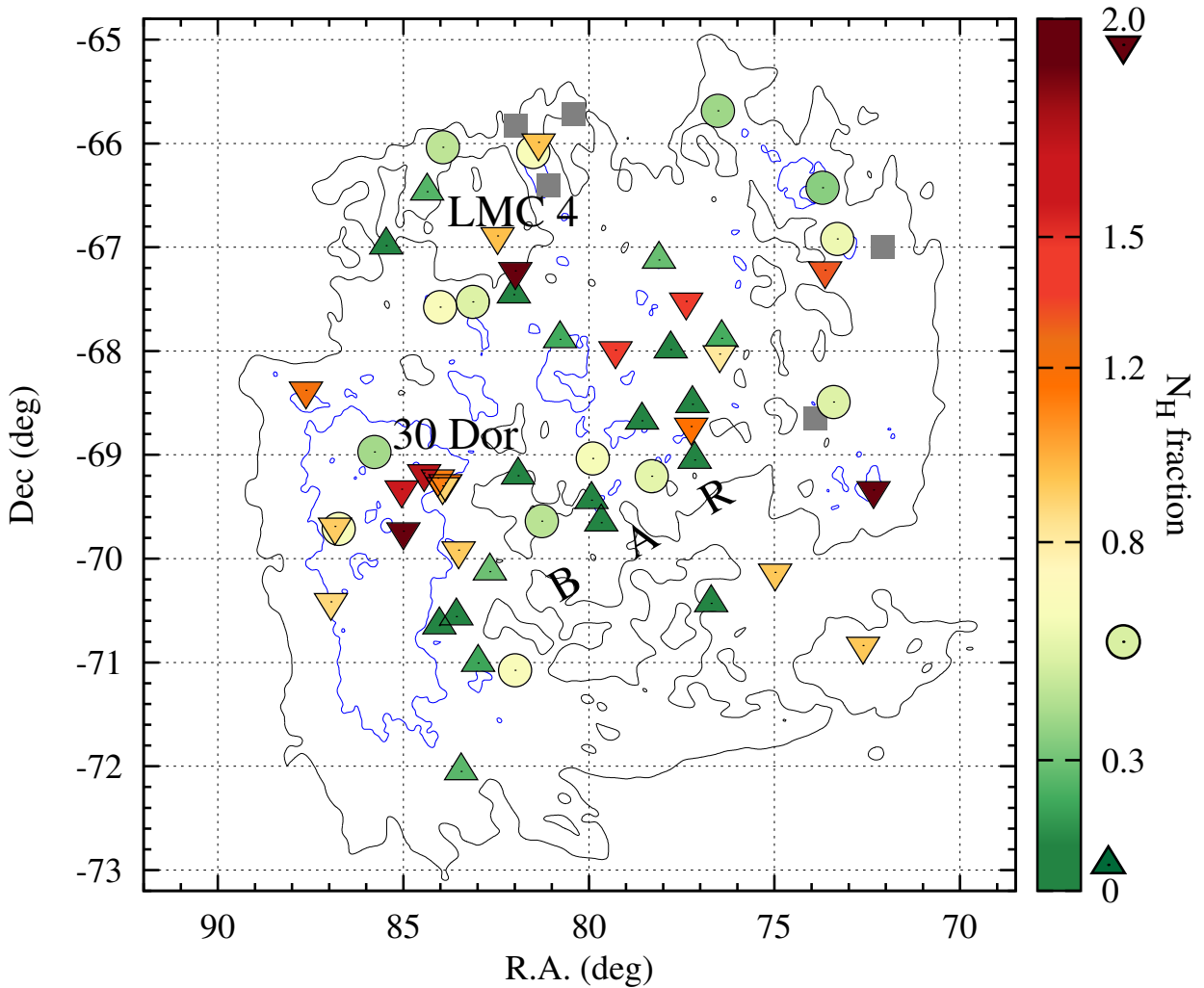


FIGURE 11.20 – “Pseudo-3D” distribution of LMC SNRs, using N_H fractions (quantified by the colour bar) as indicators of location along the line of sight. Objects “in front of the disc” (N_H fraction < 0.3) are marked by upward pointing triangles; downward pointing triangles are used for those “behind the disc” (N_H fraction > 0.8). Objects within the disc (0.3 to 0.8) are marked by dots. The black and blue contours delineate HI column densities of 1 and $3 \times 10^{21} \text{ cm}^{-2}$, respectively (same as in Fig. 11.17). Remarkable LMC structures are labelled.

Part IV.

Conclusion and Outlooks

Conclusions

IN THIS DISSERTATION, I have studied the X-ray emission of supernova remnants in the Large Magellanic Cloud, using data from the XMM-Newton observatory. First, I focused on individual SNRs, including new objects serendipitously discovered during the large XMM-Newton survey of the central regions of the LMC, and the remnant of the historical SN 1987A, target of a monitoring campaign. Later, I expanded my focus to study LMC SNRs as a *population*. This holistic approach provides insights on the evolution of SNRs and the interplay with their host galaxy.

For this work, I used all existing XMM-Newton observations towards the LMC. I combined archival observations with dedicated pointings of SNR candidates and data from the VLP survey of the LMC. Data were reduced using a pipeline developed in our research group, which I extended with several scripts tailored to the analysis of SNRs (or any faint extended object).

A vast variety of SNRs is encountered in this work. The youngest is SNR 1987A, which is less than 30 years old. It is a key system to study the first stages of a remnant. I analysed XMM-Newton data from the 2007-2012 monitoring campaign. The soft X-ray flux keeps increasing, indicating that the outer blast wave is still propagating into dense regions of the Equatorial Ring. Fe K lines from SNR 1987A could be studied in detail for the first time. The centroid energy and width of the line complex implies that Fe is in the form of many ions, including near-neutral iron, possibly in unshocked ejecta.

In contrast to SNR 1987A, all the new SNRs found in the course of my PhD work are old systems ($> 10^4$ yr). I led detailed multi-wavelength studies of six new SNRs found in the VLP survey observations. The XMM-Newton data are critical to investigate the morphological and spectral features of the remnants, allowing me to measure physical conditions of the hot plasmas, search for SN ejecta emission, and constrain some of the SNR properties. Complementary data at optical, infrared, and radio wavelengths are used to show the key role played by the local environment in the current appearance of the remnants.

After I presented analyses of individual objects, I studied the complete population of SNRs in the LMC. I compiled a sample of 59 definite SNRs, cleaned of misclassified objects and doubtful candidates. XMM-Newton data are available for the vast majority (51 SNRs) of the sample, which called for a homogeneous re-analysis of the X-ray spectra of the entire population. This alleviates the inconsistencies in spectral models and analysis methods used, and allows meaningful comparisons of, e. g., temperature, chemical composition, and luminosity of SNRs. This systematic spectral analysis has multiple benefits:

- First, it provides the best census of LMC remnants with an Fe K line (≈ 13 % of the sample), which is a powerful tool to retrieve the type of SN progenitor.
- Second, it reveals the contribution to the X-ray emission by hot SN ejecta for 23 SNRs (≈ 39 % of the sample). Since the abundance ratios measured in the ejecta components reflect the nucleosynthesis yields of either type Ia and CC SNe, this is of great help for the typing of a substantial fraction of the sample.
- And third, it allows me to select 16 SNRs (≈ 27 % of the sample) where the X-ray emission is dominated by swept-up ISM. In these objects, the fitted abundances provide a measurement of chemical abundances in the gas phase of the LMC ISM. A metallicity of $[\text{Fe}/\text{H}] = -0.46^{+0.13}_{-0.18}$ dex is found based on XMM-Newton SNRs. Light α -elements (O, Ne, Mg) have lower abundance ratios $[\alpha/\text{Fe}]$ than in the Milky Way. Although this general result was previously known, one can now study abundance ratios within the LMC as function of age. In comparison to old clusters (~ 10 Gyr) and red

giant stars (1 Gyr and older), the relatively young gas phase ISM ($\lesssim 100$ Myr) has a higher metallicity [Fe/H] and lower $[\alpha/\text{Fe}]$ (in particular [O/Fe]). This reflects the continued enrichment by type Ia SNe in the last ~ 1 Gyr, which injected large amounts of Fe back in the ISM.

Perhaps the most remarkable sub-sample of SNRs in the LMC are those of type Ia. Sorting them by age, I found a well-ordered evolution: The youngest are in the ejecta-dominated phase, before the transition to the Sedov phase, when swept-up ISM is visible as X-ray shells. The central regions, however, are still dominated by hot ejecta. After $\approx 10^4$ yr, the outer blast wave becomes radiative, efficiently losing energy in optical and UV emission lines. In X-rays, the Sedov shells become progressively fainter and softer. Strikingly, ejecta in the centre of older remnants are still hot enough to emit X-rays, resulting in SNRs seen in X-rays but essentially absent at longer wavelengths. Five such objects with iron-rich central emission have been found during my PhD thesis, thanks to the sensitivity reached by XMM-Newton observations. They make up most of the old end of the type Ia SNR sequence, revealing a late-time evolutionary phase previously overlooked.

I devised a new method to tentatively type all LMC SNRs, based on their local SFHs and stellar environments, combined with spectral information (i. e. detection of SN ejecta, when present). I calibrated this method with SNRs having a well-established type based on robust indicators. The resulting ratio of CC to type Ia SNe that exploded in the LMC over the last few 10^4 yr (i. e. very close to the current ratio of CC/Ia rates) is $N_{\text{CC}}/N_{\text{Ia}} = 1.35^{(+0.11)}_{(-0.24)}$. This is lower than the ratio typically measured in local SNe surveys and in galaxy clusters. After arguing that SNRs of both types might be absent from the sample (i. e. the current sample is not biased towards one type only), I concluded that the low $N_{\text{CC}}/N_{\text{Ia}}$ ratio is a consequence of the specific SFH of the LMC, and particularly the enhanced star formation episodes that occurred 500 Myr and 2 Gyr ago. Because the majority of type Ia SNe explode within 2 Gyr after star-forming episodes, we are coincidentally observing the LMC at a time when the type Ia SN rate is high. Integrated over an SNR lifetime, this results in the relatively low $N_{\text{CC}}/N_{\text{Ia}}$ observed.

I also assessed the spatial distribution of SNRs with respect to cool gas (traced by HI and molecular emission), star-forming regions ($\text{H}\alpha$), and stars (red continuum). A concentration of SNRs around the edge of the SGS LMC 4 exemplifies the role of SGSs in triggering star formation. The column density N_{H}^{X} obtained during the X-ray spectral analysis of the whole sample, when compared to the HI column density, provides a measurement of the position of each SNR relative to the HI structure. Since most of the neutral gas lies in a well-defined thin disc seen at a moderate inclination angle, the fraction $N_{\text{H}}^{\text{X}}/N_{\text{H}}^{21\text{cm}}$ is a good indicator of the depth along the line-of-sight, revealing the “pseudo-3D” distribution of SNRs in the LMC. Previous studies found that the Bar is “floating” in front of the disc, but this statement was challenged by some authors. My analysis shows that SNRs in the Bar regions are primarily on the near side (low N_{H} fraction), lending support to the foreground location of the Bar.

Finally, I compared the populations of SNRs in Local Group galaxies via their X-ray luminosity function. The XLF of SNRs in the SMC, M31, and M33 are relatively homogeneous over all the observed luminosity range, although that of the SMC is flatter. The LMC XLF is remarkable by its prominent bright end. The largest population of SNRs brighter than $L_{\text{X}} > 10^{36}$ erg s^{-1} is found in the LMC (13 SNRs vs. 8 and 7 in M31 and M33, respectively). This is possibly an effect of the lower metallicity in the LMC: Massive stars have smaller mass loss rates (less heavy elements to drive stellar winds) and the interaction of SN ejecta with less massive CSM shells produce brighter remnants. The number of SNRs brighter than 10^{35} erg s^{-1} in the LMC is comparable to that in M31 and M33, likely owing to its high recent SFR and high current type Ia SN rate. The LMC XLF flattens significantly because of incompleteness: Many X-ray-faint SNRs have been missed so far, due to the incomplete coverage of the LMC with sensitive X-ray instruments (i. e. Chandra or XMM-Newton).

Outlooks

This work presents the state of the art on X-ray emission of SNRs in the LMC. However, only SNRs known prior to, and those found during my PhD thesis are included. It is clear that the *current* sample (Table A.1) is incomplete, as evidenced by the flattening of the X-ray luminosity function of LMC SNRs. In the last 15 years, new SNRs were confirmed or discovered in the LMC at an almost constant rate (one or few per year), principally using X-ray observations. There is no indication that this trend will stop in the near future, so that more observations of the LMC will increase the sample of SNRs.

Nevertheless, the observing time of major observatories is limited and expensive. I present here several strategies to maximise the chance of finding “missing” SNRs:

- As shown in Sect. 11.6, star formation is intense around the SGS LMC 4, and the edges of the shell abound in SNRs. Many LMC SGS have not been (fully) surveyed by XMM-Newton, for instance (in the notation of Kim et al. 1999) SGS 3 and 6 in the north, SGS 2 and 5 in the west, and SGS 4 in the north. Targeting in particular SGSs associated to star formation (e. g. with H II region along the rims) warrants successful SNR searches.
- The follow-up of X-ray-selected candidates (usually ROSAT sources) with XMM-Newton has been extremely successful. This programme should be continued until completion of the list of candidates.
- Even the ROSAT (targeted) survey of the LMC was not covering the LMC up to its outskirts. To find SNRs in these regions, the future *eROSITA* survey (Merloni et al. 2012) will be most useful, covering the full sky in the 0.5 keV – 8 keV band. The LMC is located close to the South Ecliptic Pole and will be observed with a deeper exposure than the rest of the sky. Looking for new SNR candidates, especially evolved X-ray-only SNRs, will be of special interest.

Even in *existing* data, some SNRs might be as yet unrecognised. There is significant diffuse emission from large-scale structures of the hot ISM in the LMC (Sasaki et al. 2002), which is seen in greater spatial and spectral detail by XMM-Newton (this will be studied in a future work). By looking for ejecta-enhancement, it might be possible to distinguish old SNRs with low surface brightness hiding in the diffuse emission, e. g. Fe-rich SNRs even older than those in Sect. 10.2.

Finding new SNRs is desirable. Individual objects of special interest are often found serendipitously, without prior knowledge of their exciting nature. The evolved type Ia SNRs of Sect. 10.2, are good examples; the discovery of the SNR around the Be/X-ray binary SXP 1062 is another one (Hénault-Brunet et al. 2012; Haberl et al. 2012c). Furthermore, as demonstrated in this dissertation, SNRs are powerful probes of the ISM of their host galaxies. With more SNRs where metallicity can be measured, we will obtain a more accurate knowledge of the chemical composition of the hot ISM or better assess its homogeneity.

Acknowledgments

FINALLY, it is my pleasure to express my gratitude to everybody who contributed to the success of my PhD thesis. Without the scientific, personal, and logistic support of many, this dissertation could not have existed.

First, all my thanks to my supervisor Frank Haberl for giving me the opportunity of working at the MPE on all these XMM-Newton data. His knowledge and expertise of X-ray astronomy, which he was always ready to share, was most useful in my formation as a young scientist.

I extend my gratitude to Jochen Greiner, thanks to whom I could prepare my thesis under the auspices of the Technische Universität München. His suggestions throughout my years in Garching, and his comments on the early drafts of the dissertation, have helped to improve its final impact.

I enjoyed a stimulating environment in MPE's High Energy Group, where seminars and discussions kept me interested in the broad fields of X-ray astronomy and beyond. Special mentions to my office mate and scientific predecessor, Richard Sturm, for numerous, discussions, tips, as well as help in many administrative matters; and to Wolfgang Pietsch, whose extensive knowledge I greatly benefited from. Additionally, I never encountered issues with anything computer-related, never had to painfully install analysis softwares, and never lost data, all thanks to the flawless gestion of the IT group by Harald Baumgartner and Joachim Paul.

I also would like to thank all those I worked and interacted with as part of the LMC survey collaboration: You-Hua Chu, John Dickel, and Sean Points in America; Miroslav Filipović and Luke Bozzetto in Australia; Patrick Kavanagh, Manami Sasaki, and Georgios Vasilopoulos in Germany.

A PhD can only keep oneself busy some part of the day (alternatively too big and too small). I am grateful to my fellow PhD students and friends, for making it worth to go to Garching all the week, and making it fun to go out all week-ends. I immensely enjoyed all the discussions and debates about scientific and random topics (i. e. "life and stuff"; and yes, Haakon, the Moon *does* spin). Many thanks to all those back in France that are (suprisingly) still friends with me for always supporting, and sometimes visiting me. Thanks to all football players from the SV Plasma for providing a highly-needed weekly distraction. The victory of our MPA/MPE team in the Campus Cup was the climax of my football career. It only goes to show the benefits of collaborating with theoreticians (and, obviously, the domination of astronomy over other fields of science).

A special thought to Hsin-Yin (Dr. Chiang !) for her unwavering support during the writing of this work.

Finally, I want to thank my parents and my sister. They have been nothing but supportive for as long as I can remember. It is in great part thanks to them that I became interested in science.

Bibliography

- Abbey, T., Carpenter, J., Read, A., et al. 2006, in ESA Special Publication, Vol. 604, The X-ray Universe 2005, ed. A. Wilson, 943
- Abdo, A. A., Ackermann, M., Ajello, M., et al. 2009, ApJS, 183, 46
- Abdo, A. A., Ackermann, M., Ajello, M., et al. 2010, A&A, 523, A46
- Ackermann, M., Ajello, M., Allafort, A., et al. 2013, Science, 339, 807
- Aharonian, F., Akhperjanian, A. G., Bazer-Bachi, A. R., et al. 2006, ApJ, 636, 777
- Aharonian, F. A., Akhperjanian, A. G., Aye, K.-M., et al. 2004, Nature, 432, 75
- Aharonian, F. A., Drury, L. O., & Voelk, H. J. 1994, A&A, 285, 645
- Alpher, R. A., Bethe, H., & Gamow, G. 1948, Physical Review, 73, 803
- Alpher, R. A. & Herman, R. C. 1950, Reviews of Modern Physics, 22, 153
- Andersen, M., Rho, J., Reach, W. T., Hewitt, J. W., & Bernard, J. P. 2011, ApJ, 742, 7
- Antoniou, V., Zezas, A., Hatzidimitriou, D., & Kalogera, V. 2010, ApJ, 716, L140
- Arabadjis, J. S. & Bregman, J. N. 1999, ApJ, 510, 806
- Arnaud, K. A. 1996, in Astronomical Society of the Pacific Conference Series, Vol. 101, Astronomical Data Analysis Software and Systems V, ed. G. H. Jacoby & J. Barnes, 17
- Arnaud, M. & Raymond, J. 1992, ApJ, 398, 394
- Arnaud, M. & Rothenflug, R. 1985, A&AS, 60, 425
- Aschenbach, B., Briel, U. G., Pfeiffermann, E., et al. 1987, Nature, 330, 232
- Baade, W. & Zwicky, F. 1934, Proceedings of the National Academy of Science, 20, 254
- Badenes, C., Borkowski, K. J., & Bravo, E. 2005, ApJ, 624, 198
- Badenes, C., Bravo, E., Borkowski, K. J., & Domínguez, I. 2003, ApJ, 593, 358
- Badenes, C., Harris, J., Zaritsky, D., & Prieto, J. L. 2009, ApJ, 700, 727
- Badenes, C., Hughes, J. P., Cassam-Chenaï, G., & Bravo, E. 2008, ApJ, 680, 1149
- Badenes, C., Maoz, D., & Draine, B. T. 2010, MNRAS, 407, 1301
- Ballet, J. 2003, in EAS Publications Series, Vol. 7, EAS Publications Series, ed. C. Motch & J.-M. Hameury, 217
- Balucinska-Church, M. & McCammon, D. 1992, ApJ, 400, 699
- Bamba, A., Ueno, M., Nakajima, H., & Koyama, K. 2004, ApJ, 602, 257
- Bamba, A., Ueno, M., Nakajima, H., Mori, K., & Koyama, K. 2006, A&A, 450, 585
- Bambynek, W., Crasemann, B., Fink, R. W., et al. 1972, Reviews of Modern Physics, 44, 716
- Barret, D., den Herder, J. W., Piro, L., et al. 2013, ArXiv e-prints [arXiv:1308.6784]
- Bauer, F. E., Alexander, D. M., Brandt, W. N., et al. 2004, AJ, 128, 2048
- Behar, E., Rasmussen, A. P., Griffiths, R. G., et al. 2001, A&A, 365, L242
- Bekki, K. 2009, MNRAS, 393, L60
- Belczynski, K. & Ziolkowski, J. 2009, ApJ, 707, 870
- Bell, A. R. 1978a, MNRAS, 182, 147

- Bell, A. R. 1978b, *MNRAS*, 182, 443
- Berezhko, E. G. & Ellison, D. C. 1999, *ApJ*, 526, 385
- Bernasconi, P. A. & Maeder, A. 1996, *A&A*, 307, 829
- Besla, G., Kallivayalil, N., Hernquist, L., et al. 2012, *MNRAS*, 421, 2109
- Beuermann, K., Brandt, S., & Pietsch, W. 1994, *A&A*, 281, L45
- Bionta, R. M., Blewitt, G., Bratton, C. B., Casper, D., & Ciocio, A. 1987, *Physical Review Letters*, 58, 1494
- Blackburn, J. K. 1995, in *Astronomical Society of the Pacific Conference Series*, Vol. 77, *Astronomical Data Analysis Software and Systems IV*, ed. R. A. Shaw, H. E. Payne, & J. J. E. Hayes, 367
- Blair, W. P., Ghavamian, P., Sankrit, R., & Danforth, C. W. 2006, *ApJS*, 165, 480
- Blair, W. P. & Kirshner, R. P. 1985, *ApJ*, 289, 582
- Blandford, R. D. & Ostriker, J. P. 1978, *ApJ*, 221, L29
- Blasi, P. 2013, *A&A Rev.*, 21, 70
- Böhringer, H. & Werner, N. 2010, *A&A Rev.*, 18, 127
- Bojičić, I. S., Filipović, M. D., Parker, Q. A., et al. 2007, *MNRAS*, 378, 1237
- Bonnet-Bidaud, J. M., Motch, C., Beuermann, K., et al. 1989, *A&A*, 213, 97
- Book, L. G., Chu, Y.-H., & Gruendl, R. A. 2008, *ApJS*, 175, 165
- Book, L. G., Chu, Y.-H., Gruendl, R. A., & Fukui, Y. 2009, *AJ*, 137, 3599
- Borkowski, K. J., Hendrick, S. P., & Reynolds, S. P. 2006a, *ApJ*, 652, 1259
- Borkowski, K. J., Hendrick, S. P., & Reynolds, S. P. 2007, *ApJ*, 671, L45
- Borkowski, K. J., Lyerly, W. J., & Reynolds, S. P. 2001, *ApJ*, 548, 820
- Borkowski, K. J., Williams, B. J., Reynolds, S. P., et al. 2006b, *ApJ*, 642, L141
- Bowyer, S., Byram, E. T., Chubb, T. A., & Friedman, H. 1964, *Science*, 146, 912
- Bozzetto, L. M., Filipović, M. D., Crawford, E. J., et al. 2012a, *MNRAS*, 420, 2588
- Bozzetto, L. M., Filipovic, M. D., Crawford, E. J., et al. 2012b, *RMxAA*, 48, 41
- Bozzetto, L. M., Filipović, M. D., Crawford, E. J., et al. 2013, *MNRAS*, 432, 2177
- Bozzetto, L. M., Kavanagh, P. J., Maggi, P., et al. 2014, *MNRAS*, 439, 1110
- Branch, D. & Tammann, G. A. 1992, *ARA&A*, 30, 359
- Broughton, R. P. 1979, *JRASC*, 73, 381
- Burbidge, E. M., Burbidge, G. R., Fowler, W. A., & Hoyle, F. 1957, *Reviews of Modern Physics*, 29, 547
- Burrows, C. J., Krist, J., Hester, J. J., et al. 1995, *ApJ*, 452, 680
- Burrows, D. N., Michael, E., Hwang, U., et al. 2000, *ApJ*, 543, L149
- Cajko, K. O., Crawford, E. J., & Filipovic, M. D. 2009, *Serbian Astronomical Journal*, 179, 55
- Casares, J., Negueruela, I., Ribó, M., et al. 2014, *Nature*, 505, 378
- Cash, W. 1979, *ApJ*, 228, 939
- Castor, J., McCray, R., & Weaver, R. 1975, *ApJ*, 200, L107
- Chen, L.-W., Fabian, A. C., & Gendreau, K. C. 1997, *MNRAS*, 285, 449
- Chen, Y., Wang, Q. D., Gotthelf, E. V., et al. 2006, *ApJ*, 651, 237
- Chevalier, R. A. & Dwarkadas, V. V. 1995, *ApJ*, 452, L45
- Chevalier, R. A. & Kirshner, R. P. 1979, *ApJ*, 233, 154
- Chevalier, R. A., Kirshner, R. P., & Raymond, J. C. 1980, *ApJ*, 235, 186
- Chevalier, R. A. & Raymond, J. C. 1978, *ApJ*, 225, L27
- Chu, Y.-H. 1997, *AJ*, 113, 1815

- Chu, Y.-H. 2008, in IAU Symposium, Vol. 250, IAU Symposium, ed. F. Bresolin, P. A. Crowther, & J. Puls, 341–354
- Chu, Y.-H., Chang, H.-W., Su, Y.-L., & Mac Low, M.-M. 1995a, *ApJ*, 450, 157
- Chu, Y.-H., Dickel, J. R., Staveley-Smith, L., Osterberg, J., & Smith, R. C. 1995b, *AJ*, 109, 1729
- Chu, Y.-H., Kennicutt, R. C., Snowden, S. L., et al. 1997, *PASP*, 109, 554
- Chu, Y.-H. & Kennicutt, Jr., R. C. 1988, *AJ*, 96, 1874
- Chu, Y.-H., Kim, S., Points, S. D., Petre, R., & Snowden, S. L. 2000, *AJ*, 119, 2242
- Chu, Y.-H. & Mac Low, M.-M. 1990, *ApJ*, 365, 510
- Chu, Y.-H., Mac Low, M.-M., Garcia-Segura, G., Wakker, B., & Kennicutt, Jr., R. C. 1993, *ApJ*, 414, 213
- Cioffi, D. F., McKee, C. F., & Bertschinger, E. 1988, *ApJ*, 334, 252
- Cioni, M.-R. L., Clementini, G., Girardi, L., et al. 2011, *A&A*, 527, A116
- Cioni, M.-R. L., Girardi, L., Moretti, M. I., et al. 2014, *A&A*, 562, A32
- Cioni, M.-R. L., Kamath, D., Rubele, S., et al. 2013, *A&A*, 549, A29
- Clark, D. H. & Stephenson, F. R. 1977, *The historical supernovae*
- Coe, M., Corbets, R. H. D., McGowan, K. E., & McBride, V. A. 2010, in *Astronomical Society of the Pacific Conference Series*, Vol. 422, *High Energy Phenomena in Massive Stars*, ed. J. Martí, P. L. Luque-Escamilla, & J. A. Combi, 224
- Coe, M. J., Edge, W. R. T., Galache, J. L., & McBride, V. A. 2005, *MNRAS*, 356, 502
- Cole, A. A., Tolstoy, E., Gallagher, III, J. S., & Smecker-Hane, T. A. 2005, *AJ*, 129, 1465
- Corbelli, E. 2003, *MNRAS*, 342, 199
- Cox, D. P. & Daltabuit, E. 1971, *ApJ*, 167, 113
- Crawford, E. J., Filipović, M. D., McEntaffer, R. L., et al. 2014, *AJ*, 148, 99
- Crotts, A. P. S., Kunkel, W. E., & McCarthy, P. J. 1989, *ApJ*, 347, L61
- Da Costa, G. S. 1991, in IAU Symposium, Vol. 148, *The Magellanic Clouds*, ed. R. Haynes & D. Milne, 183
- Davies, R. D., Elliott, K. H., & Meaburn, J. 1976, *MNRAS*, 81, 89
- de Chambure, D., Laine, R., & van Katwijk, K. 1998, in *Society of Photo-Optical Instrumentation Engineers (SPIE) Conference Series*, Vol. 3444, *X-Ray Optics, Instruments, and Missions*, ed. R. B. Hoover & A. B. Walker, 313–326
- de Grijs, R., Wicker, J. E., & Bono, G. 2014, *AJ*, 147, 122
- de Horta, A. Y., Filipović, M. D., Bozzetto, L. M., et al. 2012, *A&A*, 540, A25
- de Plaa, J., Werner, N., Bleeker, J. A. M., et al. 2007, *A&A*, 465, 345
- de Vaucouleurs, G. & Freeman, K. C. 1972, *Vistas in Astronomy*, 14, 163
- Decourchelle, A., Ellison, D. C., & Ballet, J. 2000, *ApJ*, 543, L57
- den Herder, J. W., Brinkman, A. C., Kahn, S. M., et al. 2001, *A&A*, 365, L7
- Dennerl, K., Haberl, F., Aschenbach, B., et al. 2001, *A&A*, 365, L202
- Desai, K. M., Chu, Y.-H., Gruendl, R. A., et al. 2010, *AJ*, 140, 584
- Dethier, V. G. 1962, *To Know a Fly* (San Francisco: Holden-Day)
- Dewey, D., Dwarkadas, V. V., Haberl, F., Sturm, R., & Canizares, C. R. 2012, *ApJ*, 752, 103
- Dewey, D., Zhekov, S. A., McCray, R., & Canizares, C. R. 2008, *ApJ*, 676, L131
- Di Stefano, R. 2010, *ApJ*, 712, 728
- Dickel, J. R., McIntyre, V. J., Gruendl, R. A., & Milne, D. K. 2005, *AJ*, 129, 790
- Dickel, J. R., McIntyre, V. J., Gruendl, R. A., & Milne, D. K. 2010, *AJ*, 140, 1567

- Dickey, J. M. & Lockman, F. J. 1990, *ARA&A*, 28, 215
- Dobbs, C. L., Burkert, A., & Pringle, J. E. 2011, *MNRAS*, 417, 1318
- Dohm-Palmer, R. C. & Jones, T. W. 1996, *ApJ*, 471, 279
- Dopita, M. A., Blair, W. P., Long, K. S., et al. 2010, *ApJ*, 710, 964
- Dopita, M. A., Payne, J. L., Filipović, M. D., & Pannuti, T. G. 2012, *MNRAS*, 427, 956
- Dotani, T., Hayashida, K., Inoue, H., Itoh, M., & Koyama, K. 1987, *Nature*, 330, 230
- Drury, L. 1983, *Space Sci. Rev.*, 36, 57
- Drury, L. O., Aharonian, F. A., & Voelk, H. J. 1994, *A&A*, 287, 959
- Dunne, B. C., Points, S. D., & Chu, Y.-H. 2001, *ApJS*, 136, 119
- Dwarkadas, V. V. 2005, *ApJ*, 630, 892
- Dwarkadas, V. V. 2007, *ApJ*, 667, 226
- Eisenhardt, P. R. M., Brodwin, M., Gonzalez, A. H., et al. 2008, *ApJ*, 684, 905
- Elias, J. H., Matthews, K., Neugebauer, G., & Persson, S. E. 1985, *ApJ*, 296, 379
- Elmegreen, B. G. 1998, in *Astronomical Society of the Pacific Conference Series*, Vol. 148, *Origins*, ed. C. E. Woodward, J. M. Shull, & H. A. Thronson, Jr., 150
- Esposito, J. A., Hunter, S. D., Kanbach, G., & Sreekumar, P. 1996, *ApJ*, 461, 820
- Fabbiano, G. 2006, *ARA&A*, 44, 323
- Fazio, G. G., Hora, J. L., Allen, L. E., et al. 2004, *ApJS*, 154, 10
- Ferrand, G., Decourchelle, A., Ballet, J., Teyssier, R., & Frascchetti, F. 2010, *A&A*, 509, L10
- Ferrand, G., Decourchelle, A., & Safi-Harb, S. 2012, *ApJ*, 760, 34
- Ferrand, G., Decourchelle, A., & Safi-Harb, S. 2014, *ApJ*, 789, 49
- Ferrand, G. & Safi-Harb, S. 2012, *Advances in Space Research*, 49, 1313
- Fesen, R. A., Blair, W. P., & Kirshner, R. P. 1985, *ApJ*, 292, 29
- Filipović, M. D., Haberl, F., Winkler, P. F., et al. 2008, *A&A*, 485, 63
- Filipovic, M. D., Haynes, R. F., White, G. L., & Jones, P. A. 1998, *A&AS*, 130, 421
- Filipovic, M. D., Haynes, R. F., White, G. L., et al. 1995, *A&AS*, 111, 311
- Filipovic, M. D., White, G. L., Jones, P. A., et al. 1996, in *Astronomical Society of the Pacific Conference Series*, Vol. 112, *The History of the Milky Way and Its Satellite System*, ed. A. Burkert, D. H. Hartmann, & S. A. Majewski, 91
- Filippenko, A. V. 1997, *ARA&A*, 35, 309
- Foster, A. R., Ji, L., Smith, R. K., & Brickhouse, N. S. 2012, *ApJ*, 756, 128
- Freedman, W. L., Madore, B. F., Gibson, B. K., et al. 2001, *ApJ*, 553, 47
- Freyberg, M. J., Briel, U. G., Dennerl, K., et al. 2004, in *Society of Photo-Optical Instrumentation Engineers (SPIE) Conference Series*, Vol. 5165, *Society of Photo-Optical Instrumentation Engineers (SPIE) Conference Series*, ed. K. A. Flanagan & O. H. W. Siegmund, 112–122
- Fukui, Y., Kawamura, A., Minamidani, T., et al. 2008, *ApJS*, 178, 56
- Furuzawa, A., Ueno, D., Hayato, A., et al. 2009, *ApJ*, 693, L61
- Gaensler, B. M., Hendrick, S. P., Reynolds, S. P., & Borkowski, K. J. 2003, *ApJ*, 594, L111
- Gaensler, B. M., Slane, P. O., Gotthelf, E. V., & Vasisht, G. 2001, *ApJ*, 559, 963
- Gaustad, J. E., McCullough, P. R., Rosing, W., & Van Buren, D. 2001, *PASP*, 113, 1326
- Ghavamian, P., Blair, W. P., Sankrit, R., Raymond, J. C., & Hughes, J. P. 2007, *ApJ*, 664, 304
- Ghavamian, P., Rakowski, C. E., Hughes, J. P., & Williams, T. B. 2003, *ApJ*, 590, 833

- Giacconi, R., Gursky, H., Paolini, F. R., & Rossi, B. B. 1962, *Physical Review Letters*, 9, 439
- Giacconi, R., Murray, S., Gursky, H., et al. 1972, *ApJ*, 178, 281
- Giacconi, R. & Rossi, B. 1960, *J. Geophys. Res.*, 65, 773
- Gilfanov, M. & Bogdán, Á. 2010, *Nature*, 463, 924
- Graham, J. R., Evans, A., Albinson, J. S., Bode, M. F., & Meikle, W. P. S. 1987, *ApJ*, 319, 126
- Green, D. A. 2014, *Bulletin of the Astronomical Society of India*, 42, 47
- Green, D. A., Reynolds, S. P., Borkowski, K. J., et al. 2008, *MNRAS*, 387, L54
- Greiner, J., Orío, M., & Schartel, N. 2003, *A&A*, 405, 703
- Grimm, H.-J., Gilfanov, M., & Sunyaev, R. 2003, *MNRAS*, 339, 793
- Grondin, M.-H., Sasaki, M., Haberl, F., et al. 2012, *A&A*, 539, A15
- Gröningsson, P., Fransson, C., Leibundgut, B., et al. 2008, *A&A*, 492, 481
- Gruendl, R. A. & Chu, Y.-H. 2009, *ApJS*, 184, 172
- Gursky, H., Giacconi, R., Paolini, F. R., & Rossi, B. B. 1963, *Physical Review Letters*, 11, 530
- Haberl, F. 1995, *A&A*, 296, 685
- Haberl, F., Dennerl, K., Filipović, M. D., et al. 2001, *A&A*, 365, L208
- Haberl, F., Filipović, M. D., Bozzetto, L. M., et al. 2012a, *A&A*, 543, A154
- Haberl, F., Geppert, U., Aschenbach, B., & Hasinger, G. 2006, *A&A*, 460, 811
- Haberl, F. & Pietsch, W. 1999a, *A&AS*, 139, 277
- Haberl, F. & Pietsch, W. 1999b, *A&A*, 344, 521
- Haberl, F. & Pietsch, W. 2004, *A&A*, 414, 667
- Haberl, F., Sturm, R., Ballet, J., et al. 2012b, *A&A*, 545, A128
- Haberl, F., Sturm, R., Filipović, M. D., Pietsch, W., & Crawford, E. J. 2012c, *A&A*, 537, L1
- Hanke, M., Wilms, J., Nowak, M. A., Barragán, L., & Schulz, N. S. 2010, *A&A*, 509, L8
- Harris, J. & Zaritsky, D. 2004, *AJ*, 127, 1531
- Harris, J. & Zaritsky, D. 2006, *AJ*, 131, 2514
- Harris, J. & Zaritsky, D. 2008, *PASA*, 25, 116
- Harris, J. & Zaritsky, D. 2009, *AJ*, 138, 1243
- Haschke, R., Grebel, E. K., & Duffau, S. 2012, *AJ*, 144, 106
- Hasinger, G., Aschenbach, B., & Truemper, J. 1996, *A&A*, 312, L9
- Haynes, R. F., Klein, U., Wayte, S. R., et al. 1991, *A&A*, 252, 475
- Heger, A., Fryer, C. L., Woosley, S. E., Langer, N., & Hartmann, D. H. 2003, *ApJ*, 591, 288
- Helder, E. A., Broos, P. S., Dewey, D., et al. 2013, *ApJ*, 764, 11
- Helder, E. A., Vink, J., Bassa, C. G., et al. 2009, *Science*, 325, 719
- Hénault-Brunet, V., Oskinova, L. M., Guerrero, M. A., et al. 2012, *MNRAS*, 420, L13
- Hendrick, S. P., Borkowski, K. J., & Reynolds, S. P. 2003, *ApJ*, 593, 370
- Heng, K., Haberl, F., Aschenbach, B., & Hasinger, G. 2008, *ApJ*, 676, 361
- Henize, K. G. 1956, *ApJS*, 2, 315
- Henley, D. B. & Shelton, R. L. 2008, *ApJ*, 676, 335
- Henriques, B. M. B., White, S. D. M., Thomas, P. A., et al. 2013, *MNRAS*, 431, 3373
- Henze, M. 2011, PhD thesis, Max Planck Institute for Extraterrestrial Physics
- Hirata, K., Kajita, T., Koshihara, M., Nakahata, M., & Oyama, Y. 1987, *Physical Review Letters*, 58, 1490
- Hirsh, R. F. 1983, *Glimpsing an invisible universe. The emergence of x-ray astronomy*

- Hnatyk, B. & Petruk, O. 1999, *A&A*, 344, 295
- Hodge, P. W. 1960, *ApJ*, 131, 351
- Hodge, P. W. 1961, *ApJ*, 133, 413
- Høg, E., Fabricius, C., Makarov, V. V., et al. 2000, *A&A*, 355, L27
- Holtzman, J. A., Gallagher, III, J. S., Cole, A. A., et al. 1999, *AJ*, 118, 2262
- Hoyle, F. & Fowler, W. A. 1960, *ApJ*, 132, 565
- Huensch, M., Schmitt, J. H. M. M., & Voges, W. 1998a, *A&AS*, 127, 251
- Huensch, M., Schmitt, J. H. M. M., & Voges, W. 1998b, *A&AS*, 132, 155
- Hughes, A., Staveley-Smith, L., Kim, S., Wolleben, M., & Filipović, M. 2007, *MNRAS*, 382, 543
- Hughes, J. P., Ghavamian, P., Rakowski, C. E., & Slane, P. O. 2003, *ApJ*, 582, L95
- Hughes, J. P., Hayashi, I., Helfand, D., et al. 1995, *ApJ*, 444, L81
- Hughes, J. P., Hayashi, I., & Koyama, K. 1998, *ApJ*, 505, 732
- Hughes, J. P. & Helfand, D. J. 1985, *ApJ*, 291, 544
- Hughes, J. P., Rafelski, M., Warren, J. S., et al. 2006, *ApJ*, 645, L117
- Iben, Jr., I. & Tutukov, A. V. 1984, *ApJS*, 54, 335
- Iwamoto, K., Brachwitz, F., Nomoto, K., et al. 1999, *ApJS*, 125, 439
- Jansen, F., Lumb, D., Altieri, B., et al. 2001, *A&A*, 365, L1
- Jaskot, A. E., Strickland, D. K., Oey, M. S., Chu, Y.-H., & García-Segura, G. 2011, *ApJ*, 729, 28
- Jennings, Z. G., Williams, B. F., Murphy, J. W., et al. 2012, *ApJ*, 761, 26
- Jennings, Z. G., Williams, B. F., Murphy, J. W., et al. 2014, *ApJ*, 795, 170
- Johnson, J. A., Ivans, I. I., & Stetson, P. B. 2006, *ApJ*, 640, 801
- Kaaret, P., Marshall, H. L., Aldcroft, T. L., et al. 2001, *ApJ*, 546, 1159
- Kaastra, J. S. & Mewe, R. 1993, *A&AS*, 97, 443
- Kahabka, P., de Boer, K. S., & Brüns, C. 2001, *A&A*, 371, 816
- Kahabka, P., Haberl, F., Payne, J. L., & Filipović, M. D. 2006, *A&A*, 458, 285
- Kahn, F. D. 1975, in *International Cosmic Ray Conference*, Vol. 11, *International Cosmic Ray Conference*, 3566
- Kallman, T. R., Palmeri, P., Bautista, M. A., Mendoza, C., & Krolik, J. H. 2004, *ApJS*, 155, 675
- Kamper, K. W. 1980, *The Observatory*, 100, 3
- Kapferer, W., Ferrari, C., Domainko, W., et al. 2006, *A&A*, 447, 827
- Kaplan, D. L., Kulkarni, S. R., van Kerkwijk, M. H., et al. 2001, *ApJ*, 556, 399
- Katsuda, S., Tsunemi, H., Mori, K., et al. 2011, *ApJ*, 730, 24
- Katsuda, S., Tsunemi, H., Mori, K., et al. 2012, *ApJ*, 756, 49
- Kavanagh, P. J., Sasaki, M., Bozzetto, L. M., et al. 2015, *A&A*, 573, A73
- Kavanagh, P. J., Sasaki, M., Points, S. D., et al. 2013, *A&A*, 549, A99
- Kim, S., Dopita, M. A., Staveley-Smith, L., & Bessell, M. S. 1999, *AJ*, 118, 2797
- Kim, S., Staveley-Smith, L., Dopita, M. A., et al. 2003, *ApJS*, 148, 473
- Klimek, M. D., Points, S. D., Smith, R. C., Shelton, R. L., & Williams, R. 2010, *ApJ*, 725, 2281
- Koerwer, J. F. 2009, *AJ*, 138, 1
- Komin, N., Djannati-Ataï, A., Gallant, Y., et al. 2012, *ArXiv e-prints* [[arXiv:1201.0639](https://arxiv.org/abs/1201.0639)]
- Kosenko, D., Helder, E. A., & Vink, J. 2010, *A&A*, 519, A11
- Kosenko, D., Vink, J., Blinnikov, S., & Rasmussen, A. 2008, *A&A*, 490, 223

- Koyama, K., Petre, R., Gotthelf, E. V., et al. 1995, *Nature*, 378, 255
- Kozłowski, S. & Kochanek, C. S. 2009, *ApJ*, 701, 508
- Kozłowski, S., Kochanek, C. S., Jacyszyn, A. M., et al. 2012, *ApJ*, 746, 27
- Kozłowski, S., Onken, C. A., Kochanek, C. S., et al. 2013, *ApJ*, 775, 92
- Kudritzki, R.-P. & Puls, J. 2000, *ARA&A*, 38, 613
- Kuntz, K. D. & Snowden, S. L. 2008, *A&A*, 478, 575
- Kuntz, K. D. & Snowden, S. L. 2010, *ApJS*, 188, 46
- Lakićević, M., van Loon, J. T., Meixner, M., et al. 2015, *ApJ*, 799, 50
- Lapenna, E., Mucciarelli, A., Origlia, L., & Ferraro, F. R. 2012, *ApJ*, 761, 33
- Lasker, B. M. 1978, *ApJ*, 223, 109
- Lazendic, J. S. & Slane, P. O. 2006, *ApJ*, 647, 350
- Leavitt, H. S. 1908, *Annals of Harvard College Observatory*, 60, 87
- Leavitt, H. S. & Pickering, E. C. 1912, *Harvard College Observatory Circular*, 173, 1
- Lee, J.-J., Park, S., Hughes, J. P., Slane, P. O., & Burrows, D. N. 2011, *ApJ*, 731, L8
- Lejeune, T. & Schaerer, D. 2001, *A&A*, 366, 538
- Leong, C., Kellogg, E., Gursky, H., Tananbaum, H., & Giacconi, R. 1971, *ApJ*, 170, L67
- Lewis, K. T., Burrows, D. N., Hughes, J. P., et al. 2003, *ApJ*, 582, 770
- Li, W., Bloom, J. S., Podsiadlowski, P., et al. 2011a, *Nature*, 480, 348
- Li, W., Leaman, J., Chornock, R., et al. 2011b, *MNRAS*, 412, 1441
- Liedahl, D. A. 1999, in *Lecture Notes in Physics*, Berlin Springer Verlag, Vol. 520, X-Ray Spectroscopy in Astrophysics, ed. J. van Paradijs & J. A. M. Bleeker, 189
- Liedahl, D. A., Osterheld, A. L., & Goldstein, W. H. 1995, *ApJ*, 438, L115
- Long, K. S., Blair, W. P., Winkler, P. F., et al. 2010, *ApJS*, 187, 495
- Long, K. S., Helfand, D. J., & Grabelsky, D. A. 1981, *ApJ*, 248, 925
- Lopes de Oliveira, R., Motch, C., Haberl, F., Negueruela, I., & Janot-Pacheco, E. 2006, *A&A*, 454, 265
- Lopez, L. A. 2014, in *IAU Symposium*, Vol. 296, IAU Symposium, ed. A. Ray & R. A. McCray, 239–244
- Lopez, L. A., Ramirez-Ruiz, E., Badenes, C., et al. 2009, *ApJ*, 706, L106
- Lopez, L. A., Ramirez-Ruiz, E., Huppenkothen, D., Badenes, C., & Pooley, D. A. 2011, *ApJ*, 732, 114
- Lord Stanley of Alderley. 1874, *The first voyage round the world, by Magellan* (Hakluyt Society)
- Lovisari, L., Schindler, S., & Kapferer, W. 2011, *A&A*, 528, A60
- Lowry, J. D., Chu, Y.-H., Guerrero, M. A., et al. 2004, *AJ*, 127, 125
- Lucke, P. B. & Hodge, P. W. 1970, *AJ*, 75, 171
- Lumb, D. H., Schartel, N., & Jansen, F. A. 2012, *Optical Engineering*, 51, 011009
- Lumb, D. H., Warwick, R. S., Page, M., & De Luca, A. 2002, *A&A*, 389, 93
- Mac Low, M.-M. & Klessen, R. S. 2004, *Reviews of Modern Physics*, 76, 125
- Maggi, P., Haberl, F., Bozzetto, L. M., et al. 2012a, *A&A*, 546, A109
- Maggi, P., Haberl, F., Kavanagh, P. J., et al. 2014, *A&A*, 561, A76
- Maggi, P., Haberl, F., Sturm, R., & Dewey, D. 2012b, *A&A*, 548, L3
- Makishima, K. 1986, in *Lecture Notes in Physics*, Berlin Springer Verlag, Vol. 266, The Physics of Accretion onto Compact Objects, ed. K. O. Mason, M. G. Watson, & N. E. White, 249
- Maoz, D. 2008, *MNRAS*, 384, 267
- Maoz, D. & Badenes, C. 2010, *MNRAS*, 407, 1314

- Maoz, D. & Mannucci, F. 2008, MNRAS, 388, 421
- Maoz, D. & Mannucci, F. 2012, PASA, 29, 447
- Marin, F., Dovciak, M., Karas, V., et al. 2014, in *The X-ray Universe 2014*, edited by Jan-Uwe Ness
- Mark, H., Price, R., Rodrigues, R., Seward, F. D., & Swift, C. D. 1969, ApJ, 155, L143
- Masai, K. 1984, AP&SS, 98, 367
- Mathewson, D. S. & Clarke, J. N. 1973, ApJ, 180, 725
- Mathewson, D. S., Ford, V. L., Dopita, M. A., et al. 1983, ApJS, 51, 345
- Mathewson, D. S., Ford, V. L., Dopita, M. A., et al. 1984, ApJS, 55, 189
- Mathewson, D. S., Ford, V. L., Tuohy, I. R., et al. 1985, ApJS, 58, 197
- Mathewson, D. S. & Healey, J. R. 1963, Nature, 199, 681
- McKee, J. D., Fritz, G., Cruddace, R. G., Shulman, S., & Friedman, H. 1980, ApJ, 238, 93
- McSwain, M. V. & Gies, D. R. 2005, ApJS, 161, 118
- Meaburn, J. 1980, MNRAS, 192, 365
- Meixner, M., Gordon, K. D., Indebetouw, R., et al. 2006, AJ, 132, 2268
- Merloni, A., Predehl, P., Becker, W., et al. 2012, ArXiv e-prints [arXiv:1209.3114]
- Mewe, R. & Gronenschild, E. H. B. M. 1981, A&AS, 45, 11
- Mewe, R., Gronenschild, E. H. B. M., & van den Oord, G. H. J. 1985, A&AS, 62, 197
- Meynet, G., Maeder, A., Schaller, G., Schaerer, D., & Charbonnel, C. 1994, A&AS, 103, 97
- Micelotta, E. R., Jones, A. P., & Tielens, A. G. G. M. 2010a, A&A, 510, A37
- Micelotta, E. R., Jones, A. P., & Tielens, A. G. G. M. 2010b, A&A, 510, A36
- Mills, B. Y., Turtle, A. J., Little, A. G., & Durdin, J. M. 1984, Australian Journal of Physics, 37, 321
- Minkowski, R. 1941, PASP, 53, 224
- Misanovic, Z., Pietsch, W., Haberl, F., et al. 2006, A&A, 448, 1247
- Mokiem, M. R., de Koter, A., Vink, J. S., et al. 2007, A&A, 473, 603
- Morris, T. & Podsiadlowski, P. 2007, Science, 315, 1103
- Morris, T. & Podsiadlowski, P. 2009, MNRAS, 399, 515
- Morse, J. A., Winkler, P. F., & Kirshner, R. P. 1995, AJ, 109, 2104
- Munar-Adrover, P., Paredes, J. M., Ribó, M., et al. 2014, ApJ, 786, L11
- Nandra, K. & Pounds, K. A. 1994, MNRAS, 268, 405
- Ness, J.-U., Schwarz, G. J., Retter, A., et al. 2007, ApJ, 663, 505
- Nikolaev, S., Drake, A. J., Keller, S. C., et al. 2004, ApJ, 601, 260
- Nishiuchi, M., Yokogawa, J., Koyama, K., & Hughes, J. P. 2001, PASJ, 53, 99
- Nomoto, K. 1982, ApJ, 253, 798
- Nomoto, K., Kobayashi, C., & Tominaga, N. 2013, ARA&A, 51, 457
- Okazaki, A. T., Hayasaki, K., & Moritani, Y. 2013, PASJ, 65, 41
- Orio, M. & Greiner, J. 1999, A&A, 344, L13
- Orlando, S., Bocchino, F., Miceli, M., Reale, F., & Peres, G. 2009, *Memorie della Societa Astronomica Italiana Supplementi*, 13, 97
- Osterbrock, D. E. 2001, in *Bulletin of the American Astronomical Society*, Vol. 33, American Astronomical Society Meeting Abstracts, 1330
- Owen, R. A., Filipović, M. D., Ballet, J., et al. 2011, A&A, 530, A132
- Paerels, F., Rasmussen, A. P., Hartmann, H. W., et al. 2001, A&A, 365, L308

- Pagel, B. E. J. 2001, *PASP*, 113, 137
- Pakull, M. 1978, *IAU Circ.*, 3313, 2
- Pallavicini, R., Golub, L., Rosner, R., et al. 1981, *ApJ*, 248, 279
- Park, S., Burrows, D. N., Garmire, G. P., et al. 2003a, *ApJ*, 586, 210
- Park, S., Hughes, J. P., Slane, P. O., et al. 2012, *ApJ*, 748, 117
- Park, S., Hughes, J. P., Slane, P. O., et al. 2003b, *ApJ*, 592, L41
- Park, S., Zhekov, S. A., Burrows, D. N., Garmire, G. P., & McCray, R. 2004, *ApJ*, 610, 275
- Park, S., Zhekov, S. A., Burrows, D. N., & McCray, R. 2005, *ApJ*, 634, L73
- Park, S., Zhekov, S. A., Burrows, D. N., et al. 2011, *ApJ*, 733, L35
- Pawsey, J. L. 1959, in *IAU Symposium, Vol. 9, URSI Symp. 1: Paris Symposium on Radio Astronomy*, ed. R. N. Bracewell, 405
- Payne, J. L., White, G. L., & Filipović, M. D. 2008, *MNRAS*, 383, 1175
- Peñarrubia, J., Ma, Y.-Z., Walker, M. G., & McConnachie, A. 2014, *MNRAS*, 443, 2204
- Perlmutter, S., Aldering, G., Goldhaber, G., et al. 1999, *ApJ*, 517, 565
- Peters, C. L., Lopez, L. A., Ramirez-Ruiz, E., Stassun, K. G., & Figueroa-Feliciano, E. 2013, *ApJ*, 771, L38
- Pfahl, E., Rappaport, S., Podsiadlowski, P., & Spruit, H. 2002, *ApJ*, 574, 364
- Phillips, M. M. 1993, *ApJ*, 413, L105
- Piatek, S., Pryor, C., & Olszewski, E. W. 2008, *AJ*, 135, 1024
- Pietrzyński, G., Graczyk, D., Gieren, W., et al. 2013, *Nature*, 495, 76
- Pietsch, W., Freyberg, M., & Haberl, F. 2005, *A&A*, 434, 483
- Pietsch, W. & Kahabka, P. 1993, in *Lecture Notes in Physics, Berlin Springer Verlag, Vol. 416, New Aspects of Magellanic Cloud Research*, ed. B. Baschek, G. Klare, & J. Lequeux, 59–70
- Pietsch, W., Misanovic, Z., Haberl, F., et al. 2004, *A&A*, 426, 11
- Pizzolato, N., Maggio, A., Micela, G., Sciortino, S., & Ventura, P. 2003, *A&A*, 397, 147
- Plucinsky, P. P., Williams, B., Long, K. S., et al. 2008, *ApJS*, 174, 366
- Pompéia, L., Hill, V., Spite, M., et al. 2008, *A&A*, 480, 379
- Price, R. E., Groves, D. J., Rodrigues, R. M., et al. 1971, *ApJ*, 168, L7
- Racusin, J. L., Park, S., Zhekov, S., et al. 2009, *ApJ*, 703, 1752
- Raguzova, N. V. 2001, *A&A*, 367, 848
- Rakowski, C. E., Badenes, C., Gaensler, B. M., et al. 2006, *ApJ*, 646, 982
- Reid, W. A. & Parker, Q. A. 2006, *MNRAS*, 365, 401
- Reig, P. 2011, *AP&SS*, 332, 1
- Rest, A., Matheson, T., Blondin, S., et al. 2008, *ApJ*, 680, 1137
- Rest, A., Suntzeff, N. B., Olsen, K., et al. 2005, *Nature*, 438, 1132
- Reyes-Iturbide, J., Rosado, M., Rodríguez-González, A., et al. 2014, *AJ*, 148, 102
- Reynolds, S. P., Borkowski, K. J., Green, D. A., et al. 2008, *ApJ*, 680, L41
- Rho, J. & Petre, R. 1998, *ApJ*, 503, L167
- Rieke, G. H., Young, E. T., Engelbracht, C. W., et al. 2004, *ApJS*, 154, 25
- Riess, A. G., Filippenko, A. V., Challis, P., et al. 1998, *AJ*, 116, 1009
- Rosati, P., Borgani, S., & Norman, C. 2002, *ARA&A*, 40, 539
- Rubele, S., Kerber, L., Girardi, L., et al. 2012, *A&A*, 537, A106
- Ruiz-Lapuente, P., Comeron, F., Méndez, J., et al. 2004, *Nature*, 431, 1069

- Russell, S. C. & Dopita, M. A. 1992, *ApJ*, 384, 508
- Salpeter, E. E. 1964, *ApJ*, 140, 796
- Sanduleak, N. 1970, *Contributions from the Cerro Tololo Inter-American Observatory*, 89
- Sasaki, M. 2009, *New Candidates for Supernova Remnants in the Large Magellanic Cloud*, xMM-Newton Proposal
- Sasaki, M., Haberl, F., & Pietsch, W. 2000, *A&AS*, 143, 391
- Sasaki, M., Haberl, F., & Pietsch, W. 2002, *A&A*, 392, 103
- Sasaki, M., Pietsch, W., Haberl, F., et al. 2012, *A&A*, 544, A144
- Sato, K., Tokoi, K., Matsushita, K., et al. 2007, *ApJ*, 667, L41
- Scannapieco, C., Wadepuhl, M., Parry, O. H., et al. 2012, *MNRAS*, 423, 1726
- Schaefer, B. E. 2008, *AJ*, 135, 112
- Schaefer, B. E. 2013, *Nature*, 495, 51
- Schaefer, B. E. & Pagnotta, A. 2012, *Nature*, 481, 164
- Schwarz, G. J., Ness, J.-U., Osborne, J. P., et al. 2011, *ApJS*, 197, 31
- Schwering, P. B. W. 1989, *A&AS*, 79, 105
- Sedov, L. I. 1946a, *Dokl. Akad. Nauk SSSR*, 42, 17
- Sedov, L. I. 1946b, *Prikl. Mat. Mekh.*, 10, 241
- Sedov, L. I. 1959, *Similarity and Dimensional Methods in Mechanics*
- Seok, J. Y., Koo, B.-C., & Onaka, T. 2013, *ApJ*, 779, 134
- Seok, J. Y., Koo, B.-C., Onaka, T., et al. 2008, *PASJ*, 60, 453
- Seward, F. D., Charles, P. A., Foster, D. L., et al. 2012, *ApJ*, 759, 123
- Seward, F. D., Williams, R. M., Chu, Y.-H., et al. 2006, *ApJ*, 640, 327
- Shull, J. M. & van Steenberg, M. 1982, *ApJS*, 48, 95
- Skrutskie, M. F., Cutri, R. M., Stiening, R., et al. 2006, *AJ*, 131, 1163
- Smecker-Hane, T. A., Cole, A. A., Gallagher, III, J. S., & Stetson, P. B. 2002, *ApJ*, 566, 239
- Smith, C., Leiton, R., & Pizarro, S. 2000, in *Astronomical Society of the Pacific Conference Series*, Vol. 221, *Stars, Gas and Dust in Galaxies: Exploring the Links*, ed. D. Alloin, K. Olsen, & G. Galaz, 83
- Smith, R. C., Chu, Y.-H., Mac Low, M.-M., Oey, M. S., & Klein, U. 1994, *AJ*, 108, 1266
- Smith, R. K., Brickhouse, N. S., Liedahl, D. A., & Raymond, J. C. 2001, *ApJ*, 556, L91
- Snowden, S. L., Mushotzky, R. F., Kuntz, K. D., & Davis, D. S. 2008, *A&A*, 478, 615
- Sreekumar, P., Bertsch, D. L., Dingus, B. L., et al. 1992, *ApJ*, 400, L67
- Stanimirović, S., Staveley-Smith, L., & Jones, P. A. 2004, *ApJ*, 604, 176
- Staveley-Smith, L., Kim, S., Calabretta, M. R., Haynes, R. F., & Kesteven, M. J. 2003, *MNRAS*, 339, 87
- Stephenson, F. R. & Green, D. A. 2002, *Historical supernovae and their remnants*, by F. Richard Stephenson and David A. Green. *International series in astronomy and astrophysics*, vol. 5. Oxford: Clarendon Press, 2002, ISBN 0198507666, 5
- Stiele, H., Pietsch, W., Haberl, F., et al. 2011, *A&A*, 534, A55
- Strüder, L., Briel, U., Dennerl, K., et al. 2001, *A&A*, 365, L18
- Sturm, R., Haberl, F., Aschenbach, B., & Hasinger, G. 2010, *A&A*, 515, A5
- Sturm, R., Haberl, F., Hasinger, G., Kenzaki, K., & Itoh, M. 2009, *PASJ*, 61, 895
- Sturm, R., Haberl, F., Pietsch, W., et al. 2013, *A&A*, 558, A3
- Sturm, R., Haberl, F., Pietsch, W., et al. 2012a, *A&A*, 537, A76

- Sturm, R., Haberl, F., Rau, A., et al. 2012b, *A&A*, 542, A109
- Sturm, R. K. N. 2012, PhD thesis, Fakultät für Physik, Technische Universität München, Germany
- Sturmer, S. J. & Dermer, C. D. 1995, *A&A*, 293, L17
- Subramaniam, A. & Subramanian, S. 2009, *ApJ*, 703, L37
- Subramanian, S. & Subramaniam, A. 2009, *A&A*, 496, 399
- Subramanian, S. & Subramaniam, A. 2013, *A&A*, 552, A144
- Sunyaev, R., Kaniovsky, A., Efremov, V., et al. 1987, *Nature*, 330, 227
- Sunyaev, R. A. & Titarchuk, L. G. 1980, *A&A*, 86, 121
- Tabatabaei, F. S. & Berkhuijsen, E. M. 2010, *A&A*, 517, A77
- Takahashi, T., Mitsuda, K., Kelley, R., et al. 2012, in *Society of Photo-Optical Instrumentation Engineers (SPIE) Conference Series*, Vol. 8443, *Society of Photo-Optical Instrumentation Engineers (SPIE) Conference Series*
- Tappe, A., Rho, J., & Reach, W. T. 2006, *ApJ*, 653, 267
- Temim, T., Gehrz, R. D., Woodward, C. E., et al. 2006, *AJ*, 132, 1610
- Townsend, L. J., Coe, M. J., Corbet, R. H. D., & Hill, A. B. 2011, *MNRAS*, 416, 1556
- Truelove, J. K. & McKee, C. F. 1999, *ApJS*, 120, 299
- Trümper, J., Hasinger, G., Aschenbach, B., et al. 1991, *Nature*, 349, 579
- Trümper, J. E. & Hasinger, G. 2008, *The Universe in X-Rays*
- Tsujimoto, T., Nomoto, K., Yoshii, Y., et al. 1995, *MNRAS*, 277, 945
- Tuohy, I. R., Dopita, M. A., Mathewson, D. S., Long, K. S., & Helfand, D. J. 1982, *ApJ*, 261, 473
- Turner, M. J. L., Abbey, A., Arnaud, M., et al. 2001, *A&A*, 365, L27
- Turner, T. J. & Pounds, K. A. 1989, *MNRAS*, 240, 833
- Udalski, A., Soszynski, I., Szymanski, M. K., et al. 2008, *Acta Astron.*, 58, 89
- Urry, C. M. & Padovani, P. 1995, *PASP*, 107, 803
- Vaiana, G. S., Cassinelli, J. P., Fabbiano, G., et al. 1981, *ApJ*, 245, 163
- van den Heuvel, E. P. J., Bhattacharya, D., Nomoto, K., & Rappaport, S. A. 1992, *A&A*, 262, 97
- van der Heyden, K. J., Behar, E., Vink, J., et al. 2002, *A&A*, 392, 955
- van der Heyden, K. J., Bleeker, J. A. M., & Kaastra, J. S. 2004, *A&A*, 421, 1031
- van der Heyden, K. J., Bleeker, J. A. M., Kaastra, J. S., & Vink, J. 2003, *A&A*, 406, 141
- van der Marel, R. P. 2001, *AJ*, 122, 1827
- van der Marel, R. P., Alves, D. R., Hardy, E., & Suntzeff, N. B. 2002, *AJ*, 124, 2639
- van der Marel, R. P. & Cioni, M.-R. L. 2001, *AJ*, 122, 1807
- van der Marel, R. P. & Kallivayalil, N. 2014, *ApJ*, 781, 121
- Van der Swaelmen, M., Hill, V., Primas, F., & Cole, A. A. 2013, *A&A*, 560, A44
- Vanhala, H. A. T. & Cameron, A. G. W. 1998, *ApJ*, 508, 291
- Vasilopoulos, G., Haberl, F., Sturm, R., Maggi, P., & Udalski, A. 2014, *A&A*, 567, A129
- Vasilopoulos, G., Maggi, P., Haberl, F., et al. 2013, *A&A*, 558, A74
- Verley, S., Corbelli, E., Giovanardi, C., & Hunt, L. K. 2009, *A&A*, 493, 453
- Vink, J. 2012, *A&A Rev.*, 20, 49
- Vink, J. S., de Koter, A., & Lamers, H. J. G. L. M. 2001, *A&A*, 369, 574
- Vogt, F. P. A., Besel, M.-A., Krause, O., & Dullemond, C. P. 2012, *ApJ*, 750, 155
- Wang, Q., Hamilton, T., Helfand, D. J., & Wu, X. 1991, *ApJ*, 374, 475

- Wang, Q. & Helfand, D. J. 1991, *ApJ*, 373, 497
- Warren, J. S. & Hughes, J. P. 2004, *ApJ*, 608, 261
- Warren, J. S., Hughes, J. P., & Slane, P. O. 2003, *ApJ*, 583, 260
- Watson, M. G., Schröder, A. C., Fyfe, D., et al. 2009, *A&A*, 493, 339
- Weaver, R., McCray, R., Castor, J., Shapiro, P., & Moore, R. 1977, *ApJ*, 218, 377
- Webber, W. R. 1998, *ApJ*, 506, 329
- Webbink, R. F. 1984, *ApJ*, 277, 355
- Weisskopf, M. C., Bellazzini, R., Costa, E., et al. 2008, in *Society of Photo-Optical Instrumentation Engineers (SPIE) Conference Series*, Vol. 7011, Society of Photo-Optical Instrumentation Engineers (SPIE) Conference Series
- Weisz, D. R., Dolphin, A. E., Skillman, E. D., et al. 2013, *MNRAS*, 431, 364
- Westerlund, B. E. 1997, *The Magellanic Clouds*
- Westerlund, B. E. & Mathewson, D. S. 1966, *MNRAS*, 131, 371
- Whelan, E., Kavanagh, P., Sasaki, M., et al. 2014, in *The X-ray Universe 2014*, edited by Jan-Uwe Ness
- Whelan, J. & Iben, Jr., I. 1973, *ApJ*, 186, 1007
- Williams, B. J., Borkowski, K. J., Reynolds, S. P., et al. 2006a, *ApJ*, 652, L33
- Williams, R. M. & Chu, Y.-H. 2005, *ApJ*, 635, 1077
- Williams, R. M., Chu, Y.-H., Dickel, J. R., et al. 2005, *ApJ*, 628, 704
- Williams, R. M., Chu, Y.-H., Dickel, J. R., et al. 2004, *ApJ*, 613, 948
- Williams, R. M., Chu, Y.-H., Dickel, J. R., et al. 1999a, *ApJS*, 123, 467
- Williams, R. M., Chu, Y.-H., Dickel, J. R., et al. 1999b, *ApJ*, 514, 798
- Williams, R. M., Chu, Y.-H., & Gruendl, R. 2006b, *AJ*, 132, 1877
- Wilms, J., Allen, A., & McCray, R. 2000, *ApJ*, 542, 914
- Wolter, H. 1952, *Annalen der Physik*, 445, 94
- Wong, T., Hughes, A., Ott, J., et al. 2011, *ApJS*, 197, 16
- Woods, T. E. & Gilfanov, M. 2013, *MNRAS*, 432, 1640
- Woosley, S. E. & Weaver, T. A. 1995, *ApJS*, 101, 181
- Yamaguchi, H., Badenes, C., Petre, R., et al. 2014, *ApJ*, 785, L27
- Yamaguchi, H., Sawada, M., & Bamba, A. 2010, *ApJ*, 715, 412
- Yamaguchi, R., Mizuno, N., Onishi, T., Mizuno, A., & Fukui, Y. 2001a, *ApJ*, 553, L185
- Yamaguchi, R., Mizuno, N., Onishi, T., Mizuno, A., & Fukui, Y. 2001b, *PASJ*, 53, 959
- Yates, R. M., Henriques, B., Thomas, P. A., et al. 2013, *MNRAS*, 435, 3500
- Zaritsky, D. 2004, *ApJ*, 614, L37
- Zaritsky, D., Harris, J., Thompson, I. B., & Grebel, E. K. 2004, *AJ*, 128, 1606
- Zdziarski, A. A., Poutanen, J., & Johnson, W. N. 2000, *ApJ*, 542, 703
- Zel'dovich, Y. B. 1964, *Soviet Physics Doklady*, 9, 195
- Zel'dovich, Y. B. & Raizer, Y. P. 1967, *Physics of shock waves and high-temperature hydrodynamic phenomena*
- Zhang, F., Li, X.-D., & Wang, Z.-R. 2004, *ApJ*, 603, 663
- Zhang, N.-X., Chu, Y.-H., Williams, R. M., et al. 2014, *ApJ*, 792, 58
- Zhao, H. & Evans, N. W. 2000, *ApJ*, 545, L35
- Zhekov, S. A., McCray, R., Borkowski, K. J., Burrows, D. N., & Park, S. 2006, *ApJ*, 645, 293

A. SNR sample and X-ray spectral results

IN THE FOLLOWING pages, I list the sample of LMC SNRs used in this thesis (Table A.1). Then, I give the results of the X-ray spectral analysis (Sect. 11.2) for the 1T/2T sample (Table A.2) and the “bright SNR” sample (Table A.3). The columns of Table A.1 are the following:

- (1) MCSNR identifier, in the form “JHHMM–DDMM”.
- (2) Right ascension of the remnant, in J2000 equinox.
- (3) Declination in J2000 equinox.
- (4) Old “common” name used in the literature.
- (5) Flag coding the type of X-ray data available and used in this thesis. “X” indicates that XMM-Newton data are present, and “MX” that multiple XMM-Newton observation of the remnant exist. “C” or “R” are used when no XMM-Newton observations are available but Chandra or ROSAT observations were used, respectively. “N” means that no X-ray information was found.
- (6) L_X , the X-ray luminosity in the 0.3 keV – 8 keV band, in units of 10^{35} erg s⁻¹, obtained as described in Sect. 11.5.
- (7) X-ray size in arcsec. Only the *maximal* extent is given (corresponding to the diameter in a circularly symmetric case). The number between brackets gives the position angle (PA) of the maximal extent in the non-symmetric case. The PA is measured in degree, eastwards of north. Size was measured from XMM-Newton images whenever applicable (“X” and “MX” flags). For “C” SNRs, the quoted value is taken from the entry in the Chandra SNR catalogue. For the ROSAT-only SNRs (J0448–6700 and J0455–6839), I used the value quoted in Badenes et al. (2010) and Williams et al. (1999a), respectively.
- (8) N_H fraction, as defined in Sect. 11.6. Uncertainties are given at the 90 % C.L.
- (9) N_{OB} , the number of blue early-type stars within 100 pc of the remnant (see Sect. 11.4.1).
- (10) r , the ratio of CC SNe to thermonuclear SNe expected from the observed distribution of stellar ages in the neighbourhood of the remnant, as obtained by Eq. 11.1 (see Sect. 11.6 for details).
- (11) Reference in which the SNR was first published. The acronyms are defined in the Notes of Table A.1.

For Table A.2, columns are described in Sect. 11.2.3. A. Table A.3 use the same columns, except that abundances are explicitly given for each element.

TABLE A.1 – SNRs in the LMC

MCSNR	RA	DEC	Other name	X-ray data	L_X	X-ray size	N_H fraction	N_{OB}	r	ref.
(1)	(2)	(3)	(4)	(5)	(6)	(7)	(8)	(9)	(10)	(11)
J0448–6700	04:48:22	-66:59:52	[HP99] 460	R	0.46	220	—	3	$1.67^{+0.92}_{-0.20}$	BGS06
J0449–6920	04:49:20	-69:20:20		X	0.07	162 (85)	$2.33^{+0.93}_{-0.70}$	26	$6.29^{+2.33}_{-2.66}$	KPS10
J0450–7050	04:50:27	-70:50:15	B0450-709	X	0.59	340 (85)	$0.93^{+0.68}_{-0.56}$	2	$1.89^{+0.29}_{-0.39}$	MFT85
J0453–6655	04:53:14	-66:55:13	N4	X	1.17	256 (122)	$0.60^{+0.33}_{-0.29}$	83	$6.36^{+7.24}_{-2.85}$	SCM94
J0453–6829	04:53:38	-68:29:27	B0453-685	X	13.85	120	$0.54^{+0.08}_{-0.25}$	5	$2.42^{+0.46}_{-0.39}$	LHG81
J0454–6713	04:54:33	-67:13:13	N9	C	1.58	216 (5)	1.32	72	$9.69^{+5.26}_{-5.34}$	SCM94
J0454–6626	04:54:49	-66:25:32	N11L	X	0.63	106 (50)	$0.35^{+0.23}_{-0.22}$	33	$5.84^{+0.58}_{-2.39}$	MC73
J0455–6839	04:55:37	-68:38:47	N86	R	1.42	366	—	16	$2.66^{+0.23}_{-0.51}$	MC73
J0459–7008	04:59:55	-70:07:52	N186D	C	1.09	114	$0.93^{+0.42}_{-0.25}$	51	$3.73^{+0.87}_{-0.98}$	MC73
J0505–6753	05:05:42	-67:52:39	DEM L71	X	44.59	76 (5)	0.22 ± 0.01	13	$2.38^{+0.53}_{-0.52}$	LHG81
J0505–6802	05:05:55	-68:01:47	N23	MX	26.25	96	$0.81^{+0.25}_{-0.06}$	26	$2.7^{+0.47}_{-0.76}$	MC73
J0506–6541	05:06:05	-65:41:08	DEM L72	X	0.53	410 (170)	$0.39^{+0.50}_{-0.39}$	12	$1.00^{+0.08}_{-0.40}$	KPS10
J0506–7026	05:06:50	-70:25:53	[HP99] 1139	X	1.44	262 (10)	$0(< 0.11)$	82	$3.08^{+0.57}_{-0.83}$	WKS14
J0508–6902	05:08:37	-69:02:54	[HP99] 791	X	0.37	304 (33)	$0(< 0.48)$	22	$1.27^{+0.04}_{-0.11}$	BKM14
J0508–6830	05:08:50	-68:30:50	J0508-6830	X	0.09	138 (160)	$0(< 0.7)$	27	$3.09^{+0.69}_{-0.51}$	MHK14
J0509–6844	05:08:59	-68:43:35	N103B	X	51.7	30	$1.16^{+0.08}_{-0.04}$	99	$6.18^{+0.63}_{-1.31}$	MC73
J0509–6731	05:09:31	-67:31:17	B0509-67.5	X	16.51	31.8	$1.42^{+0.06}_{-0.06}$	2	$1.86^{+0.26}_{-0.41}$	LHG81
J0511–6759	05:11:11	-67:59:08		MX	0.16	112	$0(< 1.08)$	3	$1.23^{+0.04}_{-0.43}$	MHK14
J0512–6707	05:12:27	-67:07:18	[HP99] 483	X	0.09	120 (45)	$0.28^{+0.38}_{-0.23}$	25	$5.56^{+1.2}_{-2.66}$	unpublished
J0513–6912	05:13:14	-69:12:20	DEM L109	X	0.51	240 (155)	$0.56^{+0.25}_{-0.43}$	16	$1.64^{+0.23}_{-0.30}$	MFT85
J0514–6840	05:14:16	-68:40:22		MX	0.4	220	$0(< 0.05)$	7	$1.05^{+0.16}_{-0.27}$	MHK14
J0517–6759	05:17:08	-67:59:29		X	0.24	324 (30)	$1.44^{+1.98}_{-1.19}$	12	$6.37^{+2.01}_{-3.23}$	MHK14

TABLE A.1 – (continued)

MCSNR	RA	DEC	Other name	X-ray data	L_X	X-ray size	N_H fraction	N_{OB}	r	ref.
(1)	(2)	(3)	(4)	(5)	(6)	(7)	(8)	(9)	(10)	(11)
J0518–6939	05:18:41	-69:39:12	N120	MX	0.88	148 (110)	0(< 0.75)	133	4.57 ^{+0.52} _{-0.96}	MC73
J0519–6902	05:19:35	-69:02:09	B0519-690	MX	34.94	33.6	0.63 ^{+0.03} _{-0.03}	13	1.71 ^{+0.26} _{-0.34}	LHG81
J0519–6926	05:19:44	-69:26:08	B0520-694	X	2.69	190 (140)	0(< 0.05)	114	3.41 ^{+0.09} _{-0.51}	MFD83
J0521–6543	05:21:39	-65:43:07	DEM L142	N	—	168	—	36	5.97 ^{+0.30} _{-3.07}	BGS06
J0523–6753	05:23:07	-67:53:12	N44	X	0.9	255 (90)	0.21 ^{+0.13} _{-0.10}	99	6.17 ^{+2.61} _{-3.15}	CMG93
J0524–6624	05:24:20	-66:24:23	DEM L175a	N	—	240	—	39	6.88 ^{+13.1} _{-3.34}	MFT85
J0525–6938	05:25:04	-69:38:24	N132D	X	315.04	126 (60)	0.45 ^{+0.02} _{-0.02}	56	2.72 ^{+0.13} _{-0.35}	WM66
J0525–6559	05:25:25	-65:59:19	N49B	X	38.03	170	0.95 ^{+0.09} _{-0.08}	33	4.42 ^{+1.43} _{-1.76}	MC73
J0526–6605	05:26:00	-66:04:57	N49	X	64.37	84	0.64 ^{+0.04} _{-0.04}	37	6.33 ^{+3.99} _{-2.72}	WM66
J0527–6912	05:27:39	-69:12:04	B0528-692	MX	1.99	198 (142)	0(< 0.05)	224	7.59 ^{+0.29} _{-2.74}	MFD84
J0527–6550	05:27:54	-65:49:38	DEM L204	N	—	282	—	9	1.54 ^{+0.40} _{-0.50}	LHG81
J0527–6714	05:27:56	-67:13:40	B0528-6716	X	0.25	270 (40)	2.28	97	11.12 ^{+4.37} _{-6.42}	MFT85
J0527–7104	05:27:57	-71:04:30	[HP99] 1234	X	0.21	369 (155)	0.66 ^{+0.48} _{-0.16}	6	2.4 ^{+0.52} _{-0.52}	KSP13
J0528–6727	05:28:05	-67:27:20	DEM L205	X	0.58	324 (40)	0(< 0.18)	142	8.97 ^{+1.91} _{-4.9}	MHB12
J0529–6653	05:29:51	-66:53:28	DEM L214	X	1.04	145 (140)	0.96 ^{+0.74} _{-0.79}	222	14.12 ^{+13.7} _{-8.61}	BFC12a
J0530–7008	05:30:40	-70:07:30	DEM L218	X	0.72	325 (50)	0.29 ^{+0.36} _{-0.22}	19	1.97 ^{+0.16} _{-0.12}	DFB12
J0531–7100	05:31:56	-71:00:19	N206	X	2.55	180 (90)	0.20 ^{+0.25} _{-0.16}	49	5.36 ^{+0.79} _{-1.95}	MC73
J0532–6732	05:32:30	-67:31:33	B0532-675	X	2.48	285 (145)	0.54 ^{+0.43} _{-0.32}	173	8.07 ^{+3.56} _{-3.83}	MFT85
J0533–7202	05:33:46	-72:02:59	1RXSJ053353.6-7204	X	0.57	205 (85)	0.26 ^{+0.24} _{-0.23}	1	0.8 ^{+0.17} _{-0.37}	BFC13
J0534–6955	05:34:02	-69:55:03	B0534-699	X	6.33	135 (35)	0.92 ^{+0.07} _{-0.11}	8	1.18 ^{+0.05} _{-0.13}	LHG81
J0534–7033	05:34:18	-70:33:26	DEM L238	X	1.55	186 (110)	0(< 0.02)	4	2.07 ^{+0.2} _{-0.24}	LHG81
J0535–6916	05:35:28	-69:16:11	SNR1987A	MX	27.39	1.62	1.16 ^{+0.03} _{-0.05}	84	5.85 ^{+1.28} _{-1.87}	historical
J0535–6602	05:35:44	-66:02:14	N63A	X	185.68	84	0.46 ^{+0.05} _{-0.03}	45	3.95 ^{+0.73} _{-1.47}	WM66

TABLE A.1 – (continued)

MCSNR	RA	DEC	Other name	X-ray data	L_X	X-ray size	N_H fraction	N_{OB}	r	ref.
(1)	(2)	(3)	(4)	(5)	(6)	(7)	(8)	(9)	(10)	(11)
J0535–6918	05:35:46	-69:18:02	Honeycomb	MX	0.4	105 (155)	0.90±0.12	108	8.32 ^{+2.40} _{-3.05}	CDS95
J0536–6735	05:36:03	-67:34:36	DEM L241	X	3.84	310 (155)	0.66 ^{+0.06} _{-0.06}	39	2.71 ^{+0.55} _{-0.53}	MFT85
J0536–7039	05:36:07	-70:38:37	DEM L249	MX	1.43	200 (35)	0(< 0.03)	2	1.56 ^{+0.10} _{-0.10}	LHG81
J0536–6913	05:36:17	-69:13:28	B0536-6914	MX	0.22	66 (90)	1.11 ^{+0.11} _{-0.75}	92	5.85 ^{+1.28} _{-1.87}	KSB15
J0537–6628	05:37:27	-66:27:50	DEM L256	X	0.32	227 (42)	0.25 ^{+0.50} _{-0.25}	48	1.62 ^{+0.07} _{-0.17}	KPS10
J0537–6910	05:37:46	-69:10:28	N157B	MX	15.0	120	1.73 ^{+0.06} _{-0.06}	83	19.56 ^{+8.02} _{-11.0}	MC73
J0540–6944	05:39:59	-69:44:02	N159	X	0.43	92 (110)	1.92 ^{+0.20} _{-0.15}	60	3.53 ^{+0.62} _{-0.85}	CKS97
J0540–6920	05:40:11	-69:19:55	B0540-693	X	87.35	72	1.58 ^{+0.04} _{-0.04}	119	24.41 ^{+19.1} _{-15.8}	MC73
J0541–6659	05:41:51	-66:59:04	[HP99] 456	X	0.77	300	0(< 0.06)	10	2.08 ^{+0.04} _{-0.29}	GSH12
J0543–6858	05:43:08	-68:58:18	DEM L299	X	1.68	330 (55)	0.4 ^{+0.13} _{-0.05}	38	4.98 ^{+2.88} _{-1.95}	LHG81
J0547–6943	05:46:59	-69:42:50	DEM L316B	X	1.47	190 (95)	0.63 ^{+0.19} _{-0.12}	0	1.03 ^{+0.26} _{-0.56}	MC73
J0547–6941	05:47:22	-69:41:26	DEM L316A	X	1.26	190 (170)	0.92 ^{+0.24} _{-0.20}	0	1.03 ^{+0.26} _{-0.56}	MC73
J0547–7025	05:47:49	-70:24:54	B0548-704	X	2.94	118 (75)	0.88 ^{+0.11} _{-0.10}	3	0.72 ^{+0.20} _{-0.26}	MFD83
J0550–6823	05:50:30	-68:22:40		C	1.22	312 (90)	1.22	4	2.04 ^{+0.20} _{-0.39}	BFC12b

Notes. Acronyms for column (11):

WM66: Westerlund & Mathewson (1966); MC73: Mathewson & Clarke (1973); LHG81: Long et al. (1981); MFD83: Mathewson et al. (1983); MFD84: Mathewson et al. (1984); MFT85: Mathewson et al. (1985); CMG83: Chu et al. (1993); SCM94: Smith et al. (1994); CDS95: Chu et al. (1995b); CKS97: Chu et al. (1997); BGS06: Blair et al. (2006); KPS10: Klimek et al. (2010); GSH12: Grondin et al. (2012); BFC12a: Bozzetto et al. (2012a); BFC12b: Bozzetto et al. (2012b); DFB12: de Horta et al. (2012); MHB12: Maggi et al. (2012a); KSP13: Kavanagh et al. (2013); BFC13: Bozzetto et al. (2013); MHK14: Maggi et al. (2014); BKM14: Bozzetto et al. (2014); WKS14: Whelan et al. (2014); KSB15: Kavanagh et al. (2015).

TABLE A.2 – X-ray spectral results of LMC SNRs.

MCSNR	Component 1:					Component 2:					χ^2/ν
	$N_{H \text{ LMC}}$ (10^{21} cm^{-2})	kT (keV)	τ ($10^{11} \text{ s cm}^{-3}$)	EM (10^{58} cm^{-3})	Abundances	$N_{H \text{ LMC}}$ (10^{21} cm^{-2})	kT (keV)	τ ($10^{11} \text{ s cm}^{-3}$)	EM (10^{58} cm^{-3})	Abundances	
(1)	(2)	(3)	(4)	(5)	(6)	(7)	(8)	(9)	(10)	(11)	(12)
J0449–6920	$6.97^{+2.77}_{-2.08}$	$0.20^{+0.05}_{-0.12}$	CIE	$18.3^{+359}_{-16.3}$	RD92	—	—	—	—	—	1985.3/1863
J0450–7050 ^(a)	$1.31^{+0.95}_{-0.79}$	0.24 ± 0.02	CIE	$33.6^{+36.8}_{-24.1}$	O: $0.20^{+0.14}_{-0.08}$ Ne: $0.40^{+0.33}_{-0.07}$ Mg: $0.20 (< 0.48)$	—	—	—	—	—	4669.4/3294
J0453–6655	$1.10^{+0.61}_{-0.54}$	$0.36^{+0.10}_{-0.08}$	$1.38^{+2.07}_{-0.63}$	$30.7^{+36.9}_{-15.6}$	O: $0.13^{+0.05}_{-0.04}$ Ne: $0.12^{+0.07}_{-0.05}$ Mg: $0.15^{+0.20}_{-0.01}$ Fe: $0.29^{+0.12}_{-0.08}$	—	—	—	—	—	4460.9/4214
J0453–6829 ^(b)	$0.93^{+0.13}_{-0.43}$	$0.37^{+0.03}_{-0.05}$	$1.58^{+0.51}_{-0.24}$	$27.2^{+16.28}_{-3.56}$	O: 0.17 ± 0.01 Ne: $0.25^{+0.03}_{-0.01}$ Mg: 0.37 ± 0.05 Si: $0.61^{+0.24}_{-0.23}$ Fe: $0.28^{+0.03}_{-0.02}$	—	—	—	—	—	2156.2/1860
J0454–6626	$1.15^{+0.76}_{-0.71}$	$0.34^{+0.09}_{-0.07}$	$1.17^{+1.48}_{-0.70}$	$1.67^{+1.38}_{-0.99}$	O: $0.14^{+0.07}_{-0.05}$ Mg: $0.15 (< 0.39)$ Fe: $0.26^{+0.10}_{-0.08}$	—	—	—	—	—	2136.8/1811
J0505–6802 ^(c)	$1.58^{+0.49}_{-0.11}$	$0.32^{+0.02}_{-0.03}$	$3.40^{+2.26}_{-1.62}$	$107.4^{+76.1}_{-16.3}$	O: $0.11^{+0.03}_{-0.04}$ Ne: 0.16 ± 0.02 Mg: 0.18 ± 0.03 Si: $0.37^{+0.05}_{-0.06}$ Fe: $0.20^{+0.06}_{-0.03}$	1.58	$1.09^{+0.07}_{-0.09}$	$2.46^{+0.96}_{-0.48}$	$6.50^{+12.0}_{-0.60}$	—	454.4/407
J0506–6541	$0.59 (< 1.34)$	0.18 ± 0.01	CIE	$2.27^{+1.35}_{-0.71}$	Ne: $1.26^{+0.41}_{-0.28}$	—	—	—	—	—	8549.4/7232

TABLE A.2 – (continued)

MCSNR	Component 1:					Component 2:					χ^2/ν
	$N_{H\text{ LMC}}$ (10^{21} cm^{-2})	kT (keV)	τ (10^{11} s cm^{-3})	EM (10^{58} cm^{-3})	Abundances	$N_{H\text{ LMC}}$ (10^{21} cm^{-2})	kT (keV)	τ (10^{11} s cm^{-3})	EM (10^{58} cm^{-3})	Abundances	
(1)	(2)	(3)	(4)	(5)	(6)	(7)	(8)	(9)	(10)	(11)	(12)
J0506–7026	0(< 0.12)	$0.70^{+0.09}_{-0.02}$	$1.99^{+0.79}_{-0.90}$	0.61 ± 0.09	O: $0.33^{+0.07}_{-0.05}$ Ne: $0.42^{+0.17}_{-0.14}$ Mg: $0.22^{+0.13}_{-0.12}$ Fe: $1.49^{+0.17}_{-0.23}$	—	—	—	—	—	9026.4/8365
J0508–6830 ^(d)	0(< 1.80)	$0.71^{+0.06}_{-0.07}$	CIE	$1.0^{(+700)}_{-0.4} \times 10^{-4}$	O: 0 Fe: 792.9(> 1.1)	—	—	—	—	—	1488.3/1554
J0508–6902 ^(e)	0(< 0.8)	$0.41^{+0.05}_{-0.06}$	$27.0^{+42.2}_{-9.7}$	$0.48^{+0.25}_{-0.22}$	RD92	0	0.78 ± 0.03	CIE	< 48.8 0.16 ± 0.01	pure O pure Fe	267.1/219
J0511–6759 ^(d)	0(< 2.10)	$0.65^{+0.05}_{-0.04}$	CIE	$1.2^{(+8.0)}_{-1.0} \times 10^{-2}$	O: 0 Fe: 11.4(> 4.7)	—	—	—	—	—	707.5/692
J0512–6707	$0.82^{+1.09}_{-0.68}$	0.24 ± 0.01	CIE	$0.15^{+0.17}_{-0.08}$	RD92	—	—	—	—	—	3059.4/2083
J0513–6912	$1.34^{+0.59}_{-1.02}$	0.43 ± 0.08	$10.9^{+37.3}_{-6.66}$	$1.28^{+1.67}_{-0.89}$	O: $0.27^{+0.23}_{-0.08}$ Ne: $0.46^{+0.57}_{-0.13}$ Mg: $0.75^{+0.34}_{-0.27}$ Si: $1.33^{+0.79}_{-0.50}$ Fe: $0.20^{+0.23}_{-0.04}$	—	—	—	—	—	5352.3/4996
J0514–6840 ^(d)	0(< 0.09)	0.30 ± 0.01	$2.60^{+0.60}_{-0.50}$	0.51 ± 0.03	O: 0.28 ± 0.03 Fe: $0.38^{+0.13}_{-0.11}$	—	—	—	—	—	8005.3/7957
J0517–6759 ^(d)	$3.5^{+4.8}_{-2.9}$	$0.1^{+0.04}_{-0.02}$	CIE	$11.2^{+7.2}_{-9.0}$	RD92	0(< 1.7)	$0.59^{+0.05}_{-0.04}$	CIE	$0.19^{+0.002}_{-0.02}$	RD92	2558.9/2547
J0518–6939	0(< 1.16)	$0.44^{+0.30}_{-0.09}$	$4.91^{+15.0}_{-3.62}$	$1.53^{+1.43}_{-1.08}$	O: $0.14^{+0.06}_{-0.07}$ Ne: 0.23 ± 0.15 Mg: $0.31^{+0.42}_{-0.26}$ Si: $0.96^{+1.63}_{-0.90}$ Fe: $0.27^{+0.34}_{-0.10}$	—	—	—	—	—	2292.1/2190

TABLE A.2 – (continued)

MCSNR	Component 1:					Component 2:					χ^2/ν
	$N_{H \text{ LMC}}$ (10^{21} cm^{-2})	kT (keV)	τ ($10^{11} \text{ s cm}^{-3}$)	EM (10^{58} cm^{-3})	Abundances	$N_{H \text{ LMC}}$ (10^{21} cm^{-2})	kT (keV)	τ ($10^{11} \text{ s cm}^{-3}$)	EM (10^{58} cm^{-3})	Abundances	
(1)	(2)	(3)	(4)	(5)	(6)	(7)	(8)	(9)	(10)	(11)	(12)
J0519–6926	0(< 0.09)	0.39 ^{+0.06} _{-0.04}	3.58 ^{+1.65} _{-1.62}	4.53 ^{+1.65} _{-0.86}	O: 0.15 ^{+0.01} _{-0.02} Ne: 0.36 ^{+0.04} _{-0.05} Mg: 0.34±0.10 Si: 1.21 ^{+0.32} _{-0.36} Fe: 0.21±0.03	—	—	—	—	—	3602.5/3033
J0523–6753	0.75 ^{+0.45} _{-0.35}	0.62±0.04	22.7 ^{+11.0} _{-10.2}	0.66 ^{+0.02} _{-0.09}	O: 1.49 ^{+0.86} _{-0.80} Ne: 3.08 ^{+2.03} _{-1.63} Mg: 1.57 ^{+0.79} _{-0.76} Si: 1.13±0.43 Fe: 0.48±0.16	—	—	—	—	—	5075.9/4532
J0525–6559	2.17 ^{+0.20} _{-0.19}	0.60 ^{+0.06} _{-0.04}	2.34 ^{+0.69} _{-0.56}	50.3 ^{+11.3} _{-11.4}	O: 0.07±0.05 Ne: 0.27±0.04 Mg: 0.43±0.09 Si: 0.33±0.07 Fe: 0.10 ^{+0.05} _{-0.06}	2.17	0.32±0.07	4.34 ^{+17.7} _{-2.04}	43.6 ^{+45.58} _{-14.0}	RD92	3981.8/2884
J0526–6605 ^(f)	2.64 ^{+0.15} _{-0.18}	0.42±0.02	5.26 ^{+0.75} _{-0.41}	112.3 ^{+2.85} _{-3.36}	O: 0.30±0.03 Ne: 0.42 ^{+0.02} _{-0.05} Mg: 0.52 ^{+0.08} _{-0.05} Si: 1.0±0.11 Fe: 0.41 ^{+0.02} _{-0.05}	2.64	1.04 ^{+0.04} _{0.05}	> 35.0	27.4 ^{+3.03} _{-1.77}	—	3509.3/2038
J0527–6714 ^(g)	2.0	0.18±0.01	CIE	1.31±0.23	RD92	—	—	—	—	—	5999.0/5237
J0527–6912 ^(h)	2.0	0.18±0.01	CIE	1.31±0.23	0.35 ^{+0.12} _{-0.06} × RD92	—	—	—	—	—	12115.5/10771
J0527–7104	1.33 ^{+0.97} _{-0.32}	0.37 ^{+0.08} _{-0.04}	1.33 ^{+4.57} _{-0.55}	0.30 ^{+0.07} _{-0.13}	O: 0.05 ^{+0.04} _{-0.01} Ne: 0.86 ^{+0.29} _{-0.27} Fe: 1.43 ^{+0.71} _{-0.32}	—	—	—	—	—	6801.8/5788

TABLE A.2 – (continued)

MCSNR	Component 1:					Component 2:					χ^2/ν
	$N_{H\text{ LMC}}$ (10^{21} cm^{-2})	kT (keV)	τ (10^{11} s cm^{-3})	EM (10^{58} cm^{-3})	Abundances	$N_{H\text{ LMC}}$ (10^{21} cm^{-2})	kT (keV)	τ (10^{11} s cm^{-3})	EM (10^{58} cm^{-3})	Abundances	
(1)	(2)	(3)	(4)	(5)	(6)	(7)	(8)	(9)	(10)	(11)	(12)
J0528–6727	0(< 0.39)	0.22±0.02	CIE	1.70 ^{+1.80} _{-0.52}	O: 0.30 ^{+0.15} _{-0.19} Ne: 0.66 ^{+0.43} _{-0.25} Fe: 0.66 ^{+0.68} _{-0.34}			—			5510.0/5265
J0529–6653 ⁽ⁱ⁾	0.48 ^{+0.37} _{-0.40}	1.51±0.28	0.30 ^{+0.24} _{-0.10}	0.83 ^{+0.22} _{-0.18}	O: 0.09±0.02 Ne: 0.03(< 0.05) Mg: 0.07±0.06 Si: 0.21(< 0.49) Fe: 0.07 ^{+0.03} _{-0.02}			—			1961.3/2987
J0530–7008	0.37 ^{+0.45} _{-0.28}	0.18 ^{+0.02} _{-0.03}	CIE	1.34 ^{+0.45} _{-0.34}	RD92	0.37	0.74±0.06	CIE	0.36±0.06	RD92	9284.5/7105
J0531–7100	0< 0.12	0.52 ^{+0.05} _{-0.04}	2.50 ^{+1.70} _{-0.52}	1.63 ^{+0.21} _{-0.16}	RD92			—			2864.9/2361
J0532–6732	0.94 ^{+0.68} _{-0.51}	0.53 ^{+0.29} _{-0.11}	0.83 ^{+0.46} _{-0.24}	2.30 ^{+3.53} _{-1.34}	O: 0.25 ^{+0.06} _{-0.05} Ne: 0.24 ^{+0.12} _{-0.07} Mg: 0.17 ^{+0.20} _{-0.14} Si: 1.44 ^{+1.23} _{-0.83} Fe: 0.34 ^{+0.14} _{-0.09}			—			3824.0/3562
J0533–7202	0.47 ^{+0.44} _{-0.41}	0.31 ^{+0.06} _{-0.09}	1.39 ^{+1.16} _{-0.54}	1.13 ^{+0.87} _{-0.63}	O: 0.27 ^{+0.03} _{-0.05} Ne: 0.37 ^{+0.07} _{-0.09} Mg: 0(< 0.18) Fe: 0.37 ^{+0.17} _{-0.10}			—			4128.0/3265
J0534–6955 ⁽ⁱ⁾	2.27 ^{+0.18} _{-0.26}	0.31 ^{+0.03} _{-0.02}	3.04 ^{+0.66} _{-1.06}	26.1 ^{+10.83} _{-4.81}	O: 0.14±0.01 Ne: 0.23 ^{+0.02} _{-0.03} Mg: 0.27 ^{+0.04} _{-0.03} Fe: 0.34 ^{+0.04} _{-0.03}	2.27	1.32 ^{+0.09} _{-0.20}	Si: 0.05±0.01 S: 0.75 ^{+4.44} _{-0.51} Fe: 0.57 ^{+0.06} _{-0.04}	130.6 ^{+133.3} _{-94.6} 1.04 ^{+4.69} _{-0.51} 1.26 ^{+0.25} _{-0.17}	pure pure pure	3400.8/2727

TABLE A.2 – (continued)

MCSNR	Component 1:					Component 2:					χ^2/ν
	$N_{H \text{ LMC}}$ (10^{21} cm^{-2})	kT (keV)	τ ($10^{11} \text{ s cm}^{-3}$)	EM (10^{58} cm^{-3})	Abundances	$N_{H \text{ LMC}}$ (10^{21} cm^{-2})	kT (keV)	τ ($10^{11} \text{ s cm}^{-3}$)	EM (10^{58} cm^{-3})	Abundances	
(1)	(2)	(3)	(4)	(5)	(6)	(7)	(8)	(9)	(10)	(11)	(12)
J0534–7033 ^(k)	0(< 0.03)	0.78±0.01	208(> 63.1)	0.87 ^{+0.14} _{-0.16}	Mg: 0.30±0.18 Si: 0.08(< 0.27) Fe: 1.26 ^{+0.29} _{-0.24}	0	0.27 ^{+0.07} _{-0.04}	2.65 ^{+35.3} _{-1.35}	0.46 ^{+0.58} _{-0.15}	RD92	3496.61/2922
J0535–6602 ^(l)	0.68 ^{+0.08} _{-0.04}	0.52±0.01	7.49 ^{+2.34} _{-0.90}	251.1 ^{+31.0} _{-10.6}	Mg: 0.12 ^{+0.04} _{-0.03} Si: 0(< 0.13) Fe: 0.28±0.01	2.48 ^{+1.10} _{-0.81}	1.10 ^{+0.04} _{-0.01}	10.4 ^{+3.80} _{-0.90}	99.1 ^{+6.05} _{-8.63}	O: 0.71 ^{+0.23} _{-0.31} Ne: 0(< 0.12) Mg: 0.85 ^{+0.05} _{-0.07} Si: 0.76 ^{+0.05} _{-0.07} S: 0.48±0.05 Fe: 0(< 0.02) Ar: 0.14(< 0.14)	1962.4/1634
J0535–6918	2.31±0.03	0.31 ^{+0.05} _{-0.03}	1.71 ^{+1.09} _{-0.71}	1.85 ^{+0.92} _{-0.71}	O: 0.15 ^{+0.04} _{-0.03} Ne: 0.34 ^{+0.09} _{-0.07} Mg: 0.34 ^{+0.18} _{-0.14} Si: 1.60 ^{+1.13} _{-0.86} Fe: 0.30 ^{+0.10} _{-0.07}	—	—	—	—	—	1999.9/1589
J0536–6735 ^(m)	2.26±0.20	0.56 ^{+0.04} _{-0.03}	7.59 ^{+1.12} _{-1.00}	2.00 ^{+0.67} _{-0.24}	O: 1.57 ^{+0.61} _{-0.19} Ne: 2.52 ^{+0.87} _{-0.18} Mg: 1.35 ^{+0.27} _{-0.11} Fe: 0.04 ^{+0.09} _{-0.05}	—	—	—	—	—	6015.7/4816
J0536–6913 ⁽ⁿ⁾	4.89 ^{+0.50} _{-3.30}	0.75 ^{+0.27} _{-0.07}	10.5 ^{+2.34} _{-8.19}	0.11 ^{+0.02} _{-0.34}	RD92	4.89	4.22 ^{+0.40} _{-2.06}	0.08 ^{+0.03} _{-0.02}	0.06±0.02	O: 1.68 ^{+0.92} _{-0.39} Ne: 0.59 ^{+0.31} _{-0.26} Mg: 1.51 ^{+2.35} _{-1.1} Si: 7.9 ^{+17.83} _{-5.20}	1107.4/1139

TABLE A.2 – (continued)

MCSNR	Component 1:					Component 2:					χ^2/ν
	$N_{H\text{ LMC}}$ (10^{21} cm^{-2})	kT (keV)	τ (10^{11} s cm^{-3})	EM (10^{58} cm^{-3})	Abundances	$N_{H\text{ LMC}}$ (10^{21} cm^{-2})	kT (keV)	τ (10^{11} s cm^{-3})	EM (10^{58} cm^{-3})	Abundances	
(1)	(2)	(3)	(4)	(5)	(6)	(7)	(8)	(9)	(10)	(11)	(12)
J0536–7039 ^(o)	0(< 0.07)	0.27 ^{+0.14} _{-0.08}	3.85 ^{+52.9} _{-2.60}	0.56 ^{+0.26} _{-0.26}	RD92	0	0.73 ^{+0.07} _{-0.05}	7.26 ⁺⁵⁰⁰ _{-4.00}	0.50 ^{+0.18} _{-0.08}	Ne: 0.12(< 1.12) Mg: 0.37 ^{+0.57} _{-0.21} Si: 0.37(< 0.77) Fe: 1.89 ^{+0.69} _{-0.79}	3555.7/3441
J0537–6628	0.56(< 1.13)	0.42 ^{+0.11} _{-0.09}	10.2 ^{+23.4} _{-6.7}	0.60 ^{+1.30} _{-0.55}	O: 0.32 ^{+0.75} _{-0.13} Ne: 0.34 ^{+0.46} _{-0.19} Mg: 0.07(< 0.31) Fe: 0.26 ^{+0.23} _{-0.10}	—	—	—	—	—	3489.1/2983
J0537–6910 ^(p)	9.11 ^{+0.33} _{-0.29}	4.92±0.35	0.19 ^{+0.07} _{-0.06}	0.53 ^{+0.18} _{-0.14}	RD92	—	—	—	—	—	3866.8/3452
J0540–6920 ^(q)	6.85 ^{+0.18} _{-0.16}	0.49±0.06	1.87 ^{+1.06} _{-0.71}	6.03 ^{+1.32} _{-1.08}	RD92	—	—	—	—	—	5528.0/4763
J0540–6944 ^(r)	11.4 ^{+1.21} _{-0.90}	0.20±0.02	CIE	30.64 ^{+18.70} _{-16.04}	RD92	—	—	—	—	—	1323.4/770
J0541–6659	0(< 0.07)	0.40 ^{+0.15} _{-0.07}	0.36 ^{+0.19} _{-0.16}	0.38 ^{+0.10} _{-0.16}	RD92	—	—	—	—	—	6933.5/5886
J0543–6858	2.09 ^{+0.65} _{-0.24}	1.12 ^{+0.25} _{-0.51}	0.35 ^{+0.11} _{-0.08}	1.14 ^{+0.76} _{-0.59}	O: 0.37±0.10 Ne: 0.36 ^{+0.15} _{-0.12} Mg: 0.29 ^{+0.23} _{-0.16} Si: 0.36(< 0.98) Fe: 0.32 ^{+0.16} _{-0.13}	—	—	—	—	—	7211.4/6717
J0547–6941	4.91 ^{+1.31} _{-1.08}	1.25±0.18	2.38 ^{+0.67} _{-0.30}	0.83 ^{+0.24} _{-0.25}	O: 0.26 ^{+0.28} _{-0.15} Ne: 0 (< 0.37) Mg: 0.39 ^{+0.21} _{-0.14} Si: 0.71 ^{+0.33} _{-0.27} Fe: 2.30±0.70	—	—	—	—	—	3451.2/3196

TABLE A.2 – (continued)

MCSNR	Component 1:					Component 2:					χ^2/ν
	$N_{H \text{ LMC}}$ (10^{21} cm^{-2})	kT (keV)	τ ($10^{11} \text{ s cm}^{-3}$)	EM (10^{58} cm^{-3})	Abundances (6)	$N_{H \text{ LMC}}$ (10^{21} cm^{-2})	kT (keV)	τ ($10^{11} \text{ s cm}^{-3}$)	EM (10^{58} cm^{-3})	Abundances (11)	
(1)	(2)	(3)	(4)	(5)	(6)	(7)	(8)	(9)	(10)	(11)	(12)
J0547–6943 ^(s)	$3.73^{+1.15}_{-0.72}$	$0.27^{+0.26}_{-0.05}$	493(> 5.32)	$3.67^{+4.78}_{-2.72}$	O: $0.22^{+0.40}_{-0.09}$ Ne: $0.27^{+0.33}_{-0.22}$ Mg: $0.76^{+0.45}_{-0.28}$ Si: $0.58^{+0.35}_{-0.24}$ S: $0.33^{+0.34}_{-0.31}$ Fe: $0.58^{+0.26}_{-0.19}$	3.73	$2.16^{+0.45}_{0.27}$	$2.33^{+1.23}_{-0.66}$	$0.89^{+0.22}_{-0.25}$	—	4468.2/4356
J0547–7025	$3.04^{+0.37}_{-0.35}$	$0.31^{+0.01}_{-0.05}$	$3.12^{+11.7}_{-3.66}$	$4.72^{+3.14}_{-1.81}$	RD92	3.04	$0.80^{+0.13}_{-0.10}$	$1.18^{+0.90}_{-0.18}$	$1.65^{+0.35}_{-0.52}$	O: 0 (< 0.08) Ne: 0.32 ± 0.01 Mg: $0.07 (< 0.12)$ Si: 0.28 ± 0.25 S: $1.10^{+0.50}_{-0.57}$ Fe: $0.92^{+0.23}_{-0.19}$	2949.1/2559

Notes. Columns are described in Sect. 11.2.3. A. ^(a) Only MOS data available; ^(b) Fit includes a power-law component for the central PWN; ^(c) Same absorption column and abundances in the two components; Nitrogen abundance is also fitted to 0.07 solar; ^(d) Results from [MHK14](#); ^(e) Results from [BKM14](#). The first component is a Sedov model. The second is split into two pure-metal components (O and Fe) with the corresponding emission measures given as $EM_X \times (n_X/n_H)$; ^(f) Same absorption column and abundances in the two components; Fit includes a power-law component for SGR 0526–66 ([Park et al. 2012](#)); ^(g) $N_{H \text{ LMC}}$ fixed to the value from the H I map of the LMC; ^(h) Abundances from RD92 are scaled by a common factor; ⁽ⁱ⁾ Affected by strong background flare; ^(j) The second component comprises three pure-metals NEI models with a common temperature and distinct τ and EM, for each Si, S, and Fe; ^(k) C, N, O, and Ne abundances of the iron-rich component (Component 1) are fixed to 0; ^(l) Abundance of Ca fixed at 0 in the second component; fit includes an Fe K (Gaussian) line, see Sect. 11.2.3. C; ^(m) Fit includes a power-law component for the interior HMXB ([Seward et al. 2012](#)); ⁽ⁿ⁾ Elements other than O, Ne, Mg, and Si in the second component are set to 0; ^(o) C, N, and O abundances of the iron-rich component (Component 2) are fixed to 0; ^(p) Fit includes a power-law component for the interior PWN; ^(q) Strongly affected by the emission from PSR 0540–69.3 (modeled by a power law); ^(r) Dominated by the contamination from LMC X-1 (modeled by a power law); ^(s) Same absorption column and abundances in the two components.

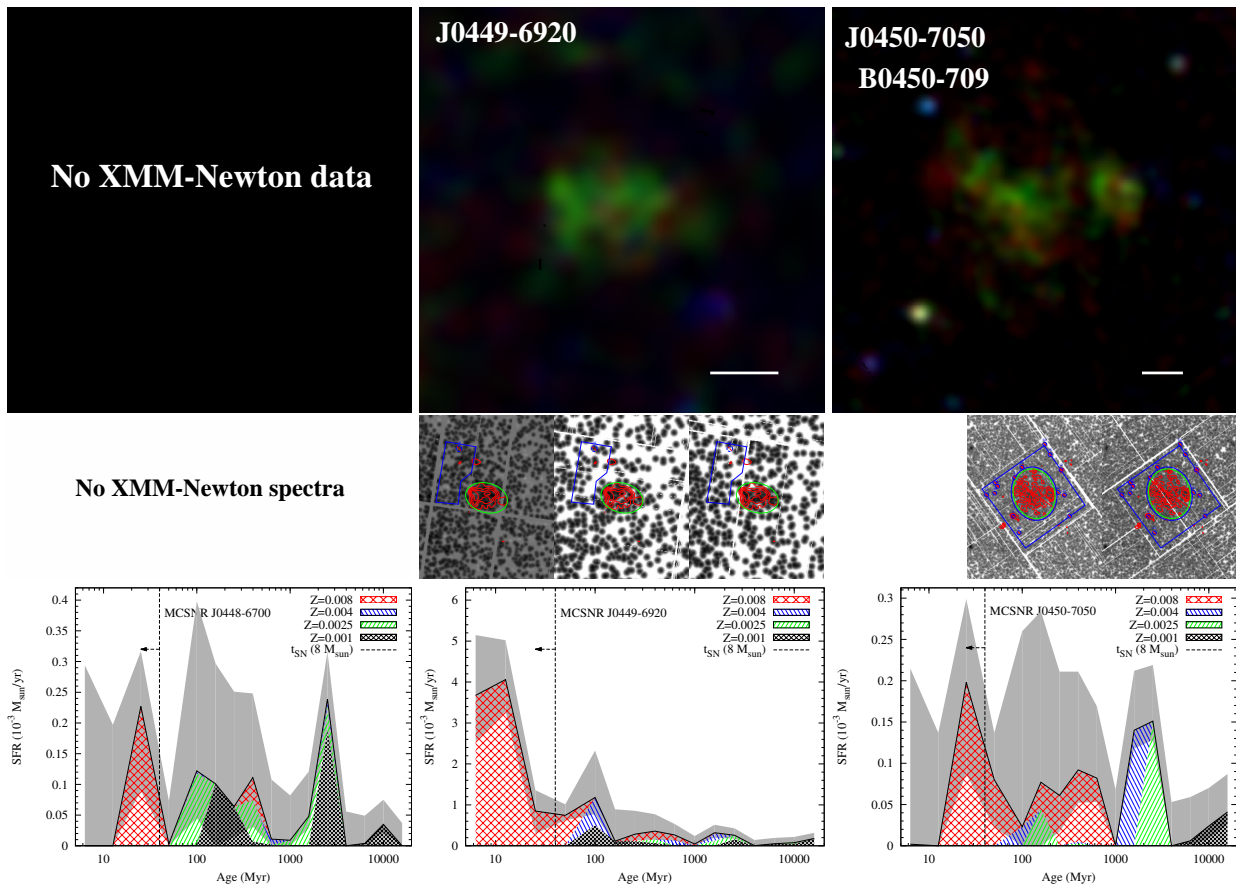
TABLE A.3 – X-ray spectral results for bright LMC SNRs.

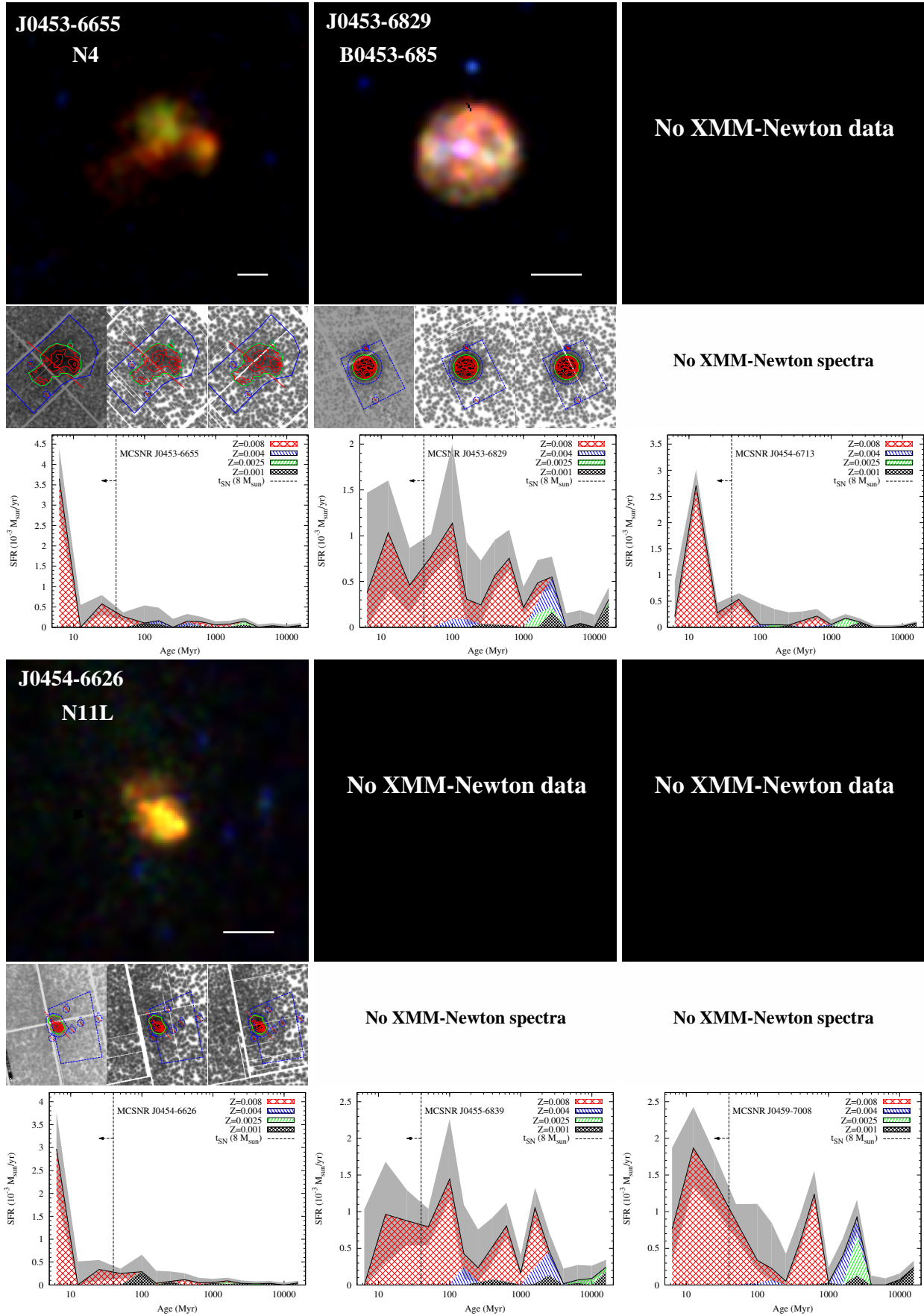
Component	$N_{H\text{ LMC}}$ (10^{21} cm^{-2})	kT (keV)	τ (10^{11} s cm^{-3})	EM (10^{58} cm^{-3})	O	Ne	Mg	Si	S	Ar	Ca	Fe
DEM L71 — MCSNR J0505–6753 : $\chi^2/\text{dof} = 3300.5/1784$												
CSM/ISM		0.46±0.01	2.59 ^{+0.03} _{-0.02}	38.2 ^{+2.88} _{-0.17}	0.26±0.001	0.40±0.001	0.49 ^{+0.01} _{-0.02}	0	0	—	—	0
Ejecta _{cool}	0.28±0.001	0.42 ^{+0.004} _{-0.009}	3.56 ^{+0.98} _{-0.40}	11.3 ^{+0.12} _{-0.14}	0	0	0	1.03 ^{+0.05} _{-0.03}	1.27 ^{+0.09} _{-0.07}	0	0	1.21±0.001
Ejecta _{hot}		0.88 ^{+0.007} _{-0.001}	1.83 ^{+0.06} _{-0.04}	7.30 ^{+0.36} _{-0.63}	0	0	0			0	0	
N103B — MCSNR J0509–6844 : $\chi^2/\text{dof} = 694.2/583$												
CSM/ISM		0.33 ^{+0.03} _{-0.10}	34.9 ^{+137.5} _{-19.7}	40.73 ^{+4.27} _{-4.68}	—	—	—	—	—	—	—	—
Ejecta _{cool}	3.09 ^{+0.20} _{-0.11}	0.71±0.02	> 41.4	25.9 ^{+1.47} _{-2.84}	0 (< 0.25)	1.71 ^{+0.49} _{-0.32}	0.33 ^{+0.10} _{-0.14}	2.84 ^{+0.56} _{-0.30}	3.48 ^{+0.33} _{-0.28}	5.26 ^{+1.0} _{-0.59}	9.51 ^{+2.43} _{-2.05}	1.10 ^{+0.36} _{-0.14}
Ejecta _{hot}		1.62 ^{+0.10} _{-0.16}	8.59 ^{+4.27} _{-2.64}	9.95 ^{+1.50} _{-0.57}								
N132D — MCSNR J0525–6938 : $\chi^2/\text{dof} = 1288.4/1116$												
CSM/ISM		0.64 ^{+0.02} _{-0.01}	5.97 ^{+0.44} _{-0.35}	358.6 ^{+4.78} _{-3.33}	0.05 ^{+0.02} _{-0.01}	0.46±0.02	0.19±0.01	0.39±0.03	—	—	—	0.28±0.01
O-rich	0.74±0.03	1.46 ^{+0.04} _{-0.02}	10.0 ^{+1.13} _{-4.030}	33.2 ^{+10.1} _{-1.81}	9.03 ^{+1.44} _{-3.48}	0 (< 0.25)	2.59 ^{+0.19} _{-0.17}	1.37 ^{+0.19} _{-0.15}	1.03 ^{+0.11} _{-0.10}	—	—	0.15 ^{+0.05} _{-0.02}
Si-S-Fe		5.12 ^{+0.93} _{-0.72}	500	7.84 ^{+1.33} _{-0.86}	0	0	0	0	0	5.29 ^{+4.05} _{-3.26}	2.20 (< 4.86)	1.0
0509–67.5 — MCSNR J0509–6731 : $\chi^2/\text{dof} = 871.1/419$												
CSM/ISM		0.27 ^{+0.09} _{-0.01}	9.44 ^{+1.69} _{-3.02}	6.26 ^{+4.42} _{-2.70}	1.14 ^{+1.58} _{-0.03}	2.37 ^{+0.06} _{-0.05}	2.45 ^{+0.29} _{-0.56}	0	0	0	0	2.84 ^{+5.78} _{-0.15}
Fe _{cool}	1.64±0.07	1.42 ^{+0.09} _{-0.05}	0.08±0.01	10.5 ^{+2.20} _{-4.46}	0	0	0	0	0	0	0	pure
Fe _{hot} -Ca		11.7 ^{+9.9} _{-1.5}	11.4 ^{+7.6} _{-4.4}	1.75 ^{+0.29} _{-0.24}	0	0	0	0	0	0	4.51 ^{+2.05} _{-1.64}	1.0
Si-S-Ar		1.18 ^{+0.11} _{-0.12}	0.23 ^{+0.014} _{-0.003}	57.3 ^{+3.5} _{-3.0}	0	0	0	1.0	3.28 ^{+0.19} _{-0.11}	3.38 ^{+0.25} _{-0.10}	0	0
0519–69.0 — MCSNR J0519–6902 : $\chi^2/\text{dof} = 5971.7/2438$												
CSM/ISM		0.60 ^{+0.02} _{-0.01}	29.4 ^{+29.6} _{-8.9}	22.5 ^{+0.53} _{-0.90}	—	—	0.35 ^{+0.03} _{-0.01}	—	—	—	—	—
Fe _{cool}		1.37 ^{+0.01} _{-0.02}	0.88±0.02	10.0 ^{+0.30} _{-0.23}	0	0	0	0	0	0	0	pure
Fe _{hot}	0.96±0.04	8.12	3.60	8.61	0	0	0	0	0	0	0	pure
Si-S		3.43 ^{+0.50} _{-0.45}	1.12 ^{+0.12} _{-0.06}	10.6 ^{+0.67} ₋₃₀	0	0	0	1.0	1.26±0.06	0	0	0
Ar-Ca		4.42±1.20	2.03 ^{+0.31} _{-0.46}	15.8 ^{+4.6} _{-5.5}	0	0	0	0	0	1.0	1.33 ^{+0.25} _{-0.18}	0
O		4.32 ^{+1.47} _{-4.03}	0.04 ^{+0.17} _{-0.02}	0.10 ^{+0.08} _{-0.03}	pure	0	0	0	0	0	0	0

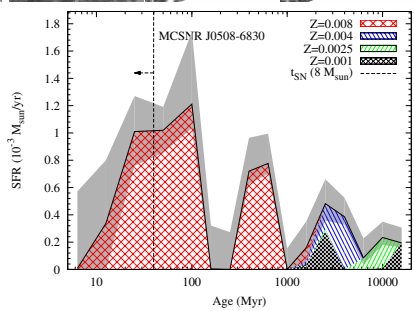
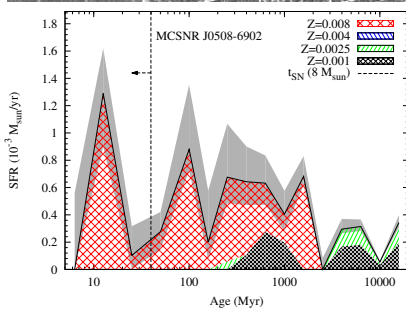
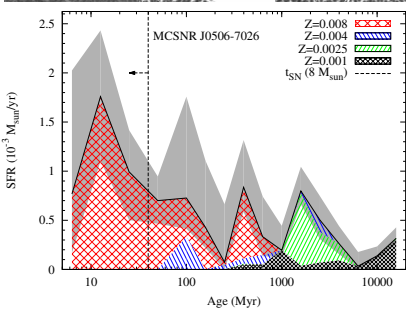
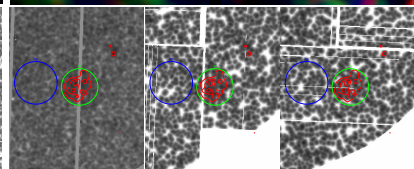
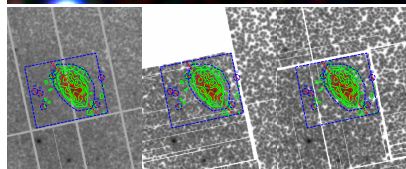
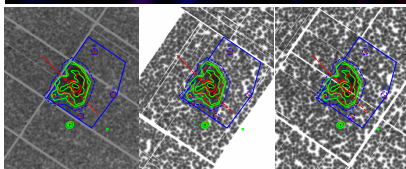
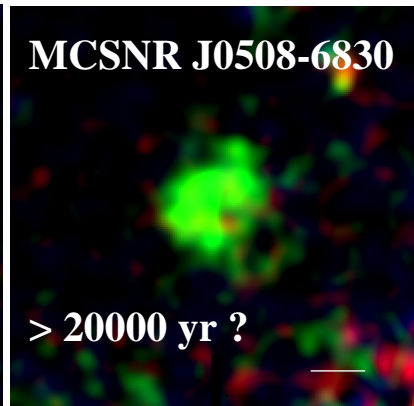
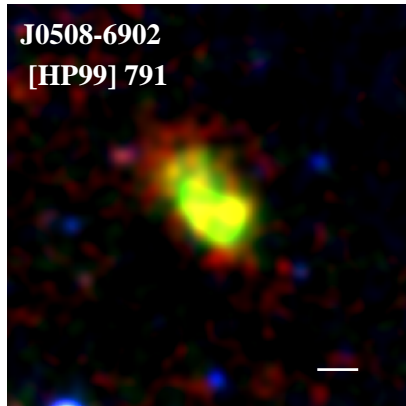
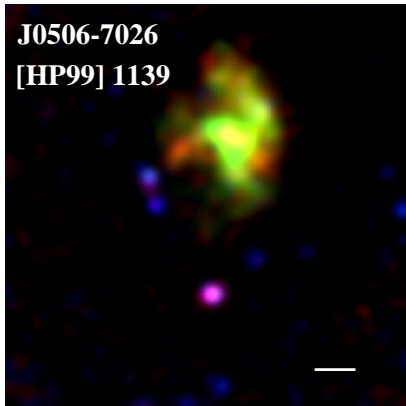
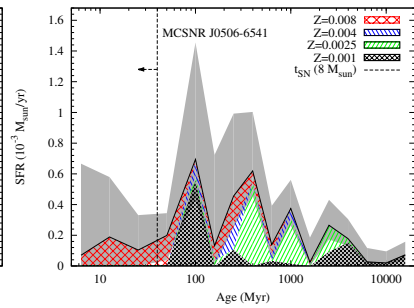
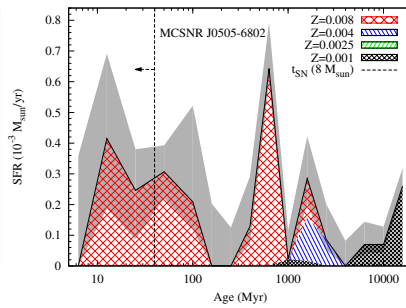
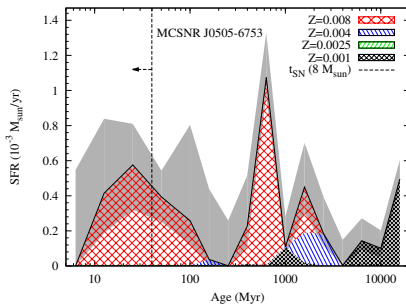
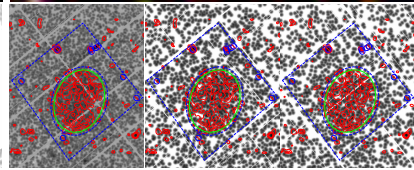
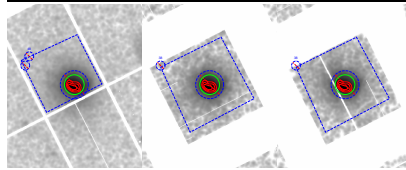
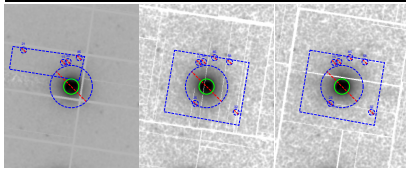
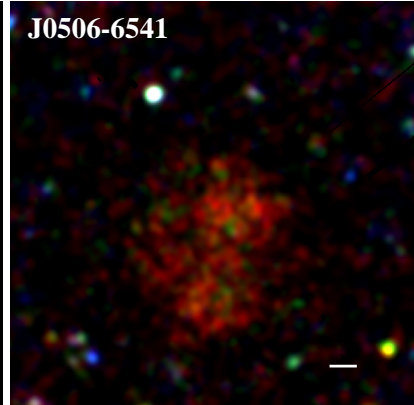
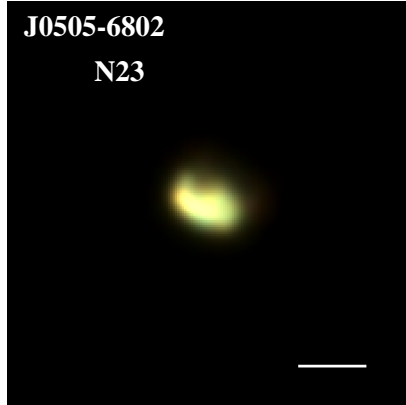
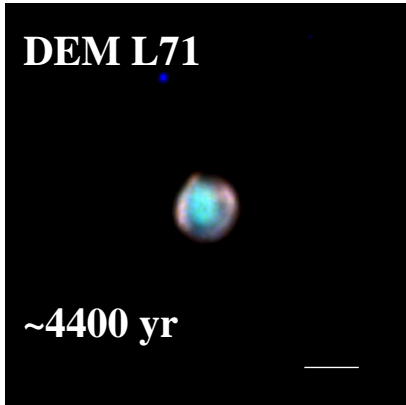
Notes. Details of the spectral models used are given in Sect. 11.2.3. B.

B. X-ray images, spectral extraction regions, and SFH for all LMC SNRs

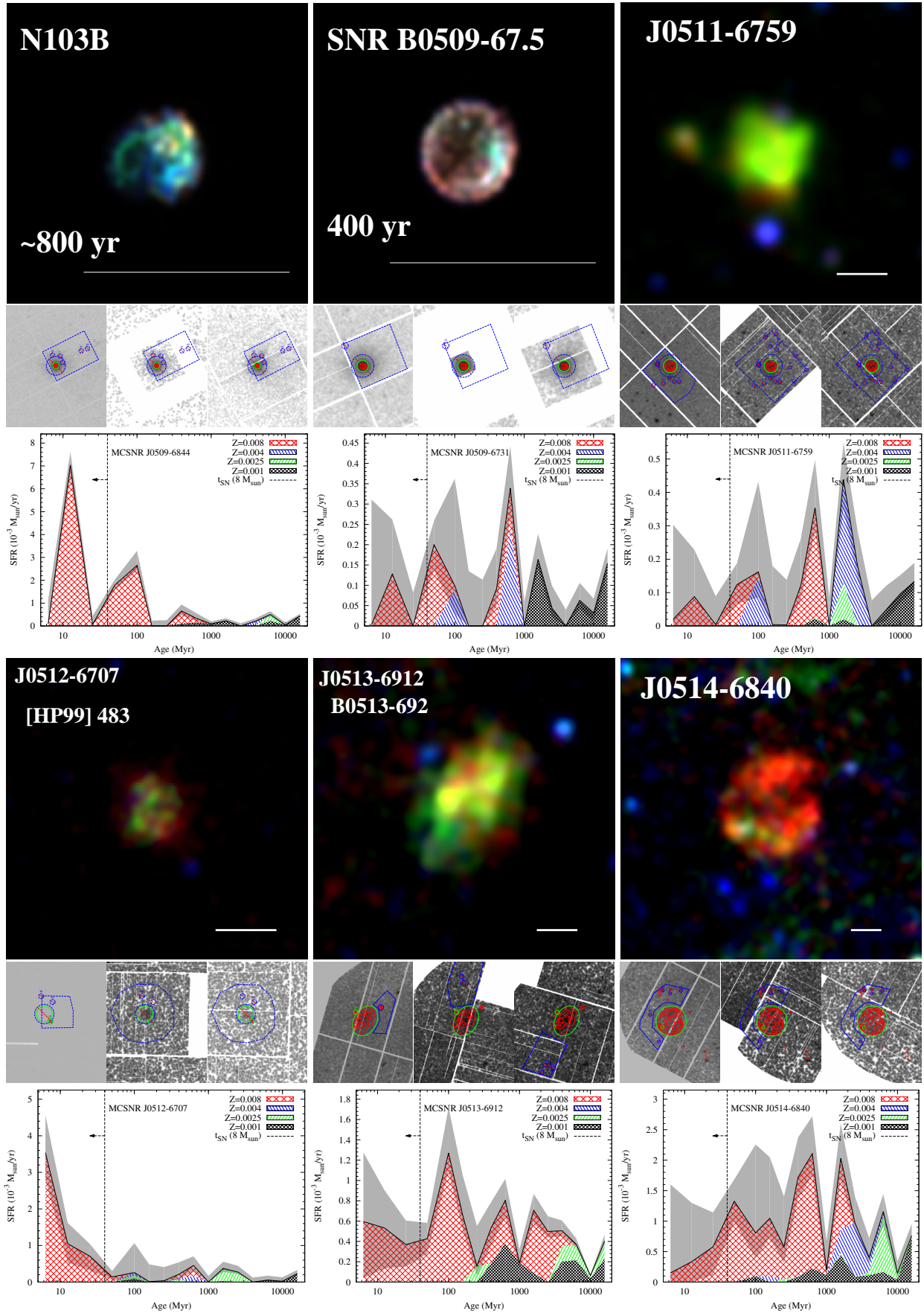
THIS APPENDIX presents, for each SNR, an X-ray image (top), the regions used for spectral analysis (middle), and the SFH of the cell including the remnant (bottom panel). The images are as in Fig. 11.7, using the (0.3–0.7 keV), medium (0.7–1.1 keV), and hard (1.1–4.2 keV) bands as red, green, and blue components, respectively. The white bars indicate the scale of $1'$. North is up and east is left. A linear scale is used to display the pixel values, but the cut levels are adapted for each SNR. The extraction regions used for spectral analysis are shown for pn, MOS1, and MOS2 detectors (left to right), as in Fig. 11.2. The star formation history plots are shown as in Fig. 11.11.

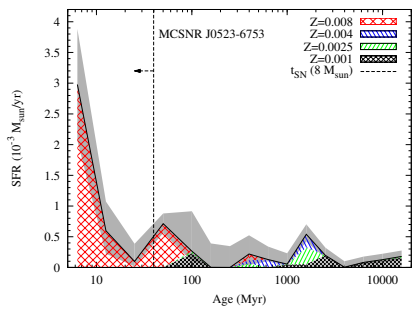
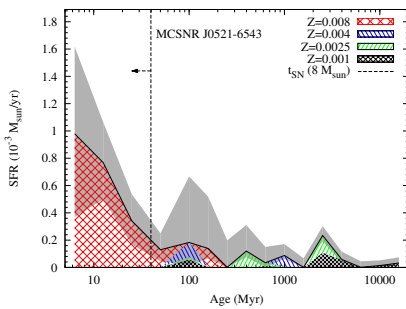
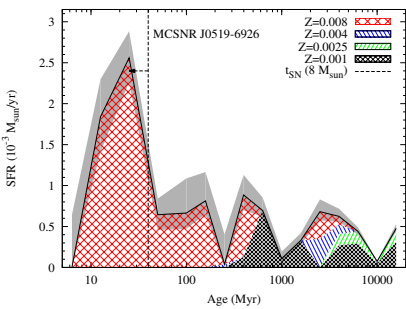
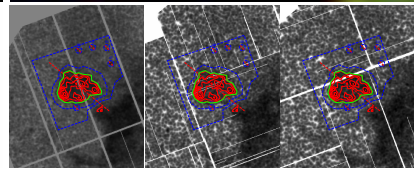
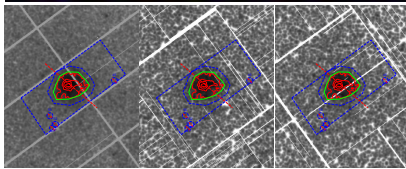
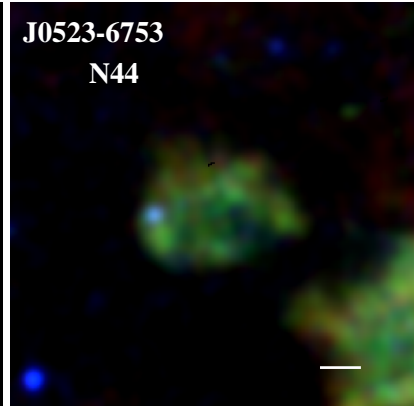
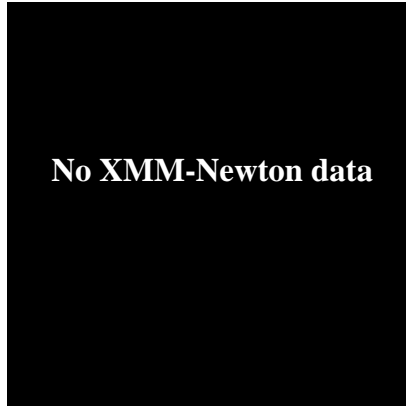
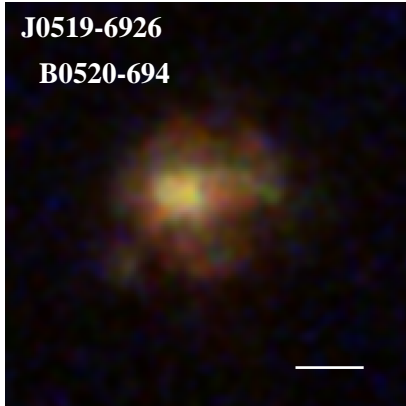
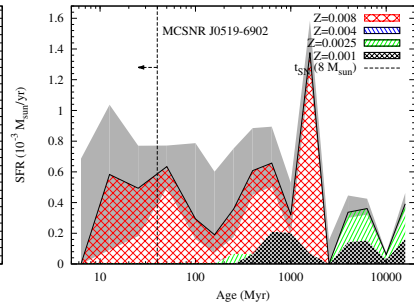
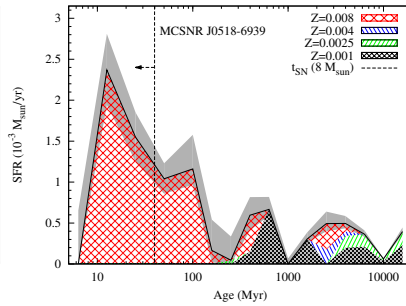
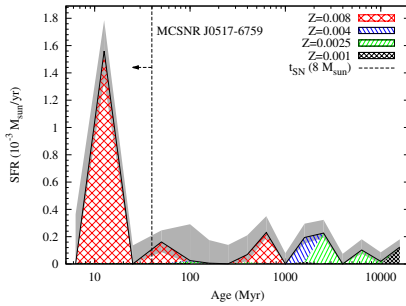
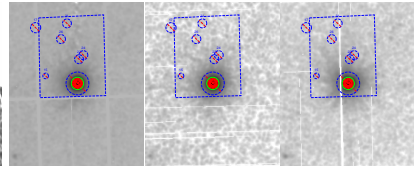
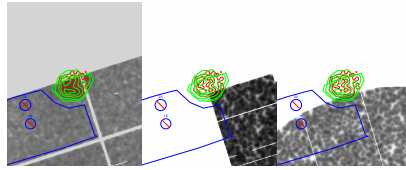
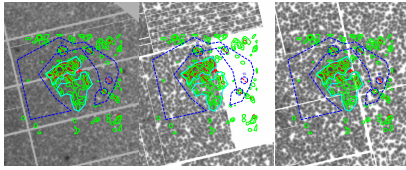
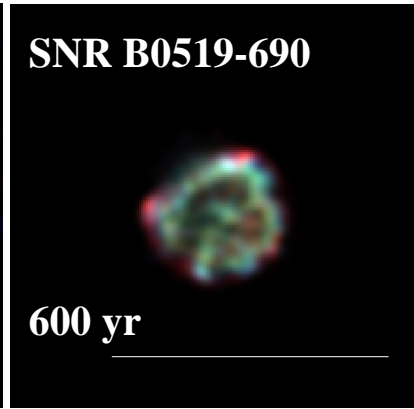
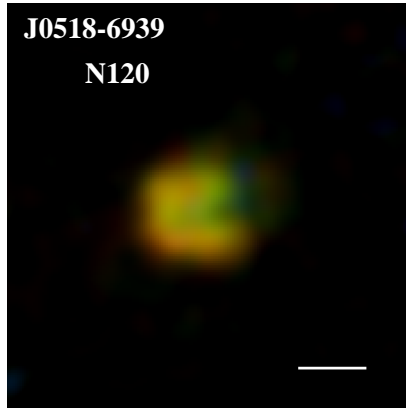
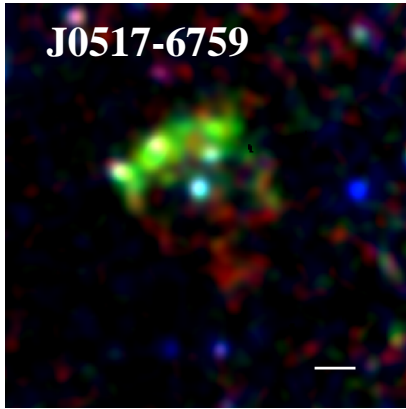


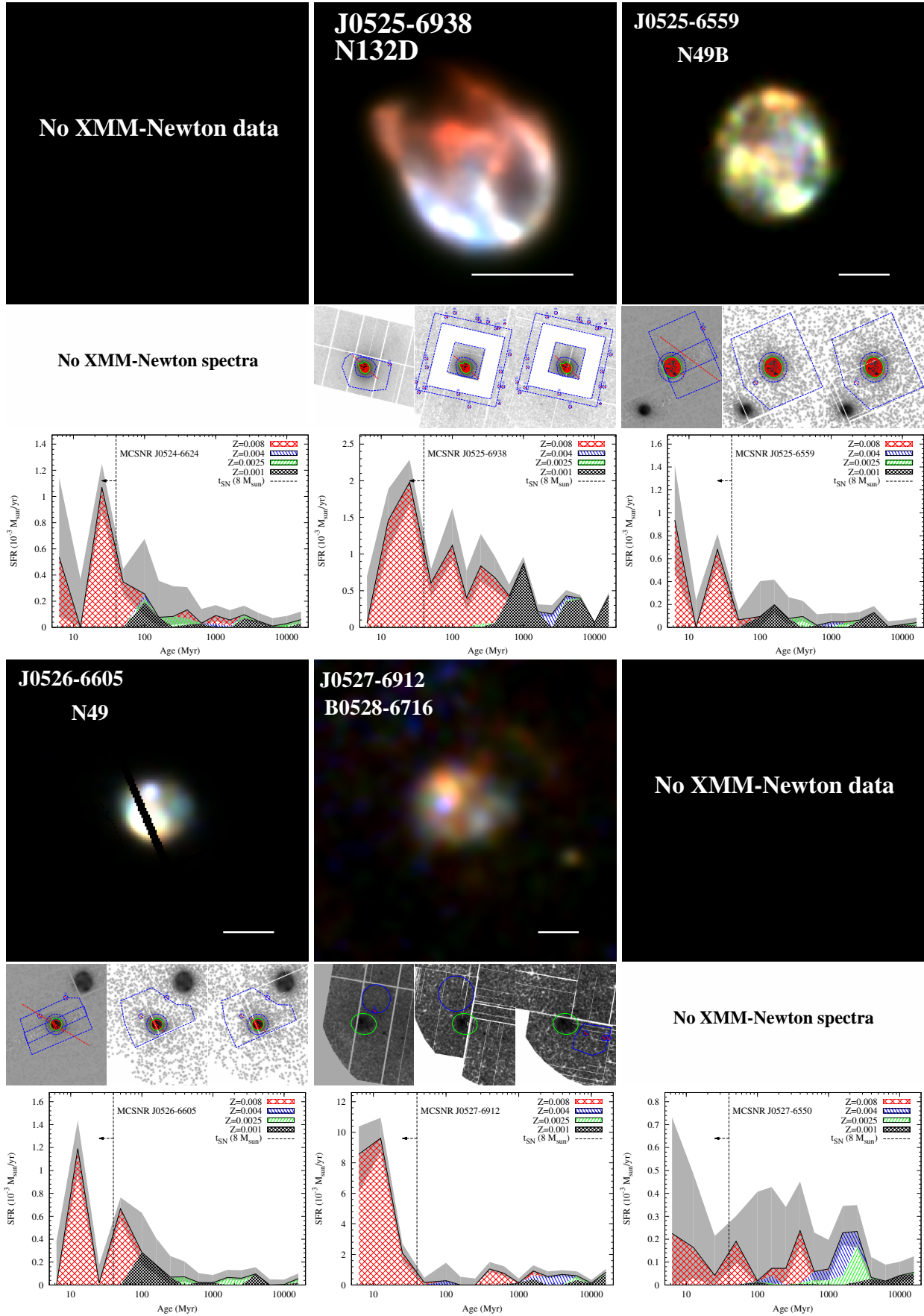


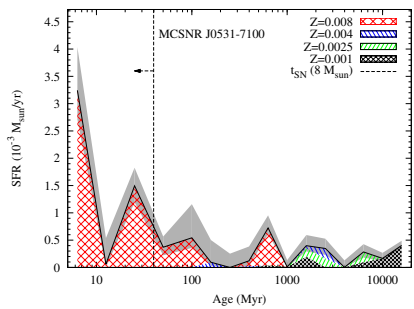
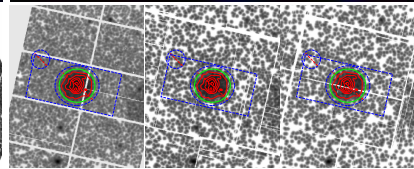
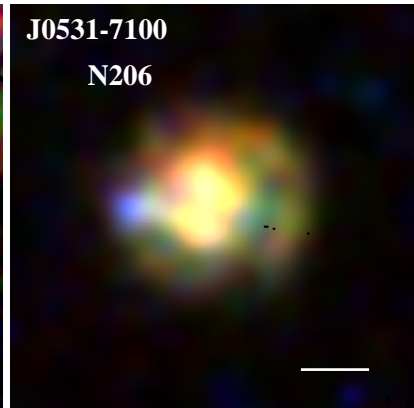
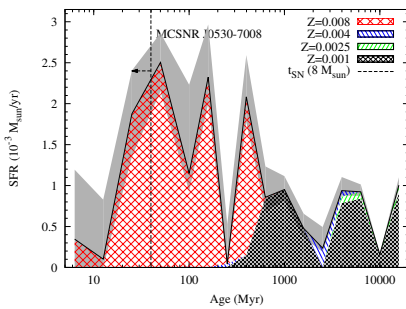
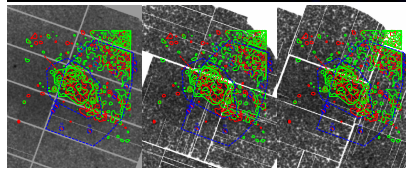
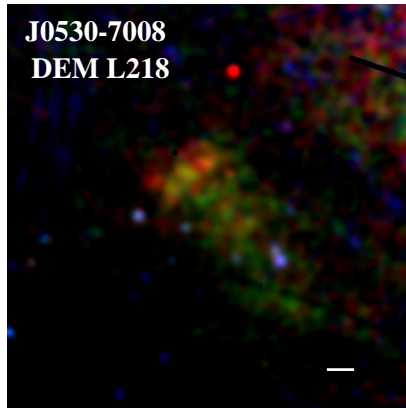
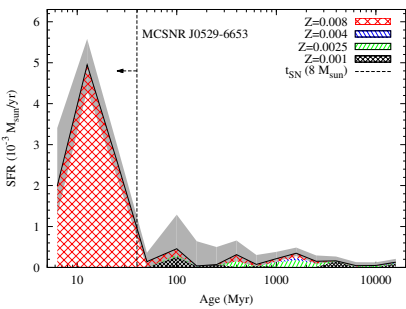
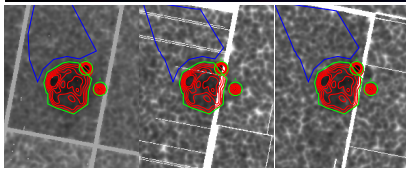
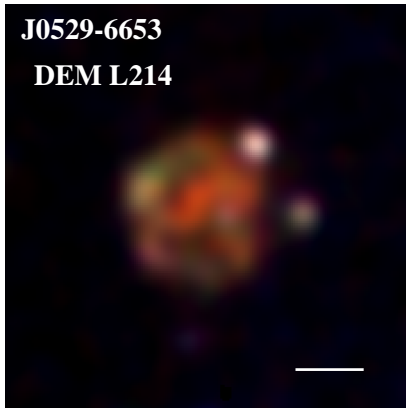
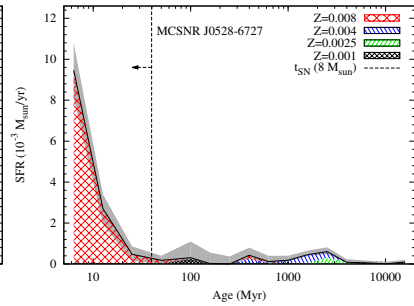
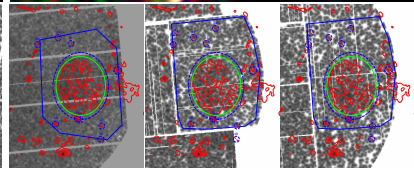
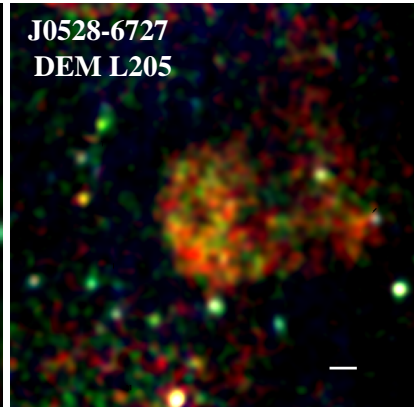
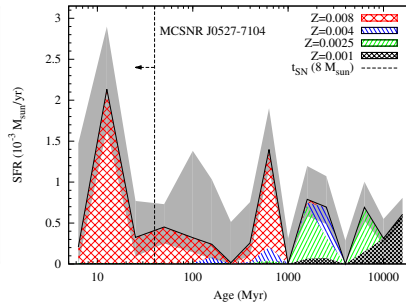
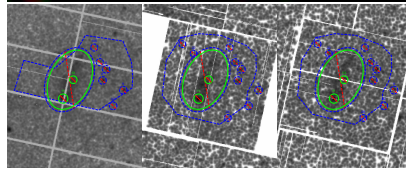
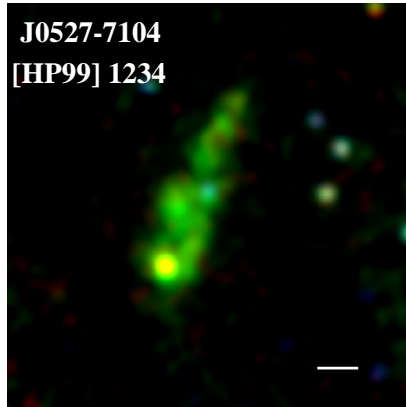
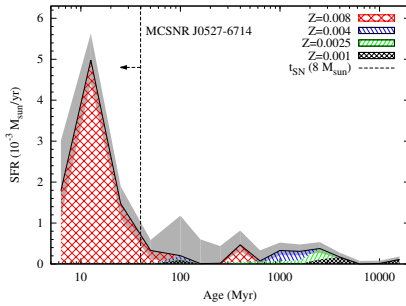
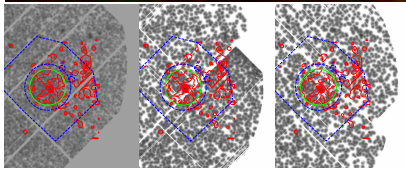
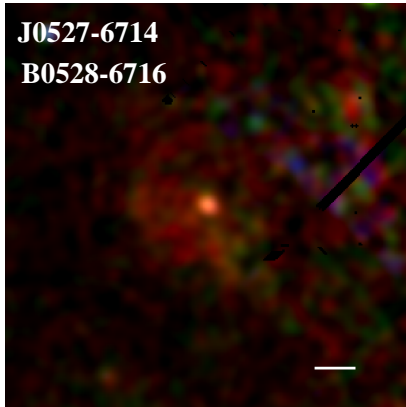


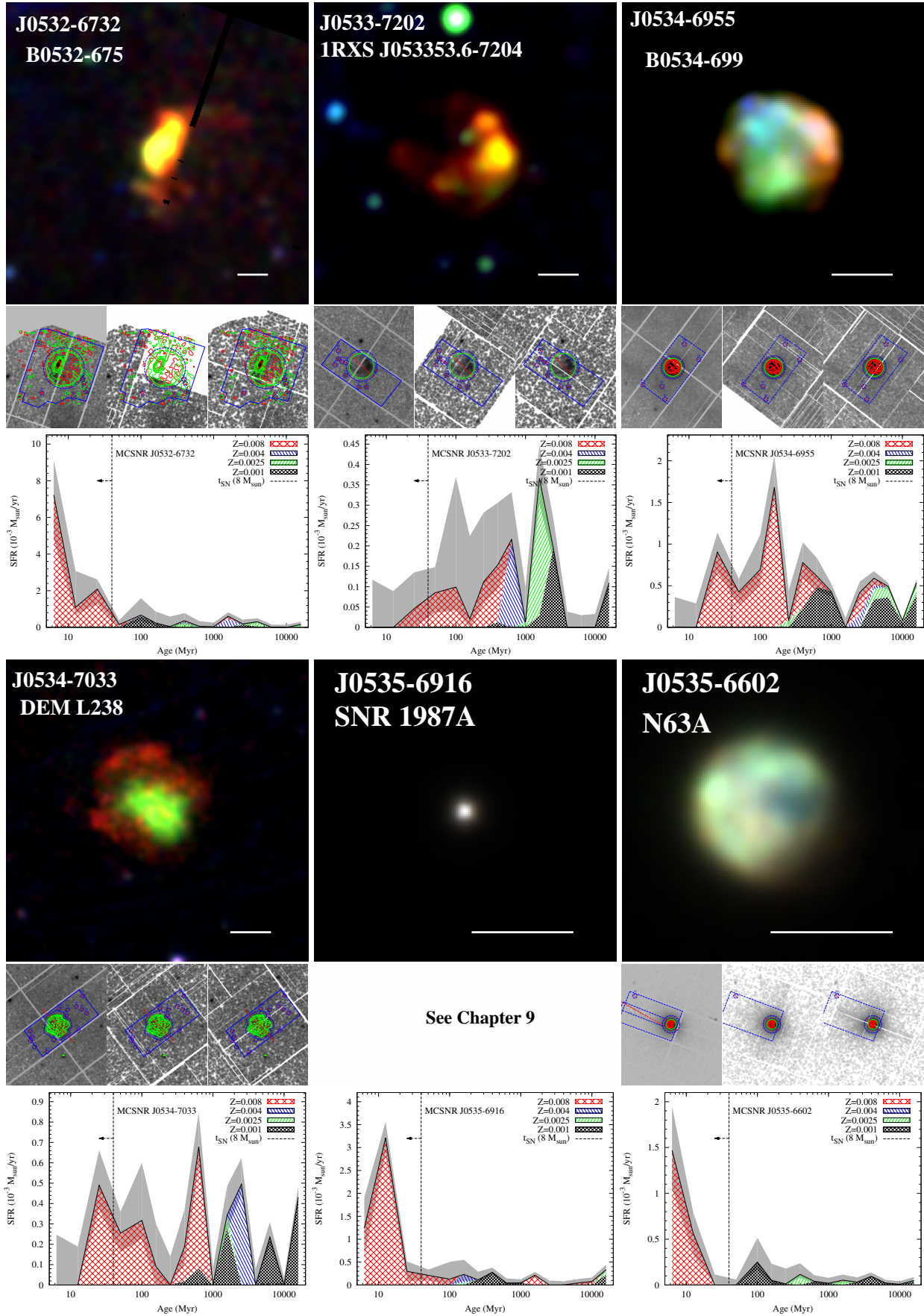
B. X-ray images, spectral extraction regions, and SFH for all LMC SNRs

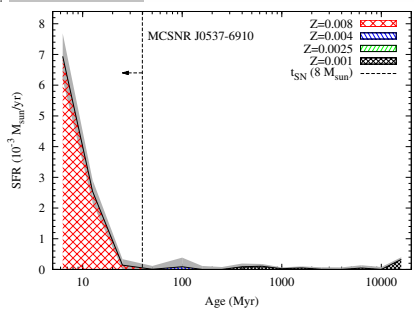
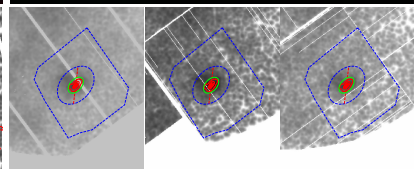
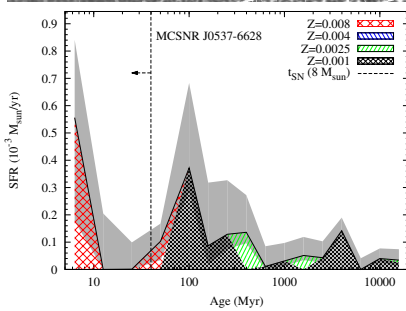
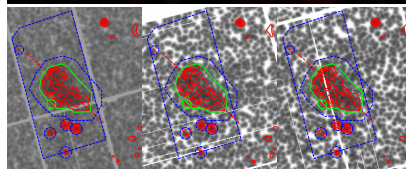
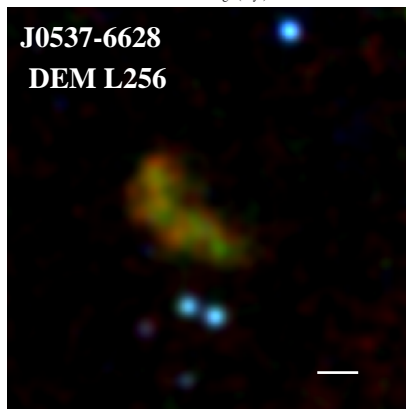
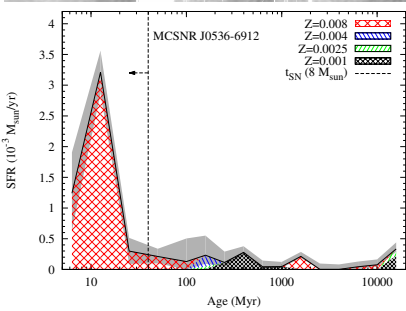
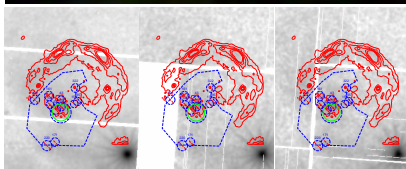
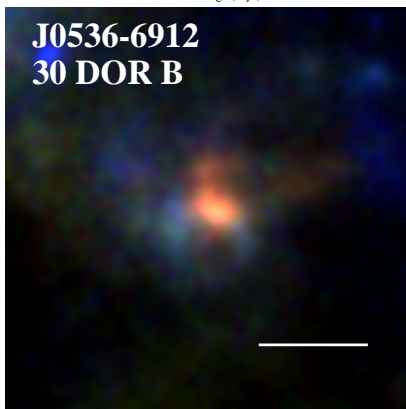
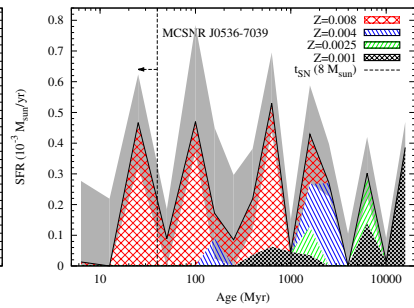
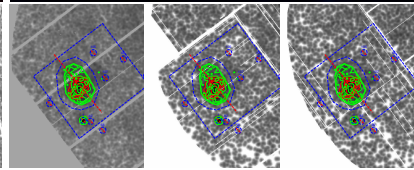
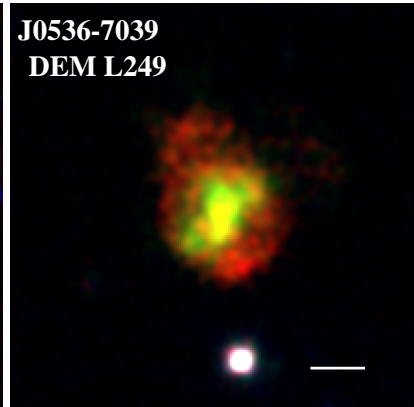
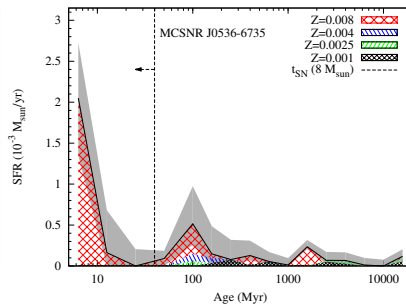
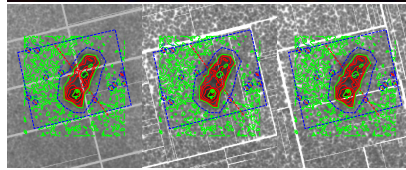
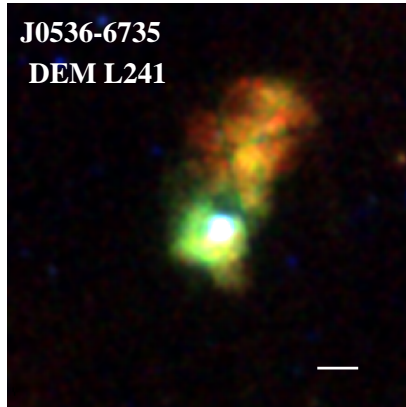
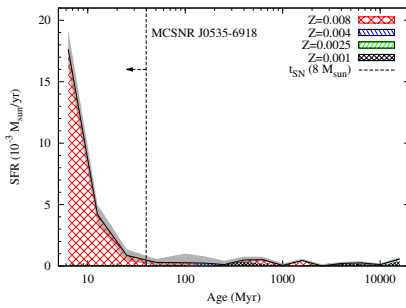
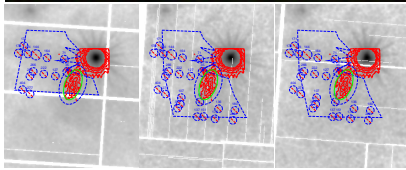
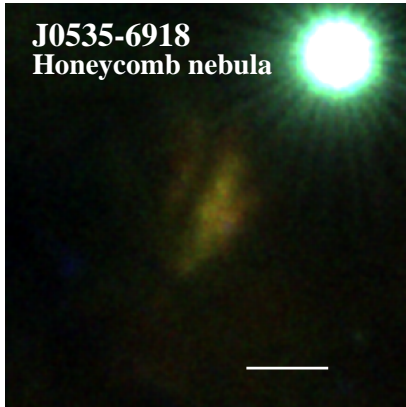




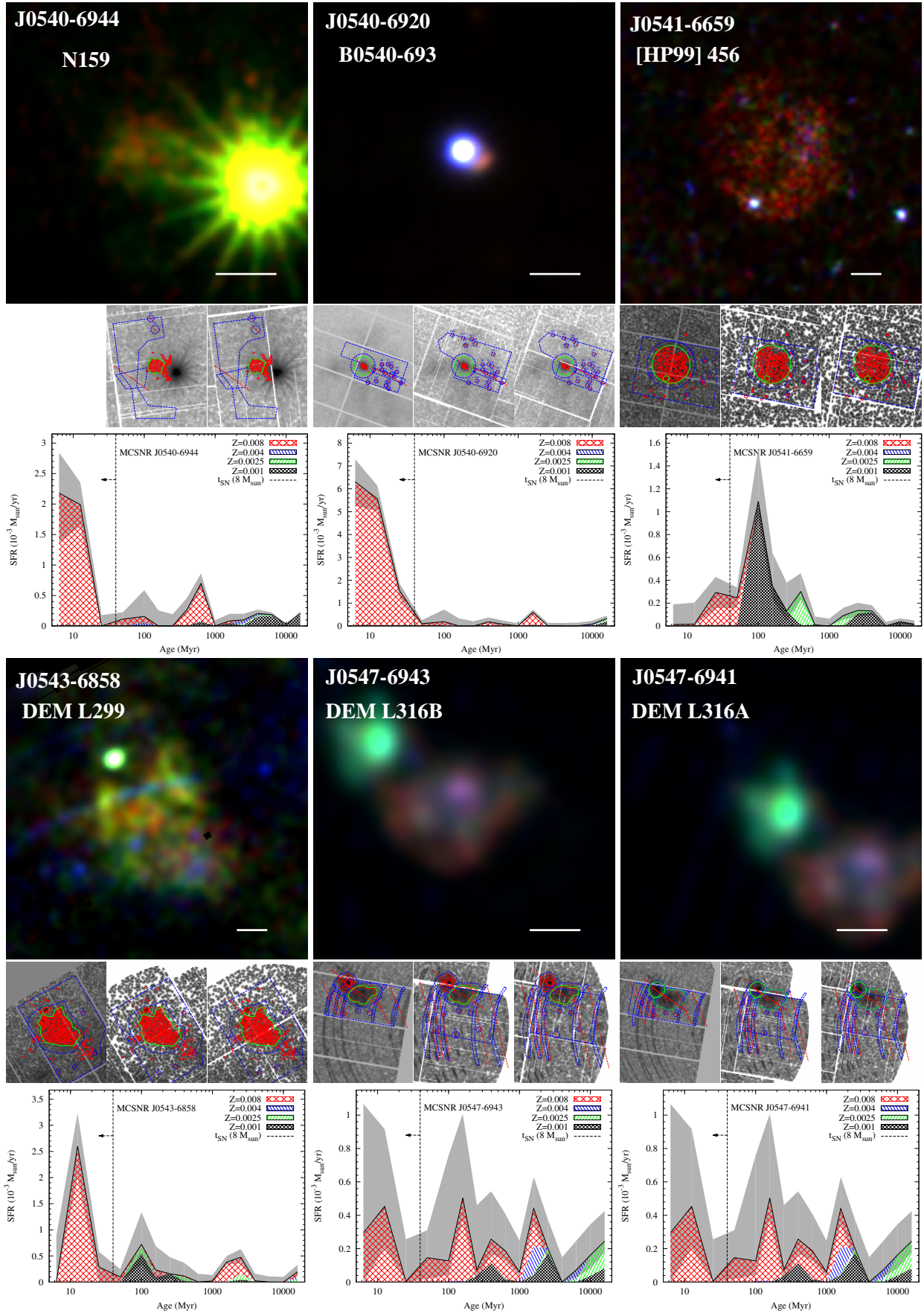


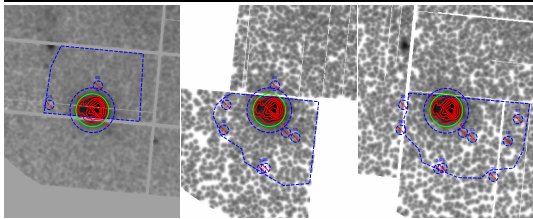
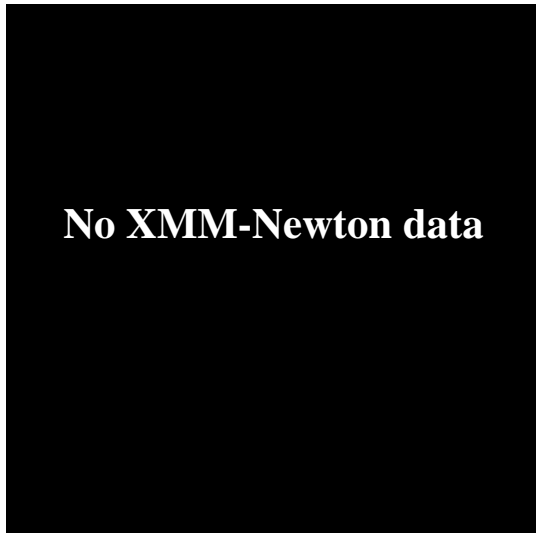
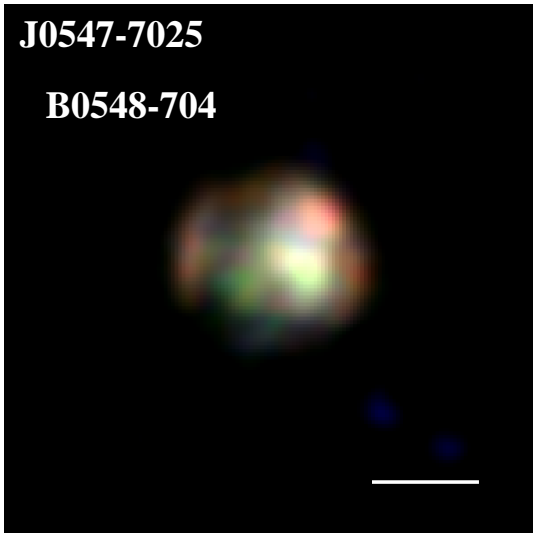




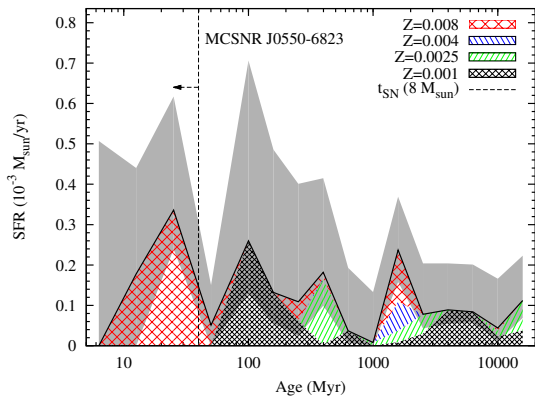
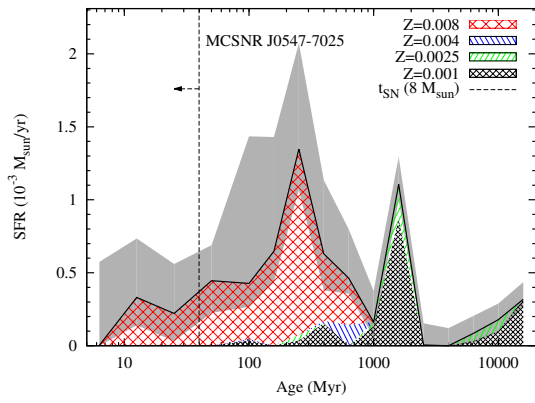


B. X-ray images, spectral extraction regions, and SFH for all LMC SNRs





No XMM-Newton spectra



Publication list

in anti-chronological order, complete as of March 25th 2015.

Refereed publications

P. J. Kavanagh, M. Sasaki, L. M. Bozzetto, M. D. Filipovic, S. D. Points, **P. Maggi**, and F. Haberl, “XMM-Newton study of 30 Dor C and a newly identified MCSNR J0536-6913 in the Large Magellanic Cloud,” *A&A*, vol. 573, p. A73, [Jan. 2015](#).

R. Sturm, F. Haberl, G. Vasilopoulos, E. S. Bartlett, **P. Maggi**, A. Rau, J. Greiner, and A. Udalski, “Discovery of SXP 265, a Be/X-ray binary pulsar in the Wing of the Small Magellanic Cloud,” *MNRAS*, vol. 444, pp. 3571–3580, [Nov. 2014](#).

G. Vasilopoulos, F. Haberl, R. Sturm, **P. Maggi**, and A. Udalski, “Spectral and temporal properties of RX J0520.5-6932 (LXP 8.04) during a type-I outburst,” *A&A*, vol. 567, p. A129, [July 2014](#).

A. Y. De Horta, E. R. Sommer, M. D. Filipović, A. O’Brien, L. M. Bozzetto, J. D. Collier, G. F. Wong, E. J. Crawford, N. F. H. Tothill, **P. Maggi**, and F. Haberl, “Multi-frequency Observations of a Superbubble in the LMC: The Case of LHA 120-N 70,” *AJ*, vol. 147, p. 162, [June 2014](#).

L. M. Bozzetto, P. J. Kavanagh, **P. Maggi**, M. D. Filipović, M. Stupar, Q. A. Parker, W. A. Reid, M. Sasaki, F. Haberl, D. Urošević, J. Dickel, R. Sturm, R. Williams, M. Ehle, R. Gruendl, Y.-H. Chu, S. Points, and E. J. Crawford, “Multifrequency study of a new Fe-rich supernova remnant in the Large Magellanic Cloud, MCSNR J0508-6902,” *MNRAS*, vol. 439, pp. 1110–1124, [Mar. 2014](#).

P. Maggi, F. Haberl, P. J. Kavanagh, S. D. Points, J. Dickel, L. M. Bozzetto, M. Sasaki, Y.-H. Chu, R. A. Gruendl, M. D. Filipović, and W. Pietsch, “Four new X-ray-selected supernova remnants in the Large Magellanic Cloud,” *A&A*, vol. 561, p. A76, [Jan. 2014](#).

G. Vasilopoulos, **P. Maggi**, F. Haberl, R. Sturm, W. Pietsch, E. S. Bartlett, and M. J. Coe, “Swift J053041.9-665426, a new Be/X-ray binary pulsar in the Large Magellanic Cloud,” *A&A*, vol. 558, p. A74, [Oct. 2013](#).

L. M. Bozzetto, M. D. Filipović, E. J. Crawford, M. Sasaki, **P. Maggi**, F. Haberl, D. Urošević, J. L. Payne, A. Y. De Horta, M. Stupar, R. Gruendl, and J. Dickel, “Multifrequency study of SNR J0533-7202, a new supernova remnant in the LMC,” *MNRAS*, vol. 432, pp. 2177–2181, [July 2013](#).

P. Maggi, F. Haberl, R. Sturm, W. Pietsch, A. Rau, J. Greiner, A. Udalski, and M. Sasaki, “Discovery of a 168.8 s X-ray pulsar transiting in front of its Be companion star in the Large Magellanic Cloud,” *A&A*, vol. 554, p. A1, [June 2013](#).

P. J. Kavanagh, M. Sasaki, S. D. Points, M. D. Filipović, **P. Maggi**, L. M. Bozzetto, E. J. Crawford, F. Haberl, and W. Pietsch, “Multiwavelength study of the newly confirmed supernova remnant MCSNR J0527-7104 in the Large Magellanic Cloud,” *A&A*, vol. 549, p. A99, [Jan. 2013](#).

P. Maggi, F. Haberl, R. Sturm, and D. Dewey, “XMM-Newton observations of SNR 1987A. II. The still increasing X-ray light curve and the properties of Fe K lines”, *A&A*, vol. 548, p. L3, [Dec. 2012](#).

P. Maggi, F. Haberl, L. M. Bozzetto, M. D. Filipović, S. D. Points, Y.-H. Chu, M. Sasaki, W. Pietsch, R. A. Gruendl, J. Dickel, R. C. Smith, R. Sturm, E. J. Crawford, and A. Y. De Horta, “Multi-frequency study of supernova remnants in the Large Magellanic Cloud. Confirmation of the supernova remnant status of DEM L205”, *A&A*, vol. 546, p. A109, [Oct. 2012](#).

A. Y. de Horta, M. D. Filipović, L. M. Bozzetto, **P. Maggi**, F. Haberl, E. J. Crawford, M. Sasaki, D. Urošević, W. Pietsch, R. Gruendl, J. Dickel, N. F. H. Tothill, Y.-H. Chu, J. L. Payne, and J. D. Collier, “Multi-frequency study of supernova remnants in the Large Magellanic Cloud. The case of LMC SNR J0530-7007”, *A&A*, vol. 540, p. A25, [Apr. 2012](#).

Non-refereed publications

R. Sturm, S. Carpano, F. Haberl, **P. Maggi**, and G. Vasilopoulos, “Swift J0513.4-6547 in outburst,” *The Astronomer’s Telegram*, 6483, [Sep. 2014](#).

P. Maggi, R. Sturm, F. Haberl, G. Vasilopoulos, and A. Udalski, “Swift J010745.0-722740, a new SMC Be/X-ray binary with possibly a very long orbital period,” *The Astronomer’s Telegram*, 5778, [Jan. 2014](#).

G. Vasilopoulos, R. Sturm, **P. Maggi**, and F. Haberl, “The X-ray outburst of RX J0520.5-6932 is reaching the Eddington luminosity,” *The Astronomer’s Telegram*, 5760, [Jan. 2014](#).

P. Maggi, R. Sturm, F. Haberl, and G. Vasilopoulos, “Confirmation of XMMU J010429.4-723136 as a high-mass X-ray binary,” *The Astronomer’s Telegram*, 5674, [Dec. 2013](#).

G. Vasilopoulos, R. Sturm, **P. Maggi**, and F. Haberl, “Discovery of the spin period and a new bright outburst of RXJ0520.5-6932,” *The Astronomer’s Telegram*, 5673, [Dec. 2013](#).

G. Vasilopoulos, R. Sturm, F. Haberl, **P. Maggi**, and A. Udalski, “Swift J045558.9-702001, a new HMXB in the LMC”, *The Astronomer’s Telegram*, 5540, [Nov. 2013](#).

F. Hofmann, R. Sturm, J. Greiner, G. Vasilopoulos, and **P. Maggi**, “New Swift UVOT transient SWIFT J004255.6+411412 in M 31”, *The Astronomer’s Telegram*, 5091, [May 2013](#).

G. Vasilopoulos, **P. Maggi**, R. Sturm, F. Haberl, W. Pietsch, A. Udalski, M. Sasaki, and S. Immler, “X-ray outburst of RX J0520.5-6932, confirmed as a Be/X-ray binary”, *The Astronomer’s Telegram*, 4748, [Jan. 2013](#).